

**School of Chemical and Petroleum Engineering**

**Development of a Hybrid Multi-Functional Adsorbent-Solar-  
Photocatalyst for Detecting and Removing Toxic Heavy Metals and  
Refractory Pollutants from Water/Wastewater**

**Khalid Khudhair Abbas**

**This thesis is presented for the Degree of  
Doctor of Philosophy  
of  
Curtin University**

**November 2018**

# Declaration

*To the best of my knowledge and belief this thesis contains no material previously published by any other person except where due acknowledgment has been made. This thesis contains no material which has been accepted for the award of any other degree or diploma in any university.*

Name: Khalid Khudhair Abbas

Signature: 

Date: November 2018

## Acknowledgements

*"In the name of God, the Most Gracious, the Most Merciful"*

I would like to express my sincere gratitude to all those who supported me in bringing this study into reality. I would also like to thank Curtin University for giving me the opportunity of undertaking my PhD.

First and foremost, I would like to express my sincere gratitude to my supervisor, Dr. Hussein Znad, who has supported me throughout my Doctoral Program in the Department of Chemical Engineering with his patience and encouragement. I truly believe that, this study would not be possible without his continuous support and supervision. I would like to convey my appreciation to Prof. Shaobin Wang and Dr. Rabiul Awual for his co-supervision and I wish to thank Dr. Sufia Hena for her support while written the articles in this thesis. Likewise, I would like to introduce my grateful to Prof. Vishnu Pareek, who has been my thesis chairperson.

Furthermore, I also extend sincere thanks to all the lab technicians, Andrew, Araya, Jason, Roshanak, Jimmy, Yu Long and Ann for their help and technical support in the labs and my research would not complete without the tremendous supports from them. Also, I am thankful to all the faculties and support staff of the Department of Chemical Engineering.

I would like to make particular thanks to my sponsor, Ministry of Higher Education and University of Technology, Baghdad, Iraq, to award me the PhD scholarship and financial support. Also, I would like acknowledge the partial support of chemical engineering department at Curtin University, Australia.

I am pleased to thank my lovely family members; parents, brothers, sisters, cousins, uncles for their utmost help and support to handle all of my obstacles and difficulties during my study.

## *Dedication*

*To my beloved spouse, Enas,  
Thanks for your great support and encouragement*

*To our children, Husham and Umniyah  
I am really grateful to both of you*



## ABSTRACT

The industrial activities have increased in the worldwide led to release a huge amount of dyes and toxic metal contaminants to the aquatic environment, and exerts effort for wastewater treatment. Several traditional methods have been applied to remediate these contaminated water including; coagulation, precipitation, filtrated membranes, adsorption and activated carbon; however, the selectivity, deficiency, post-separation as well as the high cost have affected the activity of these methods. To overcome these matters, novel catalysts such as  $\text{TiO}_2/\text{ZSM-5}$  mesoporous,  $\text{RGO}/\text{TiO}_2/\text{ZSM-5}$  mesoporous to treat water from dyes and optical conjugated mesoporous to treat water from ions were prepared and deeply effectively investigated. Using the synthesized  $\text{ZSM-5}$  mesoporous was an efficient method should consider in the solar photocatalysis and in conjugate optical mesoporous adsorbent preparations as a superiorly alternative host substrate.

In this dissertation, a novel multilayer of  $\text{TiO}_2/\text{ZSM-5}$  mesoporous was prepared using direct templating approach to study solar photocatalysis of methyl orange dye (MO). Different factors including the type of catalysts, pH solution, adsorption /photocatalysis processes, mineralization, the kinetic models and the contact time were investigated. The results showed that 99.55% of MO dye decolorized follows the conditions of  $20 \text{ mg L}^{-1}$  concentration of MO;  $2 \text{ g L}^{-1}$  concentration of  $\text{TiO}_2/\text{ZSM-5}$  mesoporous, light intensity of  $100 \text{ mW/cm}^2$ , and 180 min contact time. The results also revealed that the specific surface area ( $S_{\text{BET}}$ , Brunauer-Emmett-Teller) of  $\text{TiO}_2/\text{ZSM-5}$  mesoporous was  $1151 \text{ m}^2 \text{ g}^{-1}$ .  $\text{ZSM-5}$  multilamellar mesoporous interestingly worked as an adsorbent, electron/hole acceptor, and it's perfectly enhanced the dye photodecomposition.

Further investigation to enhance the solar photocatalysis activity of  $\text{TiO}_2/\text{ZSM-5}$  mesoporous was conducted by adding different wt % of the reduced graphene oxide (RGO). In this study, methylene blue dye (MB) was used as a pollutant model. The results showed that 10% wt of RGO in the nanocomposite of  $\text{TiO}_2/\text{ZSM-5}$  mesoporous significantly enhanced the photocatalytic activity, adsorbability and charge separation with extensively electron transfer into carbon-based nano-sheets. Based on the obtained results, 93% removal efficiency of MB was achieved after 120 min solar irradiation under the following conditions:  $10 \text{ mg L}^{-1}$  concentration of MB;  $0.5 \text{ g L}^{-1}$

concentration of 10% RGO/TiO<sub>2</sub>/ZSM-5 mesoporous; light intensity of 100 mW/cm<sup>2</sup>. The kinetic models, adsorbability, post-separation, reusability and stability of RGO/TiO<sub>2</sub>/ZSM-5 mesoporous were also investigated. The result also revealed that the intermediate were mainly found to consist of Azura (A) and Thionin compounds in the treated samples.

Ligand of 2-hydroxyacetophenone-<sup>4</sup>N-pyrrolidine thiosemicarbazones (HAPT) was anchored into a highly ordered ZSM-5 mesoporous to synthesize a novel visual mesoporous conjugate adsorbent (MCA). Mercury (Hg<sup>2+</sup>) was selected as a pollutant model in an aqueous media. Different parameters such as pH solution, interference of foreign metal ions, contact time and Hg<sup>2+</sup> concentration were investigated. The results showed that MCA exhibited a colour change from colourless to yellow at optimum pH conditions; also, a lower sensitive detection limit was calculated to be 3.69 µg L<sup>-1</sup> of Hg<sup>2+</sup>. The data well fitted with Langmuir isotherm model, and the maximum adsorption capacity of Hg<sup>2+</sup> was 166.7 mg/g; moreover, the data clarified that 0.10 M of thiourea-0.10 M HCl was used to simultaneously regenerate MCA for several run without significant loss in its initial performance.

Further research concerning mesoporous conjugate adsorbent was conducted by synthesizing a ligand of 2,6-Pyridinedicarboxaldehyde-Thiosemicarbazone (PDCTC) immobilized into ordered ZSM-5 mesoporous to prepare a new detective visual conjugate mesoporous adsorbent (MzCA). Lead (Pb<sup>2+</sup>) was selected as a pollutant model in an aqueous solution. Several factors such as pH solution, kinetics models, competing foreign ions and elution/reuses were investigated. MzCA was exhibited a distinct colour formed in both liquid/solid phases under optimum conditions. The results revealed that the detection limit of Pb<sup>2+</sup> was estimated to be 5.0 µg L<sup>-1</sup>, and maximum sorption capacity was 15.75 mg/g at optimum pH condition of 6.0. MzCA was eluted using 0.1 M of HCl and reused several cycles without considerable decadence in its activity.

# List of Publications

## Journal Papers

Abbas, K., Znad, H., & Awual, M. R. (2018). A ligand anchored conjugate adsorbent for effective mercury (II) detection and removal from aqueous media. *Chemical Engineering Journal*, 334, 432-443.

Znad, H., Abbas, K., Hena, S., & Awual, M. R. (2018). Synthesis a novel multilamellar mesoporous TiO<sub>2</sub>/ZSM-5 for photo-catalytic degradation of methyl orange dye in aqueous media. *Journal of Environmental Chemical Engineering*, 6(1), 218-227.

## Conference Paper

Abbas, K., Znad, H. & Hena, S., (23-28 July 2017). A sensitive ligand anchored high surface area ZSM-5 mesoporous for effective mercury (II) ions capturing and visual detection of contaminated water. Poster presentation, *Chemeca Conference, Centenary Congress (RACI)*, Melbourne, Australia.

# Table of contents

Declaration .....	I
Acknowledgements .....	II
Dedication .....	III
ABSTRACT.....	IV
List of Publications .....	VI
Table of contents .....	VII
List of Figures .....	XIII
List of Tables.....	XX
Nomenclature and Abbreviations.....	XXIII
<b>CHAPTER 1</b> .....	1
1 Thesis Overview .....	1
1.1 Background and Motives.....	1
1.1.1 Hybrid photocatalysts.....	2
1.1.2 Conjugate mesoporous visual adsorption.....	3
1.2 Research objectives .....	3
1.3 Research significant .....	4
1.4 Thesis Structure .....	5
<b>CHAPTER 2</b> .....	8
2 Literature Reviews.....	8
2.1 Introduction .....	8
2.2 Industrial effluent dyes .....	9
2.2.1 Treatment technologies of dyes .....	10
2.2.2 Advanced oxidation processes (AOPs).....	10
2.2.3 Enhanced the photocatalytic degradation process.....	12
2.2.3.1 TiO <sub>2</sub> - modified mesoporous silicate.....	13
2.2.3.2 TiO <sub>2</sub> - modified raw Zeolites.....	14
2.2.3.3 TiO <sub>2</sub> - modified reduced graphene oxide (RGO) .....	15
2.3 Industrial effluent of heavy metal ions .....	20

2.3.1	Treatment technologies of heavy metal ions.....	21
2.4	Ligand and the fundamental field theory .....	22
2.4.1	Ligand design concept.....	23
2.5	Ligands conjugate mesoporous .....	28
2.5.1	Mesoporous synthesis methods.....	28
2.5.1.1	Liquid-crystal templating (LCT) .....	28
2.6	Pathways of functionalized mesoporous / ligand .....	32
2.6.1	Post- synthetic grafting pathway .....	32
2.6.2	Co-condensation/or direct synthesis pathway .....	33
2.6.3	Hydrolysis and condensation pathway .....	34
2.7	Mesoporous zeolite.....	34
2.7.1	Pathways of the synthesis of mesoporous zeolites.....	35
2.7.1.1	Nanostructured carbon templating .....	35
2.7.1.2	Carbon and polymer aerogel templating .....	35
2.7.1.3	Cationic polymer templating .....	36
2.7.1.4	Organosilane templating.....	36
2.7.1.5	Hydrothermal pathway .....	37
2.8	Kinetic models.....	37
2.8.1	Equilibrium isotherm models.....	37
2.9	Summary .....	39
<b>CHAPTER 3</b>	.....	<b>41</b>
<b>3</b>	<b>Experimental Methods.....</b>	<b>41</b>
3.1	Introduction .....	41
3.2	Chemicals .....	41
3.2.1	Chemicals for catalysts preparation .....	41
3.2.2	Organic pollutant model and their intermediates .....	42
3.2.3	Inorganic pollutants.....	43
3.3	Synthesis of the catalysts.....	43
3.3.1	Synthesis of TiO <sub>2</sub> /ZSM-5 multilamellar mesoporous.....	43
3.3.2	Synthesis of RGO/TiO <sub>2</sub> /ZSM-5 Mesoporous .....	44
3.3.3	Synthesis of mesoporous conjugate adsorbent (MCA).....	45
3.3.3.1	ZSM-5 mesoporous .....	45
3.3.3.2	Ligand HAPT (2-hydroxyacetophenone- <sup>4</sup> N –pyrrolidine thiosemicarbazones).....	46
3.3.3.3	MCA catalyst.....	46

3.3.4	Synthesis of mesoporous ZSM-5 conjugate adsorbent (MzCA): Pb <sup>+2</sup> detection	47
3.3.4.1	ZSM-5 mesoporous	47
3.3.4.2	Ligand PDCTC (2,6-Pyridinedicarboxaldehyde-Thiosemicarbazone)	47
3.3.4.3	MzCA catalyst	48
3.4	Characterization instruments	48
3.4.1	Field emission scanning electron microscope (FESEM)	48
3.4.2	The specific surface area and pore size measurement	48
3.4.3	Powder X-Ray Diffractionometric Measurement	49
3.4.4	Fourier-transformed infrared spectroscopy (FTIR)	49
3.5	Experimental procedures	49
3.5.1	Solar photocatalytic degradation experiments	49
3.5.1.1	Methyl Orange model (MO)	49
3.5.1.2	Methylene Blue model (MB)	50
3.5.2	Visual mesoporous conjugate adsorbent experiments	51
3.5.2.1	Mercury Hg <sup>+2</sup> detection	51
3.5.2.2	Lead Pb <sup>+2</sup> detection	51
3.6	Analytical procedures	52
3.6.1	Total organic carbon analyser TOC	52
3.6.2	High Performance Liquid Chromatograph analysis HPLC	52
3.6.3	ICP- Mass Spectrometer	53
3.6.4	UV-Vis diffuse spectrophotometer analysis	54
3.6.5	Specific surface area and porosity analyzer	54
3.6.6	Rotary evaporator	55
3.6.7	Autoclave	56
<b>CHAPTER 4</b>		<b>57</b>
4	Synthesis a novel multilamellar mesoporous TiO <sub>2</sub> /ZSM-5 for photocatalytic degradation of methyl orange dye in aqueous media	57
4.1	Introduction	57
4.2	Experimental work	59
4.2.1	Chemicals	59
4.2.2	Synthesis of TiO <sub>2</sub> /ZSM-5 mesoporous multilamellar	59
4.2.3	Characterizations of samples	60
4.2.4	Photocatalytic experiments of MO dye	60
4.3	Results and discussion	61

4.3.1	Characterization of the photocatalys .....	61
4.3.1.1	XRD.....	61
4.3.1.2	BET surface areas and pore distribution .....	62
4.3.1.3	FESEM images .....	68
4.3.1.4	Fourier-transformed infrared spectroscopy (FTIR) Analysis.....	69
4.4	Photocatalyst activities .....	70
4.4.1	Effects of the catalyst type .....	70
4.4.2	Effects of the pH .....	72
4.4.3	Kinetics studies .....	73
4.4.4	TOC removal.....	76
4.4.5	Recycling and regeneration of the TiO <sub>2</sub> /ZSM-5 mesoporous.....	77
4.5	Summary .....	80
<b>CHAPTER 5 .....</b>		<b>82</b>
5	Synthesis novel RGO/TiO <sub>2</sub> /ZSM-5 Mesoporous for Adsorption and Photocatalytic Degradation of Methylene Blue from aqueous media .....	82
5.1	Introduction .....	82
5.2	Experimental work .....	84
5.2.1	Chemicals.....	84
5.2.2	Incorporation of TiO <sub>2</sub> /ZSM-5 mesoporous onto RGO .....	84
5.2.3	Characterizations of photocatalysts.....	85
5.2.4	Adsorption and photocatalytic experiments.....	85
5.3	Results and discussion.....	86
5.3.1	Characterizations of the catalysts.....	86
5.3.1.1	XRD analysis.....	86
5.3.1.2	BET specific surface areas and pore distribution.....	87
5.3.1.3	Fourier-transformed infrared spectroscopy (FTIR) analysis.....	92
5.3.1.4	FESEM images and EDX analysis.....	93
5.3.2	Removal efficiency of MB dye .....	96
5.3.3	Kinetic studies .....	99
5.3.4	Decolourisation of the MB dye .....	101
5.3.5	The mineralization of MB dye .....	102
5.3.6	Intermediates and mineralization of MB dye.....	103
5.3.7	Stability and regeneration .....	105
5.4	Summary .....	107

<b>CHAPTER 6</b> .....	108
6 A ligand anchored conjugate adsorbent for effective mercury (II) detection and removal from aqueous media .....	108
6.1 Introduction .....	108
6.2 Experimental work .....	112
6.2.1 Chemicals .....	112
6.2.2 Synthesis of 2-hydroxyacetophenone- <sup>4</sup> N –pyrrolidine thiosemicarbazones (HAPT) ligand .....	112
6.2.3 Synthesis of mesoporous silica and mesoporous-conjugate adsorbent (MCA) .....	113
6.2.4 Characterization of MCA .....	113
6.2.5 Determination of Hg (II) ions .....	114
6.2.6 Hg (II) ions removal, regeneration and reuses .....	114
6.2.7 Influence of co-existing ions .....	115
6.3 Results and discussion .....	115
6.3.1 Characterizations .....	115
6.3.1.1 BET specific surface areas and pore distribution .....	115
6.3.1.2 Fourier-transformed infrared spectroscopy (FTIR) analysis .....	119
6.3.1.3 FESEM analysis .....	120
6.3.2 Hg (II) ions recognition parameters .....	121
6.3.3 Hg (II) ions adsorption .....	125
6.3.4 Equilibrium adsorption isotherms .....	128
6.3.5 Comparison of adsorption capacity .....	129
6.3.6 Effect of foreign ions .....	130
6.3.7 Elution and recycle of MCA catalyst .....	131
6.4 Summary .....	132
<b>CHAPTER 7</b> .....	134
7 A novel optical mesoporous conjugate adsorbent for monitoring and sorption of ultra-trace Lead (II) from aqueous media .....	134
7.1 Introduction .....	134
7.2 Experimental work .....	137
7.2.1 Chemicals .....	137
7.2.2 Synthesis of 2,6-Pyridinedicarboxaldehyde-Thiosemicarbazone (PDCTC) ligand .....	138
7.2.3 Synthesis of mesoporous silica and mesoporous-conjugate adsorbent (MzCA) .....	138
7.2.4 Characterization of MzCA .....	139



7.2.5	Optical Pb <sup>2+</sup> sensing and capturing .....	139
7.2.6	Lead (Pb <sup>2+</sup> ) sorption, regeneration and reuses .....	140
7.2.7	Influence of foreign co-existing ions.....	141
7.3	Results and discussion.....	141
7.3.1	BET specific surface areas and pore distribution.....	141
7.3.2	Fourier-transformed infrared spectroscopy (FTIR) analysis.....	145
7.3.3	FESEM analysis .....	146
7.3.4	Lead (Pb <sup>2+</sup> ) detection .....	148
7.3.5	Lead (Pb <sup>2+</sup> ) sorption parameters .....	153
7.3.5.1	Effect of pH.....	153
7.3.5.2	Effect of contact time .....	154
7.3.5.3	Equilibrium sorption isotherm.....	155
7.3.5.4	Effect of foreign competing ions.....	157
7.4	Elution and regeneration .....	158
7.5	Summary .....	159
<b>CHAPTER 8</b>	.....	161
8	Conclusion and Recommendations.....	161
8.1	General Conclusions and Discussions.....	161
8.2	Recommendations for future research.....	163
<b>References</b>	.....	166
<b>APPENDICES</b>	.....	187
APPENDIX A	.....	187
APPENDIX B	.....	200
APPENDIX C	.....	203

## List of Figures

<b>Figure 1-1</b> Thesis structure.....	7
<b>Figure 2-1</b> Treatment techniques for the removal of dyes from wastewater effluent (Saratale et al., 2011) .....	10
<b>Figure 2-2</b> Principles of oxidative decomposition of photocatalysts .....	12
<b>Figure 2-3</b> Synthesis of multilayered Titania through mesoporous silica channels..	14
<b>Figure 2-4</b> Scheme showing the formation process of TiO <sub>2</sub> fibres on mesoporous spheres.....	14
<b>Figure 2-5</b> Oxidation of graphene to form graphene oxide.....	16
<b>Figure 2-6</b> The chemical structure of reduced graphene oxide (RGO).....	17
<b>Figure 2-7</b> A simplified schematic description the key features for synthesis of RGO/semiconductor nanocomposite with the major mechanism reaction steps in photocatalytic degradation under solar light irradiation .....	18
<b>Figure 2-8</b> Schematic illustration for the synthesis and the structure of SnO <sub>2</sub> /Graphene nanosheets.....	19
<b>Figure 2-9</b> Treatment techniques for heavy metal ions (Mohammed et al., 2011) ...	22
<b>Figure 2-10</b> Complex formation during the recognition of (a) Se(IV), (b) pd(II), (c)Cd(II), Cu(II) and pd(II) ions in solution at a temperature of 25 <sup>0</sup> C and pH = 1.5, 1.5, 12.5, 12, 7, respectively .....	25
<b>Figure 2-11</b> The range of pH for different ions solution that can be detected by several ligands.....	25
<b>Figure 2-12</b> Liquid crystal templating mechanism using structure directing agent: pathway 1) true liquid-crystal template mechanism, pathway 2) cooperative liquid-crystal template mechanism .....	29

<b>Figure 2-13</b> Schematic showing the aggregation of amphiphiles into micelles and then into lyotropic liquid crystalline phases as a function of amphiphile concentration and temperature.....	30
<b>Figure 2-14</b> The post- synthetic grafting method for organic modification of mesoporous phases with organosilanes of the type (R'O)3SiR. R=organic functional group .....	32
<b>Figure 2-15</b> Co-condensation pathway for the organic modification of mesoporous pure silica phases. R=organic functional group .....	33
<b>Figure 2-16</b> The hydrolysis and condensation pathway constructed by bissilylated organic bridging units. R= organic bridge .....	34
<b>Figure 2-17</b> types of the equilibrium adsorption isotherm models .....	38
<b>Figure 3-1</b> Summary of the direct template method for synthesis of TiO <sub>2</sub> /ZSM-5 multilamellar mesoporous.....	44
<b>Figure 3-2</b> Systematic consequences of the preparation 10% RGO-TiO <sub>2</sub> /ZSM-5 using 22 mg RGO and 200 mg of TiO <sub>2</sub> /ZSM-5 mesoporous .....	45
<b>Figure 3-3</b> the synthesized method of visual MCA adsorbent mesoporous.....	47
<b>Figure 3-4</b> Solar simulator (100 mW/cm <sup>2</sup> ) used for the solar photocatalytic degradation experiments .....	50
<b>Figure 3-5</b> Total Organic Carbon (TOC) Analyser.....	52
<b>Figure 3-6</b> High Performance Liquid Chromatograph (HPLC) instrument.....	53
<b>Figure 3-7</b> ICP- Mass Spectrometer instrument.....	54
<b>Figure 3-8</b> UV-Vis spectrophotometer.....	54
<b>Figure 3-9</b> Specific surface area and porosity analyser.....	55
<b>Figure 3-10</b> Vacuum Rotary evaporator.....	55
<b>Figure 3-11</b> Autoclave.....	56
<b>Figure 4-1</b> Schematic diagram for the preparation of photocatalysts (TiO <sub>2</sub> /ZSM-5)60	

<b>Figure 4-2</b> X-ray diffraction patterns of ZSM-5, TiO <sub>2</sub> /ZSM-5, TiO <sub>2</sub> Degussa, ZnO/ZSM-5 and TiO <sub>2</sub> -mesoporous .....	62
<b>Figure 4-3</b> N <sub>2</sub> adsorption-desorption isotherms of (a) ZSM-5, (b) TiO <sub>2</sub> /ZSM-5 (c) TiO <sub>2</sub> -mesopores and (d) ZnO/ZSM-5 and also corresponding BJH pore size distribution curves of samples (e) .....	65
<b>Figure 4-4</b> SEM images of a) ZSM-5, b) TiO <sub>2</sub> /ZSM-5, c) ZnO/ZSM-5, d) TiO <sub>2</sub> -mesoporous .....	69
<b>Figure 4-5</b> FTIR spectra of ZSM-5, ZnO/ZSM-5, TiO <sub>2</sub> /ZSM-5, TiO <sub>2</sub> -mesoporous.	70
<b>Figure 4-6</b> Removal efficiency of MO dye decolourization using TiO <sub>2</sub> /ZSM-5, TiO <sub>2</sub> -mesopores, TiO <sub>2</sub> Degussa, ZnO/ZSM-5 and ZSM-5 .....	71
<b>Figure 4-7</b> Effect of pH of solution on removal efficiency of MO .....	72
<b>Figure 4-8</b> The pseudo-first order reaction rate .....	75
<b>Figure 4-9</b> The pseudo-Second order reaction rate .....	75
<b>Figure 4-10</b> TOC removal of 20 mg L <sup>-1</sup> methyl orange dye by using different types of catalyst .....	77
<b>Figure 4-11</b> the regeneration efficiency of TiO <sub>2</sub> /ZSM-5 mesoporous after a number of cycles for methyl orange dye contamination .....	78
<b>Figure 4-12</b> The BET surface area of TiO <sub>2</sub> /ZSM-5 mesoporous after six completed cycles of usage .....	79
<b>Figure 4-13</b> the XRD comparison between the TiO <sub>2</sub> /ZSM-5 before used and after 6 <sup>th</sup> cycle's usage .....	79
<b>Figure 4-14</b> FTIR spectra of the regenerated TiO <sub>2</sub> /ZSM-5 after 6 <sup>th</sup> run .....	80
<b>Figure 5-1</b> XRD patterns of RGO, TiO <sub>2</sub> , ZSM-5, TiO <sub>2</sub> /ZSM-5 mesoporous, 5% RGO/TiO <sub>2</sub> /ZSM-5, 10% RGO/TiO <sub>2</sub> /ZSM-5 and 15% RGO/TiO <sub>2</sub> /ZSM-5 .....	86
<b>Figure 5-2</b> N <sub>2</sub> adsorption-desorption isotherms of (a) TiO <sub>2</sub> /ZSM-5 mesoporous (b) 5% RGO/TiO <sub>2</sub> /ZSM-5 (c) 10% RGO/TiO <sub>2</sub> /ZSM-5 (d) 15% RGO/TiO <sub>2</sub> /ZSM-5 and also corresponding BJH pore size distribution curves of the samples (e).....	91

<b>Figure 5-3</b> FTIR spectra of TiO <sub>2</sub> /ZSM-5, 5% RGO/TiO <sub>2</sub> /ZSM-5, 10% RGO/TiO <sub>2</sub> /ZSM-5 and 15% RGO/TiO <sub>2</sub> /ZSM-5.....	93
<b>Figure 5-4</b> FESEM and EDX analysis of (a, b) RGO, (c, d) 10% RGO/TiO <sub>2</sub> /ZSM-5, (e, f) TiO <sub>2</sub> /ZSM-5, (g, h) 10% RGO/TiO <sub>2</sub> /ZSM-5.....	96
<b>Figure 5-5</b> (a) The plot of C <sub>t</sub> /C <sub>0</sub> versus time in the presence of photocatalyst under the solar light, the concentration of the catalysts were 0.5 g L <sup>-1</sup> and a solar exposure time of 120 min (b) removal efficiency of different catalysts for adsorption and photo-degradation regions.....	98
<b>Figure 5-6</b> (a) Pseudo first-order kinetic plots (b) Pseudo second-order kinetic plots for the 10 mg L <sup>-1</sup> MB dye concentration using different catalyst.....	100
<b>Figure 5-7</b> decolonization of various concentrations of MB dye versus time .....	102
<b>Figure 5-8</b> the removal efficiency of TOC using different types of the catalysts 0.5 g L <sup>-1</sup> concentration at initial MB dye concentration is 10 mg L <sup>-1</sup> .....	103
<b>Figure 5-9</b> HPLC profile of MB dye before and after photocatalytic degradation	104
<b>Figure 5-10</b> Proposed pathways for photocatalytic degradation of MB dye solution .....	105
<b>Figure 5-11</b> the regeneration efficiency of 10%RGO/TiO <sub>2</sub> /ZSM-5 mesoporous after a number of cycles .....	106
<b>Figure 5-12</b> the proposed mesoporosity effects on the TiO <sub>2</sub> particles.....	106
<b>Figure 6-1</b> the chemical reaction steps of synthesized 2-hydroxyacetophenone- <sup>4</sup> N – pyrrolidine thiosemicarbazones (HAPT) Ligand.....	112
<b>Figure 6-2</b> the N <sub>2</sub> adsorption-desorption isotherms curves (a, b, c) and corresponding the BJH pore size distribution curves of samples (d).....	118
<b>Figure 6-3</b> Specific functional group observation by FTIR spectrum of HAPT ligand .....	119
<b>Figure 6-4</b> FESEM images of ZSM-5 (a), ZSM-5 mesoporous (b, c) and micrograph of HAPT immobilized composite adsorbent (d) .....	121

<b>Figure 6-5</b> The pH effect for Hg(II) ions treatment during the measurement of absorbance spectra of [Hg(II)-HAPT] <sup>n+</sup> complexes solution at $\lambda=387$ nm and with condition 2.0 mg L <sup>-1</sup> of Hg (II) ions, 20 mg of MCA catalyst at 25°C in 10 ml volume for 15 min.....	123
<b>Figure 6-6</b> The change of colour optimization of Hg (II) ions concentrations at pH 12.5 and (b) was represented the calibration profile of Hg (II) ions concentrations with spectral absorbance at $\lambda=387$ nm. The inset in graph (b) shows the low limited responses for Hg (II) ions with a liner fit in the Hg (II) ions concentration range. The A and A <sub>0</sub> are represented the absorbance signal responses of the solution after and before addition of Hg (II) ions .....	124
<b>Figure 6-7</b> Effect of competing ions (cations and anions) when the Hg (II) ions concentration was 2.0 mg L <sup>-1</sup> , the cations concentration was 40 mg L <sup>-1</sup> . The listed foreign ions area: (1) Pb <sup>2+</sup> , (2) Zn <sup>2+</sup> , (3) Cd <sup>2+</sup> , (4) Al <sup>3+</sup> , (5) Fe <sup>3+</sup> , (6) Mg <sup>2+</sup> , (7) Ca <sup>2+</sup> , (8) Ag <sup>2+</sup> , (9) K <sup>+</sup> , (10) Na <sup>+</sup> (11) (blank and (12) Hg(II) ions 2.0 mg L <sup>-1</sup> . The interfering (150 mg L <sup>-1</sup> ) anions listed in order (4–10): (4) chloride, (5) sulphate, (6) carbonate, (7) citrate, (8) nitrate, (9) bicarbonate and (10) phosphate.....	124
<b>Figure 6-8</b> the pH effect on the Hg (II) ions adsorption on the ligand (HAPT) anchored mesoporous adsorbent where initial Hg (II) ions concentration was 2.0 mg L <sup>-1</sup> (a) and the effect of reaction time for Hg (II) ions where the initial Hg (II) ions concentration was 2.0 mg L <sup>-1</sup> (b) .....	127
<b>Figure 6-9</b> the possible stable complex formation of Hg (II) ions and HAPT ligand at optimum conditions.....	127
<b>Figure 6-10</b> Adsorption isotherm of Hg (II) ions of the MCA with the linear form as fitted by the Langmuir isotherms model (initial concentrations: 2.65–75 mg L <sup>-1</sup> ; shaking time: 2 h; adsorbent amount (MCA): 20 mg; volume of solution: 100 ml. ....	129
<b>Figure 6-11</b> Selectivity of the MCA catalyst towards Hg (II) ions in the presence of different ions .....	131
<b>Figure 6-12</b> Regeneration of the adsorbent where elution was performed with 0.10M thiourea-0.10M HCl .....	132

<b>Figure 7-1</b> Chemical reaction of synthesized 2,6-Pyridinedicarboxaldehyde-Thiosemicarbazone (PDCTC) ligand.....	138
<b>Figure 7-2</b> N <sub>2</sub> adsorption-desorption isotherms curves (a) ZSM-5, (b) mesoporous ZSM-5 (c) mesoporous ZSM-5 conjugate adsorbent (MzCA) and corresponding the BJH pore size distribution curves of samples (d).....	144
<b>Figure 7-3</b> Specific functional groups of PDCTC ligand analysed by FTIR spectroscopy.....	146
<b>Figure 7-4</b> FESEM images of ZSM-5 (a), ZSM-5 mesoporous (b) and micrograph of PDCTC incorporated into composite adsorbent (c), MzCA after used in the adsorption process (d) .....	148
<b>Figure 7-5</b> effect of pH on the Pb <sup>2+</sup> during the absorbance spectra measurement of [pb <sup>2+</sup> - PDCTC] <sup>n+</sup> complexes solution at λ= 440 nm, concentration of 2.0 mg L <sup>-1</sup> of Pb <sup>2+</sup> , 10 mg of MzCA at 25°C in 20 ml volume for 30 minutes.....	149
<b>Figure 7-6</b> The optimization of the change of different Pb <sup>2+</sup> concentrations at pH 6.0 .....	150
<b>Figure 7-7</b> The calibration curve of Pb <sup>2+</sup> concentrations with spectral absorbance at λ= 440 nm. The inset in graph (B) shows the low limited responses for Pb <sup>2+</sup> with a linear fit in the Pb <sup>2+</sup> concentration range. The R and R <sub>0</sub> represented the absorbance signal responses of the solution after and before addition of Pb <sup>2+</sup> .....	151
<b>Figure 7-8</b> Effect of competing ions (cations/ anions) when the Pb <sup>2+</sup> concentration was 2.0 mg L <sup>-1</sup> , the cations concentration was 20 mg L <sup>-1</sup> . The listed foreign ions area: (1) Cu <sup>2+</sup> , (2) Fe <sup>3+</sup> , (3) Hg <sup>2+</sup> , (4) Ag <sup>2+</sup> , (5) Co <sup>2+</sup> , (6) Na <sup>+</sup> , (7) AL <sup>3+</sup> (8) Ca <sup>2+</sup> , (9)K <sup>+</sup> , (10)Mn <sup>2+</sup> , (11)Zn <sup>2+</sup> , (12 ) Cd <sup>2+</sup> (blank and (13) Pb <sup>2+</sup> 2.0 mg L <sup>-1</sup> . The different concentrations of interfering anions listed in order (6–13): (6) Cl <sup>-</sup> , (7) HCO <sub>3</sub> , (8) NO <sub>3</sub> , (9) CO <sub>3</sub> <sup>2-</sup> , (10) PO <sub>4</sub> <sup>3-</sup> , (11) SO <sub>4</sub> <sup>2-</sup> , (12) SO <sub>3</sub> <sup>2-</sup> , (13) SCN <sup>-</sup> .....	152
<b>Figure 7-9</b> The effect of pH on the sorption efficiency of Pb <sup>2+</sup> when the initial Pb <sup>2+</sup> concentration was 2.0 mg L <sup>-1</sup> .....	154
<b>Figure 7-10</b> Effect of reaction time on the sorption efficiency of Pb <sup>2+</sup> when the initial concentration of Pb <sup>2+</sup> was 2.0 mg L <sup>-1</sup> .....	155
<b>Figure 7-11</b> Adsorption isotherm of Pb <sup>2+</sup> as fitted by the Langmuir isotherms model with the linear form (inset). The initial concentrations of Pb <sup>2+</sup> : 8.0-50.0 mg L <sup>-1</sup> ;	

stirring time: 2h; conjugated adsorbent amount is 10 mg; the solution volume is 20 ml .....	156
<b>Figure 7-12</b> The sorption efficiency of Pb <sup>2+</sup> in the presence of different metal ions in aqueous media.....	157
<b>Figure 7-13</b> The proposed stable complex formation of Pb <sup>2+</sup> and PDCTC ligand at optimum conditions.....	158
<b>Figure 7-14</b> The stable complex formation of Pb <sup>2+</sup> and PDCTC ligand at pH 6.0 and elution/regeneration is 0.1 M HCl eluent.....	159
<b>Figure 7-15</b> The performance of the regenerated conjugated mesoporous adsorbent after conducting several cycles using 0.1 M HCl eluent.....	159
<b>Figure A. 1</b> the spectra absorbance of MB dye at different concentration (a) 10 mg L <sup>-1</sup> , 20 mg L <sup>-1</sup> , 30 mg L <sup>-1</sup> and 40 mg L <sup>-1</sup> during 120 min contact time, 500 mg L <sup>-1</sup> of 10%RGO/TiO <sub>2</sub> /ZSM-5 mesoporous at room temperature.....	195
<b>Figure A. 2</b> BET specific surface area of the Non-mesoporous 10%RGO/TiO <sub>2</sub> /ZSM-5.....	196
<b>Figure A. 3</b> Preparation procedure of the HATP ligand .....	196
<b>Figure A. 4</b> FTIR analysis spectrum of the synthesized MCA before and after used .....	197



## List of Tables

<b>Table 2-1</b> Different types of zeolite modified TiO <sub>2</sub> applied in wastewater treatment .....	15
<b>Table 2-2</b> Classification of hard and soft ions According to the HSAB (Hard and Soft acids and Bases) Principle of Pearson .....	23
<b>Table 2-3</b> Various ligands, chemical structure that adsorbed heavy metal ions from aqueous solution at different condition .....	25
<b>Table 2-4</b> Syntheses of mesoporous in the presence of, cationic or non-ionic surfactants .....	31
<b>Table 3-1</b> Names, abbreviations and chemical structures of the organic pollutants and their intermediate compounds in this study include: .....	42
<b>Table 4-1</b> Specific surface area (S <sub>BET</sub> ), pore volume (V) and average pore diameter (d) for ZSM-5, TiO <sub>2</sub> Degussa, TiO <sub>2</sub> /ZSM-5, ZnO/ZSM-5, and TiO <sub>2</sub> -mesoporous ...	66
<b>Table 4-2</b> Comparison of surface area among different catalysts .....	67
<b>Table 5-1</b> Specific surface area (S <sub>BET</sub> ), pore volume (V) and average pore diameter (d) for catalysts.....	91
<b>Table 5-2</b> Parameters of pseudo first order and second order kinetic models with the removal efficiency .....	101
Table 6. 1 Specific surface area (S <sub>BET</sub> ), pore volume (V) and average pore diameter (d) for commercial ZSM-5, ZSM-5mesopoures and ZSM-5mesopoures/HAPT ....	116
<b>Table 6-2</b> Comparison of maximum adsorption capacity of Hg (II) ions with different forms of adsorbent materials .....	130

<b>Table 7-1</b> Specific surface area ( $S_{\text{BET}}$ ), pore volume (V) and average pore diameter (D) for ZSM-5, ZSM-5mesopoures and ZSM-5 mesoporous/ PDCTC.....	145
<b>Table 7-2</b> Tolerance limit for competing cations and anions adding 2.0 mg L <sup>-1</sup> of Pb <sup>2+</sup> detection with conjugated adsorbent.....	153
<b>Table A.1</b> the raw data of the first order reaction rate of MO dye .....	187
<b>Table A.2</b> the raw data of the second order reaction rate of MO dye .....	188
<b>Table A.3</b> the raw data of the first order reaction rate of the 10 mg L <sup>-1</sup> concentration of the MB degradation .....	189
<b>Table A.4</b> the raw data of the second order reaction rate of the 10 mg L <sup>-1</sup> concentration of the MB degradation.....	190
<b>Table A.5</b> the raw data of the first order reaction rate of the 20 mg L <sup>-1</sup> concentration of the MB degradation .....	191
<b>Table A.6</b> the raw data of the second order reaction rate of the 20 mg L <sup>-1</sup> concentration of the MB degradation.....	191
<b>Table A.7</b> the raw data of the first order reaction rate of the 30 mg L <sup>-1</sup> concentration of the MB degradation .....	192
<b>Table A.8</b> The raw data of the second order reaction rate of the 30 mg L <sup>-1</sup> concentration of the MB degradation.....	192
<b>Table A.9</b> The raw data of the first order reaction rate of the 40 mg L <sup>-1</sup> concentration of the MB degradation .....	193
<b>Table A.10</b> The raw data of the second order reaction rate of the 40 mg L <sup>-1</sup> concentration of the MB degradation.....	193
<b>Table A. 11</b> the change of colour optimization of Hg(II) ions concentrations at pH 12.5 and (b) was represented the calibration profile of Hg(II) ions concentrations with spectral absorbance at $\lambda=387$ nm .....	197
<b>Table A. 12</b> the low limited responses for Hg (II) ions with a liner fit in the Hg (II) ions concentration range .....	198

<b>Table A. 13</b> Adsorption isotherm of Hg (II) ions of the MCA. (Initial concentrations: 2.65–75 mg L <sup>-1</sup> ; shaking time: 2 h; adsorbent amount (MCA): 20 mg; volume of solution: 100 ml .....	198
<b>Table A. 14</b> the linear form as fitted by the Langmuir isotherms model .....	198
<b>Table A. 15</b> the change of colour optimization of Pb <sup>2+</sup> concentrations at pH 6.0 and (b) was represented the calibration profile of Pb <sup>2+</sup> concentrations with spectral absorbance at $\lambda= 440$ nm.....	199
<b>Table A. 16</b> the low limited responses for Pb <sup>2+</sup> with a liner fit in the Pb <sup>2+</sup> concentration range .....	199
<b>Table A. 17</b> Adsorption isotherm of Pb <sup>2+</sup> of the MzCA. (Initial concentrations: 8.0-50.0 mg L <sup>-1</sup> ; shaking time: 2 h; adsorbent amount (MzCA): 10 mg; volume of solution: 20 ml .....	199
<b>Table A. 18</b> the linear form as fitted by the Langmuir isotherms model for lead ions detection. ....	199
<b>Table 1-C: Co-Author attribution for chapter 4</b> .....	204
<b>Table 2-C: Co-Author attribution for chapter 6</b> .....	204

## Nomenclature and Abbreviations

UNICEF	United Nations International Children's Emergency Fund
TMOS	Tetramethyl Orthosilicate
TEOS	Tetraethyl Orthosilicate
ZSM-5	Zeolite Socony Mobil-5
TiO <sub>2</sub>	Titanium Dioxide
P <sub>25</sub>	Degussa Titanium Dioxide
MO	Methyl orange dye
HSAB	Hard and Soft acids and Bases
COD	Chemical Oxygen Demand
TOC	Total Organic Carbon
MB	Methylene blue dye
G	Graphene
GO	Graphene oxide
RGO	Reduced graphene oxide
HAPT	2-hydroxyacetophenone- <sup>4</sup> N-pyrrolidine thiosemicarbazones
Hg <sup>+2</sup>	Mercury ions
PDCTC	2,6-Pyridinedicarboxaldehyde-Thiosemicarbazone
Pb <sup>+2</sup>	Lead ions
LD	The detection ions limit
MCA	Mesoporous conjugate adsorbent
MzCA	Mesoporous Zeolite conjugate adsorbent
ICP-MS	Inductively coupled plasma mass spectrometry
ICP-AES	Inductively coupled plasma atomic emission spectroscopy
η	Degradation Efficiency
AOPs	Advanced Oxidation Processes
UV	Ultra Violet
SBA-15	Santa Barbara Amorphous-15
MCM-41	Mobil Catalytic Material Number 41
HSS	Hydrolytic Surface Sol-gel Process

2D	Two- Dimensional
3D	Three-Dimensional
SNs	Semiconductor nanocomposites
NIR	Near Infrared
NHE	Standard hydrogen electrode
WHO	World Health Organization
LCT	Liquid-Crystal Templating
M41S	Mesoporous molecular sieves Number 41
P <sub>123</sub>	Pluronic surfactant
TIPB	1,3,5-triisopropylbenzene
MCM	Mobil Composition of Matter No. 41
SBA	Santa Barbara Amorphous
PMOs	Periodic Mesoporous Organosilicas
PDADMAC	Polydiallyldimethyl Ammonium Chloride
L-H	Langmuir-Hinshelwood
q <sub>e</sub>	Equilibrium adsorption capacity
qt	Adsorption capacity
q <sub>m</sub>	Maximum adsorption capacity
C <sub>o</sub>	Initial concentration
C	Final concentration
C <sub>e</sub>	Equilibrium concentration
FESEM	Field emission scanning electron microscope
EDX	Energy-dispersive X-ray spectroscopy
FTIR	Fourier-transformed infrared spectroscopy
HPLC	High Performance Liquid Chromatograph analysis
XRD	X-Ray Diffraction
S <sub>BET</sub>	Specific surface area of the Brunnauer-Emmett-Teller method
λ	wavelength
BJH	Barrett–Joyner–Halenda model
BET	Brunauer-Emmett-Teller theory
He	Helium
DAF	Dissolved air floatation

HPS	High-Purity Standards
DI	Deionized water
MLVs	Multilamellar vesicles
IUPAC	International Union of Pure and Applied Chemistry
KPa	kilopascal

### Units

Å	Angstrom
wt %	weight percent
g	gram
mg	Milligram
mW	Miliwatt
Min	Minute
h	Hour
V	Volume
°C	Degree Celsius
μ	Micro
cm	Centimetre
m	Meter
nm	Nanometre
ml	Millilitre
mmo:	Millimoles
P/Po	Gas's Relative Pressure
μM	Micrometre

# CHAPTER 1

## 1 Thesis Overview

### 1.1 Background and Motives

According to UNICEF at least 1.1 billion people live without access to potable water. Water is a basic need for everyday living not only for human consumption, but also for energy, industries and agricultural activities (Melo Zurita et al., 2018), which created major challenges for wastewater treatment processes. About 10% of diseases worldwide could be prevented by access to potable water (Lonergan, 2018). Such environmental and health issues have motivated a lot of researchers to design innovative and effective technologies with low energy consumption and high efficiency for treating wastewater. Chemicals that can contaminate water sources could be organic (such as alkanes, aliphatic, alcohols and aromatic compounds) and inorganic pollutants (such as alkaline compounds, nitrate or nitrite, sulphate) and heavy metal ions such as lead, mercury, nickel, silver and cadmium and so forth. Since the dawn of the industrial age, the coexistence of toxic inorganic and organic refractory pollutants in aquatic systems has continued to rise to an alarming rate that pose a serious threat to worldwide health (H. Chen, Wang, Li, & Wang, 2015). These contaminants are released from several industrial activities such as textile and dye manufacturing, municipal wastewater effluent, detergents, surfactants, pesticides, pharmaceutical manufactures, mining and metallurgical industries. These are majorly non-biodegradable contaminants that are difficult to remove from aquatic systems when traditional purification treatments applied. These (treatments) limitations has therefore prompted the investigate and discovery of new commercial hybrid photocatalysts and conjugate mesoporous visual adsorption catalysts for the purposes

of removing organic and inorganic refractory pollutants from water sources to mitigate the impact of water quality (Awual, Rahman, Yaita, Khaleque, & Ferdows, 2014; Dong et al., 2014; Ghosh & Bhattacharyya, 2002; Kaplan, Yildirim, Yildirim, & Tayhan, 2011).

### 1.1.1 Hybrid photocatalysts

Titanium dioxide (TiO<sub>2</sub>) photocatalyst is efficiently used for wastewater remediation process; however, it has been found that post-separation and hole/electron pair recombination of TiO<sub>2</sub> photocatalyst are challenging in this process. To resolve the post separation problems, different immobilizer silica substrates were employed to improve the post-separation such as clays composites which could prepare using the blending techniques (Chong, Vimonses, et al., 2009). Compare to other immobilizer, the natural zeolites are abundant, inexpensive, having alumino-silicates structure with different size of cavity, tectosilicates with microporous channels, pore spaces, high ion exchange and adsorption capacities (Vimonses, Lei, Jin, Chow, & Saint, 2009; S. Wang & Peng, 2010). Many research have been done on the ways to enhanced the surface of ZSM-5 zeolite by TiO<sub>2</sub> to yield efficient photocatalyst for post separation treatment of wastewater (Khatamian, Hashemian, & Sabae, 2010; Panpa, Sujaridworakun, & Jinawath, 2008). However, to the best of our knowledge no work has been addressed, the synthesis of mesoporous ZSM-5 and the effect of the mesoposity on photocatalytic post separation and stability.

Another crucial factor that could affect the photocatalytic activity is the hole/electron recombination phenomenon. In recent years, considerable efforts have been made to design and fabricate heterojunction photocatalysts for improving photocatalytic activity by mitigating the hole/electron recombination (Q. Xiang, Yu, & Jaroniec, 2012). To address this issue, we considered the use of graphene, a single layer of graphite which possesses a unique two-dimensional structure, high conductivity, superior electron mobility and extremely high specific surface area. Moreover graphene can also be produced on a large scale at low cost; thus, it has been regarded as an important guest/host component for making various functional substance of photocatalysis usage. Although, there have been numerous attempts to combine graphene with photocatalysts to promote charge separation, restrain the hole–electron recombination as well as provide a large surface area for heterogeneous reactions at



the interface (X. Huang, Qi, Boey, & Zhang, 2012; Q. Xiang et al., 2012), however, little attention has been paid to the modification of graphene.

This dissertation showed some of the criteria for choosing zeolite and modified graphene as a substrates for enhanced photocatalytic activity. On the basis of these criteria, the characterizations of a new set of hybrid photocatalysts have been investigated. The combination of zeolite and modified graphene has revealed a novel hybrid photocatalyst which significantly increased the photocatalytic efficiency.

### **1.1.2 Conjugate mesoporous visual adsorption**

Conjugate mesoporous adsorbent is a ligand anchoring appropriate mesoporous silica substrate prepared by direct templating method for removal of heavy metals from aqueous solution (Abbas, Znad, & Awual, 2018; Awual, 2016a). In this technique, ligand (which can be defined as a molecule that binds to a central metal atom to form a coordination complex) play a vital role in capturing and selecting ions from aqueous solution. The merit that has made this type of conjugate adsorption unique is the visual detection of ions with naked eyes in water samples. More research efforts in recent years have focused on the development of conjugate mesoporous adsorbent which are environmentally friendly. Most conjugate mesoporous adsorbents have a better efficiency, quality and applicability up to the nano-scale; however, the challenges with this conjugate mesoporous adsorbent is their instability which has remained unresolved due to the weakness and the poisonous nature of the silica substrates which is used in this technique. Substrate of conjugate adsorbent are made of either tetramethyl orthosilicate (TMOS) or tetraethyl orthosilicat (TEOS), which are widely used as precursor substrate (Awual, Hasan, Eldesoky, et al., 2016; Awual, Khaleque, et al., 2015) are known to be toxic and unstable in water samples resulting to deposit of silica (Si) in aqueous solution. The search for a new substrate to improve the adsorption ability without loss of the overall effectiveness; and to design an appropriate ligand that can adsorb ultra-trace heavy metal ions in an aqueous solution is in high demand.

## **1.2 Research objectives**

The two main objectives of this thesis are to synthesize: (i) a new TiO<sub>2</sub> based mesoporous photocatalysts for decolourization and mineralization of dyed aqueous

solution, and (ii) novel visual conjugate mesoporous adsorbent for detecting and removing heavy metal ions from aqueous medium. To achieve these goals, the following specific objectives will be thoroughly investigated:

- ❖ Fabrication and characterization of a hybrid multilamellar TiO<sub>2</sub>/ZSM-5 mesoporous: Methyl orange as a pollutant model.
- ❖ Preparing, characterizing, testing and evaluating the TiO<sub>2</sub>/ZSM-5 mesoporous enhanced with reduced graphene oxide (RGO) as a potential and alternative photocatalyst for removal of methylene blue from aqueous coloured solution.
- ❖ Identify and quantify the intermediate compounds formed during the photocatalytic degradation.
- ❖ Synthesis of a novel visual conjugate adsorbent mesoporous which consists of ligand type (*HAPT*) 2-hydroxyacetophenone-<sup>4</sup>N-pyrrolidine thiosemicarbazones immobilizes onto mesoporous zeolite type ZSM-5 substrate to detect and remove mercury (Hg<sup>2+</sup>) ions from an aqueous solution.
- ❖ Synthesis of a novel visual conjugate adsorbent mesoporous consists of ligand type PDCTC (2,6-Pyridinedicarboxaldehyde-Thiosemicarbazone) immobilizes onto ZSM-5 mesoporous substrate to detect and remove lead (Pb<sup>2+</sup>) ions from an aqueous solution.

### 1.3 Research significant

- ❖ Previous studies have applied TiO<sub>2</sub> with different types of natural zeolites substrate for wastewater treatment, which relatively has a specific surface area limits. To the best of our knowledge, there has been no detailed study that used modified mesoporous zeolite type of ZSM-5 (which contains multi- active sites with high specific surface area) in photocatalysis, which gives high efficient and post-separation.
- ❖ This is the first research to utilize reduced graphene oxide in the synthesis of multilamellar TiO<sub>2</sub>/ZSM-5 mesoporous photocatalyst to efficiently enhanced solar photocatalytic degradation, making the photodecomposition more rapidly.
- ❖ Previous researches have achieved the preparation different types of conjugate mesoporous adsorbents with high specific surface area using a precursor substrate of TEOS or TMOS. In this thesis, a relatively higher specific surface area conjugate

mesoporous adsorbent was prepared using ZSM-5 mesoporous as an alternative substrate.

- ❖ Another innovative component in this research is the novel design of stable ligands type of *2-hydroxyacetophenone-<sup>4</sup>N-pyrrolidine thiosemicarbazones* and (2,6-Pyridinediecarboxaldehyde-Thiosemicarbazone) functionalized ZSM-5 mesoporous adsorbent.
- ❖ When the above objectives are achieved successfully, the impacts may reduce the risk of dyes and heavy metal ions contaminations in water bodies.

### 1.4 Thesis Structure

This dissertation consists of eight chapters that are linked systematically together to achieve the targeted objectives. Below is a brief description of each chapter and Figure 1.1 shows the dissertation structure:

**Chapter One:** General overview of the present research work which includes a motivation and brief background of the thesis topic as well as the thesis's main objectives, significance and structure.

**Chapter two:** Literature review of the current study which includes the photocatalysis, adsorption processes, current progress and research studies of functionalized ligands and conjugate mesoporous adsorbent. An extensive theoretical view including the preparation methods, characterizations, problems and potential applications are also presented in this chapter.

**Chapter three:** Description of the experimental methods, chemicals and analytical equipment used in this thesis.

**Chapter four:** experimental procedure to synthesis multilamellar TiO<sub>2</sub>/ZSM-5 mesoporous catalyst, characterization and the results of solar-photocatalytic degradation of methyl orange.

**Chapter Five:** Enhancement of solar-photocatalytic degradation of methylene blue using the synthesized reduced graphene oxide with multilamellar TiO<sub>2</sub>/ZSM-5 mesoporous catalyst. The isotherm kinetic models are also reported in this chapter.

**Chapter Six:** Demonstrations and explanation of the experimental procedure for synthesize of a ligand (2-hydroxyacetophenone-<sup>4</sup>N-pyrrolidine thiosemicarbazones)

(HAPT) embedded conjugate mesoporous adsorbent for detection and effective removal  $\text{Hg}^{2+}$  from aqueous media. The effects of pH solution, contact time, maximum adsorption capacity, equilibrium sorption isotherm and foreign competing ions are also studied.

**Chapter Seven:** Investigations and explanation of the experimental procedure to synthesize a ligand of 2,6-Pyridinedicarboxaldehyde-Thiosemicarbazone (PDCTC) functionalized conjugate mesoporous adsorbent for monitoring and sorption of ultra-trace  $\text{Pb}^{2+}$  from aqueous media. The influences of the key factors (pH solution, contact time, maximum adsorption capacity, equilibrium sorption isotherm, foreign competing ions are also investigated.

**Chapter Eight:** This chapter presents the conclusions drawn from this study, as well as the recommendations for future works.

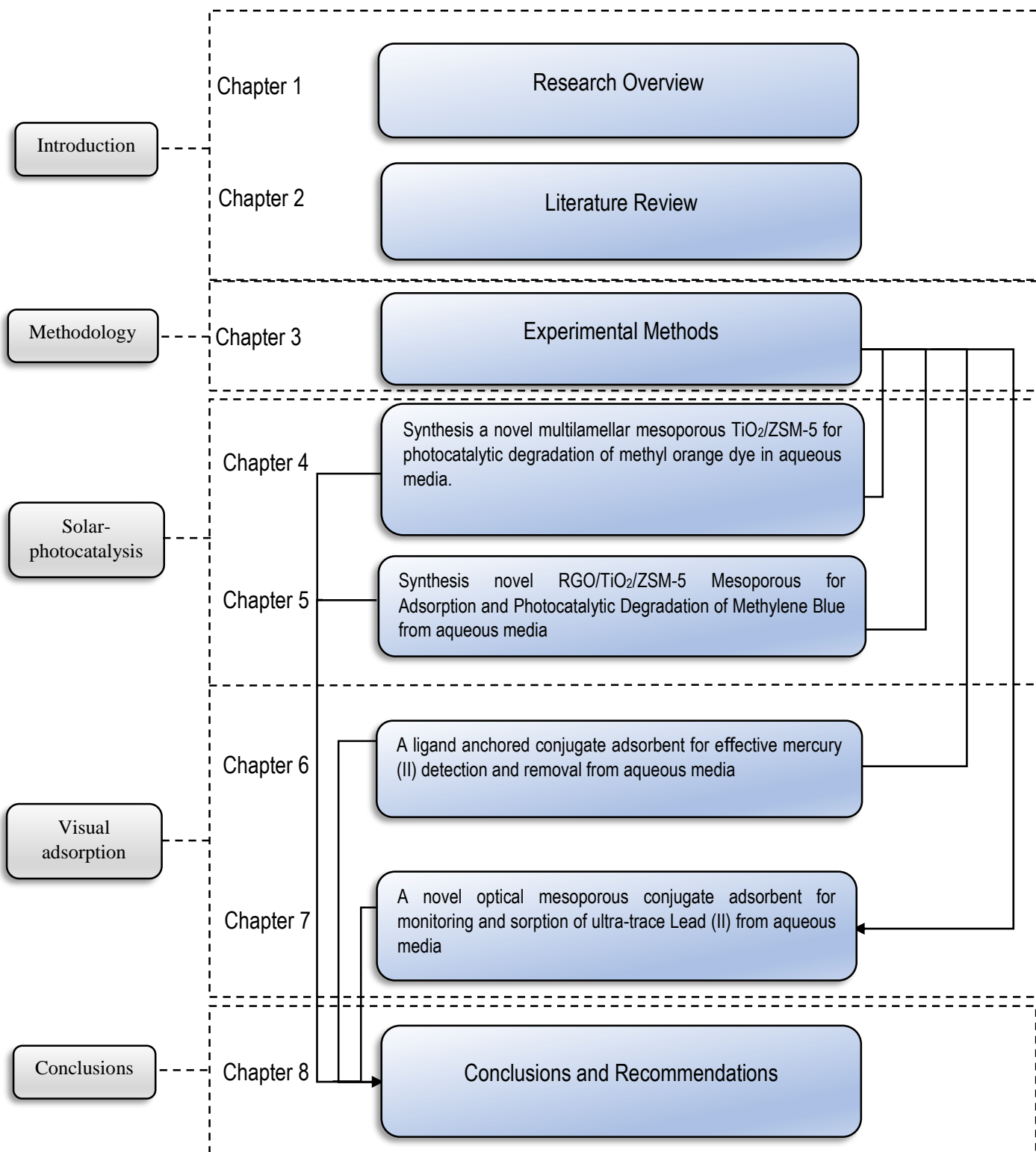


Figure 1-1 Thesis structure

# CHAPTER 2

## 2

## Literature Reviews

### 2.1 Introduction

The tremendous development in industrialization and urbanization has escalated series of environmental issues globally. One of the most significant issues is the disposal of industrial contaminates in form of effluents containing non-biodegradable toxic materials into rivers, lakes, oceans and ground water. Many industries that impact on the ecosystem such as metallurgy, petroleum refineries, plastic, leather, pesticide, herbicides, detergents, textile dye and pharmaceutical manufacturers release highly concentrated organic refractory and heavy metal ions pollutants. These pollutants can be classified into organic pollutants, including aliphatic, alkanes, alcohols, aromatic compounds and inorganic pollutants such as mercury ( $\text{Hg}^{2+}$ ), lead ( $\text{pb}^{2+}$ ), cadmium ( $\text{Cd}^{2+}$ ) and nickel ( $\text{Ni}^+$ ). In general, these pollutants are considered a real threat to public health and the ecosystem such as plant, animals and aquatic organisms (Chong, Jin, Chow, & Saint, 2010; Dong et al., 2014; Gogate & Pandit, 2004); therefore, their complete removal from the environment is an urgently demanded.

Physical treatments such as coagulation, reverse osmosis, and membrane filtration are widely used to remove organic contaminants from water, however, they are quite expensive, time-consuming and incompetent techniques. In addition to physical treatment, chemical treatments are also applied such as reduction, oxidation, electrochemical oxidation, and ion exchange, but they cause the formation of by-products such as sulfonate, phenol and plenty of aromatic compounds (Chong et al., 2010; F. Ma, Guo, Zhao, Chang, & Cui, 2009; Slokar & Le Marechal, 1998). For detecting toxic ions, various analyses equipment have been reported including ICP-

MS, ICP-AES, fluorescence spectroscopy, chemiluminescence and neutron activation analysis (Arshad et al., 2017; Awual, 2017b; Awual, Hasan, Eldesoky, et al., 2016; Kamath, Netalkar, Kokare, Naik, & Revankar, 2012; B. Li, Wang, Lv, & Zhang, 2006; Naushad, ALOthman, Awual, Alam, & Eldesoky, 2015; Sakamoto-Arnold & Johnson, 1987; Sheikh et al., 2017; Souza & Tarley, 2009; Zi, Huang, Yan, & Liao, 2014). Although, these methods are adequate for detection of ions, the complex operational procedures which involve a large infrastructure backup and high cost have compromised these techniques. The following sections present the major industrial effluent contaminants and the treatment methods.

### 2.2 Industrial effluent dyes

Annually,  $7 \times 10^5$  tons of synthetic dyes are produced worldwide, and are largely consumed by the textile industries. 10-50% of the dyes are released into the ecosystem, which are highly water soluble. The product of their degradation, mainly aromatic amines can be carcinogenic or mutagenic to life forms (Rajamohan, Rajasimman, Rajeshkannan, & Sivaprakash, 2013). Unfortunately, most of the dyes escape traditional wastewater treatment processes and are retained in the environment as a result of their high stability to light, detergent, chemicals, temperature and other parameters, for instance, bleach and perspiration. Dyes can remain in the environment for an extended period of time and resist bio-degradation due to high thermal and photo stability (Nidheesh, Zhou, & Oturan, 2018). Different azo dyes affect water quality such as Rhodamine B, Orange 7, Orange II, Reactive Blue, Reactive green, Congo red and Reactive red. Methyl orange dye (MO,  $C_{14}H_{14}N_3NaO_3S$ ) is a significant example of anionic azo (-N=N-) groups in the substituted aromatic rings, is a synthetic dye that is widely used as a colouring agent in textile, food, leather and pharmaceutical industries. MO can be used to determine Itopride hydrochloride and also as a colouring agent to detect hydrogen gas (Choudhary, Goyal, & Khokra, 2009). The discharging of a high concentration of MO dye into rivers causes health hazards such as mutagenic, carcinogenic and teratogenic effects which affects humans, microorganisms, and fish species (Mathur, Bhatnagar, & Sharma, 2012; Parshetti, Telke, Kalyani, & Govindwar, 2010). Another example is methylene blue cationic heterocyclic dye (MB,  $C_{16}H_{18}N_3S$ ) which stands out amongst the most regularly used dye in dyeing wood, cotton, and silk. It causes serious harmful effect when inhaled, and when ingested

through the mouth it causes smouldering sensation, spewing, mental perplexity and methemoglobinemia (Ghosh & Bhattacharyya, 2002). (Saratale, Saratale, Chang, & Govindwar, 2011)

### 2.2.1 Treatment technologies of dyes

Various physical/ chemical methods, such as adsorption, chemical precipitation, photolysis, chemical oxidation and reduction, and electrochemical treatment, have been used for the removal of dyes from wastewater (see Figure 2.1) (Saratale et al., 2011); however, these treatment processes cannot oxidise or completely degrade the recalcitrant components present in wastewater effluents. Additionally, there are many drawbacks including the slow biodegradation and disposable sludge which are greatly activated in the treated water (Kusvuran & Erbatur, 2004). Therefore, an effective advanced treatment is required to disintegrate and mineralise these non-biodegradable compounds.

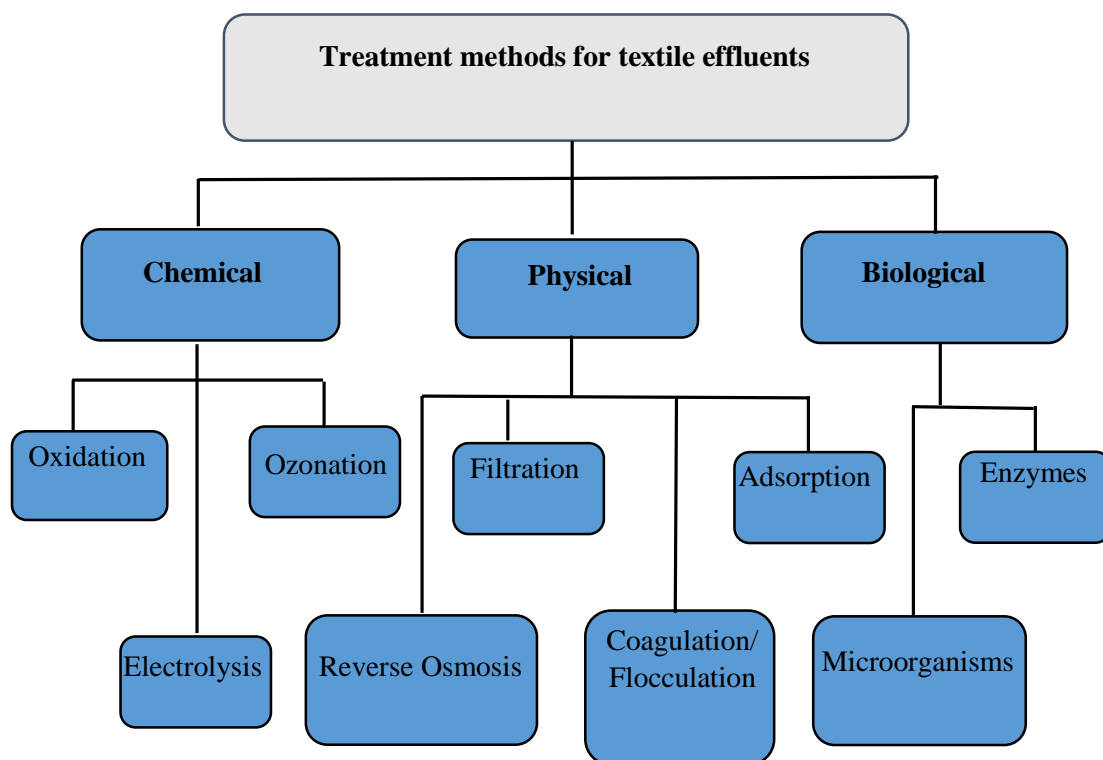


**Figure 2-1** Treatment techniques for the removal of dyes from wastewater effluent (Saratale et al., 2011)

### 2.2.2 Advanced oxidation processes (AOPs)

Advanced oxidation processes (AOPs) are the most effective technologies for treatment of wastewater effluent contaminants they include electrochemical (P. Ma,



Ma, Sabatino, Galia, & Scialdone, 2018), solar phot-Fenton (Karci, Wurtzler, Armah, Wendell, & Dionysiou, 2018), catalytic oxidation (Cheng et al., 2018), catalytic wet oxidation (Xing, Chen, & Zhang, 2018), microwave catalytic wet air oxidation (Sassi et al., 2018) and photocatalytic degradation (Gholami, Ghasemi, Anvaripour, & Jorfi, 2018). AOPs suggest many advantages such as a complete mineralization of the organic pollutants, utilizing solar light instead of UV as an alternative to the light source. Among the AOPs, photocatalytic degradation using an appropriate semiconductor such  $\text{TiO}_2$  and UV light source has been widely applied for the mineralization of most of the organic pollutants present in wastewater with no significant drawbacks, except energy cost. To solve this problem, solar light instead of UV could successfully decrease the operating cost thus making this technique more economically feasible (Giannakis, Androulaki, Comninellis, & Pulgarin, 2018).

The major power of this technique comes from the production of superoxide ( $\text{O}^{\cdot -}$ ) /hydroxyl ( $\text{OH}^{\cdot}$ ) radicals by stimulating  $\text{TiO}_2$  via light sources which destroy the organic pollutant compounds, mineralizing them to  $\text{CO}_2$  and  $\text{H}_2\text{O}$  as illustrated in Figure 2.2. Titanium dioxide  $\text{TiO}_2$  is one of the major photocatalyst used in photodegradation process due to its non-toxic, stable, inexpensive and reusable nature. However, the main challenges facing its use is associated with the problem of post-separation of the spent  $\text{TiO}_2$  (Chong, Jin, Zhu, Chow, & Saint, 2009) and the recombination of electron/hole pair producing heat. Thus, it is necessary to modify  $\text{TiO}_2$  in order to meet the requirements of photocatalysis process.

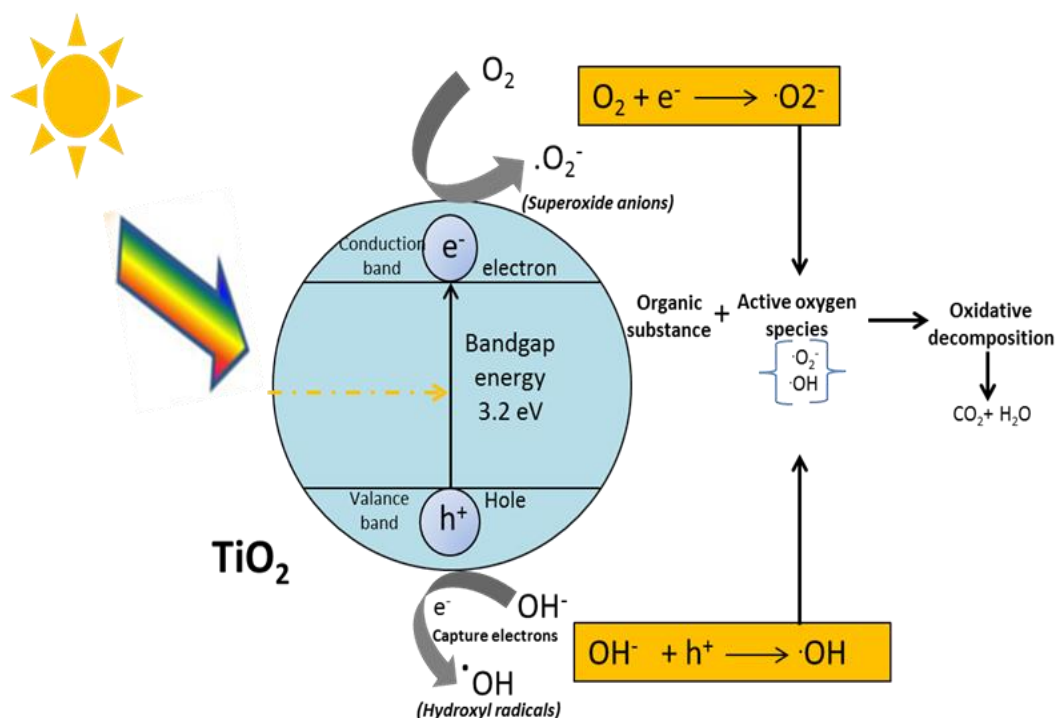


**Figure 2-2** Principles of oxidative decomposition of photocatalysts

### 2.2.3 Enhanced the photocatalytic degradation process

The main challenges of photocatalytic processes are the post separation and the recombination of  $e^-/h^+$  pairs leading to decreased degradation efficiency (Joseph & Thiripuranthagan, 2018; Sacco, Vaiano, & Matarangolo, 2018). To overcome the post separation drawback,  $\text{TiO}_2$  immobilized into appropriate porous molecular substrate to accelerates the post separation process (MiarAlipour, Friedmann, Scott, & Amal, 2018). Different immobilizer substrates such as activated carbon (Shi, Zheng, & Ji, 2010), magnetite core (Beydoun & Amal, 2002), and clays (Paul, Martens, & Frost, 2012) have been used to enhance the post-separation and adsorption of contaminants from bulk water. Conditionally, the penetration of the incident light UV/or sunlight should easily go through a catalyst to extremely excite  $\text{TiO}_2$ ; hence,  $\text{TiO}_2$  modified transparent components such as porous materials are significantly recommended in this manner (MiarAlipour et al., 2018).

Another challenge facing the photocatalytic process is the recombination of  $e^+/h^-$  pairs phenomenon. To resolve this drawback, various crystal phase of  $\text{TiO}_2$  such as anatase, rutile or brookite have been applied in order to enhance the photocatalytic degradation (Mutuma, Shao, Kim, & Kim, 2015; Wei, McMaster, Tan, Chen, & Caruso, 2018).

Other solar/UV photocatalytic degradation processes have been applied, for example,  $\text{Ag}^+/\text{TiO}_2/\text{UV}$  (Shintre & Thakur, 2016),  $\text{H}_2\text{O}_2/\text{TiO}_2/\text{UV}$  (Apollo, Onyongo, & Ochieng, 2014), Co-doped  $\text{TiO}_2$  (Shang, Wu, & Xie, 2016) Solar/ $\text{TiO}_2$ /photo-Fenton (Eissa, Zidan, & Sakugawa, 2015) and  $\text{WO}_3/\text{UV}$  (Mohagheghian, Karimi, Yang, & Shirzad-Siboni, 2015).

### 2.2.3.1 $\text{TiO}_2$ - modified mesoporous silicate

Titanium dioxide ( $\text{TiO}_2$ ) has been widely investigated as a fascinating photocatalytic catalyst for environmental application due to its fabulous properties such as non-toxic, high efficiency and chemical stability (X. Chen & Mao, 2007; Fujishima, Rao, & Tryk, 2000; Liao et al., 2012). Numerous studies in the literature have dealt with  $\text{TiO}_2$ /modified mesoporous silicate, but the reason behind using mesoporous silicate in this composite has been given less attention. The next section will explain the main techniques for synthesizing  $\text{TiO}_2$  /modified mesoporous silicate:

#### 2.2.3.1.1 *Sol-gel/Hydrolysis technique*

Multilayers of  $\text{TiO}_2$  coating are made into SBA-15 mesoporous, whose silanol groups; has been treated with  $\text{Ti}(\text{O}^i\text{Pr})_4/\text{TiCl}_4$  precursor via sol-gel and hydrolysis process. It was prepared by Yan and colleagues (Yan, Mahurin, Overbury, & Dai, 2005) under the name hydrolytic surface sol-gel (HSS) process as illustrated in Figure 2.3. This composite catalyst exhibits good photocatalytic activity. The synthesizing was consistent with the study by Zheng; however, Zheng et al. examined MCM-41 mesoporous silicate instead of SBA-15 (Zheng, Gao, Zhang, & Guo, 2000). This technique was discarded by the experiments of Li and coworkers (X. Li, Xiong, Li, & Xie, 2006) who considered a novel method for generating  $\text{TiO}_2$  nanofiber via  $\text{TiCl}_4$  precursor or metal oxide that is filled into mesoporous silica at a temperature range from 90- 150<sup>0</sup>C, but in this technique the experiments were conducted under pressure following a hydrolysis process to generate  $\text{TiO}_2$  as a nanofiber on the surface of the mesoporous as shown in Figure 2.4. The advantage of this technique is that the mesophase template is not removed preventing the damage that could occur for the  $\text{TiO}_2$  nanofibers.

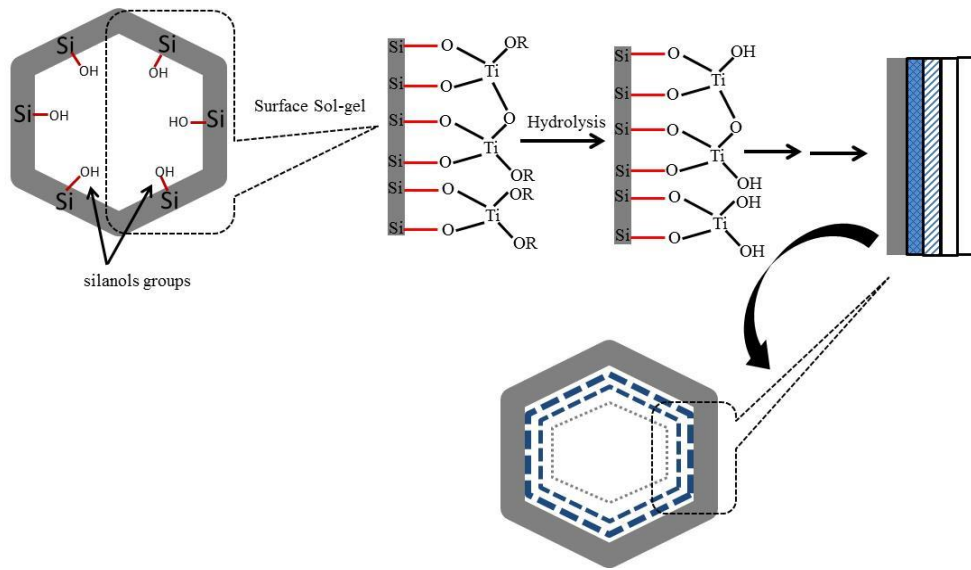


**Figure 2-3** Synthesis of multilayered Titania through mesoporous silica channels

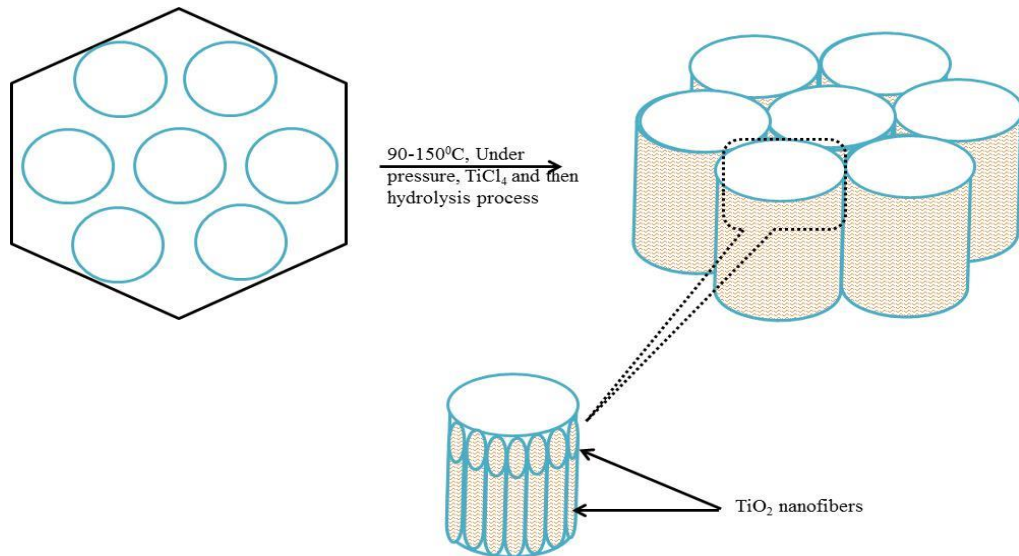


**Figure 2-4** Scheme showing the formation process of  $\text{TiO}_2$  fibres on mesoporous spheres

### 2.2.3.2 $\text{TiO}_2$ - modified raw Zeolites

There have been several studies in the literature reporting  $\text{TiO}_2$ /raw zeolite composites. Zeolites are one of the most significant microporous silica source materials considered as a member of the large family of aluminosilicates and are widely applied in catalysis and separation process. Typically, zeolites applied as FCC (Face Centred Cubic

Structure catalysts) are of types ZSM-5, X and Y (Faujasite type). ZSM-5 zeolite is a highly porous aluminosilicates with a high silica/alumina ratio. So far, there has been little discussion about the influence of this aluminosilicates on photocatalytic activity. The Sol-gel/Hydrolysis technique is widely applied to synthesize these composite catalysts. Table 2.1 shows the different types of TiO<sub>2</sub>/zeolites composites applied for wastewater treatments.

**Table 2-1** Different types of zeolite modified TiO<sub>2</sub> applied in wastewater treatment

Composite catalyst	Pollutant	Degradation rate (%)	References
TiO <sub>2</sub> /zeolite Y	Fluoroquinolones	96-98	(Maraschi et al., 2014)
TiO <sub>2</sub> / zeolite HY	2,4-dichlorophenoxyacetic acid (2,4-D)	82.9	(Shankar, Anandan, Venkatachalam, Arabindoo, & Murugesan, 2006)
TiO <sub>2</sub> /zeolite HY	Methylene blue dye	97	(Tayade, Kulkarni, & Jasra, 2007)
TiO <sub>2</sub> / β-zeolite	U(VI)	90	(Peng et al., 2017)
TiO <sub>2</sub> / zeolite prepared by Kaoline	Methylene blue dye	99.43	(Setthaya, Chindaprasirt, Yin, & Pimraksa, 2017)
Titania/ HP-zeolite Y	Formaldehyde	90	(Jin et al., 2018)
TiO <sub>2</sub> rutile/Clinopotilolite zeolite	Terephthalic acid	94	(Yener, Yilmaz, Deliismail, Özkan, & Helvacı, 2017)
TiO <sub>2</sub> /zeolite fly ash bead	RhB	95	(Yang et al., 2017)
TiO <sub>2</sub> / zeolite Y treated ammonium acetate ammonium fluoride	Methyl orange	92	(Guesh, Márquez-Álvarez, Chebude, & Díaz, 2016)

### 2.2.3.3 TiO<sub>2</sub>- modified reduced graphene oxide (RGO)

Graphene can be described as a two-dimensional (2D) sheet of sp<sup>2</sup>-hybridized carbon, which reveals a honeycomb network. The peculiarity of the long-range π-conjugation in graphene enhances the remarkable thermal, electrical, mechanical properties (Allen,

Tung, & Kaner, 2009), chemical inertness, and super hydrophobicity at the nanometre scale of graphene which are considered in many different theoretical and practical studies (Geim & Kim, 2008). The fundamental difference between graphene (G) and graphene oxide (GO) is the additional oxygen atoms, which are bound with the carbon scaffold (see Figure 2.5).

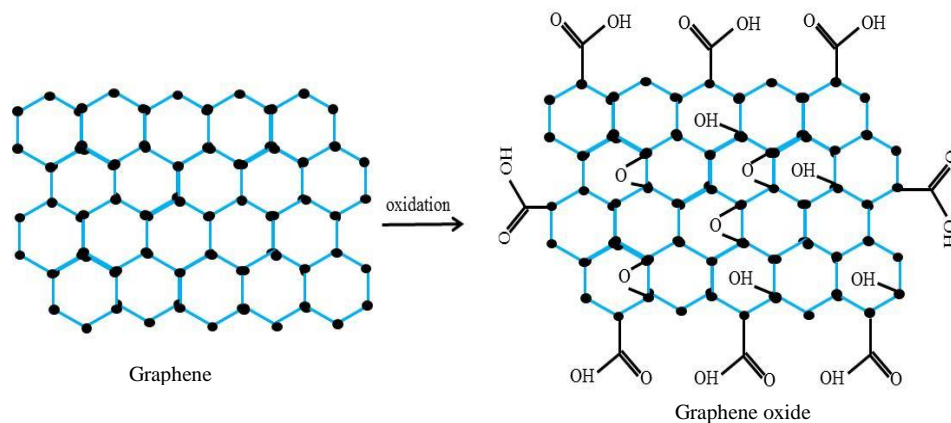


**Figure 2-5** Oxidation of graphene to form graphene oxide

The most common technique applied for synthesizing graphene oxide is Hummers and Offeman technique (Hummers Jr & Offeman, 1958), which utilizes a mixture of very strong oxidizers consisting of sulphuric acid, sodium nitrate and potassium permanganate which treated with graphene to produces GO (Sakthivel, Josephine, Sethuraman, & Dhakshinamoorthy, 2018). To obtain 70% conversion during this oxidation reaction, increased quantities of potassium permanganate and phosphoric acid are combined with the sulphuric acid, instead of utilizing sodium nitrate (L. Chen et al., 2018). Reduced graphene oxide (RGO) has similar structure as GO, however, it contains various functionalities of (-O, -OH, -COOH) on its surface (Barpuzary & Qureshi, 2013; Iwase, Ng, Ishiguro, Kudo, & Amal, 2011) as depicted in Figure 2.6. From the cost point of view, graphene is expensive, but RGO can be synthesized utilizing inexpensive techniques, which makes it easily applied in various fields (e.g. photocatalysis, sensing, optoelectronics, energetic materials, bio-sensing, catalytic and biomedical applications) (Georgakilas et al., 2016; Selvaraj, Sun, Sukumaran, & Singh, 2016).

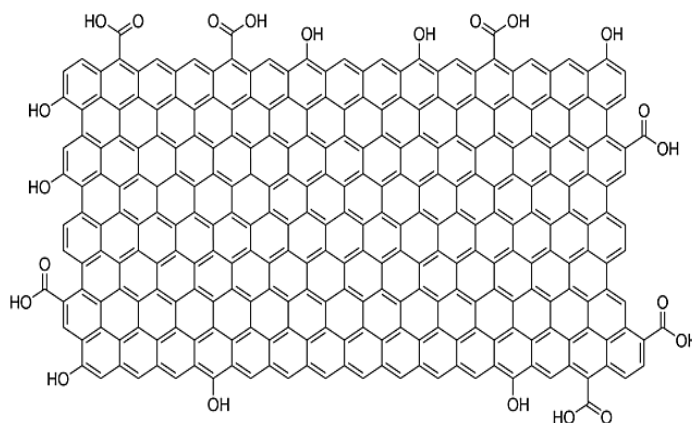


**Figure 2-6** The chemical structure of reduced graphene oxide (RGO)

Several researchers have investigated the use of semiconductor nanocomposites (SNs) /RGO for wastewater treatment. Example are, TiO<sub>2</sub>/RGO (Ismail, Chovelon, Ferronato, Jaber, & Rifai, 2016; Khavar, Moussavi, & Mahjoub, 2018; Yanan Li et al., 2018; W. Liu, Cai, Ding, & Li, 2015; Marco, Claudio, & Fabrizio, 2017; Tang, Wang, & Wang, 2018), S-TiO<sub>2</sub>/RGO (Khavar, Moussavi, Mahjoub, Satari, & Abdolmaleki, 2018), Au-TiO<sub>2</sub>/RGO (Lv et al., 2018), Bi<sub>2</sub>S<sub>3</sub>-, N-doped- and TiO<sub>2</sub>/RGO microspheres (Wu, Zeng, Tong, Li, & Xu, 2018). The unique characteristics that make reduced graphene oxide a successful substrate in the photocatalytic process are as follows:

- Electrons excitation in a semiconductor by a light source during the photocatalysis process are transmitted onto RGO surface sheet and thus promote the separation of charges.
- The strong optical absorption ability of GO from visible to near infrared (NIR) regions can be harvested as soon as it receives light or irradiated.
- The RGO also forms a relatively formed a high molecular weight which is beneficial for post separation from aqueous solution. The key features for synthesis of TiO<sub>2</sub>/RGO and the reaction mechanism steps of photocatalytic degradation onto the surface of reduced graphene oxide are depicted in Figure 2.7.

The next section briefly explains with illustrations the main technique to functionalized TiO<sub>2</sub> into the graphene:

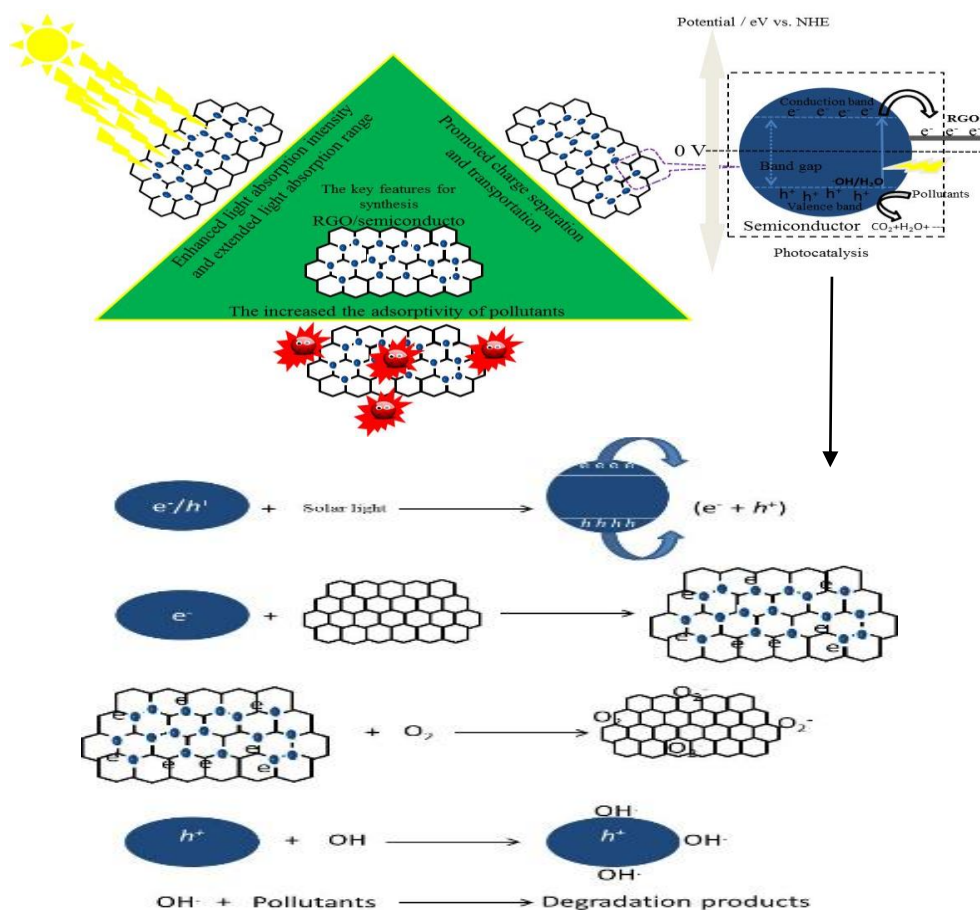


**Figure 2-7** A simplified schematic description the key features for synthesis of RGO/semiconductor nanocomposite with the major mechanism reaction steps in photocatalytic degradation under solar light irradiation

### 2.2.3.3.1 Solution mixing method

Solution mixing technique has been widely employed for the fabrication of graphene/semiconductor composite. It is considered as a simple, cost effective, scalable and feasible method. In this method, the graphene oxide colloids are ultrasonically mixed with TiO<sub>2</sub> particles, followed by ultraviolet (UV) assisted light to reduce the graphene oxide (Akhavan & Ghaderi, 2009; Bell et al., 2011). This method can be applied for different types of semiconductors; for example, SnO<sub>2</sub> semiconductor which can be prepared by the hydrolysis of SnCl<sub>4</sub> precursor with NaOH fabricated onto graphene (Paek, Yoo, & Honma, 2008). SnO<sub>2</sub> solution mixed with graphene is dispersed in ethylene glycol solution, then adding lithium ions to this solution produces SnO<sub>2</sub>/graphene composite as depicted in Figure 2.8. This method can be applied



effectively for the preparation of semiconductor/graphene composite (Q. Xiang et al., 2012).

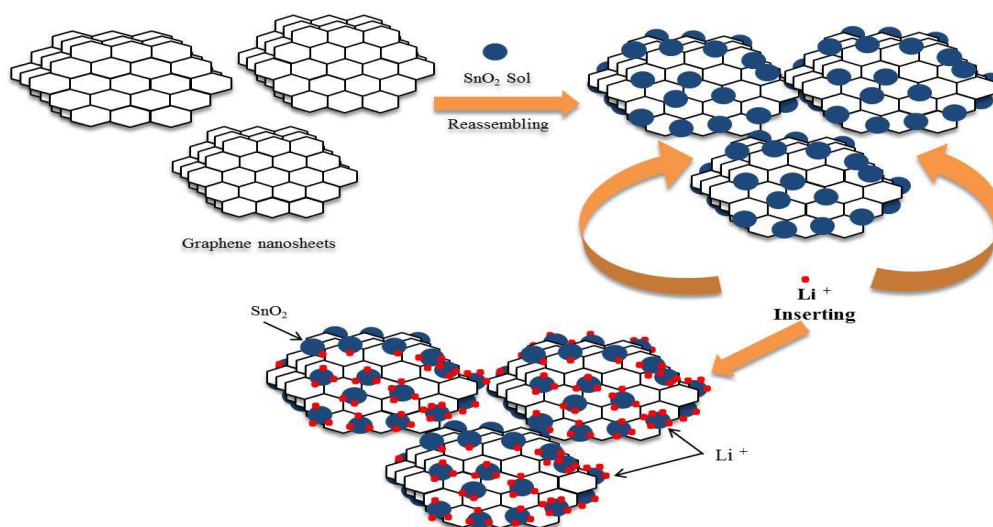


**Figure 2-8** Schematic illustration for the synthesis and the structure of SnO<sub>2</sub>/Graphene nanosheets

### 2.2.3.3.2 Hydrothermal method

In this method, either semiconductor nanoparticles or their precursors are anchored on the graphene oxide sheets to produce special morphology which can be efficiently utilized for different applications. For example, thermal treatment of graphene/ultrathin anatase TiO<sub>2</sub> nano-sheets under N<sub>2</sub>/H<sub>2</sub> gases produced crystals type of (001) high-energy facet in a study by Ding and co-workers (Ding et al., 2011). In another study by Zhang and co-workers (H. Zhang, Lv, Li, Wang, & Li, 2009) involving the use of a different titanium sources such as Degussa P<sub>25</sub> TiO<sub>2</sub> powder in one-step hydrothermal treatment was completely dissolved in ethanol-water solution. In another investigation by Fan and colleagues, one-step solvothermal strategy for the preparation of graphene–TiO<sub>2</sub> nanocomposites by controlling the hydrolysis rate of titanium isopropoxide as a precursor resulted in well-dispersed particles on the graphene sheets (Fan, Lai, Zhang, & Wang, 2011).

### 2.3 Industrial effluent of heavy metal ions

Over the past three decades, rapid development in industrialization has greatly increased the rate of release of trace metal ions into the ecosystem which has negatively affected freshwater bodies to be greatly altered. Metal ions are mostly released during mining and processing activities, and according to Ross (Ross, 1994), these anthropogenic sources of metal contamination can be divided into five main groups: 1. Industry ( $\text{As}^{3+}$ ,  $\text{Cd}^{2+}$ ,  $\text{Cr}^{2+}$ ,  $\text{Co}^{2+}$ ,  $\text{Cu}^{2+}$ ,  $\text{Hg}^{2+}$ ,  $\text{Ni}^{+}$ ,  $\text{Zn}^{2+}$ ), 2. Atmospheric deposition ( $\text{As}^{3+}$ ,  $\text{Cd}^{2+}$ ,  $\text{Cr}^{2+}$ ,  $\text{Cu}^{2+}$ ,  $\text{Pb}^{2+}$ ,  $\text{Hg}^{2+}$ , U), 3. Agriculture ( $\text{As}^{3+}$ ,  $\text{Cd}^{2+}$ ,  $\text{Cu}^{2+}$ ,  $\text{Pb}^{2+}$ ,  $\text{Si}^{+}$ , U,  $\text{Zn}^{2+}$ ), 4. Waste disposal ( $\text{As}^{3+}$ ,  $\text{Cd}^{2+}$ ,  $\text{Cr}^{2+}$ ,  $\text{Cu}^{2+}$ ,  $\text{Pb}^{2+}$ ,  $\text{Hg}^{2+}$ ,  $\text{Zn}^{2+}$ ) and 5. Metalliferous mining and smelting ( $\text{As}^{3+}$ ,  $\text{Cd}^{2+}$ ,  $\text{Pb}^{2+}$ ,  $\text{Hg}^{2+}$ ). According to this classification, lead and mercury are the major contaminants affecting the environment. Mercury  $\text{Hg}^{2+}$  is one of the most ubiquitous and dangerous heavy metal ion global contaminant which ranks sixth position among the most toxic chemicals in the list of hazardous compounds. Moreover,  $\text{Hg}^{2+}$  is widely distributed in the water, soil and organisms from industrial activities, for instance, production of chlorine, caustic soda and electrical applications such as lamps, arc rectifiers and mercury cells cause serious human health risks. The toxicological and carcinogenic effects of ultra-trace  $\text{Hg}^{2+}$  (*permissible level:  $1 \mu\text{L}^{-1}$  to  $10 \mu\text{g L}^{-1}$* ) can destroy the central nervous system, kidney, liver, skin, lungs, and bones (Kaplan, Yildirim, Yildirim, & Tayhan, 2011; Mohammed, Kapri, & Goel, 2011).

Lead  $\text{Pb}^{2+}$  is also a widespread hazardous pollutant, which is considered as one of the most heavy metal ions in the ecosystem (Karve & Rajgor, 2007). The largest use of lead, which has prompted environmental and health issues, is the utilization of  $\text{Pb}^{2+}$  in fuel as an antiknock agent and paint pigments. The fundamental source of  $\text{Pb}^{2+}$  in water bodies is connected to ore processing and mining, industrial effluents discharge,  $\text{Pb}^{2+}$  plumbing, and public road or motorways runoffs (Yıldız, Citak, Tuzen, & Soylak, 2011).  $\text{Pb}^{2+}$  contamination is an essential environmental problem due to its steadiness in polluted locations and the complexity of the mechanism for biological intoxication (Chooto, Wararatananurak, & Innuphat, 2010). Trace quantities of  $\text{Pb}^{2+}$  in ecological samples could lead to environmental contamination as well as several deadly diseases, for instance, neurological systems and renal blood dysfunction are diagnosis caused by presence of toxic level lead ions which leads to irreversible brain damage, severe anaemia and colic shock (Memon, Hasany, Bhangar, & Khuhawar, 2005). To prevent

the toxic impacts of lead on the environmental agencies have placed rigorous measures to check the maximum allowable limits of metal ions drained into the lakes, rivers and landscapes. The maximum permissible limit of  $\text{Pb}^{2+}$  in drinking water was reported by The World Health Organization (WHO) to be  $10 \mu\text{g L}^{-1}$  (Organization, 2013). However, it is important to completely expel and detect ultra-trace level lead (II) from wastewater to safe guard the water quality.

### 2.3.1 Treatment technologies of heavy metal ions

The physical/ chemical properties of water has been employed in different treatment technologies, such as physical acid leaching, electro-reclamation, chemical precipitation, chemical oxidation and reduction, ion exchange, filtration, electrochemical treatment, reverse osmosis, freeze crystallization, electro dialysis, cementation, starch xanthate adsorption, and solvent extraction for removing heavy metal ions from diluted solutions. Biochemical techniques also used for treatment include microorganisms, bio sorption and flotation, biotransformation, monitoring biosensors, bioremediation and phytoremediation as shown in Figure 2.9. Owing to their higher operational cost or difficulty in treating solid and liquid wastes, most of these techniques are expensive and incompetent, practically when the metal ions are dissolved in large volume of solutions (Mohammed et al., 2011).

As an alternative to these physical/chemical and biological techniques researchers have developed an effective ligand-ion complexes route to remove heavy metals from aqueous systems. This route is the most common and widely used technique for wastewater treatment.

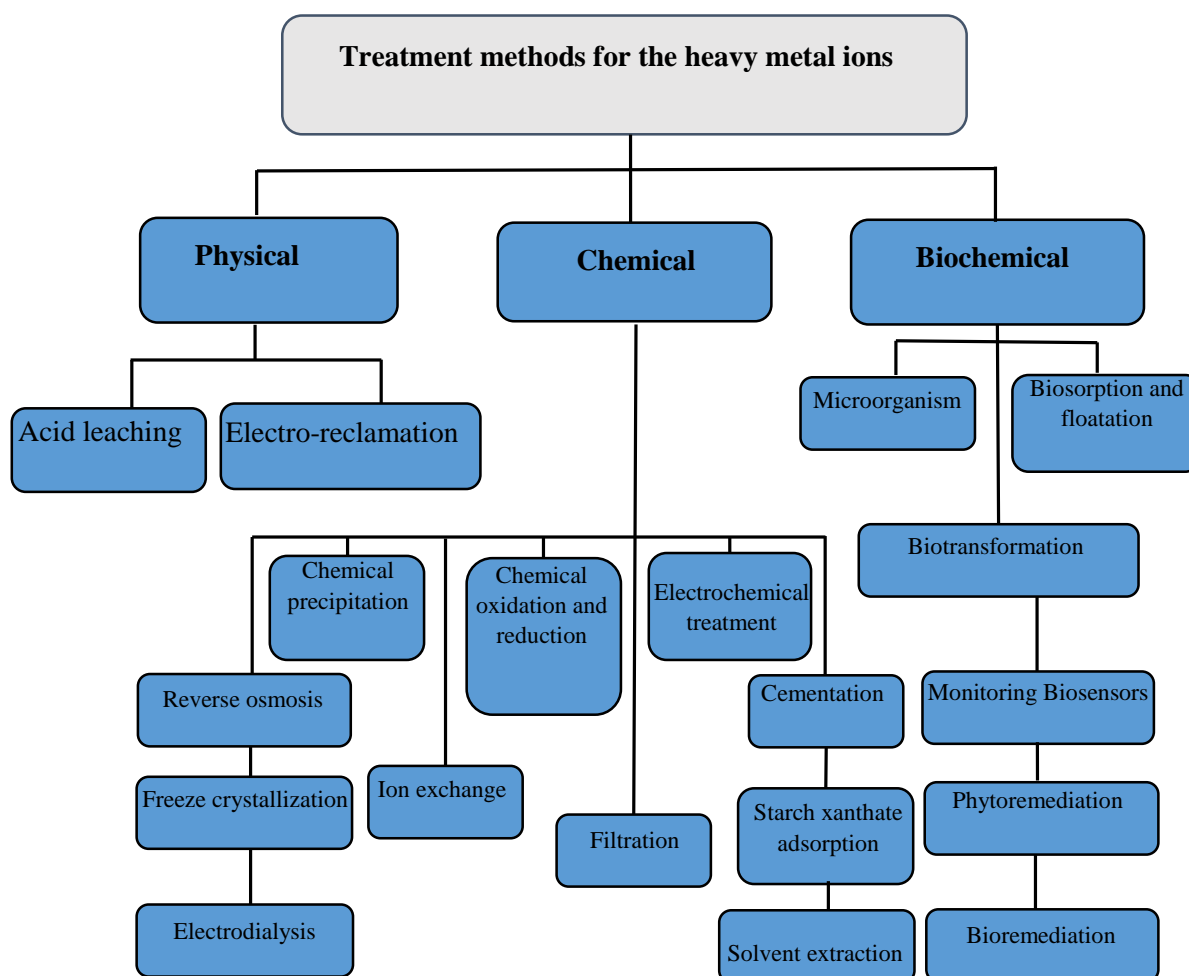


**Figure 2-9** Treatment techniques for heavy metal ions (Mohammed et al., 2011)

## 2.4 Ligand and the fundamental field theory

A ligand is an ion or organic molecule with functional group that is bonded to a central metal atom to form a coordination complex. The bonding between metal and ligand generally involves formal donation of one or more of the ligand electron pairs. The presence of ligand allows a complex formation of [metal ions-ligand]<sup>n+</sup> complex in aqueous solution, which cause the colour variation in the aqueous solution, forming a complex with a certain ligand (S. A. El-Safy, Shenashen, et al., 2013; Prakash & Malhotra, 2018). Ligand field theory describes the transition metal complex system [ligand-metal ion]<sup>n+</sup> which consists of a central metal atom surrounded by a group of electron-rich atoms or molecules called ligand. In 1963, Pearson claimed that the metal ions can be divided into ‘soft’ metal ions and ‘hard’ metal ions which referred to as weak field ligands and strong field ligands under an acid or base solution medium,

respectively (Pearson, 1963) as shown in Table 2.2. According to Pearson, there are four types of ligand donor including (O-) hard, (N-) hard, (S-N) soft, and (S-N-O) soft at a specific pH solution. Based on this classification, the next section will give more details regarding how to choose an appropriate ligand for the transition metal ions as presented in table 2.2.

**Table 2-2** Classification of hard and soft ions According to the HSAB (Hard and Soft acids and Bases) Principle of Pearson

<i>Medium</i>	<i>Hard (ions)</i>	<i>Soft (ions)</i>
<b>Acids</b>	H <sup>+</sup> , Li <sup>+</sup> , Na <sup>+</sup> , K <sup>+</sup> , Be <sup>2+</sup> , Mg <sup>2+</sup> , Ca <sup>2+</sup> , Sr <sup>2+</sup> , Ba <sup>2+</sup> , Al <sup>3+</sup> , Sc <sup>3+</sup> , Ga <sup>3+</sup> , In <sup>3+</sup> , La <sup>3+</sup> , Gd <sup>3+</sup> , Lu <sup>3+</sup> , Cr <sup>3+</sup> , Co <sup>3+</sup> , Fe <sup>3+</sup> , As <sup>3+</sup> , Si <sup>4+</sup> , Ti <sup>4+</sup> , Zr <sup>4+</sup> , Hf <sup>4+</sup> , Th <sup>4+</sup> , U <sup>4+</sup> , Pu <sup>4+</sup> , Ce <sup>4+</sup> , WO <sup>4+</sup> , Sn <sup>4+</sup> , UO <sup>2+</sup> , VO <sup>2+</sup> , MoO <sup>3+</sup>	Cu <sup>+</sup> , Ag <sup>+</sup> , Au <sup>+</sup> , Tl <sup>+</sup> , Hg <sup>+</sup> , Pd <sup>2+</sup> , Cd <sup>2+</sup> , Pt <sup>2+</sup> , Hg <sup>2+</sup> , Se <sup>2+</sup> , CH <sub>3</sub> Hg <sup>+</sup> , Co(CN) <sub>5</sub> <sup>2-</sup> , Pt <sup>4+</sup> , Te <sup>4+</sup> , Br <sup>+</sup> , I <sup>+</sup>
	<b>Borderline</b> Fe <sup>2+</sup> , Co <sup>2+</sup> , Ni <sup>2+</sup> , Cu <sup>2+</sup> , Zn <sup>2+</sup> , Pb <sup>2+</sup> , Sn <sup>2+</sup> , Sb <sup>3+</sup> , Bi <sup>3+</sup> , Rh <sup>3+</sup> , Ir <sup>3+</sup> , B(CH <sub>3</sub> ) <sub>3</sub>	
<b>Bases</b>	H <sub>2</sub> O, OH <sup>-</sup> , F <sup>-</sup> , CH <sub>3</sub> CO <sub>2</sub> <sup>-</sup> , PO <sub>4</sub> <sup>3-</sup> , SO <sub>4</sub> <sup>2-</sup> , Cl <sup>-</sup> , CO <sub>3</sub> <sup>2-</sup> , ClO <sub>4</sub> <sup>-</sup> , NO <sub>3</sub> <sup>-</sup> , ROH, RO <sup>-</sup> , R <sub>2</sub> O, NH <sub>3</sub> , RNH <sub>2</sub> , NH <sub>2</sub> NH <sub>2</sub>	R <sub>2</sub> S, RSH, RS <sup>-</sup> , I <sup>-</sup> , SCN <sup>-</sup> , S <sub>2</sub> O <sub>3</sub> <sup>2-</sup> , R <sub>3</sub> P, R <sub>3</sub> As, (RO) <sub>3</sub> P, CN <sup>-</sup> , RNC, CO, C <sub>2</sub> H <sub>4</sub> , H <sup>-</sup> , R <sup>-</sup>
	<b>Borderline</b> C <sub>6</sub> H <sub>5</sub> NH <sub>2</sub> , C <sub>5</sub> H <sub>5</sub> N, N <sup>3-</sup> , Br <sup>-</sup> , NO <sub>2</sub> <sup>-</sup> , N <sub>2</sub> , SO <sub>3</sub> <sup>2-</sup>	

### 2.4.1 Ligand design concept

Ligands can be successfully designed to be detective and selective of transition metals ions, a process widely applied for heavy metal ions adsorption. For example, to design a specific ligand for capturing hard Fe<sup>3+</sup> requires selecting a hard donor atom such as a negative oxygen donor, within an acid solution medium (see table 2.2). Essentially, the nature of atoms binding here can be classified in a wide range from covalent to ionic bond. This atomic binding provides excellent chromatic properties in a specific aqueous solution. Such successful strategy of colorimetric formation of [ligand-metal ion]<sup>n+</sup> extremely depends on solution pH and careful application of the ligand field

theory to obtain a maximum adsorption capacity as well as a highly obvious visual colour change. In accordance with these conditions herein are some critical examples from literatures:

Ligands of *(3-(3-(methoxycarbonyl) benzylidene)hydrazinyl) benzoic acid* and *N,N(octane-1,8-diylidene)di(2-hydroxy-3,5-dimethylaniline)* were used to detect selenium (IV) and palladium (II) (Awual & Hasan, 2015a, 2015b) at a pH=1.5 (see Figure 2.9a, b). Selenium (IV) and palladium (II) classified as soft acid ions were efficiently adsorbed to 99% in an acidic condition. The strong link of these ions with the soft donor ligands that consist of –N-O- was obtained (Figure 2.9a, b), indicating that there is an affinity between the soft acid ions and the soft donor ligand. Failure to apply the ligand field theory possibly leads to reduced efficiency in linking between the transition metal ions with the ligands. To clarify this inadequate application, *(dicarboxylate 1-(phenylamino)-3-phenylimino-thiourea)* ligand was used to detect  $Cd^{2+}$  in buffer solution of pH = 12.5 (M. A. Shenashen et al., 2014), and *4-(2-pyridylazo)-1,3-benzenediol* ligand was used to detect Cu(II) at a pH = 12.5 (Hua et al., 2014) (Figure 2.9c,d); however, percentage clearance of Cd (II) and Cu (II) was lower than 97% under strong basic conditions. In this case and by applying the ligand field theory, Cd (II) and Cu (II) are classified as soft acid ions as shown in Table 2.2 and the ligands were designed to be soft donor types (–N-O-), but the reaction medium was strongly basic and according to Pearson theory, the aqueous solution must be acidic to achieve a high clearance.

More examples that investigate the broad line of transition metal are presented in table 2.2. ligand of *(tetrakis (3-carboxysalicylidene)) naphthalene-1, 2,5,5-tetramine* that was prepared could successfully to remove up to 99.85% of pb (II) ions at pH=7.0 (Awual & Hasan, 2014b) as shown in Figure 2.10 e; also, ligand of *dicarboxylate 1,5-diphenyl-3-thiocarbazone* synthesized could efficiently adsorb 99.5% of Co (II) at pH= 8.0. These findings highlight that the borderline ions are not affected by hard/soft ligands, but an acidic condition is highly recommended to obtain a complete adsorption efficiency. Therefore, it is significantly recommend the application of ligand field theory before designing [ligand-metal ion]<sup>n+</sup> complex systems. To support this claim, numerous examples have been conclusively shown in table 2.3; also, appropriate pH values are highly recommended and summarized in Figure 2.11.

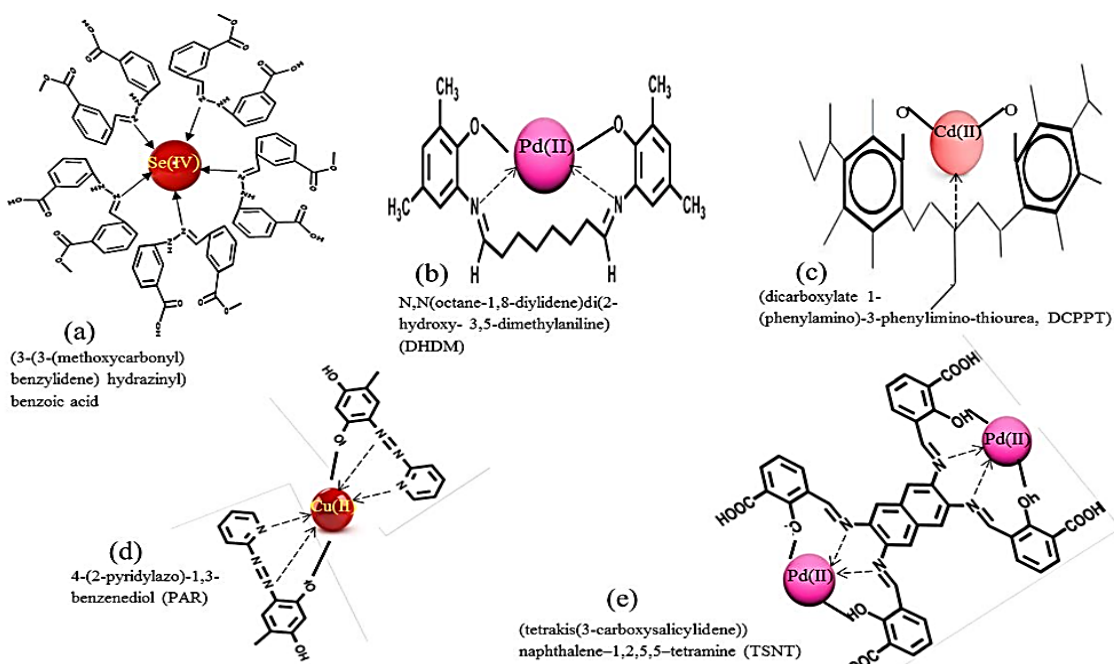


**Figure 2-10** Complex formation during the recognition of (a) Se(IV), (b) pd(II), (c)Cd(II), Cu(II) and pd(II) ions in solution at a temperature of 25<sup>0</sup>C and pH = 1.5, 1.5, 12.5, 12, 7, respectively

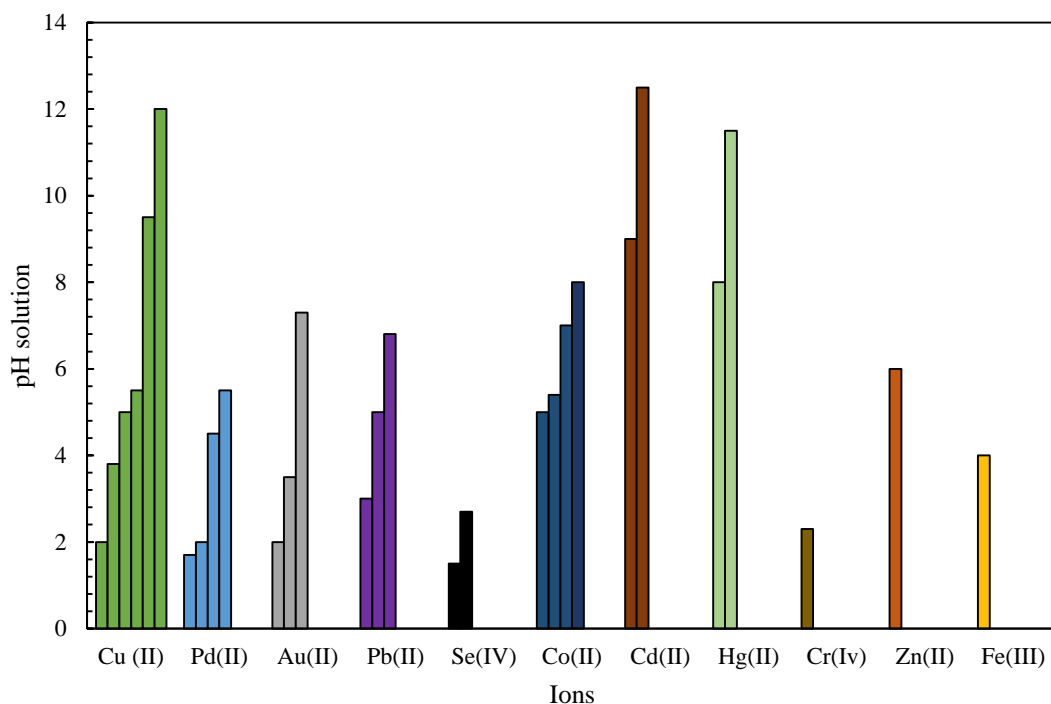


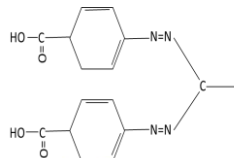
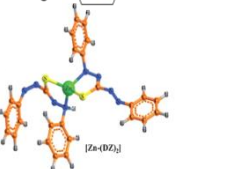
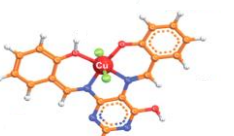
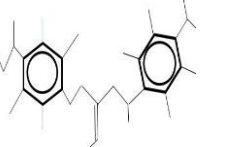
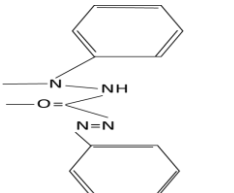
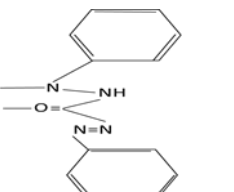
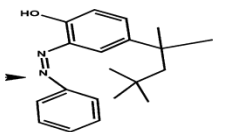
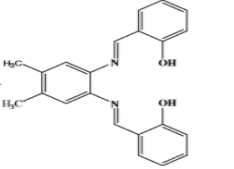
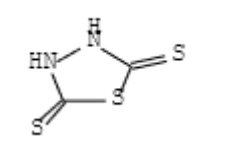
**Figure 2-11** The range of pH for different ions solution that can be detected by several ligands

**Table 2-3** Various ligands, chemical structure that adsorbed heavy metal ions from aqueous solution at different condition

Ligand formula	Chemical	Metal ions	Medium	Sorption efficiency (%)	References
	3-(((5-ethoxybenzenethiol)imino)methyl)salicylic acid (EBMS)	Cu (II)	pH=7.0, 3-morpholinopropane sulfonic acid (MOPS) with NaOH) buffer	97%	(Md Rabiul Awwal, Mohamed Ismael, et al., 2013)
	Monophosphonic acid	Arsenic (V) and phosphate	pH=2.01, 6.97, 0.1 mol/L NaOH. Buffer	99% 74%	(Awwal, El-Safty, & Jyo, 2011)
	N,N-bis(2-salicylidene)-1,2-bis(2-aminophenyl)ethane	Pd(II)	pH=3.50, 0.2 M of KCl with HCl, as buffer	98%	(Awwal & Yaita, 2013)
	6-((2-(2-hydroxy-1-naphthoyl)hydrazono)methyl)benzoic acid	Au(III)	pH=2.0, 0.2 M of KCl with HCl as buffer	96%	(Awwal & Ismael, 2014)
	((3-(3-methoxycarbonyl)benzylidene)hydrazinyl)benzoic acid	Pd(II)	pH=3.50, 0.2 M of KCl with HCl as buffer solution	98%	(Awwal, Khaleque, Ratna, & Znad, 2015)
	(tetrakis(3-carboxysalicylidene)naphthalene-1,2,5,5-tetramine) (TSNT)	Pd(II)	pH =2.0, 0.2 M of KCl with HCl as buffer solution	95%	(Awwal & Hasan, 2015b)
	N,N'-(octane-1,8-diylidene)di(2-hydroxy-3,5-dimethylaniline) (DHDM)	Au(II)	pH=3.5, (0.2 M of KCl with HCl as buffer solution	98%	(Awwal, 2014)
	dibenzo-24-crown-8 ether	Cs	pH=7.0, adding of HCl or NaOH as buffer solution	99%	(Awwal, Yaita, Taguchi, et al.,
	$\alpha$ , $\beta$ , $\gamma$ , and $\delta$ -tetrakis(1-methylpyridinium-4-yl)porphine r-toluene sulfonate (TMPyP)	Cd(II)	pH=9.5, using 0.2M of 3-morpholinopropane sulfonic acid, MOPS	96-99%	(S. A. El-Safty, Shenashen, & Khairy, 2012)

Table 2-3: (Continued)



Ligand formula	Chemical	Metal ions	Medium	Sorption efficiency (%)	References
	dicarboxylate 1,5-diphenyl-3-thiocarbazone	Hg(II)	pH=11.5, perchlorate as buffer solution	99.5%	(M. Shenashen, El-Safty, & Elshehy, 2013)
	Diphenylthiocarbazone (DZ)	Zn(II)	pH=6.0, using 0.2 MCH <sub>3</sub> COOH/CH <sub>3</sub> -COONa with 0.1 M NaOH as buffer solution	96-99%	(S. A. El-Safty, Shenashen, Ismael, et al., 2012)
	4,5-diamino-6-hydroxy-2-mercaptopyrimidine (DSAHMP)	Cu(II)	pH =7.0, using 0.2 M 3-morpholinopropane sulfonic acid, MOPS	96-99%	(S. A. El-Safty, Shenashen, Ismael, Khairy, & Awual, 2012)
	(dicarboxylate 1-(phenylamino)-3-phenyliminothiourea, DCPPT)	Co(II)	pH =7.0, (MOPS with NaOH as buffer solution	97%	(M. A. Shenashen, El-Safty, & Elshehy, 2014)
	Diphenyl carbazide chelating	Fe(III)	pH =4.0, using CH <sub>3</sub> COOH-CH <sub>3</sub> -COONa as buffer solution	94-96%	(S. A. El-Safty & Shenashen, 2013)
	Diphenyl carbazide chelating	Hg(II)	pH =8.0, using a mixture of CHES/MOPS as buffer solution	94-96%	(S. A. El-Safty & Shenashen, 2013)
	4-tert-octyl-4-((phenyl)diazenyl)phenol (TPDP)	Pb(II)	pH=7.0, 0.2 M MOPS with NaOH as buffer solution	98%	(Awual, Hasan, & Shahat, 2014)
	N,N-disalicylidene-4,5-dimethylphenylenedene (DDPD).	Hg(II)	pH= 7.0 morpholinopropane sulfonic acid (MOPS) and sodium acetate	99%	(Awual, 2017b)
	2,5-dimercapto-1,3,4thiadiazole	Pb(II)	pH=2.5, 0.2M KCl-HCl and 0.1M CH <sub>3</sub> COOH-CH <sub>3</sub> COONa	99%	(Shahat et al., 2018)

### 2.5 Ligands conjugate mesoporous

At the dawn of the 20<sup>th</sup> century, many attempts were made to immobilize azo-chromophore ligand, which is part of the molecules responsible for its colour onto mesoporous type MCM-41 for optical sensor applications have been done. One of this attempt by Fowler and colleagues who synthesized 3-(2,4-dinitrophenylamino)propyl chromophore ligand functionalized mesophase type MCM-41 as sensors to detect molecules within the channel-like pores of MCM-41 phases fabricated in the form of thin membranes (Fowler, Mann, & Lebeau, 1998; Lebeau, Fowler, Hall, & Mann, 1999). Six years later, Rodman and co-workers developed an optical sensor anchored into mesoporous silica monoliths for Cu (II) ions detection by formation of a copper tetra amine complex, taking advantage of the diffusion of Cu (II) ions into the pores which are lined with amino groups (Rodman, Pan, Clavier, Feng, & Xue, 2005).

Nowadays, numerous studies have been conducted to find a novel conjugate mesoporous which has new hierarchical mesophase and high specific surface area. For instance, several studies have been done by El-safty and co-workers who synthesize ligands conjugate into 3D well-defined mesoporous phase cage cavities enhancing the sensitivity with naked-eye detection of several toxic heavy metal ions in aqueous media (S. A. El-Safty, Ismail, Matsunaga, Nanjo, & Mizukami, 2008; S. A. El-Safty, Prabhakaran, Ismail, Matsunaga, & Mizukami, 2008; El-Safty, Ismail, Matsunaga, Hanaoka, & Mizukami, 2008; El-Safty, Ismail, Matsunaga, & Mizukami, 2007; El-Safty, Prabhakaran, Ismail, Matsunaga, & Mizukami, 2007).

#### 2.5.1 Mesoporous synthesis methods

##### 2.5.1.1 Liquid-crystal templating (LCT)

Liquid-crystal templating technique is very common and was invented by Mobil Company scientists who prepared the type of M41S mesophase by using supramolecular surfactant micelles e.g: alkyltrimethylammonium surfactants which were assembled together to form a mesophase. Different mesophase types such as hexagonal, lamellar, or cubic meso-structures can be successfully synthesized under a certain pH condition, anionic silicate species, and cationic or neutral surfactant molecules. The condensation of silicate species is proposed to form a hexagonal structure around the preformed surfactant array under certain conditions. These silicate species that are located on the external surfaces can also be randomly organized rod-

like micelles via columbic force or other types of interactions. Thus, these ordered composite species are spontaneously collected into a highly ordered mesoporous phase as illustrated in Figure 2.12 (ALothman, 2012).

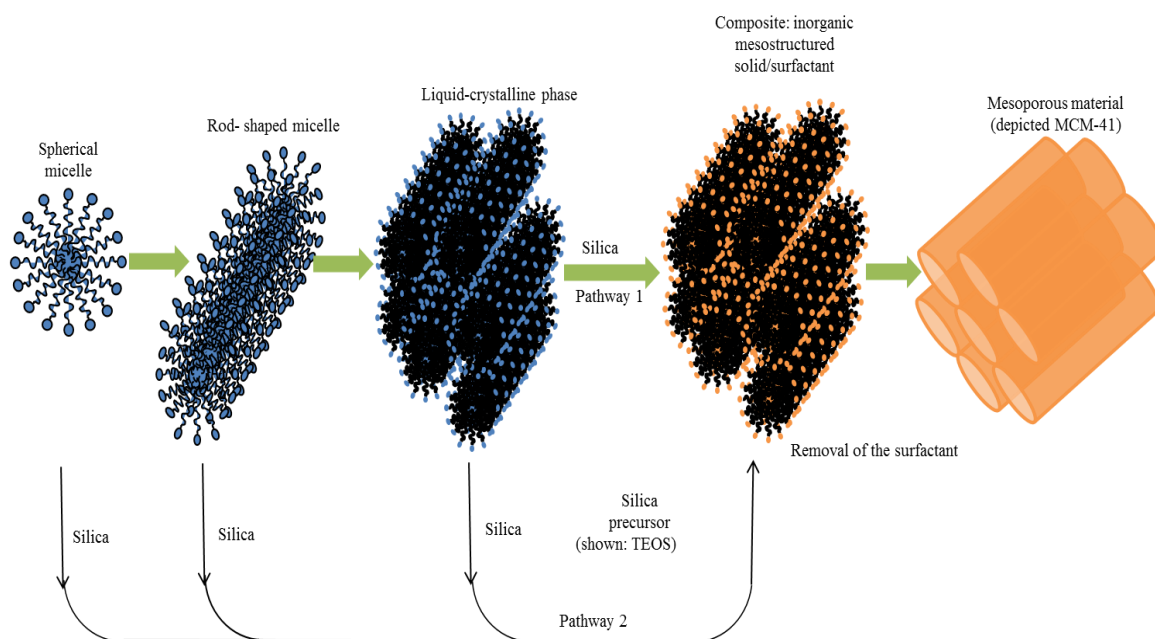


**Figure 2-12** Liquid crystal templating mechanism using structure directing agent: pathway 1) true liquid-crystal template mechanism, pathway 2) cooperative liquid-crystal template mechanism

The formation of spherical micelles in aqueous solution can be organized in various shapes such as cubic, cylindrical,  $1a3d$  cubic and lamellar phases based on the temperature of the aqueous solution as well as the surfactant concentration as shown in Figure 2.13. All these phases can be obtained by adding inorganic framework such as tetraethylortho silicate (TEOS) or tetramethylortho silicate (TMOS) as a silica source. The simplest liquid crystalline phases formed via spherical micelles are the micellar cubic and hexagonal phases. The cubic phase is a highly viscous, optically isotropic phase in which the micelles arranged as a cubic lattice with roughly formed conditions around 30-40% concentrations of amphiphilic surfactant at 35<sup>0</sup>C (Figure 2.13, symbol  $I_1$ ). Whilst, amphiphilic surfactant at concentrations of 35-70% and at 50<sup>0</sup>C are possibly fused to form cylindrical aggregates of indefinite length, and arranged as a long-ranged hexagonal lattice, symbol  $H_1$ . The  $1a3d$  cubic phase can be possibly formed around 50% and > 75% amphiphilic surfactant concentrations at 60<sup>0</sup>C, symbol  $V_1$ . The lamellar phase formed at concentrations of 60 - 95% amphiphilic surfactant under 70<sup>0</sup>C, symbol  $L\alpha$ . This mesophase consists of

amphiphilic molecules arranging in bilayer sheets separated by layers of water (Evans & Wennerström, 1999; Holmberg, Jönsson, Kronberg, & Lindman, 2003).

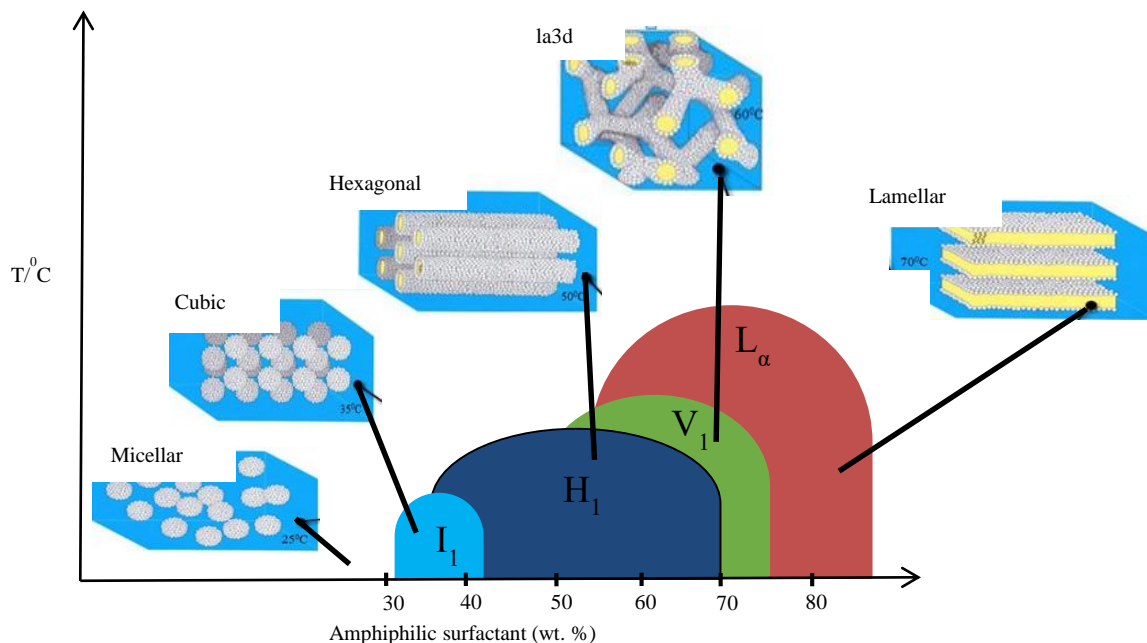


**Figure 2-13** Schematic showing the aggregation of amphiphiles into micelles and then into lyotropic liquid crystalline phases as a function of amphiphile concentration and temperature

For an overview of the literatures, there is a strong relationship between the mass ratios of silica/ surfactants/acid concentration to obtain various types of the mesophase morphology as shown in table 2.4. From table 2.4, cationic and non-ionic surfactants of C<sub>12</sub>TMAB/decane/P<sub>123</sub> provides cubic Fd<sub>3</sub>m mesophase shape with highest specific surface area 1110 m<sup>2</sup> g<sup>-1</sup> (S. A. El-Safty, Shahat, & Ismael, 2012) and also the mesophase of KIT-6 provides a specific surface area 1096 m<sup>2</sup>g<sup>-1</sup> (Fayed et al., 2014).

**Table 2-4** Syntheses of mesoporous in the presence of, cationic or non-ionic surfactants

Precursors	Surfactant	Mass ratios	SBET (m <sup>2</sup> g <sup>-1</sup> )	Mesophase	V <sub>p</sub> (cm <sup>3</sup> g <sup>-1</sup> )	D (n.m)	References
Tetramethyl orthosilicate (TMOS)	F <sub>108</sub> (Non-ionic)	F <sub>108</sub> /TMOS:HC1/H <sub>2</sub> O 1.4:2:1	585	2D Hexagonal	0.75	12.7	(Md Rabiul Awual, Mohamed Ismael, et al., 2013)
Tetramethyl orthosilicate (TMOS)	F <sub>108</sub> (Non-ionic)	F <sub>108</sub> /TMOS:HC1/H <sub>2</sub> O 1.4:2:1	675	Cage-pored	0.72	12.7	(Md Rabiul Awual, Tohru Kobayashi, Hideaki Shiwaku, et al., 2013)
Aluminosilicate	F <sub>68</sub> (Non-ionic)	F <sub>68</sub> /aluminosilicate:H <sub>2</sub> O/ 1,3,5-trimethylbenzene neutral	545	Pm <sub>3n</sub> cubic cage	0.66	7.2	(M. A. Shenashen et al., 2014)
Aluminosilicate	F <sub>68</sub> (Non-ionic)	F <sub>108</sub> used as a template in both the lyotropic and microemulsion systems.	439	Im3m cubic cage	0.65	9.7	(M. A. Shenashen et al., 2014)
Aluminosilicate	F <sub>68</sub> (Non-ionic)	F <sub>108</sub> aluminosilicate/H <sub>2</sub> O neutral	419	Ia3d cubic cage	0.54	8.3	(M. A. Shenashen et al., 2014)
Tetraethyl orthosilicate TEOS	CTAB (non-ionic)	NH <sub>4</sub> OH:ethanol:DIW:TEOS 3.16:27.54:1.8:1	200	Core/double-shell	0.3	4.5	(M. Shenashen et al., 2013)
Tetraethyl orthosilicate TEOS	Brij56 (non-ionic)	Brij56/TMOS: HCl/H <sub>2</sub> O	556	Hexagonal P6mm	0.7	4.3	(S. A. El-Safty, Shenashen, Ismael, Khairy, & Awual, 2013)
Tetraethyl orthosilicate TEOS	Pluronic P <sub>123</sub> ( non-ionic)	P <sub>123</sub> /HCl/H <sub>2</sub> O/ butanol	1096	KIT-6	0.95	10.4	(Fayed, Shaaban, El-Nahass, & Hassan, 2014)
TMOS/ Al(NO <sub>3</sub> ) <sub>3</sub> .9H <sub>2</sub> O, 1.125g of H <sub>2</sub> O-HCl	F <sub>68</sub> (Non-ionic)	F <sub>68</sub> /TMOS:HC1/H <sub>2</sub> O 1:2:1	705	Cubic Ia3d	0.9	6.0	(S. A. El-Safty, Shenashen, & Khairy, 2012)
Tetramethyl orthosilicate (TMOS)	C <sub>12</sub> TMAB/decane	C <sub>12</sub> TMAB:decane:TMOS:H <sub>2</sub> O/HCl 1:0.5:2:1	1110	Cubic Fd3m	0.17	1.9	(S. A. El-Safty, Khairy, & Ismael, 2012)

## 2.6 Pathways of functionalized mesoporous / ligand

### 2.6.1 Post- synthetic grafting pathway

Grafting pathway can be defined as the subsequent modification of inner mesoporous structure phases by organic groups. This pathway is mistakenly named “immobilization” which is a term widely used in adsorption techniques such as the removal of toxic heavy metal ions. Fundamentally, there are three types of these organic groups such as  $(R'O)_3SiR$ , chlorosilanes  $(ClSiR_3)$  and silazanes  $HN(SiR_3)_3$  can be reacted with the inner free silanol groups of the pore surfaces of mesoporous material which is often done in an organic solvent (e.g., toluene) as depicted in Figure 2.14. The advantage of this pathway is that the external mesostructured silica phase usually retains their shape while the porosity of the lining walls of this mesostructured phase is reduced depending on the size of the molecular groups and the degree of occupation. The disadvantage of this pathway is that the organosilanes react abundantly at the pore openings within the initial stages of the synthesis process and then the pores can be loaded to a complete closure with non-homogeneous distribution of the organic groups (Hoffmann, Cornelius, Morell, & Fröba, 2006).

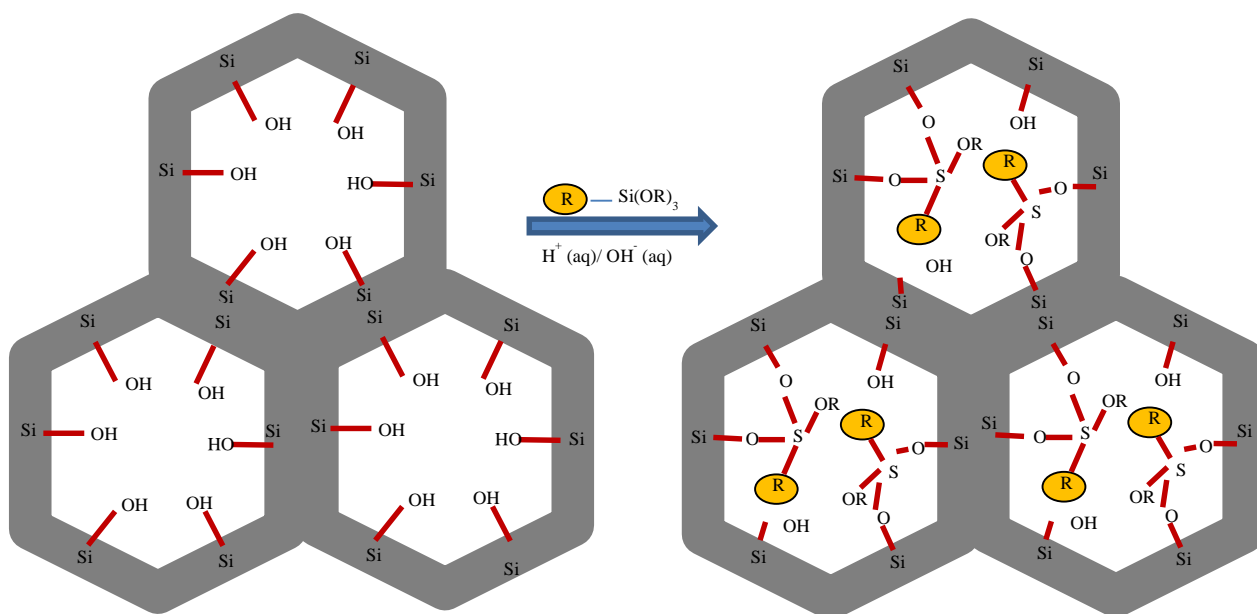


**Figure 2-14** The post- synthetic grafting method for organic modification of mesoporous phases with organosilanes of the type  $(R'O)_3SiR$ . R=organic functional group

### 2.6.2 Co-condensation/or direct synthesis pathway

The alternative possible pathway is a direct synthesis named one-pot synthesis process. In this pathway, there is a co-condensation of both tetraalkoxysilanes  $(RO)_4Si$  such as TEOS or TMOS with organosilanes type  $(R'O)_3SiR$  in the presence of directing-structure agents (template) which could lead to immobilization of the organic residues into the pore walls by covalent bonds as illustrated in Figure 2.15. It can also be possible to modify silica by employing a commercial mesoporous silica phase instead of TEOS/or TMOS precursors such as using MCM or SBA mesophases. The advantage of this pathway is the absence of pore blocking problem within an organically formed immobilization. Compared to the previous pathways, the molecular organic units are more homogeneously distributed, while the disadvantage is the increase in concentration of  $(R'O)_3SiR$  increases in the reaction mixture, causing a totally disordered mesophase. This tendency towards homocondensation reaction is a consistent problem due to the fact that the organic materials cannot be guaranteed a homogeneous distribution in the framework of the mesoporous phase. Hence, the incorporation of more organic groups could lead to a reduction in the pore volume, pore diameter, and thus reduced specific surface area. In the direct synthesis pathway, the chemical extractive method is recommended instead of the calcination process, which is used for removing the surfactant template because the calcination process may destroy the organic functional groups during the removal process (Hoffmann et al., 2006).

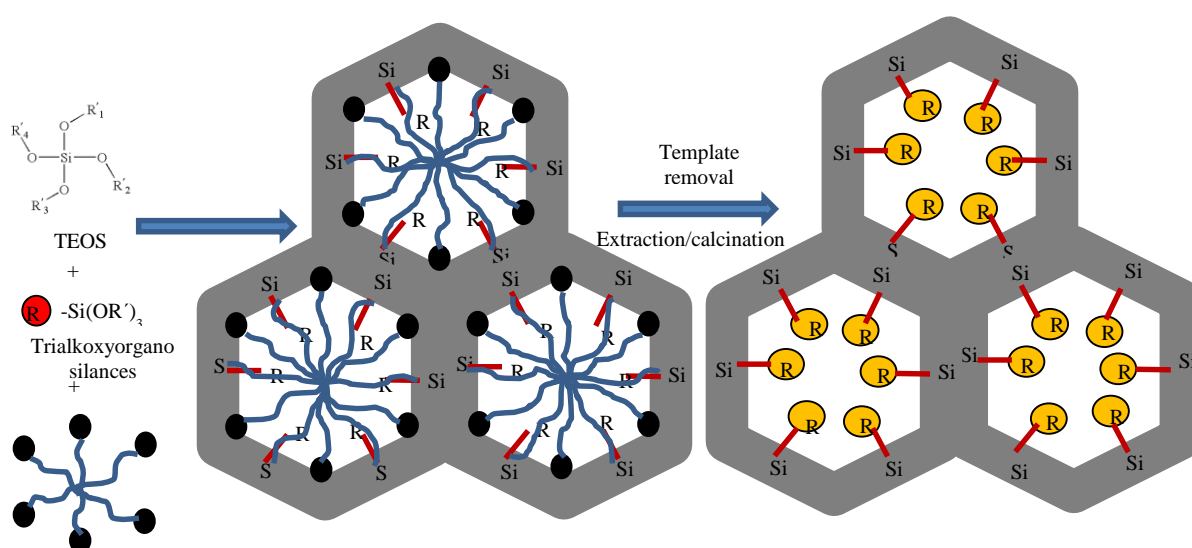


**Figure 2-15** Co-condensation pathway for the organic modification of mesoporous pure silica phases. R=organic functional group

### 2.6.3 Hydrolysis and condensation pathway

This technique has been known for the preparation of periodic mesoporous organosilicas (PMOs), which can be synthesized by hydrolysis and condensations of bridged bisilylated organosilica precursors of the type of  $(R'O)_3Si-R-Si(OR')_3$  by sol-gel chemistry method as shown in Figure 2.16 (Loy & Shea, 1995; Shea & Loy, 2001). In the hydrolysis pathway, the organic molecule units are incorporated by two covalent bonds into the external silica matrix in a three-dimensional network structure which is entirely homogeneously distributed in the pore walls of the silica matrix. The advantages of the hydrolysis pathway are good thermal stability as well as large inner surface areas of up to  $1800 \text{ m}^2 \text{ g}^{-1}$ . However, the major issue which reduces the efficiency of this method is the completely disordered pore systems and also the pore radius is exhibited relatively in a wide direction. PMOs are suitable candidates for a series of technical applications, for example, in the field of catalysis, adsorption, nano-electronics and chromatography.

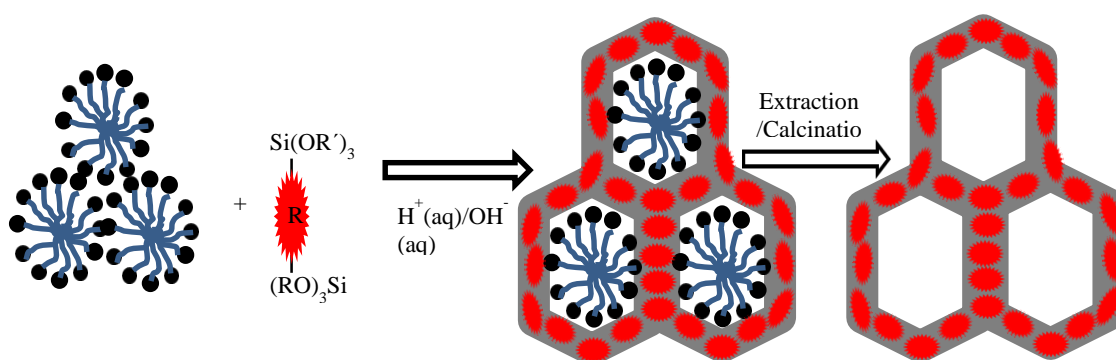


**Figure 2-16** The hydrolysis and condensation pathway constructed by bisilylated organic bridging units. R= organic bridge

### 2.7 Mesoporous zeolite

Global industrial pollution issues and the development of fundamental studies have continually increased the interest in the demands to expand the pore sizes of zeotype materials from the micropore region to the mesopore region (Christensen, Johannsen, Schmidt, & Christensen, 2003; Jacobsen, Madsen, Houzvicka, Schmidt, & Carlsson, 2000). Wastewater treatment is one of the issues that encouraged researchers to develop a mesoporous zeolite for the separation and selective adsorption of a wide



range of organic molecules from water. Zeolite mesoporous crystals have much larger external surface area, which could expose more active sites than conventional zeolite crystals (Meng, Nawaz, & Xiao, 2009). The strategies for the synthesis of zeolite mesotype are carried out by using nanostructured carbon, carbon and polymer aerogel, cationic polymer, organosilane templates and sol-gel method (Egeblad, Christensen, Kustova, & Christensen, 2007; Meng et al., 2009); (Chal, Gerardin, Bulut, & Van Donk, 2011; Y. Tao, Kanoh, Abrams, & Kaneko, 2006).

### **2.7.1 Pathways of the synthesis of mesoporous zeolites**

#### **2.7.1.1 Nanostructured carbon templating**

Nano-sized carbon particles about 12 nm was utilized by Jacobsen et al. (Jacobsen et al., 2000) as mesoscale templates to disperse into the aluminosilicate zeolite gel. These carbon nanoparticles are encapsulated by growing up the zeolite crystals, fabricating ZSM-5 embedded with nanocarbon particles. Removing the embedded nanocarbon matrix by calcination at 550<sup>0</sup>C results in the formation of ZSM-5 mesoporous. Schmidt et al. (Schmidt et al., 2001) and Boisen et al. (Boisen et al., 2003) have proposed using carbon nanotubes as templates to synthesize ZSM-5 mesoporous channels which have uniform and straight widths of 12-30 nm pore size. The drawback of this route is that nano carbon particles are mostly hydrophobic, and it is not easy to disperse into the gels homogenously through synthesis of ZSM-5 mesoporous process.

#### **2.7.1.2 Carbon and polymer aerogel templating**

Mesoporous carbon aerogel (CA) and mesoporous resorcinol—formaldehyde (RF) aerogels as templates to synthesize mesoporous zeolite has reported by Tao et al. to obtain open mesopore of ZSM-5 (Y. Tao, Hattori, Matumoto, Kanoh, & Kaneko, 2005; Y. Tao, Kanoh, Hanzawa, & Kaneko, 2004; Y. Tao, Kanoh, & Kaneko, 2003a, 2003b, 2005). Both these aerogels have large and thick mesopores, which could be basically stable during synthesis of mesoporous zeolites. For example, W.-C. Li et al. has demonstrated that silicalite-I zeolites can synthesize with hierarchically porous structures and the monolithic zeolites observe a high selectivity above 80% to  $\epsilon$ -caprolactam combined with a high rate of reaction in the Beckmann rearrangement of cyclohexanone oxime (W.-C. Li et al., 2005). The disadvantage of this route is larger pore walls compared to less mesopore volume.

### 2.7.1.3 Cationic polymer templating

To simplify the procedure of preparing zeolite mesoporous, the mesoscale soft-template is suitable for use in this route due to the fact that the soft-template is easy to self-assemble with aluminosilicate in the synthesis of mesoporous zeolite. The following factors are carefully considered when selecting the soft-template route: (1) the soft-templates should be stable in alkaline/ acid media even at relatively high temperatures of 140-180 °C, otherwise, the templates could be decomposed during the synthesis of zeolites mesoporous; (2) the soft-templates should interact with silica species easily and strongly. It is well known that Coulomb force at a molecular level is very strong and silica species under alkaline conditions for synthesizing zeolites have negative charges, thereupon, soft-templates with positive charges are preferred; (3) the soft-templates should have a suitable mesoscale sizes and their morphology in aqueous solution should be fibre-like; (4) the soft-templates should be of low cost, which is very important for the largescale industrial production of zeolites mesoporous (Meng et al., 2009). Xiao et al. reported synthesizing hierarchical zeolite mesoporous type of Beta-H using soft-template mesoscale cationic polymer of polydiallyldimethylammonium chloride, (PDADMAC) has successfully prepared (F. S. Xiao et al., 2006).

### 2.7.1.4 Organosilane templating

The amphiphilic organosilane such as  $[(\text{CH}_3\text{O})_3\text{SiC}_3\text{H}_6\text{N}(\text{CH}_3)_2\text{C}_n\text{H}_{2n+1}]\text{Cl}$  can be used as a mesopore-directing agent to synthesize mesoporous aluminosilicate (Choi, Cho, et al., 2006; Choi, Srivastava, & Ryoo, 2006; Srivastava, Choi, & Ryoo, 2006), and the first preparation method using this organosilane templating with tuneable mesoporosity was reported in the middle of 2006 by Choi et al. (Choi, Cho, et al., 2006). In more details, the mesoporous diameters can be tuned to the range of 2-20 nm, based on the molecular structure of the mesopore directing silanes and the hydrothermal synthesis conditions. Furthermore, this pathway is also reported to synthesize series of aluminosilicate zeolites such as LTA (Choi, Cho, et al., 2006) and aluminophosphates zeolites (Choi, Srivastava, et al., 2006).

### 2.7.1.5 Hydrothermal pathway

This pathway is one of the most successful routes for the synthesis of stable ordered mesoporous aluminosilicates using a strong acidity media. In this route, the zeolite nanoclusters assembled with surfactant micelle is prepared by combining the advantages of mesoporous and zeolites crystals, announced almost simultaneously by two research groups of Xiao (Di et al., 2003; Han et al., 2002; Han et al., 2001; Lin, Sun, Lin, Jiang, & Xiao, 2004; Y. Sun et al., 2003; F.-S. Xiao et al., 2002; Z. Zhang et al., 2001) and Pinnavaia (Y. Liu & Pinnavaia, 2003, 2004; Triantafyllidis et al., 2006; H. Wang, Liu, & Pinnavaia, 2006).

## 2.8 Kinetic models

Previous studies have investigated the two main kinetic models associated with adsorption processes they are; the linear first order and Langmuir- Hinshelwood (L-H) non-linear kinetic model (Awual, 2017b; Plazinski, Rudzinski, & Plazinska, 2009; Shahat, Awual, & Naushad, 2015). The adsorption capacity is also associated with equilibrium between the amount of adsorbent and adsorbate in the solution; hence the resulting equilibrium relationship can be described by these kinetic models. Furthermore, adsorption isotherm is relating with the equilibrium concentration of a solute on the surface of an adsorbent,  $q_e$ , to the concentration of the solute in the liquid,  $C_e$ , and can be described with the following equation:

$$q_e = (C_o - C_e)V/m \quad (2.1)$$

$q_e$  = the amount of solute adsorbed per unit weight of solid at equilibrium condition. The unit is either g/g or mg/g,  $C_o$  is the initial concentration,  $C_e$  = Equilibrium concentration of solute remaining in solution when the adsorbed solute is equals.

### 2.8.1 Equilibrium isotherm models

There are several isotherm models that can simulate the type of equilibrium distribution. The following isotherm models with equations and are illustrated in Figure 2.17.

i. Linear:  $q_e = K \cdot C_e \quad (2.2)$

ii. Langmuir:  $q_e = q_{max} \cdot K_L \cdot C_e / 1 + K_L \cdot C_e \quad (2.3)$

iii. Freundlich:  $q_e = K_f \cdot C_e^{1/n}$  (2.4)

iv. Brunauer, Emmet, and Teller (BET):

$$q_e = K_b \cdot C_e \cdot Q^o / (C_S - C_e) (1 + (K_b - 1)(C_e/C_S)) \quad (2.5)$$

Where  $k$ ,  $q_{max}$ ,  $K_L$ ,  $k_f$ ,  $K_B$  are all empirical constants. Also, the following parameters are constant and used in eq. 2.5:  $C_S$  = saturation (solubility limit) concentration of the solute. ( $\text{mg L}^{-1}$ ),  $K_B$  = a parameter related to the binding intensity for all layers. The most commonly assume conditions that clarified each isotherm model are illustrated in table 2.5: Isotherm models with commonly assume conditions.

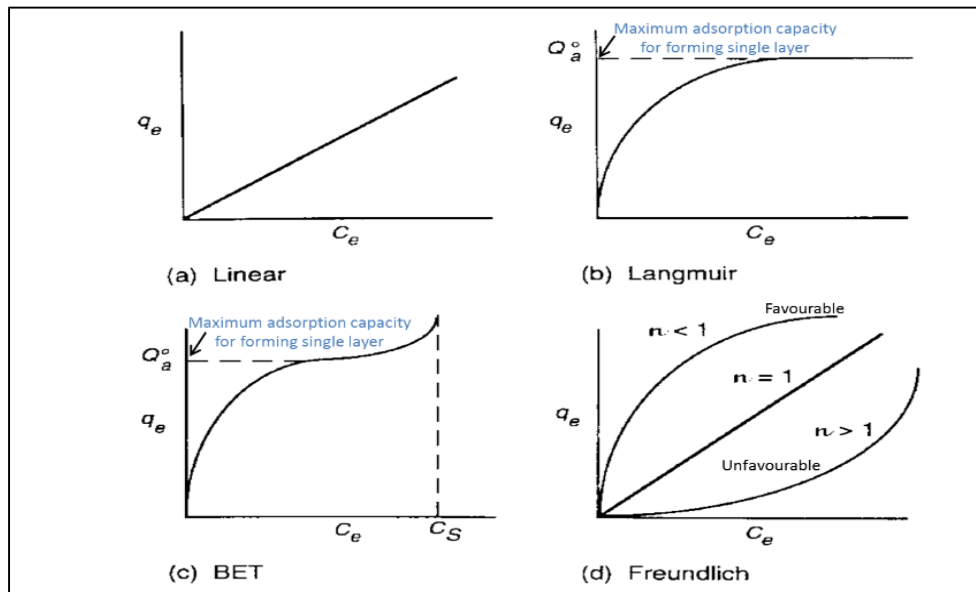


**Figure 2-17** types of the equilibrium adsorption isotherm models

The most commonly assumed conditions that clarify each kinetic model are as follows: the linear isotherm can be applied for the first order reaction rate and monolayer coverage; whereas the Langmuir isotherm model can be applied for second order reaction equilibrium model, with the particles adsorption sites and monolayers equal. In case of the Brunauer, Emmet, and Teller (BET) isotherm model, multi-layer model and Langmuir isotherm are applied to each layer. No transmigration occurs between layers and also there is an equal energy of adsorption for each layer except for the first layer. As depicted in Figure 2.10 C,  $C_S$  is the saturation (solubility limit) concentration of the solute ( $\text{mg L}^{-1}$ ),  $K_B$  = a parameter related to the binding intensity for all layers. Note: when  $C_e \ll C_S$  and  $K_B \gg 1$  and  $K_{ad} = K_B/C_S$  BET isotherm approaches Langmuir isotherm. Freundlich isotherm is an empirical model and can be widely used. From Figure 2.10 d,  $1/n$  is a measure of the adsorption intensity; the higher the  $1/n$  value, the more favourable is the adsorption (generally,  $n < 1$  or  $1/n > 1$ ).

### 2.9 Summary

This chapter illustrated the influence of the distribution of industrial contaminants such as dyes and heavy metal ions into waterbodies and then discussed the conventional water treatment methods. The advantages and disadvantages of these treatment methods were discussed. This chapter also clarified the different technologies and modified systems used to achieve a solar photocatalytic degradation and synthesis of conjugate mesoporous adsorbent catalysts a new sustainable concept in advanced water treatment processes, which have been recently gained the attention of researchers; thereafter, a review of researches and their results were summarized. This chapter was followed by an explanation of the fundamental field theory and ligands design method which is highly recommended in the synthesis of mesoporous adsorbent strategy, and then explained with extensively critical examples necessary to avoid failure with field theory. Following this, mesoporous synthesis methods and the adjusted forms of mesophase were summarized; also, the functionalized ligand strategies were discussed. This chapter was concluded by describing the kinetic models and clarified the assumptions of using these models.

Dyes such as methyl orange and methylene blue; the heavy metal ions including mercury ( $\text{Hg}^{2+}$ ) and lead ( $\text{Pb}^{2+}$ ) are major toxic pollutants present in wastewater effluents. These contaminants negatively affects human and aquatic bodies. To treat these pollutants, solar photocatalytic degradation is a potential treatment for complete mineralisation of the organic contaminants present in water. To further enhance this method, modified zeolite type of ZSM-5 and reduced graphene oxide are recommended as substrates. The synthesis of mesoporous zeolite pathways including nanostructured carbon templating, carbon and polymer aerogel templating, cationic polymer templating and organosilane templating are discussed. Among these pathways, cationic polymer templating is preferable due to their soft-templates which are easily self-assembled with aluminosilicate. In this chapter, reduced graphene oxide is also recommended as a substrate in the photocatalytic process to enhance light absorption and increase the adsorption of pollutants and also promotes charge separation and transformation.

According to Pearson theory, there are so many types of ligands donor such as (O-) hard, (N-) hard, (S-N) soft, and (S-N-O) soft that can effectively form complexes of [ligand –metal ion]<sup>n+</sup>, depending on both the pH of the solution and the type of metal

ions (hard/or soft ions), which will release in aqueous solution. Appropriate, stable and high specific surface area modified ZSM-5 mesoporous substrate which hosts the organic ligand instead of the TEOS/or TMOS precursor substrate is highly recommended. Finally, the mesophase morphology can be effectively controlled by adjusting the parameters such as solution temperatures, type of surfactants, surfactant concentrations and pH of solution.

# CHAPTER 3

## 3 Experimental Methods

### 3.1 Introduction

This chapter reports the experimental procedure and apparatuses employed in this PhD research project. It also contains details of the chemicals, the technique and characterization for synthesizing the catalyst as well as the analytical technique for the identification and qualification of the pollutants and their intermediates.

### 3.2 Chemicals

#### 3.2.1 Chemicals for catalysts preparation

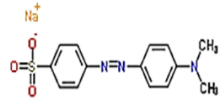
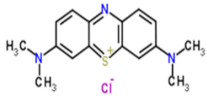
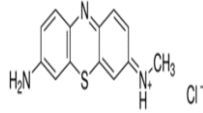
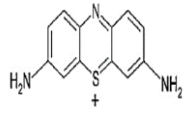
Zeolite ZSM-5 (Molar ratio  $\text{SiO}_2/\text{Al}_2\text{O}_3 = 600$ ,  $300 \text{ m}^2 \text{ g}^{-1}$  specific surface area, 2– $3 \mu\text{m}$  particle size, 2.4 nm pore size) was provided from ACROS Organics, A Thermo Fisher Scientific Brand, New Jersey–USA. Titanium dioxide ( $\text{TiO}_2$ , Degussa P25, 70% anatase: 30% rutile,  $53 \text{ mg}^{-1}$  specific surface area), tetraethoxysilane (TEOS, 99%), Pluronic ( $\text{P}_{123}$ ) surfactant (poly (ethylene oxide)-block-poly (propylene oxide)-block-poly (ethylene oxide),  $\text{EO}_{20}\text{PO}_{70}\text{EO}_{20}$ ,  $M_w = 5800$ ), Hydrochloric acid ( $\text{HCl}$ , 32%), 1,3,5-triisopropylbenzene (TIPB, 98%), Zinc oxide ( $\text{ZnO}$ ,  $\geq 99.0\%$ ), graphite powder (99.0%, particles size  $<20 \mu\text{m}$ ), Sulphuric acid ( $\text{H}_2\text{SO}_4$ , 98%), sodium nitrate ( $\text{NaNO}_3$ ,  $\geq 99.0\%$ ), potassium permanganate ( $\text{KMnO}_4$ , 99.0%), hydrogen peroxide ( $\text{H}_2\text{O}_2$ , 30% w/w), hydrazine hydrate ( $\text{N}_2\text{H}_4$ , 99.99%), ethanol ( $\text{C}_2\text{H}_6\text{O}$ , 38% w/w), Carbon disulfide ( $\text{CS}_2$ , 99.0%), N-methylaniline ( $\text{C}_6\text{H}_5\text{NHCH}_3$ , 98%), sodium chloroacetate ( $\text{C}_2\text{H}_2\text{ClNaO}_2$ , 98%), Pyrrolidine ( $\text{C}_4\text{H}_9\text{N}$ ,  $\geq 99.0\%$ ), 2-hydroxyacetophenone ( $\text{C}_6\text{H}_5\text{COCH}_2\text{OH}$ , 98%), buffer solutions of *N*-cyclohexyl-3-aminopropane sulfonic acid (CAPS,  $\geq 99.0\%$ ),

3-morpholinopropane sulfonic acid (MOPS,  $\geq 99.0\%$ ), 2-(cyclohexylamino) ethane sulfonic acid (CHES,  $\geq 99.0\%$ ), Thiourea ( $\text{NH}_2\text{CSNH}_2$ ,  $\geq 99.0\%$ ) and Hydrochloric acid ( $\text{HCl}$ ,  $\geq 99.0\%$ ), Potassium chloride ( $\text{KCl}$ ,  $\geq 99.0\%$ ), Sodium hydroxide ( $\text{NaOH}$ ,  $\geq 99.0\%$ ), Nitric acid ( $\text{HNO}_3$ , 70%), 2,2'-Azobis (2-Methylpropionamide) Dihydrochloride,  $\geq 99.0\%$ , 2,6-Pyridinedicarboxaldehyde ( $\text{C}_7\text{H}_5\text{NO}_2$ ,  $\geq 98\%$ ), Thiosemicarbazone ( $\text{CH}_5\text{N}_3\text{S}$ ,  $\geq 99\%$ ) were products of Sigma-Aldrich PTY. LTD (AUS). All aqueous solutions were prepared with deionised water (DI).

### 3.2.2 Organic pollutant model and their intermediates

Methyl orange (Sodium 4-[[4-(dimethylamino)phenyl]diazenyl]benzene-1-sulfonate, content 85% dye) and Methylene Blue (3,7-bis(Dimethyl amino)-phenothiazin-5-ium chloride),  $\geq 97.0\%$  were used as the organic pollutants model, while, Azure A (dye content~ 80%) and Thionin ( $\geq 99.0\%$ ) were used to identify the intermediate compounds (AR grade). These chemicals were purchased from Sigma-Aldrich PTY. LTD. (AUS). Table 3.1 shows the compounds, abbreviations, molecular formula and chemical structures for the organic pollutants and their intermediate compounds used in this research work.

**Table 3-1** Names, abbreviations and chemical structures of the organic pollutants and their intermediate compounds in this study include:

Chemicals model	Abbreviation	Molecular formula	Chemical structure
Methyl orange	MO	$\text{C}_{14}\text{H}_{14}\text{N}_3\text{O}_3\text{S}_4$	
Methylene blue	MB	$\text{C}_{16}\text{H}_{18}\text{ClN}_3\text{S}$	
Azure A	AA	$\text{C}_{14}\text{H}_{14}\text{ClN}_3\text{S}$	
Thionin	Th	$\text{C}_{12}\text{H}_9\text{N}_3\text{S}$	



### **3.2.3 Inorganic pollutants**

The standard solution of Hg<sup>2+</sup> and Pb<sup>2+</sup> with concentrations of 1000 µg L<sup>-1</sup> were used as pollutant models in this dissertation. Several foreign heavy metal ions were also used as competition ions prepared as AAS grade 1000 µg L<sup>-1</sup> solutions. Examples are; Zn<sup>2+</sup>, Cd<sup>2+</sup>, Al<sup>3+</sup>, Fe<sup>3+</sup>, Mg<sup>2+</sup>, Ca<sup>2+</sup>, Ni<sup>2+</sup>, Ag<sup>+</sup>, K<sup>1+</sup>, Na<sup>1+</sup>, Mn<sup>2+</sup>, Hg<sup>2+</sup>, Co<sup>2+</sup>, and Cu<sup>2+</sup> ions. The interfering (150 mg L<sup>-1</sup>) anions such as chloride (Cl<sup>-</sup>), sulfite (SO<sub>3</sub><sup>2-</sup>), sulphate (SO<sub>4</sub><sup>2-</sup>), carbonate (CO<sub>3</sub><sup>2-</sup>), citrate, nitrate (NO<sub>3</sub>), bicarbonate (HCO<sub>3</sub><sup>-</sup>), perchlorate (ClO<sub>4</sub><sup>-</sup>) and phosphate (PO<sub>4</sub><sup>3-</sup>) were also used in this study. All these inorganic chemicals were procured from High-Purity Standards, Inc. (HPS), USA.

## **3.3 Synthesis of the catalysts**

### **3.3.1 Synthesis of TiO<sub>2</sub>/ZSM-5 multilamellar mesoporous**

The direct template method was slightly modified to fabricate TiO<sub>2</sub> with commercial Alumina-silica zeolite (ZSM-5) which uses surfactant monolithic mesoporous materials (G. Zhou, Chen, Yang, & Yang, 2007). A summary of the catalyst preparation procedure is given in Figure 3.1. In the synthesis, 1 g of P<sub>123</sub> was dissolved in an aqueous solution containing 4 ml of HCl in 20 ml of DI water using a magnetic stirrer 500 rpm at ambient temperature for 4 h until the mixture became a homogeneous transparent solution. Thereafter, 0.85 g of TIPB (TIPB: P<sub>123</sub>; 0.85:1 wt. ratio or 24.1:1 molar ratio) was added to the solution in drops, and the mixture was continuously stirred for 20 h. Afterwards, ZSM-5 was added immediately to the above solution under vigorous stirring at 35<sup>0</sup>C for 12 h and, later followed by the addition of TiO<sub>2</sub> at (ZSM-5: TiO<sub>2</sub>) wt. ratio of 2:1, directly into the same solution under stirring at 35 °C for another 12 h; finally a white suspension was formed which was placed in a Teflon-lined autoclave at 121.90 °C and 122 kPa for 45 min, until a white viscous solution was formed which was heated to dryness at 50 °C for 24 h to form a white particles. The dried white particles were washed with DI for several times, filtered and dried. Eventually, the TiO<sub>2</sub>/ZSM-5 were calcined at 500°C for 4 h to remove the organic templates.

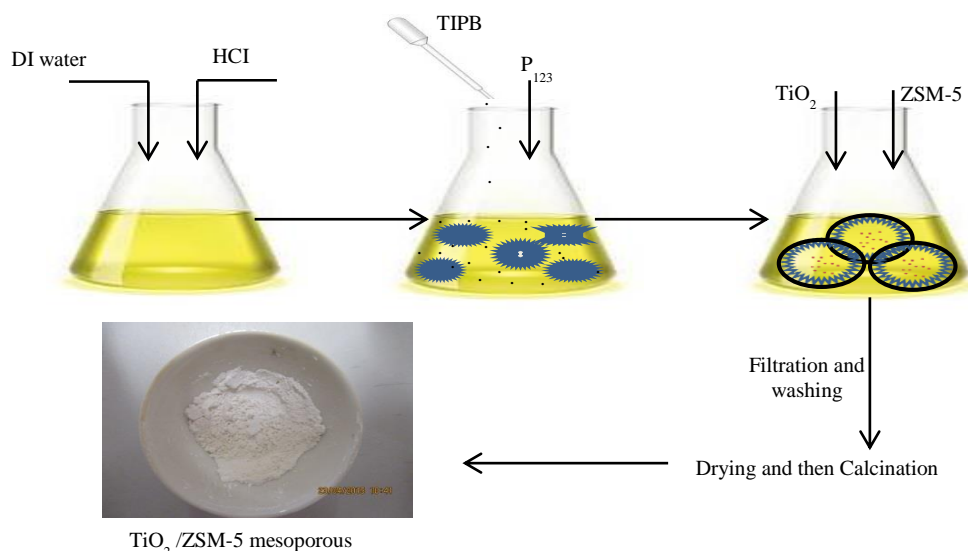


**Figure 3-1** Summary of the direct template method for synthesis of TiO<sub>2</sub>/ZSM-5 multilamellar mesoporous

### 3.3.2 Synthesis of RGO/TiO<sub>2</sub>/ZSM-5 Mesoporous

The Hummers method was adopted to synthesize graphene oxide GO from graphite (Johra & Jung, 2015), the reduced graphene oxide RGO was prepared following this procedure: 600 mg GO was dispersed in 100 ml DI water and sonicated in an ultrasonic bath for 2 h to exfoliate GO nano-sheets to obtain a homogenously dispersed solution. 6 ml of hydrazine hydrate was then added and the mixture was heated up to 100 °C for 2.30 hours. After a while, RGO was progressively precipitated as black particles. For further purification, this product was filtrated and washed with ethanol and DI water for 2-3 times, and finally dried at a temperature of 80 °C.

To synthesize 10% RGO/TiO<sub>2</sub>/ZSM-5 mesoporous, 22 mg of RGO was dispersed in a mixture of 80 ml of DI water and 50 ml of ethanol by ultrasonic treatment for 1 h; 200 mg of TiO<sub>2</sub>/ZSM-5 mesoporous, which is prepared from the procedure mentioned above was added, and then stirred for another 2 h to ensure a homogenous suspension is formed. This suspension was kept in Teflon fixed autoclave for 3 h at 120°C to accomplish the deposition of TiO<sub>2</sub>/ZSM-5 mesoporous onto the RGO as shown in Figure 3.2. Finally, the subsequent composite photo-adsorb catalyst was filtered out, and rinsed with DI water for 10 times, and thereafter dried at 70°C for 12 h.

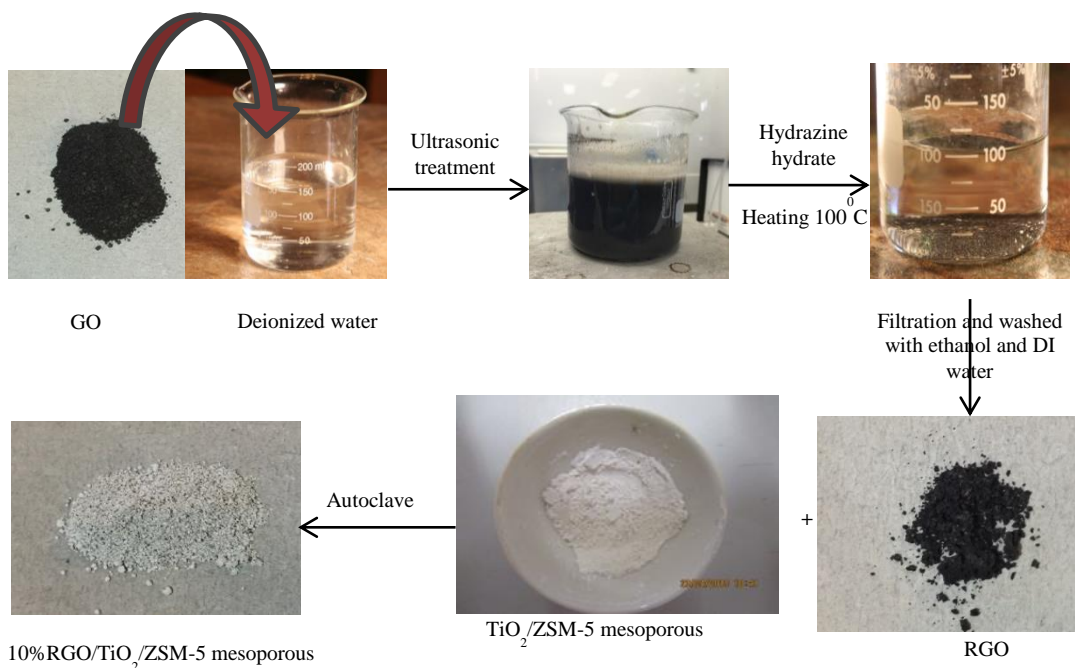


**Figure 3-2** Systematic consequences of the preparation 10% RGO-TiO<sub>2</sub>/ZSM-5 using 22 mg RGO and 200 mg of TiO<sub>2</sub>/ZSM-5 mesoporous

### 3.3.3 Synthesis of mesoporous conjugate adsorbent (MCA)

#### 3.3.3.1 ZSM-5 mesoporous

ZSM-5 mesoporous was synthesized following this procedure: the direct-templating method with slight modification was used to fabricate translucent ZSM-5 mesoporous silica and surfactant monolithic mesoporous materials (G. Zhou et al., 2007). In this procedure, 1g of triblock copolymers (P<sub>123</sub>) was mixed with 20 ml of deionized water and HCl (4 ml, 32%) under magnetic stirring (500 rpm) at room temperature for 20 h. The mixture was stirred continuously until a transparent homogenous solution was obtained. Afterwards, 0.85 g TIPB was added to the solution in drops at mass ratio of 0.85:1 (TIPB: P<sub>123</sub>) and the mixture continuously stirred for 20 h. Subsequently, 2 g of ZSM5 was added directly to the solution under vigorous magnetic stirring at 35°C for 24 h. After this addition, the white suspension mixture was put into a Teflon-lined autoclave at 121.9°C, under pressure 122 kPa for 45 min. Thereafter, the white viscous solution was dried at 60°C for 24 h. The dried white powder formed was filtrated and repeatedly washed for three times with deionized water, and air-dried at room temperature. Finally, the filtrate was calcined at 500°C for 4 h at a heating rate of 2°C per min in a muffle furnace. This was done

to remove the organic moieties template. The resultant material was grinded to nano-sizes and ready to use for building-block immobilization of organic ligand.

### 3.3.3.2 Ligand HAPT (2-hydroxyacetophenone-<sup>4</sup>N –pyrrolidine thiosemicarbazones)

The conjugated ligand type HAPT was prepared the following this procedure: The synthesis was conducted with slight modification of the previous procedure (Scovill, 1991; Sivakumar & Prathapachandra Kurup, 2002). The major step for the preparation of HAPT ligand was synthesis of *carboxymethyl-N-methyl-N-phenyl dithiocarbamate (CN<sub>2</sub>D)* material. In this procedure, a mixture consisting of 12 ml of carbon disulfide (CS<sub>2</sub>), and 21.6 ml of N-methylaniline were treated with an aqueous solution containing 8.4 g of NaOH in a 250 ml conical flask with stirring at room temperature for 4h, until the organic layer has disappeared completely. At this point, the straw-colored solution of the above mixture obtained was treated with sodium chloroacetate (C<sub>2</sub>H<sub>2</sub>CINaO<sub>2</sub>) and allowed to stand overnight. The resulting solution was acidified with 25 ml of concentrated HCl, and the buff colored solid particles (CN<sub>2</sub>D) that appeared was separated, collected, and dried at 42 °C for 24 h. The next step is the preparation of 4-methyl-4-phenyl-3- thiosemicarbazones (MPT) by mixing 17.7 g of CN<sub>2</sub>D in 20 ml of 98% hydrazine hydrate, and 10 ml of ultra-pure water the mixture was kept in an autoclave at 150 °C for 2 h until it crystallized. The crystals were removed from the mixture by filtration, thereafter thoroughly washed with ultra-pure water, and dried at 40 °C. For further purification, the crystals were treated with ethanol in 25ml of ultra-pure water. This gave 10.8 g of stout colorless rods of MPT. Finally, 0.48 g MPT in 5ml of ethanol was mixed with 392 mg of Pyrrolidine and 664 mg of 2-hydroxyacetophenone, and the mixture was heated to 150 °C with reflux for 20 min. Pale yellow rods HAPT were obtained and collected, then thoroughly washed with methanol for further purification; and then it was dried at 50 °C for 24 h to obtain pure HAPT as azo-chromophore ligand.

### 3.3.3.3 MCA catalyst

The mesoporous conjugate adsorbent (MCA) was fabricated via direct immobilization method using 50 mg of HAPT dissolved in ethanol solution into 1g ZSM-5 mesoporous as shown in Figure 3.3. This immobilized method was carried

out under vacuum at 45 °C until HAPT ligand saturation to ZSM-5 mesoporous silica was achieved. The ethanol was removed by a rotary evaporator at 45 °C and the resulting MCA was washed with warm water to check the stability and elution of HAPT from mesoporous silica. Then MCA was dried at 50 °C for 10 h and grinded into fine powder.

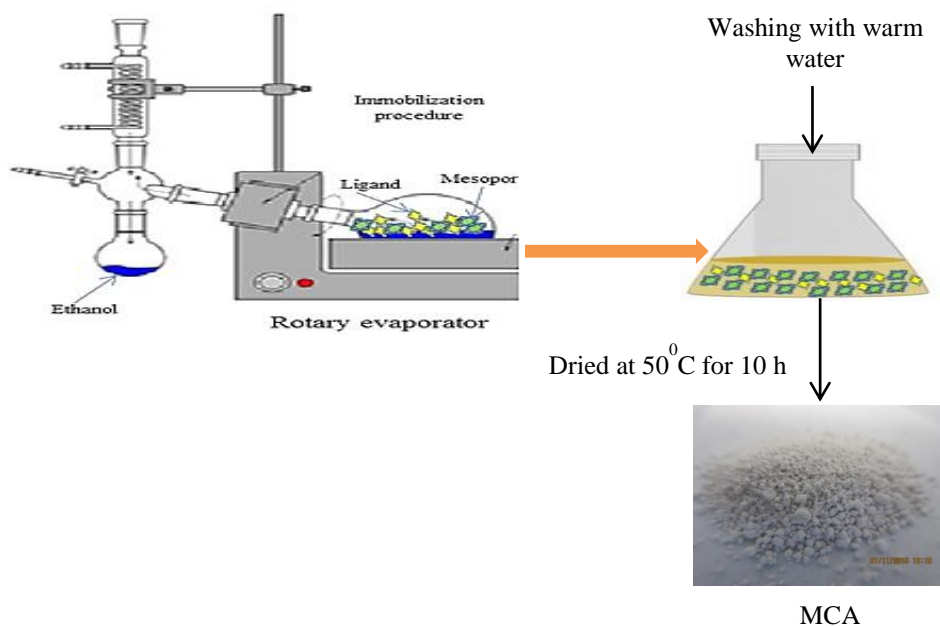


**Figure 3-3** the synthesized method of visual MCA adsorbent mesoporous

### 3.3.4 Synthesis of mesoporous ZSM-5 conjugate adsorbent (MzCA): Pb<sup>2+</sup> detection

#### 3.3.4.1 ZSM-5 mesoporous

The procedure to synthesis ZSM-5 mesoporous is mentioned in previous section (3.3.3.1)

#### 3.3.4.2 Ligand PDCTC (2,6-Pyridinedicarboxaldehyde-Thiosemicarbazone)

The conjugated ligand type PDCTC was prepared thus; this preparation involves, a slight modification of the procedures in previous studies (Ahmed & Yunus, 2014). The PDCTC was prepared by the reaction of 2, 6-Pyridinedicarboxaldehyde, (2g, 0.01183mol in 20 ml of methanol), Thiosemicarbazone (1.0787g, 0.01183 mole in 20 ml of methanol) and 2 ml of concentrated HCl. The resultant was heated under reflux condition for 10 h in a 250 ml round bottom flask, and left to cool at ambient

temperature. The light yellow colored shaped particle formed was collected by suction filtration. The filtrate was washed with hot water and thereafter with cold methanol (w/w 50%) respectively. The resultant was recrystallized using dichloromethane/methanol 1/1, and then dried at 50<sup>0</sup>C under vacuum for 24 h.

### 3.3.4.3 MzCA catalyst

The MzCA was synthesized with direct immobilization technique. 100 mg of PDCTC ligand in ethanol solution was mixed with 2g ZSM-5 mesoporous silica monoliths. This immobilization procedure was carried out under vacuum at 40<sup>0</sup>C for 6 h stirring until saturation of PDCTC ligand to ZSM-5 mesoporous was achieved. The residual ethanol was evaporated via a rotary evaporator at 40<sup>0</sup>C. MzCA was then rinsed with warm water for five times until no supernatant of PDCTC was observed to check the elution and stability of PDCTC ligand on mesoporous silica. Thereafter, the mesoporous adsorbent was dried at 60 <sup>0</sup>C for 4h, and grinded into fine particles of nano sizes.

## 3.4 Characterization instruments

### 3.4.1 Field emission scanning electron microscope (FESEM)

Morphological and surface characteristics of the synthesized mesoporous catalysts were analysed using FESEM (MIRA-3-TESCAN with a high vacuum mode microscope) at an acceleration voltage of 5Kv and a current of 10  $\mu$ A. The samples were mounted on a surface of carbon tap with a very thin platinum coating prior to when the analysis was to be conducted. In addition, the EDX/or EDS (Energy-dispersive X-ray spectroscopy) analysis was used to provided information on the elemental composition of the synthesized catalysts.

### 3.4.2 The specific surface area and pore size measurement

The specific surface area was measured based on the Brunnauer-Emmett-Teller method according to N<sub>2</sub> adsorption-desorption isotherms equations. The pore size distributions were derived from the adsorption branches of isotherms using the Barrett–Joyner–Halenda (BJH) model at 77 $\pm$  0.5k in liquid nitrogen, with BET, Micrometrics, Tristar II Surface area and Porosity apparatus. The sample vessels

were loaded with 0.5-1.0 g and degassed at a high temperature of up to 200 °C overnight with evacuation pressure of 50 mTorr prior to the measurement of the BET surface area.

### 3.4.3 Powder X-Ray Diffractionometric Measurement

The crystalline structures of the catalysts, which are used in this thesis, were identified by XRD using a Bruker D<sub>8</sub> diffractometer in the range of  $2\theta = 10-80^\circ$  and scanning rate of  $28 \text{ min}^{-1}$  operating at 40 mA and 40 Kv with Cu-K $\alpha$  radiation ( $\lambda = 1.5418 \text{ \AA}$ ). In the case of the synthesized TiO<sub>2</sub>/ZSM-5 mesoporous, the average crystallite diameter of the TiO<sub>2</sub> nanocrystals,  $D$ , was evaluated using the Debye-Scherrer equation [ $D = K\lambda / \beta \cos \theta$ ]. Where  $K$  is the crystalline shape with Warren's correction value for instrumental broadening of 0.89,  $\beta$  is the line broadening, while  $\lambda$  and  $\theta$  are the radiation wavelength of  $1.5418 \text{ \AA}$  and Bragg angle respectively.

### 3.4.4 Fourier-transformed infrared spectroscopy (FTIR)

The intensity peaks of the functional groups were obtained using an FTIR spectrometer (100 FT-IR, PerkinElmer). The spectrum was scanned from 500 to  $4000 \text{ cm}^{-1}$  with a resolution of  $4 \text{ cm}^{-1}$  using the attenuated total reflectance (ATR) technique.

## 3.5 Experimental procedures

### 3.5.1 Solar photocatalytic degradation experiments

#### 3.5.1.1 Methyl Orange model (MO)

The photocatalytic activities were conducted in a cylindrical photo-catalytic reactor of 5.5 cm in diameter and 9 cm height. The MO solution with concentration of  $20 \text{ mg L}^{-1}$  was taken as the initial concentration for the batch studies. A light intensity of  $100 \text{ mW/cm}^2$  using a solar simulator (solar simulator 2000,  $100 \text{ mW/cm}^2$ , 18-25Amps, 550W Max Lamp, ABET Technologies) as shown in Figure 3.4, was employed for the photodecomposition. Before the solar simulator light was turned on, MO dye solution with different concentrations ( $1, 2, 2.5, 3 \text{ g L}^{-1}$ ) of TiO<sub>2</sub>/ZSM-5 mesoporous was magnetically stirred for 30 minutes in the dark to achieve adsorption-desorption equilibrium. Each experiment was carried out for 180 min

under solar light irradiation. Samples were collected every 30 minutes from the suspension using syringes and Whatman filter (pore size 2.5 $\mu$ m) was used for removing the catalyst before further analysis. MO dye concentrations were then measured by UV-vis spectrophotometer (JASCO/ V-670) at the maximum absorption wavelength ( $\lambda$ ) of 462 nm.

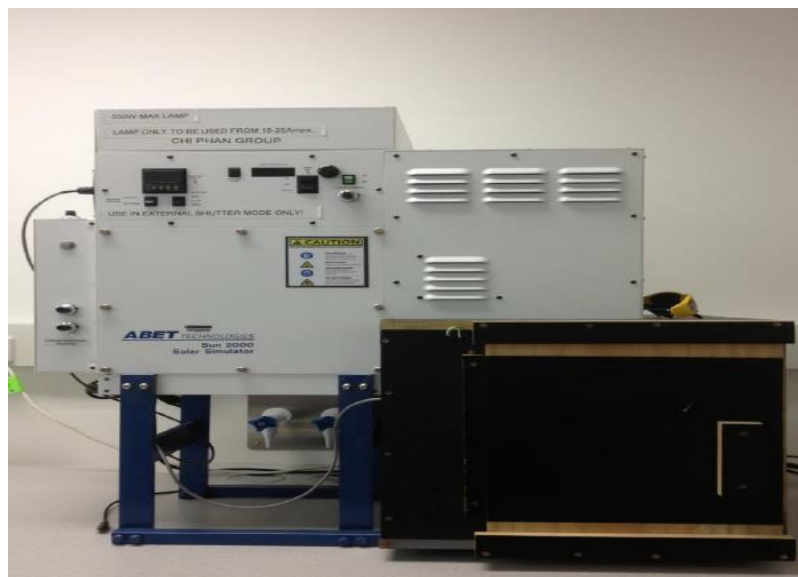


**Figure 3-4** Solar simulator (100 mW/cm<sup>2</sup>) used for the solar photocatalytic degradation experiments

### 3.5.1.2 Methylene Blue model (MB)

The batch photocatalytic process was carried out in 100 ml capacity of a cylindrical beaker with magnetic stirrer. Different concentrations of MB 10, 20, 30, and 40 mg L<sup>-1</sup> were observed in this study. The solar simulator was utilized in the same way as depicted in Figure 3.4. Different catalysts such as; commercial ZSM-5, 5%RGO/TiO<sub>2</sub>/ZSM-5, 10% RGO/TiO<sub>2</sub>/ZSM-5, and 15%RGO/TiO<sub>2</sub>/ZSM-5 were added to MB, and the mixtures stirred in the dark for 30 minutes; 5 ml of aliquot was drawn out from each mixtures under stirring at every 15 minutes interval each, these were filtrated and centrifuge to quantify the adsorbed concentration of MB. Subsequently, all samples were kept under solar irradiation for 60 minutes. The change in MB concentrations within photodecomposition process was measured by UV-vis spectrophotometer (JASCO/ V-670) at the maximum absorption wavelength ( $\lambda$ ) of 664 nm.



### 3.5.2 Visual mesoporous conjugate adsorbent experiments

#### 3.5.2.1 Mercury $\text{Hg}^{+2}$ detection

In Hg (II) ion detective experiments, the batch adsorption process was conducted in 100 ml capacity of a cylindrical beaker with magnetic stirrer. 10 mg of optical MCA captor was immersed in solutions containing  $2.0 \text{ mg L}^{-1}$  of Hg (II) ion. The aqueous solutions were then adjusted to pH of 2.0, 4.3, and 6.2 using (0.2 M of KCl with HCl), pH of 9.4, and 11.1 with (MOPS with NaOH), and pH of 12.5, and 12.8 using (CHES with NaOH). These mixtures were properly stirred in a temperature controlled water bath at  $25^{\circ}\text{C}$  with magnetic stirrer for 10 minutes to achieve good colour separation. Blank solutions were also prepared by the same procedure for comparison with optimum colour formation. After colour optimization, the mixtures were then applied for qualitative estimation of Hg (II) ions using colour assessment and absorbance measurements via UV-spectrophotometer. Furthermore, the mixtures were filtrated to remove the solid materials using Whatman filter paper, and the resulting filtrate was then taken for colour assessment of absorbance measurements applying solid-state UV-Vis-NIR spectrophotometer. The filtrated MCA was grinded to fine particles to achieve homogeneity in the spectrum absorbance.

#### 3.5.2.2 Lead $\text{Pb}^{+2}$ detection

In optical Pb (II) ions detective experiments, 10 mg of MzCA was immersed in solutions containing  $2.0 \text{ mg L}^{-1}$  of Pb (II) ions. Then, the solutions were adjusted to pH of 1.5, 2.2, 3.0, and 4.0 using (0.1 M of KCl and HCl), pH of 6.0, and 7.7 using (3-morpholinopropane sulfonic acid (MOPS) and NaOH), and 11.7 using (2-(cyclohexylamino) ethane sulfonic acid (CHES) and NaOH) at a constant volume of 20 ml. These solutions were vigorously stirred with a magnetic stirrer at constant agitation speed of 100 rpm for 30 minutes in a water bath maintained at a temperature of  $25^{\circ}\text{C}$  to enable a sufficient coloration separation. A blank solution (without Pb (II) ions) was also prepared using the same as procedure for comparison of color formation. After color optimization, the solid materials were filtrated using Whatman filter paper (50 mm; Shibata filter holder) and the filtrate utilized for qualitative estimation of lead (II) ions by color assessment and absorbance measurements with solid-state UV-Vis-NIR spectrophotometer. The absorbance

spectra quality depends on the sizes of the particle, hence it is recommended to grind the synthesized mesoporous adsorbent catalyst to nano-size particles.

### 3.6 Analytical procedures

#### 3.6.1 Total organic carbon analyser TOC

The residual organic contaminants were estimated in term of TOC, which the total amount of carbon (mg) is found in organic pollutants per litre of the sample solution. The TOC measurement was obtained through the Shimadza TOC-VCPH analyser apparatus as shown in Figure 3.5. Prior to sample injection into the TOC, 20 ml of samples each were filtrated with PTFE 0.45  $\mu\text{m}$  membrane filters to remove the remaining catalyst in the aqueous solution. The concentration of total organic carbon (TOC) was determined by using SHIMADZU, TOC-VCPH scientific apparatus.

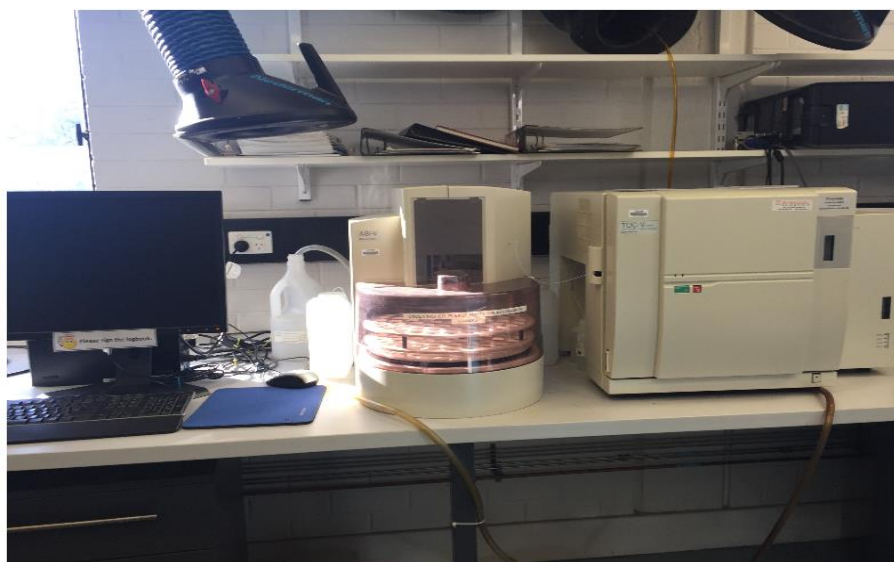


**Figure 3-5** Total Organic Carbon (TOC) Analyser

#### 3.6.2 High Performance Liquid Chromatograph analysis HPLC

Methylene blue and their intermediate compounds were identified and quantified by the High Performance Liquid Chromatograph (HPLC) analysis illustrated in Figure 3.6. The detection of the authentic samples and the main intermediate organic pollutants was achieved at 270 nm, using a Varian Prostar 210 chromatography with UV-Vis detector, and a  $\text{C}_{18}$  reverse phase column (25cm x 4.6 mm x 5 $\mu\text{m}$ ). In this analysis, the mobile phase comprised of two solutions; A and B. Solution A contained 300 ml of 0.1 M ammonium acetate, mixed with 35 ml of 3% acetic acid of pH 5.3, while solution B contain from 600 ml of acetonitrile. The injection flow

rate was 0.8 ml/min and the injection volume was 100  $\mu\text{L}$ . The column temperature was kept at 25°C throughout the analyses. The identification of the intermediate compounds by HPLC was achieved by the comparison of the retention time of the peaks in the discharged sample and that of the standard sample. The concentrations of compounds were calculated using the equations derived from the calibration measurements for authentic samples (see Appendix B).



**Figure 3-6** High Performance Liquid Chromatograph (HPLC) instrument

### 3.6.3 ICP- Mass Spectrometer

The residual inorganic pollutants of  $\text{Hg}^{2+}$  and  $\text{Pb}^{2+}$  were determined by ICP- Mass Spectrometer instrument (ICP-MS or/ICP-AES, Nixon 350D, PerkinElmer) as shown in Figure 3.7. The  $\text{Hg}^{2+}$  concentrations were measured depending on the calibration curve using five standard solutions containing about 0.5, 0.7, 1, 1.5, and 2.0  $\text{mg L}^{-1}$  of  $\text{Hg}^{2+}$ . The correlation coefficient of the calibration curve was higher than 0.9989. The  $\text{Pb}^{2+}$  was also calibrated using six standard solutions containing 0, 0.5, 0.75, 1, 1.5, and 2.0  $\text{mg L}^{-1}$  of Pb (II) ions (also for each foreign element) and the correlation coefficient of the calibration curve was higher than 0.9999.

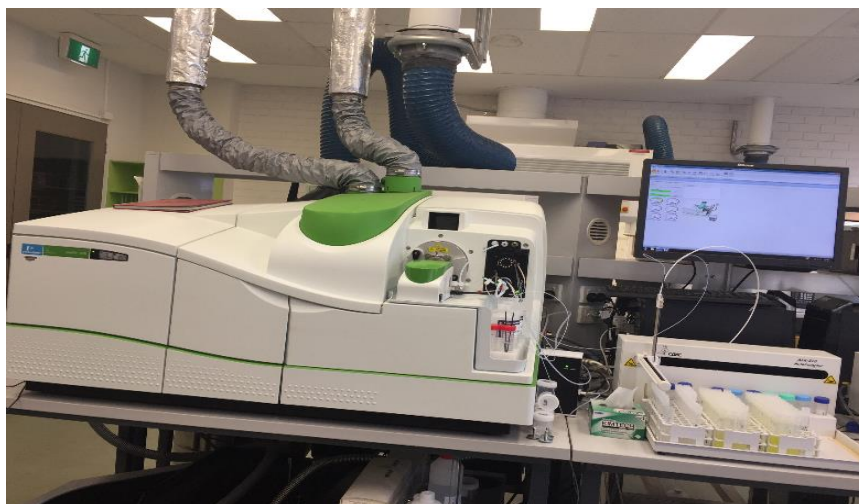


**Figure 3-7** ICP- Mass Spectrometer instrument

### 3.6.4 UV-Vis diffuse spectrophotometer analysis

The optical adsorption characteristics of the MO and; MB pollutant model during photodecomposition was measured by UV-vis spectrophotometer, JASCO/ V-670 as illustrated in Figure 3.8 between the absorption wavelength ( $\lambda$ ) range of 300-700 nm to recognize the concentrations in the aqueous solution before and after the treatment process. The solid-state UV-vis-NIR spectrophotometer was also applied to detect the colour deviation of the optical MCA catalyst after  $\text{Hg}^{2+}$  and  $\text{Pb}^{2+}$  adsorption processes.



**Figure 3-8** UV-Vis spectrophotometer

### 3.6.5 Specific surface area and porosity analyzer

The pore size distribution was measured with the Barrett–Joyner–Halenda (BJH) model using (Micrometrics (Tri-Star II, Germany) at  $77^{\circ}\text{K}$  as shown in Figure 3.9. Before the  $\text{N}_2$  isothermal analysis, all the catalysts synthesized in this project were preheated at  $150^{\circ}\text{C}$  for 5 hours under vacuum until the pressure was equilibrated to

$10^{-5}$  Torr. The specific surface area ( $S_{BET}$ ) was calculated by multi-point adsorption data using the Brunauer-Emmett-Teller (BET) theory.



**Figure 3-9** Specific surface area and porosity analyser

### 3.6.6 Rotary evaporator

The rotary evaporator is a device used for the efficient and gentle removal of solvents from samples by evaporation. To obtain HART/mesoporous-ZSM-5 catalyst, the HAPT ligand and ZSM-5 mesoporous were placed in a 1 liter flask containing aqueous ethanol solution and mixed in the vacuum of a rotary evaporator at a temperature of  $45^{\circ}\text{C}$ , BUCHI ROTARY EVAPORA, R-210 as shown in Figure 3.10. Afterwards, the ethanol was condensed using a dry ice kept in the jacket condenser of the rotary evaporator. The same procedure was repeated to obtain the PDCTC/mesoporous-ZSM-5 catalyst.



**Figure 3-10** Vacuum Rotary evaporator



### 3.6.7 Autoclave

Autoclave Siltex 250D, Australia shown in Figure 3.11 was used during synthesis where high temperature and pressure was required. The temperatures and pressures were adjusted to 120 °C, 191 Kpa and 135 °C, 230 Kpa respectively.



**Figure 3-11** Autoclave

## CHAPTER 4

# 4

### **Synthesis a novel multilamellar mesoporous TiO<sub>2</sub>/ZSM-5 for photocatalytic degradation of methyl orange dye in aqueous media**

#### **4.1 Introduction**

The environmental pollution caused by industrial wastewater has become a common threat for most of the countries. The presence of both organic and inorganic pollutants in water bodies due to industrial activities led to deteriorate the quality of the rivers and groundwater. However, the organic pollutants are more concern due to their carcinogenic and mutagenic effects on human even after exposure to minute concentrations (Brown & Dietrich, 1983; Mathur et al., 2012; Parshetti et al., 2010). Among all sources that cause water pollution is the release of recalcitrant organic pollutants from textile, food colouring, printing, cosmetic and paper making industries (Khataee, Pons, & Zahraa, 2009). Methyl orange (MO) (4-[4-(dimethylamino) phenylazo] benzene sulfonic acid, C<sub>14</sub>H<sub>14</sub>N<sub>3</sub>NaO<sub>3</sub>S) represents one of the most important dyes, which is widely used as a colouring agent in textile and leather industries.

During few recent decades, several techniques have been developed for devastating the behaviour of recalcitrant methyl orange (Jain & Sikarwar, 2008). Enormous amount of research articles has been published on the adsorption of the methyl orange using an agricultural waste material due to their low-cost and widespread availability (Hameed, Mahmoud, & Ahmad, 2008; Ho, 2006; Mittal, Gupta, Malviya, & Mittal, 2008; Mittal, Malviya, Kaur, Mittal, & Kurup, 2007) (Khattri & Singh, 2009),

however, this material does not meet the requirement to solve the environmental issue. Other physical treatments such as coagulation, reverse osmosis, and membrane filtration are also expensive and incompetent techniques. Moreover, the chemical treatments such as reduction, oxidation, ion exchange, and complex metric methods cause by-products such as sulfonate, phenol and plenty of aromatic compounds which are more toxic than the original contaminants (Chong et al., 2010; Slokar & Le Marechal, 1998).

Advanced oxidation processes (AOPs) such as TiO<sub>2</sub> nano-photocatalyst is one of the promising technologies for removing industrial dyes. TiO<sub>2</sub> is stable, inexpensive, non-toxic and potentially reusable in water, however, the post-separation of TiO<sub>2</sub> is remained as a challenging issue (Chong, Jin, et al., 2009). Therefore, the key challenge of using TiO<sub>2</sub> for advanced treatment of industrial dyes mediated wastewater is to provide a plausible solution via immobilising the semiconductor photo-catalysts on larger immobiliser substrates to ease the process of post-separation and recovery of catalyst from treated water (Chong, Tneu, Poh, Jin, & Aryal, 2015). Many immobilizer substrates such as activated carbon (Shi et al., 2010), magnetite core (Beydoun & Amal, 2002), and clays (Chong, Jin, et al., 2009; Paul et al., 2012) have been used to enhance the post-separation and recovery of photo-catalyst from the treated water. The black activated carbon is normally opaque material, preventing the incident UV-radiation light and low porosity (Uchida, Itoh, & Yoneyama, 1993; Yamashita et al., 2000). Therefore, TiO<sub>2</sub> immobilised on transparent as well as mesoporous scaffold were desired (Ooka, Yoshida, Suzuki, & Hattori, 2003; Takeda, Torimoto, Sampath, Kuwabata, & Yoneyama, 1995; L. Zhang et al., 2009).

In comparison with any synthetic substrate porous materials, natural zeolites are abundant, inexpensive and high stability to host the semiconductor metal oxides (S. Liu, Lim, & Amal, 2014). Furthermore, zeolites possess crystalline aluminosilicate, high ion exchange capacity, tectosilicates with microporous channels, molecular sieving, pore spaces, adsorbed capacity (Vimonses et al., 2009; S. Wang & Peng, 2010). Few researchers have reported utilisation of a photocatalyst immobilised on natural zeolites. For example, TiO<sub>2</sub> / zeolite (ZSM-5) (Takeuchi, Kimura, Hidaka, Rakhmawaty, & Anpo, 2007) and TiO<sub>2</sub>/ zeolite (MOR) (Takeuchi et al., 2009) which observed as an excellent removal efficiency of volatile acetaldehyde compound from wastewater. TiO<sub>2</sub>/Y-zeolite photo-catalyst was also efficiently prepared to remove benzene and toluene molecules from petroleum wastewater (Takeuchi, Hidaka, &



Anpo, 2012). Recently, TiO<sub>2</sub>/ZSM-5 nanocomposite has been prepared for the degradation of humic acid from potable water sources (V. Gupta, Gupta, Rastogi, Agarwal, & Nayak, 2011). The best way to synthesize a high specific surface area material is to use multi-lamellar vesicles (MLVs) template shape using surfactant and a hydrophobic additive. In MLVs template, ZSM-5 aggregates in unit of cluster to form a high surface area scaffold allowed TiO<sub>2</sub> particles to immobilize onto different sites. Tanev et al. were the first who reported the feasibility of forming mesoporous vesicular silica by utilizing Bola-type surfactants H<sub>2</sub>N(CH<sub>2</sub>)<sub>n</sub>NH<sub>2</sub> (n = 12–22) in aqueous medium (Tanev & Pinnavaia, 1996). Later Zhou et al. [32] found that the morphology of mesoporous silica can be controlled by the molar ratio of hydrophobic additive and surfactant (TIPB: P123)(G. Zhou et al., 2007), however, the highest specific surface area they achieved was 518 m<sup>2</sup> g<sup>-1</sup>. Therefore, the objective of the present study was to synthesize multi-lamellar mesoporous photocatalyst TiO<sub>2</sub>/ZSM-5 with a high specific surface area as well as with good crystallinity for efficient MO degradation under solar light irradiation via a simple and cost-effective direct template method. The photo-degradation efficiency of proposed catalyst was compared with different catalysts (ZnO/ZSM-5, TiO<sub>2</sub>-mesoporous). The influence of pH, catalyst loading, reuses, and the kinetics studies were also investigated.

## 4.2 Experimental work

### 4.2.1 Chemicals

As mentioned in chapter 3 (section 3.2.1) the zeolite ZSM-5 (Molar ratio SiO<sub>2</sub>/Al<sub>2</sub>O<sub>3</sub> =600, 300 m<sup>2</sup> g<sup>-1</sup> specific surface area, 2–3µm particle size, 2.4 nm pore size) was provided from ACROS Organics, A Thermo Fisher Scientific Brand, New Jersey–USA. Titanium dioxide (TiO<sub>2</sub>, Degussa P<sub>25</sub>, 70% anatase: 30% rutile, 53 mg<sup>-1</sup> specific surface area, particle size, 21nm were supplied by Sigma-Aldrich Co, Castle Hill NSW, AUSTRALIA.

### 4.2.2 Synthesis of TiO<sub>2</sub>/ZSM-5 mesoporous multilamellar

As mentioned in chapter 3 section (3.3.1), a high surface area TiO<sub>2</sub>/ZSM-5 mesoporous can be synthesized by the direct-templating method using P<sub>123</sub> surfactant and a hydrophobic additive 1, 3, 5-triisopropylbenzene (TIPB) to form a template

structure. The ZSM-5 as a source of alumina/silica was considered the framework structure of proposed catalyst after the calcination process as depicted in Figure 4.1. In this chapter, multilamellar vesicle-like silica of ZSM-5 supported TiO<sub>2</sub> was synthesized by the direct templating method described elsewhere (G. Zhou et al., 2007) with a little modification by replacing SBA-15 with ZSM-5 as a silica source. This procedure forms bonds such as Ti-O-Si units inside and outside the structure of MLVs (for more details see section 4.3.1.4) that can improve the catalyst performance.

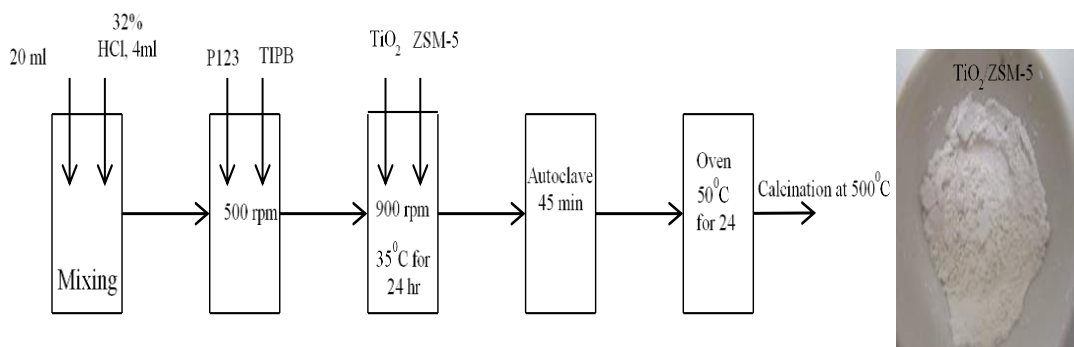


**Figure 4-1** Schematic diagram for the preparation of photocatalysts (TiO<sub>2</sub>/ZSM-5)

### 4.2.3 Characterizations of samples

The crystalline structures of the synthesized catalysts were analysed by X-ray diffraction (XRD) using a Bruker D8 diffractometer. The specific surface area was measured by the N<sub>2</sub> adsorption-desorption isotherms according to the Brunauer-Emmett-Teller (BET) method, Micromeritics, Tri-Star II Surface area and Porosity) equation. The surface morphologies of the ZSM-5, TiO<sub>2</sub> or ZnO/ ZSM-5, TiO<sub>2</sub> mesoporous catalysts were also determined by using Scanning Electron Microscope (SEM). Fourier-Transformed Infrared (FTIR) spectroscopy was conducted to determine the functional groups of the different photo-catalysts. The total organic carbon (TOC) was measured using SHIMADZU, TOC-VcpH Scientific apparatus.

### 4.2.4 Photocatalytic experiments of MO dye

The photocatalytic activities were conducted in a cylindrical photocatalytic reactor. A fixed volume of 100 ml methyl orange solution of 20 mg L<sup>-1</sup> concentration was taken as initial concentration for batch studies. The photo-reactor was externally irradiated with a light intensity of 100 mW/cm<sup>2</sup> using a solar simulator. All the experiments were conducted at fixed temperature of 30°C with various initial pH in the range of 2–9.

Different dosages of the catalyst were also investigated to evaluate the optimum amount of photocatalyst for a specific concentration and volume of methyl orange solution (for more details see chapter 3, section 3.5.1.1).

$$\eta_{MO} = \frac{C_o - C}{C_o} \times 100 \quad (4.1)$$

### 4.3 Results and discussion

#### 4.3.1 Characterization of the photocatalysts

##### 4.3.1.1 XRD

The XRD patterns of ZSM-5, TiO<sub>2</sub>/ZSM-5, TiO<sub>2</sub> Degussa, ZnO/ZSM-5 and TiO<sub>2</sub>-mesoporous catalysts were investigated and the obtained diffraction peaks are shown in Figure 4.2 The diffraction peaks of ZSM-5 were observed at 7.5°, 8°, 13.2°, 13.9°, 14.7°, 15.5°, 23.1°, 29.8°, 45.0°, 45.2° and typically coincided with the data, reported in the literature for sodium aluminium silicate (Na<sub>1.5</sub> Si<sub>93</sub> O<sub>192</sub>) (J.-J. Wang, Jing, Ouyang, & Chang, 2015). While, the signals of TiO<sub>2</sub> Degussa with high crystallinity were found at 25.4°, 37.5°, 48.0°, 54.1°, 54.8°, and 62.6° indicated the d 101, d 004, d 200, d106, d 211, and d 204 planes of anatase (Ba-Abbad, Kadhum, Mohamad, Takriff, & Sopian, 2012; Jung et al., 2012; Thamaphat, Limsuwan, & Ngotawornchai, 2008). Moreover, the peaks at 68.5°, 71.2°, 75.5° indicated the d110 plane of rutile. However, no significant peaks shift were noticed after modifying ZSM-5 with TiO<sub>2</sub> Degussa. Though, the peak intensity corresponds to crystallite meso-ZSM-5/TiO<sub>2</sub> was found less prominent than that of ZSM-5 itself due to slight line broadening of the diffraction peaks. It is noteworthy that the crystallinity of TiO<sub>2</sub> particles was slightly changed from 21 to 21.27 nm after loading onto ZSM-5 framework. Although, in case of ZnO/ZSM-5, few peaks correspond to ZSM-5 disappeared during ZnO loading such as 45.0° and 45.2° and few appeared less intensified such as 7.5°, 8°, 13.2°, 13.9°, 14.7°, 15.5°, 23.1°, 29.8° due to the formation of mesoporous phase (Na<sub>1.2</sub> Al<sub>1.1</sub> Si<sub>93.7</sub> O<sub>192</sub>). This phenomenon explained that the loading of ZnO onto ZSM-5 framework was less stable. In TiO<sub>2</sub>- mesoporous catalyst the instability of TiO<sub>2</sub> was observed due to the destruction of anatase phase at 2θ=25.4° and 48° as shown in Figure 4.2. This might have obtained due to the precursor thermal reaction of TEOS on the surface of TiO<sub>2</sub>, and hence the condensation of TEOS on TiO<sub>2</sub> particles affected the crystallinity of

TiO<sub>2</sub> particles, which can be proved by the size of the crystal particle as discuss below. The average crystal size of TiO<sub>2</sub> particle in TiO<sub>2</sub>/ZSM-5 can be calculated from the Debye-Scherrer formula (Hamadani, Reisi-Vanani, & Majedi, 2009). It was found that the average anatase crystalline size was 21.27 nm.

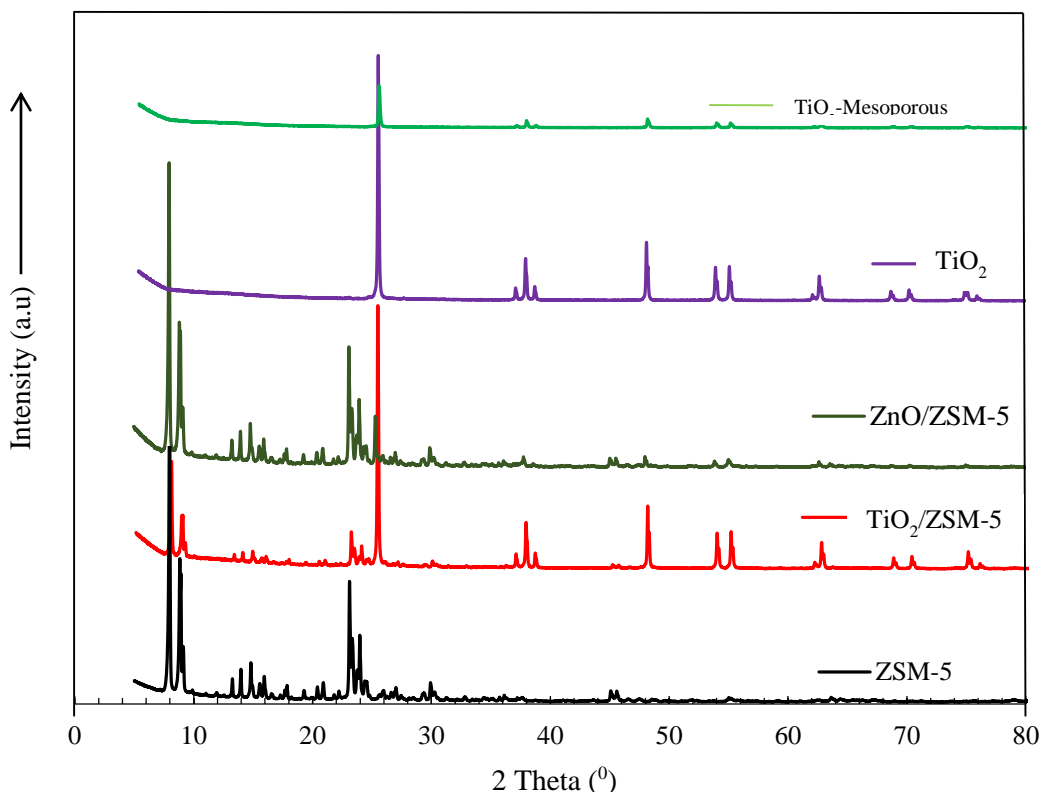


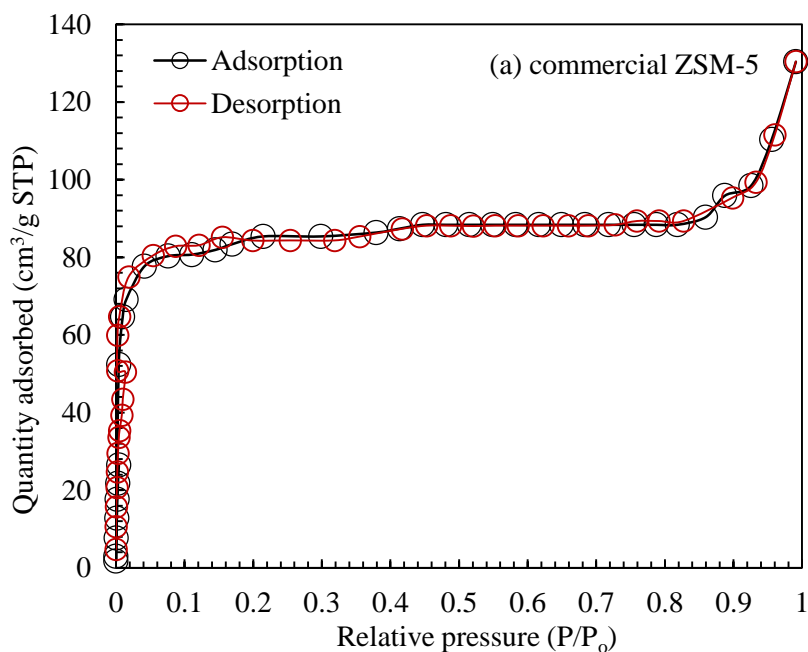
**Figure 4-2** X-ray diffraction patterns of ZSM-5, TiO<sub>2</sub>/ZSM-5, TiO<sub>2</sub> Degussa, ZnO/ZSM-5 and TiO<sub>2</sub>-mesoporous

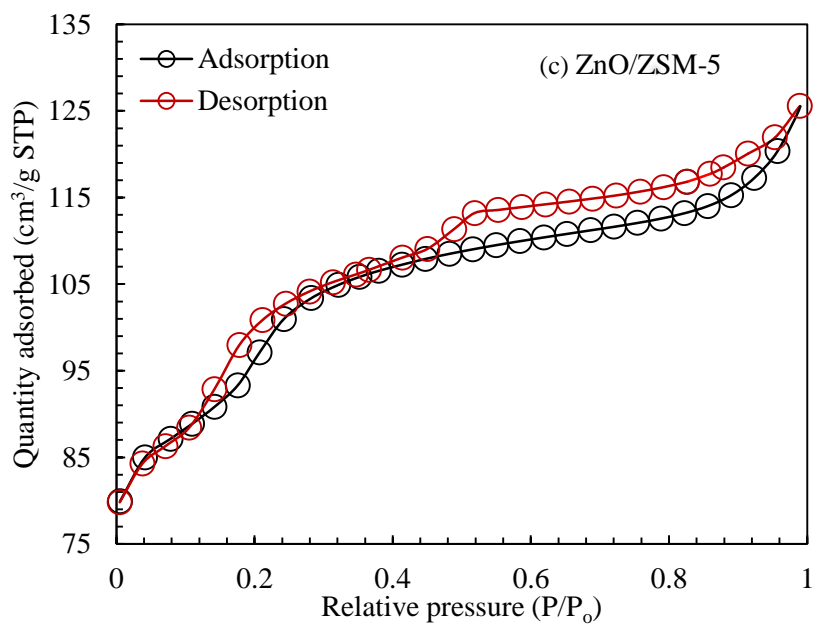
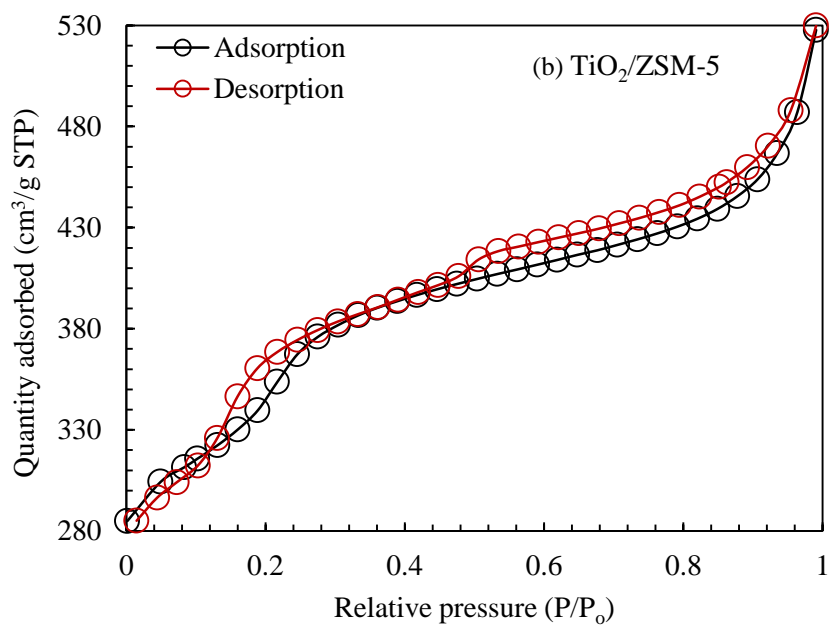
#### 4.3.1.2 BET surface areas and pore distribution

The specific surface area and pore structure of the commercial ZSM-5, TiO<sub>2</sub>/ZSM-5 mesoporous, TiO<sub>2</sub>-mesopores and ZnO/ ZSM-5 were characterized by Brunauer-Emmett-Teller method (BET). Figures 4.3a-d illustrate nitrogen adsorption-desorption isotherms to describe the surface area while the BJH pore size distribution of corresponding samples is shown in Figure 4.3e. For comparison, the results of BET surface areas and pore structures are summarized in table 1.

According to IUPAC classification, The adsorption/desorption isotherms of the commercial ZSM-5 is a type of I isotherm and exhibits an almost horizontal plateau starting at low relative pressure < 0.15 (Thommes et al., 2015; Valero-Romero et al., 2016), indicating that the porous morphology consist predominantly of very narrow micropores having relatively small external surfaces as shown in Figure 4.3a. The

steep uptake at very low  $P/P_0$  is due to enhanced adsorbent-adsorptive interactions in narrow micropores, resulting in micropore filling at very low  $P/P_0$  (Thommes et al., 2015). The specific surface area and the pore diameter of commercial ZSM-5 were estimated to be  $311 \text{ m}^2 \text{ g}^{-1}$  and  $8.6 \text{ nm}$ , respectively. The nitrogen adsorption-desorption isotherms of TiO<sub>2</sub>/ZSM-5 and ZnO/ZSM-5 exhibit type H<sub>4</sub> hysteresis loops at  $P/P_0$  ranges 0.1-0.3, and 0.4-0.99, suggesting the presence of abundant mesoporous structure in the samples as illustrated in Figures 4.3b and c, which give BET surface area of 1151 and  $305 \text{ m}^2 \text{ g}^{-1}$ , respectively, and uniform pore diameter around 5.0-11.0 nm as shown in Figure 4.3e. The hysteresis loop of TiO<sub>2</sub>-mesopores catalyst was also exhibited type H<sub>4</sub> hysteresis loop at  $P/P_0$  range 0.5-0.99 as depicted in Figure 4.3 d, with disordered pore diameter distribution around 2-24 nm (see Figure 4.3e). This disordered pore diameter could be affected by calcination temperature and the hydrolysis process of TEOS, which largely caused the damage and collapse of the mesoporous structure.





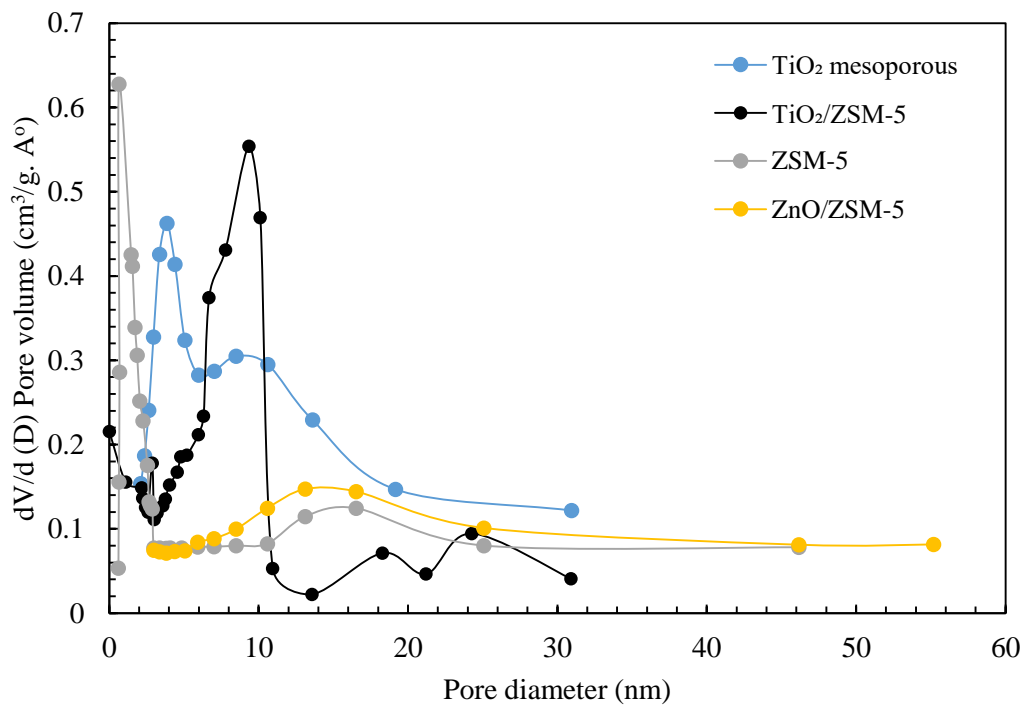
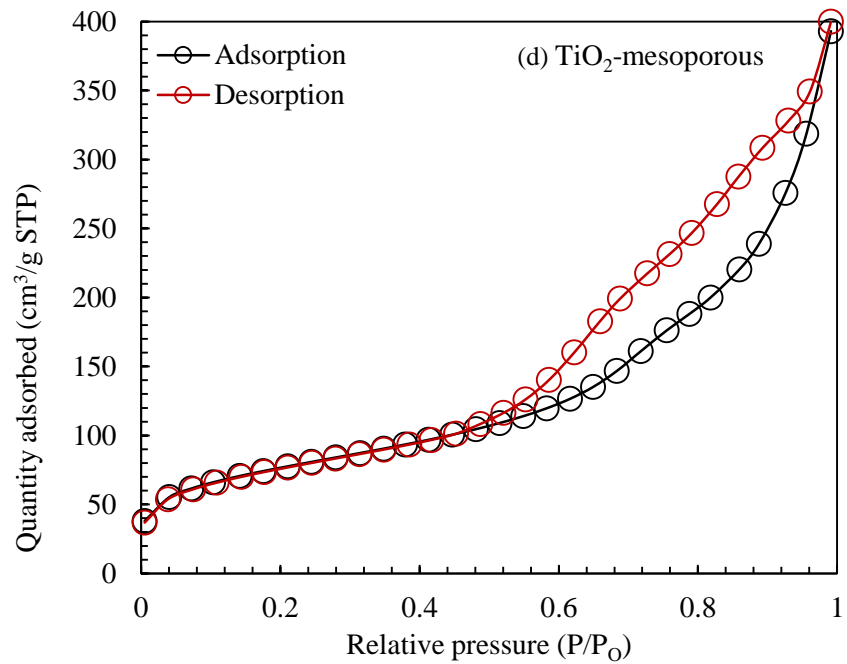


**Figure 4-3** N<sub>2</sub> adsorption-desorption isotherms of (a) ZSM-5, (b) TiO<sub>2</sub>/ZSM-5 (c) TiO<sub>2</sub>-mesopores and (d) ZnO/ZSM-5 and also corresponding BJH pore size distribution curves of samples (e)

**Table 4-1** Specific surface area ( $S_{\text{BET}}$ ), pore volume (V) and average pore diameter (d) for ZSM-5, TiO<sub>2</sub> Degussa, TiO<sub>2</sub>/ZSM-5, ZnO/ZSM-5, and TiO<sub>2</sub>-mesoporous

Sample	$S_{\text{BET}}$ ( $\text{m}^2 \text{g}^{-1}$ ) <sup>a</sup>	V ( $\text{cm}^3 \text{g}^{-1}$ ) <sup>b</sup>	D (nm) <sup>c</sup>
ZSM-5	311	0.014	8.6
TiO <sub>2</sub> Degussa	45-55	--	<25
TiO <sub>2</sub> /ZSM-5	1151	0.2	5.2
ZnO/ZSM-5	380	0.17	6.1
TiO <sub>2</sub> -mesoporous	360	0.42	5.6

<sup>a</sup> The specific surface area was calculated by BET method

<sup>b</sup> The pore volume was obtained from the BJH Desorption cumulative volume of pores between 1.0000 nm and 50.0000 nm diameter.

<sup>c</sup> The average pore diameter was estimated using the desorption branch of the isotherm and BJH model.

As shown in Table 4.1, the BET surface area of TiO<sub>2</sub>/ZSM-5 mesoporous are much larger than the commercial ZSM-5, suggesting that the direct template process has effected on the porosity of commercial ZSM-5. However, replacement of TiO<sub>2</sub> by ZnO, caused a decrease in surface area and pore volume from 1151  $\text{m}^2 \text{g}^{-1}$  and 0.2  $\text{m}^3 \text{g}^{-1}$  to 380  $\text{m}^2 \text{g}^{-1}$  and 0.17  $\text{m}^3 \text{g}^{-1}$ , respectively. The high surface area of TiO<sub>2</sub>/ZSM-5 can be explained by the isotherms graph, which is revealed that the type of H<sub>4</sub> hysteresis did not exhibit any limiting adsorption at high  $P/P_0$ , which is true with non-rigid aggregates of plate-like particles giving rise to slit-shaped pores while the desorption branch contained a steep region associated with a (forced) closure of the hysteresis loop, due to the tensile strength has effected as shown in Figure 4.3b. Furthermore, It is noteworthy that the low pressure hysteresis which occurred at range 0.1- 0.3 for TiO<sub>2</sub>/ZSM-5 catalyst may be associated with the change in volume of the adsorbent, i.e. the swelling of non-rigid pores or with the irreversible uptake of molecules in the pores of about the same width as that of the adsorptive molecule. In addition, chemisorption was also led to cause “open” hysteresis loops at the low  $P/P_0$  range (0.01-0.1) (Sing, 1985). This phenomenon was observed in the isotherms of TiO<sub>2</sub>/ZSM-5 while it was absent in the isotherms of ZnO/ZSM-5 mesoporous (see Figures 4.3c).



It can be concluded that the ZSM-5 modified with TiO<sub>2</sub> by using the direct template method was achieved successfully with high specific surface area (1151m<sup>2</sup> g<sup>-1</sup>), large pore volume (0.2 m<sup>3</sup> g<sup>-1</sup>) and pore size (5.2 nm). For better understanding and comparison few catalysts from previous literature have been listed down in Table 4.2 with property of surface area and preparation method.

**Table 4-2** Comparison of surface area among different catalysts

Catalyst	Preparation method	BET surface area (m <sup>2</sup> g <sup>-1</sup> )	References
TiO <sub>2</sub> nanoparticules supported on natural zeolite (TI-ZE).	A simple hydrolysis	80.04	(Q. Sun et al., 2015)
TiO <sub>2</sub> nanoparticles supported on zeolite type 13X.	Two steps sol-gel	324.1	(Chong, Tneu, et al., 2015)
TiO <sub>2</sub> nanoparticules supported on zeolite type ZSM-5.	Sol-gel	343	(Chang, Wang, Ouyang, Zhang, & Jing, 2015)
TiO <sub>2</sub> (25%) nanoparticles supported on zeolite type MCM-41molecular sieve.	Hydrothermal	669	(Reddy, Davydov, & Smirniotis, 2003)
TiO <sub>2</sub> nanoparticles Supported on HZSM-11 Zeolite (10%).	Hydrothermal crystallization	365	(Montañez, Gómez, Santiago, & Pierella, 2015)
HB zeolite-supported TiO <sub>2</sub> (amount of TiO <sub>2</sub> (g) per gram of HB 0.01)	Sol-gel	545	(Mahalakshmi, Priya, Arabindoo, Palanichamy, & Murugesan, 2009)
1.5% Pt- TiO <sub>2</sub> /natural zeolite	Sol-gel	118.7	(M. Huang et al., 2008)
Cr/ TiO <sub>2</sub> /zeolite (10%Cr)	Sol-gel	205	(C. Wang, Shi, & Li, 2012)
Beta zeolite supported TiO <sub>2</sub>	Sol-gel	31	(Lafjah, Djafri, Bengueddach, Keller, & Keller, 2011)
N-Ti/13X/MCM-41	Templating	664	(H. Tao, Nguyen, Hei, Liang, & Chang, 2015)
TiO <sub>2</sub> -Zeolite type ZSM-5	Templating	1151	This study

**4.3.1.3 FESEM images**

High magnification images of 2 $\mu$ m of the ZSM-5, TiO<sub>2</sub>/ZSM-5, ZnO/ZSM-5 and TiO<sub>2</sub>-mesoporous catalyst were investigated using SEM as shown in Figure 4.4. The surface of ZSM-5 was found to be relatively smooth (Figure 4.4a), however small particles can be clearly seen dispersing on the surface of ZSM-5 when TiO<sub>2</sub> particles were loaded onto ZSM-5 surface (Figure 4.4b). Nevertheless, clusters of large particles were observed due to the aggregation of ZSM-5 particles and dispersion and attachment of TiO<sub>2</sub> onto aggregated particles of ZSM-5 as shown in Figure 4.4b. It was predicted that ZSM-5 might have formed channels and cavities inside and between the ZSM-5 particles during the aggregation process since ZSM-5 forms multilamellar scaffold, as mentioned in section 3.1, which would have provide surplus space for TiO<sub>2</sub> crystallites to bind inside and out of the cavities and channels formed by ZSM-5 particles and consequently formed heavy particles with high porosity. It was anticipated that this behaviour of TiO<sub>2</sub>/ZSM-5 catalyst can be exhibited ease of post-operational separation of catalyst from treated wastewater. It was interesting to note that the vesicular (spherical) ZSM-5 was tended to form grape-like clusters of aggregating vesicles rather than separate vesicular particles (Figures 4.4b-d). The reason behind that is the high condensation of silanol groups (Si-OH) on the surface of the individual silica particles, as discussed by earlier researchers (L. Huang et al., 2000; Baojian Zhang, Davis, Mendelson, & Mann, 2000). More interestingly, The SEM results were in agreement with the proposed study as discussed in section 4.3.1.1 and with the finding of XRD as there was no major change in the structure of ZSM-5. Consequently, the direct template method was proved to be suitable for the synthesis of a unique, stable structure and high surface area of TiO<sub>2</sub>/ZSM-5 catalyst (Figure 4.4b).

Whereas, the ZnO particles loading on the surface of ZSM-5 were tended to aggregate predominantly together rather than on the surface of ZSM-5 particles, as a result, the silanol groups of ZSM-5 particles cannot formed bonds with ZnO (Figure 4.4c) and thus have unstable and weak binding structure of ZnO/ZSM-5. In case of TiO<sub>2</sub> - mesoporous catalyst, TEOS was used as a source of silica instead of ZSM-5 (Figure 4.4d). It can be observed that the TEOS condensed randomly around TiO<sub>2</sub> particles to form dense grape-like network cluster, where vesicles like structure of silica were disordered and that might formed potentially unstable TiO<sub>2</sub> particles.

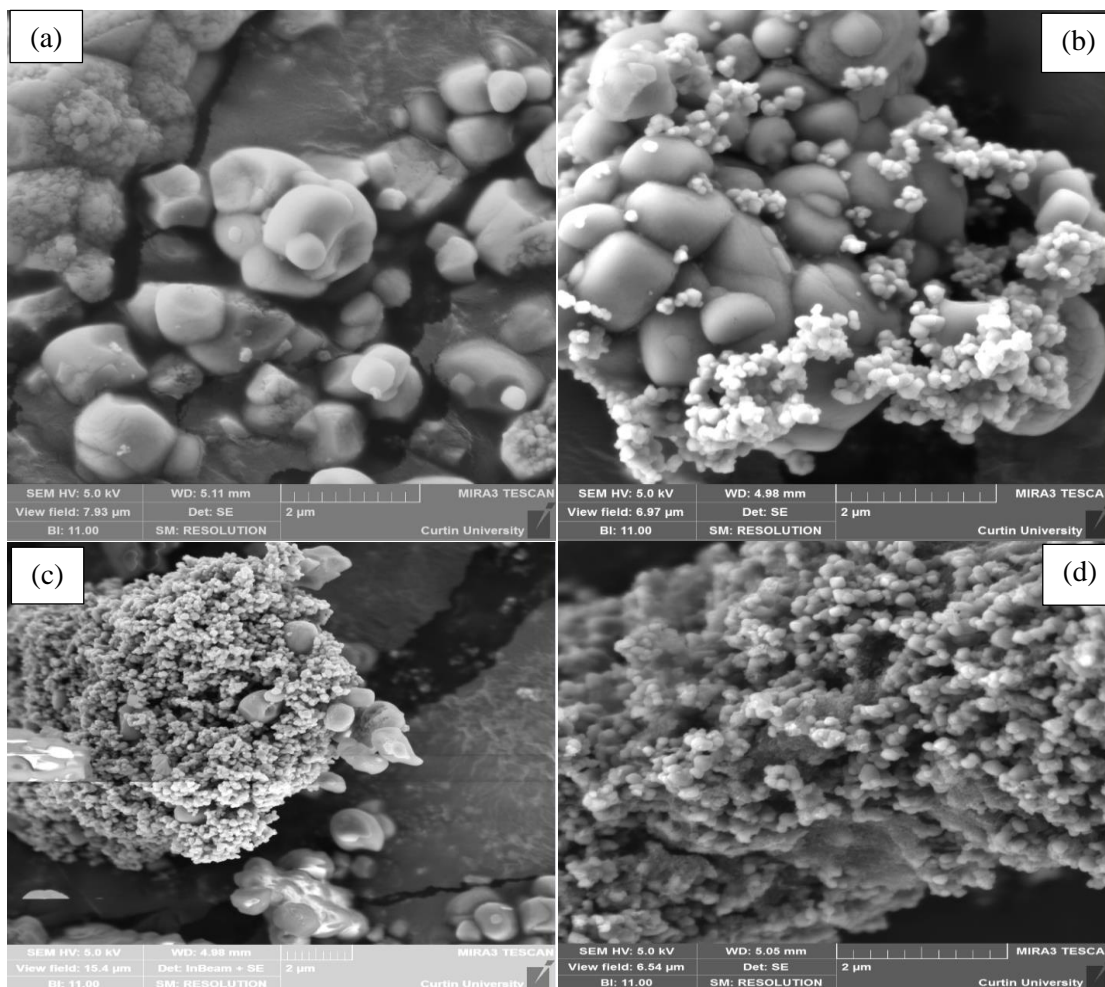


**Figure 4-4** SEM images of a) ZSM-5, b) TiO<sub>2</sub>/ZSM-5, c) ZnO/ZSM-5, d) TiO<sub>2</sub>-mesoporous

#### 4.3.1.4 Fourier-transformed infrared spectroscopy (FTIR) Analysis

The functional groups present in TiO<sub>2</sub>/ZSM-5, ZnO/ZSM-5, TiO<sub>2</sub> - mesoporous and ZSM-5 was studied using the FTIR spectroscopy. From Figure 4.5, it is observed that the TiO<sub>2</sub>/ZSM-5 exhibited similar FTIR spectra characteristics as of commercial ZSM-5 for extended band at 1100 cm<sup>-1</sup> without shifting. This indicated that the ZSM-5 structure was not affected when TiO<sub>2</sub> used as immobilizer onto ZSM-5 surface due to the high stable framework of ZSM-5 particles. However, ZnO/ZSM-5 showed the narrow band at 1064 cm<sup>-1</sup> and band at 838 cm<sup>-1</sup> were disappeared, which proved unsuitable of immobilization of ZnO particles due to causing disturbance in framework and no interstitial binding with ZSM-5 structure. Whereas, TiO<sub>2</sub> mesoporous catalyst sample possessed broadband at 3429 cm<sup>-1</sup> that was related to the -OH stretching and bending vibrations of silanol groups (Si-OH) and due to the interaction between water molecules and -Si-OH groups. Whilst, the small band at 1228 cm<sup>-1</sup> is associated with

the bending vibrations of H-O-H bonds in water molecules and –Si-OH groups. Besides, the sharp band of TiO<sub>2</sub>/ZSM-5 was observed at 838 cm<sup>-1</sup> due to the Al-O-Al or Si-O-Si symmetric stretching vibrations in the tetrahedral SiO<sub>4</sub> and AlO<sub>4</sub> structures, formed in ZSM-5 framework. Previously Gamba et al. (Gamba, Colella, & Coluccia, 2001) have reported that the immobilization of TiO<sub>2</sub> onto the ZSM-5 structure can be resulted in the asymmetric or antisymmetric for TiO<sub>2</sub> and Ti-O-Si units in the infrared band range of 960-1097 cm<sup>-1</sup>. It was also noticed that the band intensity was proportional to the amount of Ti presenting in the ZSM-5 framework.

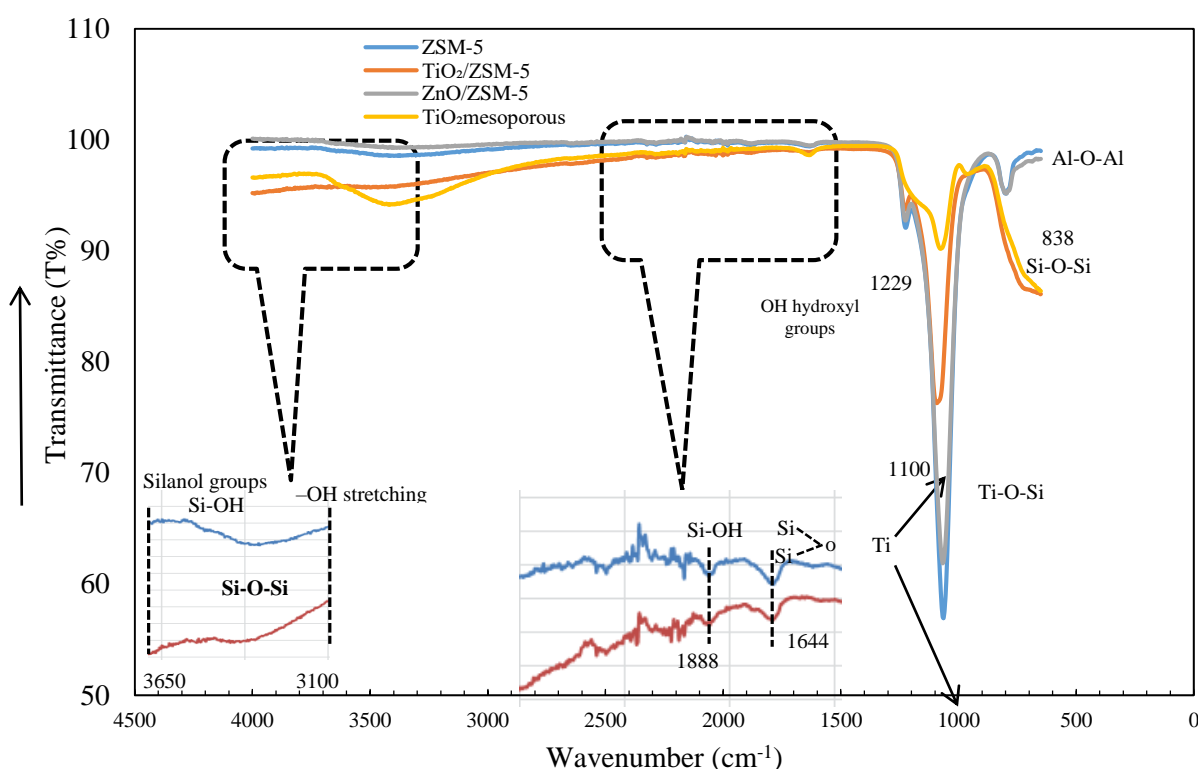


**Figure 4-5** FTIR spectra of ZSM-5, ZnO/ZSM-5, TiO<sub>2</sub>/ZSM-5, TiO<sub>2</sub>-mesoporous.

## 4.4 Photocatalyst activities

### 4.4.1 Effects of the catalyst type

To find the best catalyst for the degradation of methyl orange in aqueous solution under solar irradiation, three types of catalysts were synthesized TiO<sub>2</sub>/ZSM-5, TiO<sub>2</sub>-mesoporous, and ZnO/ZSM-5. TiO<sub>2</sub> Degussa and conventional ZSM-5 were also used for comparison. The initial concentration of MO in aqueous solution was 20 mg L<sup>-1</sup>. The photo-catalysts loading were controlled at 2 g L<sup>-1</sup> and the pH was kept at the initial value of 7.5 because in these conditions TiO<sub>2</sub>/ZSM-5 effectiveness was reached to the

optimum removal efficiency of the dye. The results shown (see Figure 4.6) that the best catalyst was TiO<sub>2</sub>/ZSM-5 because of the maximum decolouration of MO achieved (99.55%) during 180 min of solar irradiation. Figure 4.6 shown that the decolouration rate of MO increased rapidly within the first 60 min, however, it continued up to 150 min till it reached in the state of equilibrium. The photo-degradation of MO by using TiO<sub>2</sub> Degussa and TiO<sub>2</sub>- mesoporous were also studied, it can be observed that the degradation efficiency of MO after 180min were 80.7% and 83.4% respectively as a shown in Figure 4.6; however, the high degradation percentage of TiO<sub>2</sub> Degussa and TiO<sub>2</sub>-mesoporous were proved inefficient due to post-operation recovery of these catalysts from the aqueous solution as shown in Figure 4.6 (inset).

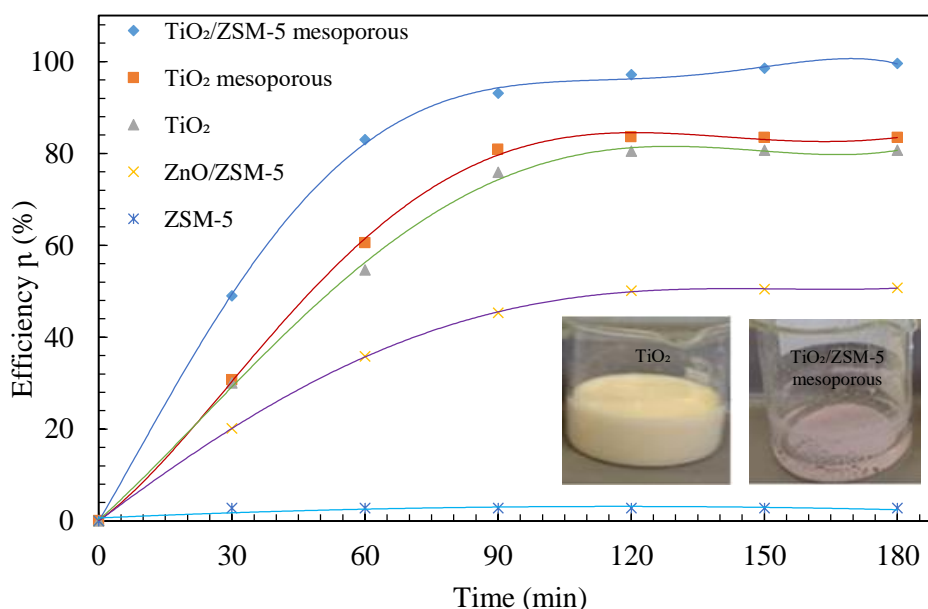


**Figure 4-6** Removal efficiency of MO dye decolourization using TiO<sub>2</sub>/ZSM-5, TiO<sub>2</sub>-mesopores, TiO<sub>2</sub> Degussa, ZnO/ZSM-5 and ZSM-5

On the basis of the results and the discussion of the structural properties described in previous sections, the reasons behind to be TiO<sub>2</sub>/ZSM-5 as an efficient catalyst is the high specific surface area up to 1151m<sup>2</sup> g<sup>-1</sup> which provided additional active sites on the surface of TiO<sub>2</sub>/ZSM-5 and perfect distribution of TiO<sub>2</sub> particles onto the morphology of ZSM-5 mesoporous, which in turn enhanced the photodegradation efficiency of the catalyst. Moreover, the wide pore size of TiO<sub>2</sub>/ZSM-5 was increased the solar light penetration directly without any reflection light intensity outside the bulk solution. The photocatalysis ability of ZnO/ZSM-5 was also studied, where it was noticed that the degradation efficiency of MO after 180 min was only 50.71% (Figure

4.6). In case of ZnO/ZSM-5, the decolouration of MO increased slowly up to 90 min which was remarkably slower than the rate achieved by TiO<sub>2</sub>/ZSM, TiO<sub>2</sub>-Mesopoures and TiO<sub>2</sub> Degussa, however the degradation remained continue, but the rate of degradation gradually decreased till it reached in the state of equilibrium at 120 min. The low specific surface area 380 m<sup>2</sup> g<sup>-1</sup> and disordered distribution of ZnO onto ZSM-5 surface make this catalyst less efficient. Nevertheless, ZSM-5 was exhibited completely inefficient catalyst; there was no perceptible colour change in MO dye. Thus, the results above demonstrated that the TiO<sub>2</sub>/ZSM-5 was the excellent catalyst in comparison to others prepared via direct template method.

#### 4.4.2 Effects of the pH

The pH value is a crucial influence on the photocatalytic degradation process, its affects the generation of the oxidizing species ( $\bullet\text{OH}$ ,  $\text{O}_2\bullet^-$ ,  $\text{H}_2\text{O}_2$  and  $\text{HO}_2\bullet$ ) that result in photodegrading (Zepp, Faust, & Hoigne, 1992), thus it is necessary to study the effect of the pH on the methyl orange photo-degradation process. Experiments were carried out at pH values of 2, 4, 6, 7, 7.5, 8 and 9 with 20 mg L<sup>-1</sup> of MO, 2 g L<sup>-1</sup> dosage of TiO<sub>2</sub>/ZSM-5 in 100 ml reaction volume, for 180 min reaction time and the pH was adjusted by using 1M KOH and HCl solution.

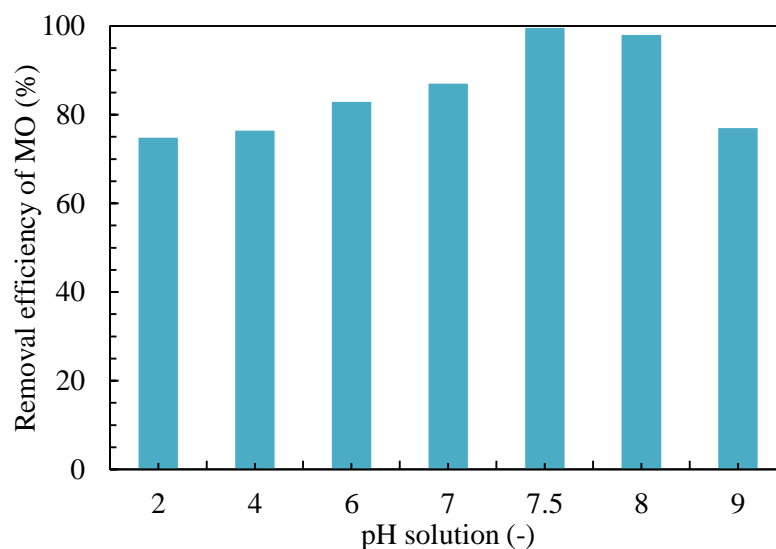


**Figure 4-7** Effect of pH of solution on removal efficiency of MO

In the presence of TiO<sub>2</sub>/ZSM-5 catalyst, the degradation was increased with the increase of pH from 2.0 to 7.5, and reached to its maximum MO removal efficiency at pH 7.5 but started to decrease with the increase of pH from 7.5 and beyond (Figure 4.7). The highest removal of MO at almost neutral pH (7.5) has been a great

achievement since after treatment there was no need to adjust the pH of water before joining the water bodies. It is to be believed that the surface of TiO<sub>2</sub>/ZSM-5 is positively charged under acidic conditions pH<7.5 by the adsorbed H<sup>+</sup> ions on the semiconductor surface, whereas, it is negatively charged under alkaline conditions pH >7.5 by the adsorbed OH<sup>-</sup> ions on the semiconductor surface. The photodegradation efficiency affects by an anionic or cationic form of the MO dye. Two reaction mechanism contribute to MO dye degradation such as a direct oxidation by positive holes, and direct reduction by electrons. It was observed that the degradation efficiency of MO in acidic to neutral (pH of 2, 4, 6, 7, 7.5) was significantly increased than the basic solution of pH 9.0 which is made the catalyst surface negative charge. Therefore, in acidic to neutral media, a strong adsorption of MO on the composite particles is preferred as a result of the electrostatic attraction of the positively charged particles toward the MO to be a higher at neutral region. However, in basic solutions of pH= 9.0, MO dye dissociated forming sodium ions that can react with the adsorbed OH<sup>-</sup> ions, which reduced the amount of OH<sup>-</sup> radicals (L. Zhang et al., 2009).

#### 4.4.3 Kinetics studies

In order to evaluate the kinetics of photo-degradation of MO via TiO<sub>2</sub>/ZSM-5 catalyst were simulated using pseudo-first order and pseudo-second order model and the best fitted model were selected based on the highest correlation coefficient R<sup>2</sup> value. The pseudo first order model of photo-degradation reaction can be described by Langmuir-Hinshelwood kinetic model, which can be simplified to an apparent first order equation as shown in Eq. (4.2). Chong et al. found that the Langmuir-Hinshelwood model could be simplified when the KC-value is less than 1 to pseudo-first order kinetic model as given in Eq. (4.3) (Chong, Jin, et al., 2009).

$$\frac{dC}{dt} = \frac{k \cdot KC}{1 + KC} = r \quad (4.2)$$

$$\ln\left(\frac{C_0}{C}\right) = k \cdot K \cdot t = -k_{app(MO)} \quad (4.3)$$

Where  $r$  is the reaction rate,  $k$  is the reaction rate constant,  $K$  is the dynamic Langmuir adsorption constant,  $C$  is the dye concentration and  $k_{app(MO)}$  is the obvious pseudo-first order reaction rate constant.

From plot  $\ln(C_0/C)$  versus  $t$ , the decolourization rate,  $k_{app(MO)}$  (min<sup>-1</sup>) of MO by TiO<sub>2</sub>/ZSM-5 catalysts at different dosages was shown in Figure 4.8.

The experimental data were also analysed with pseudo-second order model, using the linear equation (4.4):

$$\frac{t}{q_t} = \frac{1}{k_{2(MO)} \cdot q_e^2} + \frac{1}{q_e \cdot t} \quad (4.4)$$

where  $k_{2(MO)}$  is the reaction rate constant for pseudo-second order model,  $q_e$  is the amount of MO at equilibrium and  $q_t$  is the amount of MO photo-degraded at time  $t$ . From plot  $t/q_t$  versus  $t$ , the decolourization rate,  $k_{2(MO)}$  (g.mg<sup>-1</sup>.min<sup>-1</sup>) by TiO<sub>2</sub>/ZSM-5 catalysts at different dosages was shown in Figure 4.9.

The values of correlation coefficients  $R^2$  indicated a better fit of pseudo-second order model with dosage 2 mg L<sup>-1</sup> of TiO<sub>2</sub>/ZSM-5 catalysts.

Catalyst loading is a significant factor in photo-catalytic wastewater treatment processes (Chong, Cho, Poh, & Jin, 2015). The optimum photo-catalyst loading not only preventing unnecessary excess use of applied catalysts but also gives a maximum photo-activity. It was noticed that photo-activity increased with increase of TiO<sub>2</sub>/ZSM-5 loading and achieved the maximum photo-activity at 2 g L<sup>-1</sup> due to the availability of more reactive radicals for surface reaction and also the highest number of active sites. However, catalyst loading more than 2 g L<sup>-1</sup> caused cloudiness in the reaction solution which blocked the penetration of solar illumination.

Mahadwad et al. have explained that the increase in catalyst concentration caused deactivation of molecules (Mahadwad, Parikh, Jasra, & Patil, 2011). Thus, the optimum TiO<sub>2</sub>/ZSM-5 mesoporous loading for the photocatalytic degradation of 20 mg L<sup>-1</sup> model MO dye in aqueous solution was 2 g L<sup>-1</sup>.



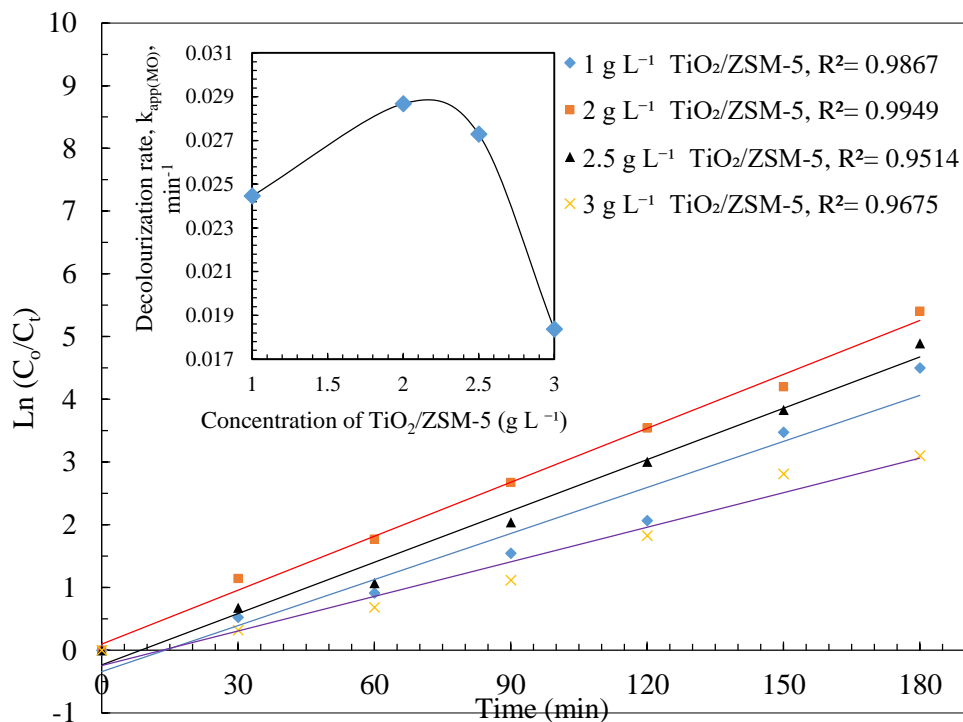


Figure 4-8 The pseudo-first order reaction rate

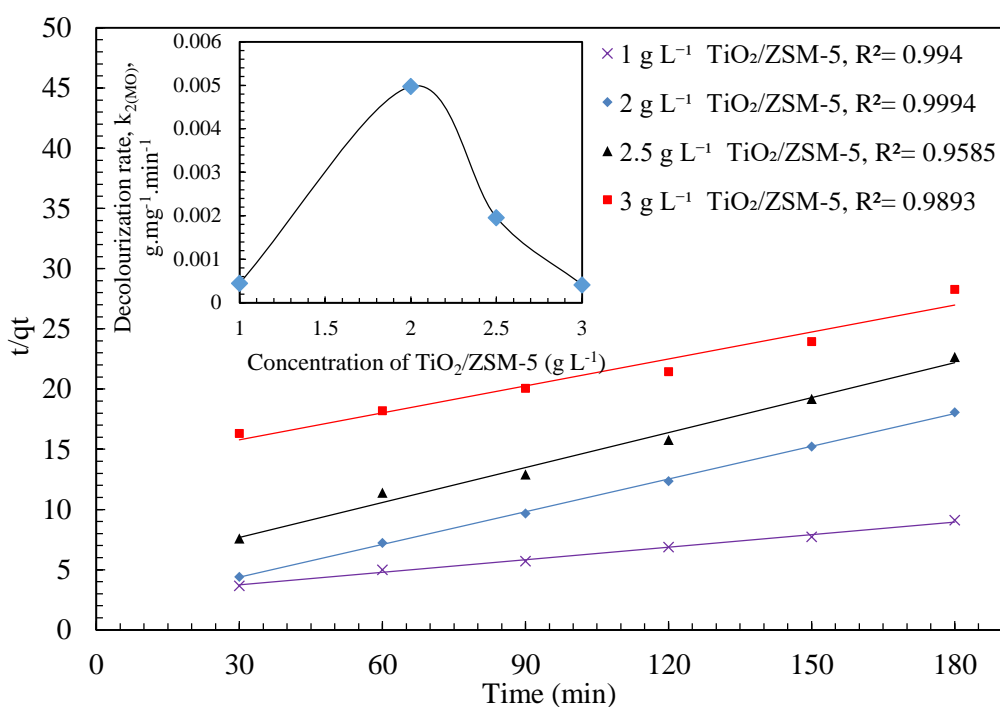
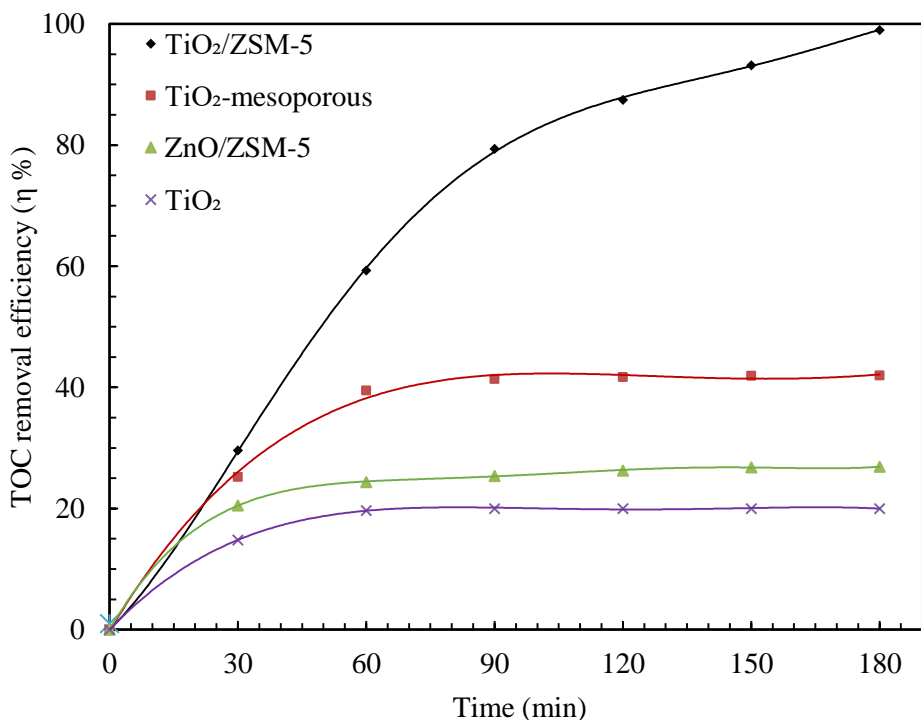


Figure 4-9 The pseudo-Second order reaction rate

### 4.4.4 TOC removal

The mineralization of the total organic carbon of 20 mg L<sup>-1</sup> MO solution using TiO<sub>2</sub>/ZSM-5, TiO<sub>2</sub>-mesoporous, ZnO/ZSM-5 and TiO<sub>2</sub> Degussa were investigated. The results were presented in Figure 4.10, indicated that TiO<sub>2</sub>/ZSM-5 managed to remove completely (99%) TOC of MO in 180 min of solar irradiation, however, some of the intermediate by-products (1%) remained in the solution even after its treatment of 180 min. As reflected in Figure 4.10, it can be fairly concluded that MO dye was decoloured via photocatalytic degradation process using TiO<sub>2</sub>/ZSM-5 and at the same time the by-products were efficiently mineralized. Figure 4.10 also depicted that the relative concentration of TOC reduced quickly within 90 min and it remained decreased, but with lower rates than before till 180 min without showing any obvious equilibrium. However, in case of TiO<sub>2</sub>-mesoporous, it was noticed that the TOC removal was 42% under solar irradiation after 180 min as shown in Figure 4.10. The ZnO/ZSM-5 and TiO<sub>2</sub> Degussa catalysts were just able to remove 28% and 17% TOC for the same time span of 180 min, respectively. Among all catalysts studied in this study, TiO<sub>2</sub> Degussa reached to its equilibrium state within 60 min, which was considered as quite before in respect of others. Hence it could be concluded that some of intermediate by-products and few percentage of MO itself cannot be degraded by TiO<sub>2</sub> Degussa. ZnO/ZSM-5 and TiO<sub>2</sub>-mesoporous have not acquired their equilibrium event at 180 min, however the rate was extremely low and from application point of view, it would not be suggested to use these catalysts for MO mediated wastewater treatment. Combining the results depicted in Figures 4.6 and 4.10, it could be concluded that TiO<sub>2</sub>-mesoporous, ZnO/ZSM-5 and TiO<sub>2</sub> Degussa were better with decolouration of MO than their efficiency to degrade TOC. Finally, it was speculated that the TiO<sub>2</sub>/ZSM-5 has strong reduction-oxidation ability as a result of the hole-pair electron recombination, which given high activation sites on the surface of the catalyst and consequently proved to be the most appropriate catalyst for TOC removal of MO dye in aqueous media.



**Figure 4-10** TOC removal of 20 mg L<sup>-1</sup> methyl orange dye by using different types of catalyst

#### 4.4.5 Recycling and regeneration of the TiO<sub>2</sub>/ZSM-5 mesoporous

Studying regeneration and reuses of the photocatalyst were important aspects in terms of potential practical applications, cost effectiveness and eco-friendly nature of proposed catalyst; therefore, the used TiO<sub>2</sub>/ZSM-5 mesoporous in solar photocatalytic experiments of the MO dye was regenerated and used several times. The experimental data were illustrated in Figure 4.11.

After the end of first complete photocatalyst cycle of MO, the catalyst was filtrated, washed with deionized water, dried at 100°C, and followed by the calcination process at 400°C for 3h to remove adsorbed MO dye and its intermediate molecules, if any present onto the surface of TiO<sub>2</sub>/ZSM-5 catalyst. The same above mentioned procedure was conducted after every cycle of usage. The degradation efficiency of MO dye after several cycles is shown in Figure 4.11. At the end of the six cycles, a slight reduction in the degradation efficiency of MO from 99.55% to 95.0 was noticed. It was likely due to the accumulation of the intermediate by-products on the surface of the catalyst or might be because of slight leaching of TiO<sub>2</sub> particles.

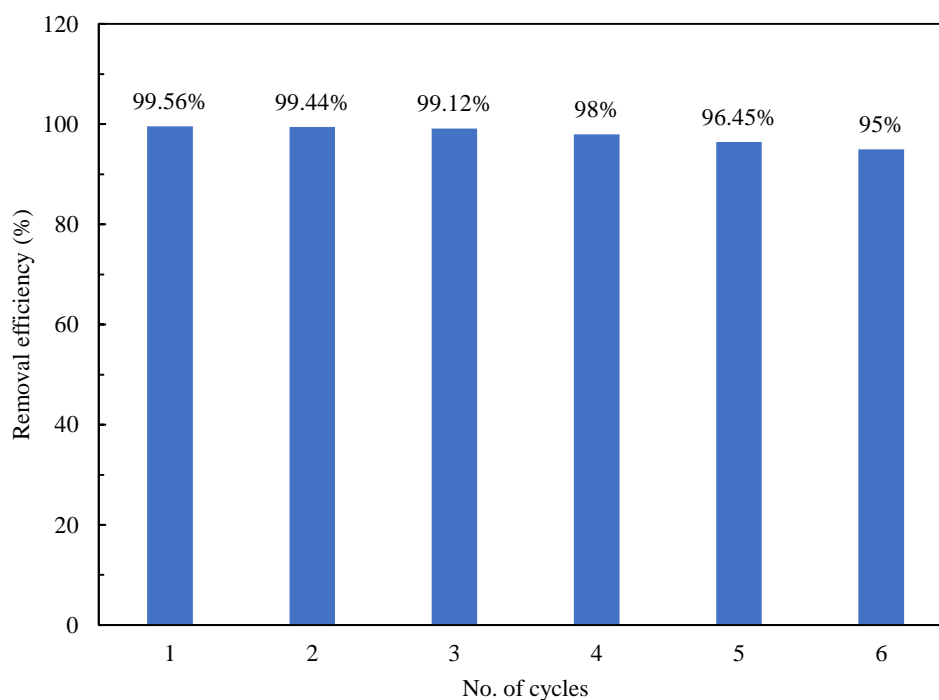


**Figure 4-11** the regeneration efficiency of TiO<sub>2</sub>/ZSM-5 mesoporous after a number of cycles for methyl orange dye contamination

In order to study the durability of the TiO<sub>2</sub>/ZSM-5 catalyst, the surface area of the recycled catalyst after six complete cycles of usage was tested by N<sub>2</sub> adsorption - desorption analyzer (Figure 4.12) and the surface was characterized by XRD spectra (Figure 4.13). The results clarified that the specific surface area, XRD and FTIR (Figure 4.14) results of regenerated catalyst after complete six cycles possessed no significance changes which indicated the durability and feasibility of TiO<sub>2</sub>/ZSM-5 mesoporous.

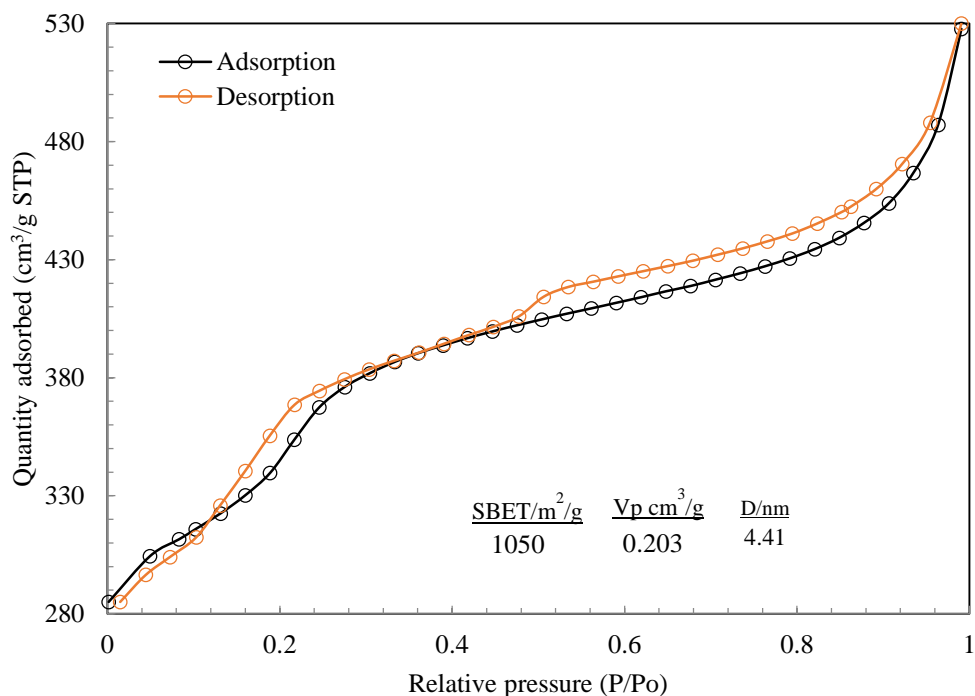


**Figure 4-12** The BET surface area of TiO<sub>2</sub>/ZSM-5 mesoporous after six completed cycles of usage

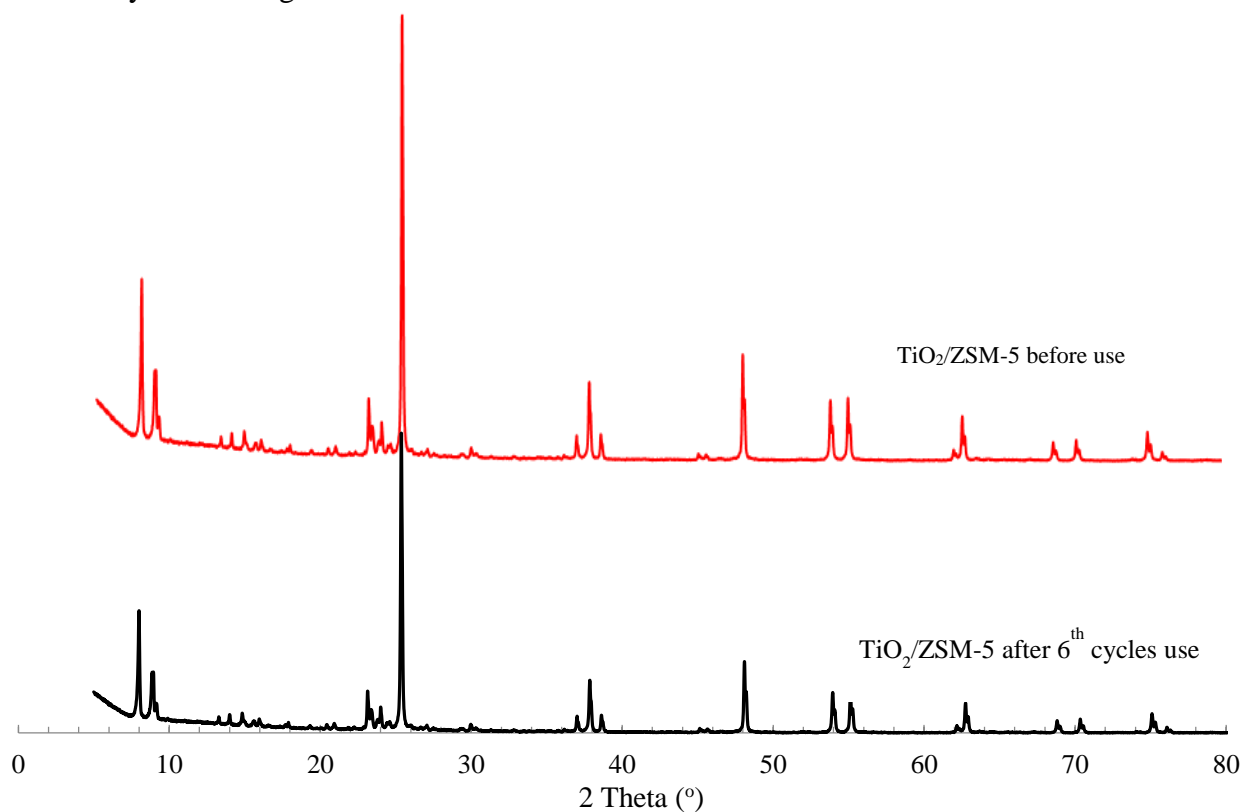


**Figure 4-13** the XRD comparison between the TiO<sub>2</sub>/ZSM-5 before used and after 6<sup>th</sup> cycle's usage

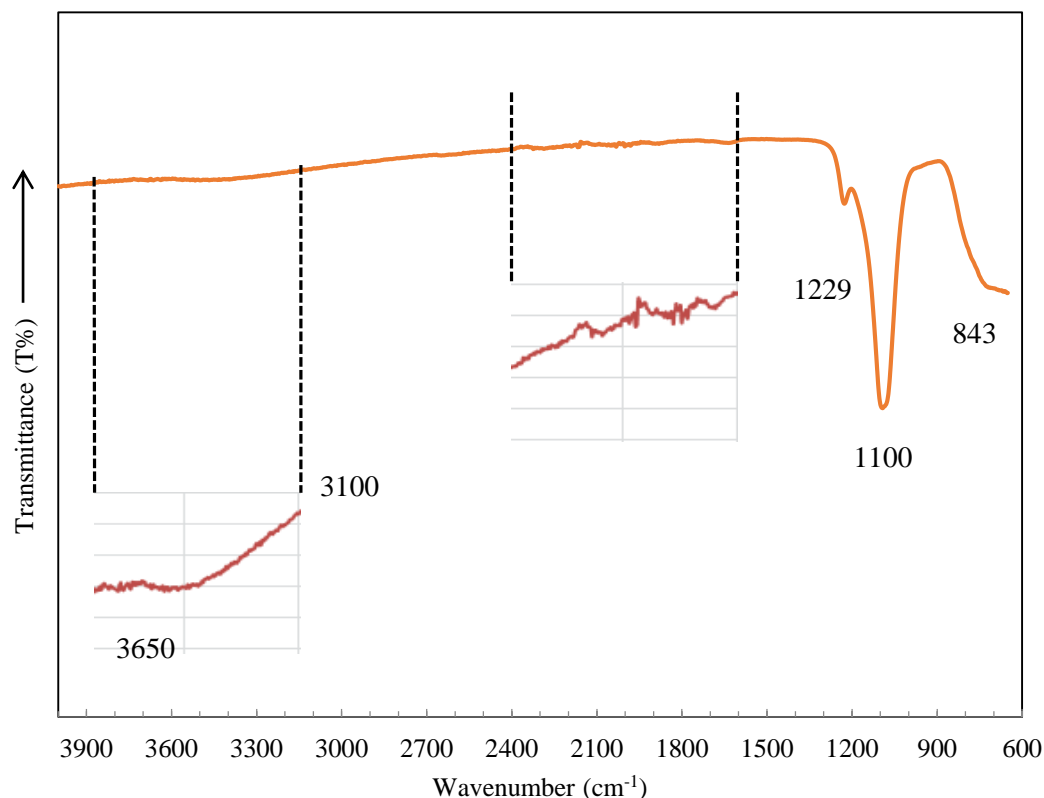


**Figure 4-14** FTIR spectra of the regenerated TiO<sub>2</sub>/ZSM-5 after 6<sup>th</sup> run

It can be noticed that the TiO<sub>2</sub>/ZSM-5 exhibited high structural stability even after multi-cycles usage. Based on these findings, it can be concluded that the TiO<sub>2</sub>/ZSM-5 catalyst has unique adsorption photocatalytic ability, which is highly recommended in the advanced wastewater treatment. The findings have demonstrated that TiO<sub>2</sub>/ZSM-5 mesoporous that prepared by the direct template method is durable and reusable after several treatment cycles without a significant losing its photocatalytic efficiency.

## 4.5 Summary

TiO<sub>2</sub> immobilized onto a new multilamellar vesicles (MLVs) ZSM-5 mesoporous substrate were fabricated by the direct templating approach. Based on the results presented in this chapter, the highly ZSM-5 mesoporous content was effectively enhanced to degrade MO dye due to multi-layers mesoporous provide several effective sites as well as a high molecular weight for post separation. The decolourization and mineralization removal effectiveness can reach 99.55% and 99%, respectively, for initial MO concentration of 20 mg L<sup>-1</sup> under 180 min sunlight irradiation. The high specific surface area of the TiO<sub>2</sub>/ZSM-5 (1151 m<sup>2</sup> g<sup>-1</sup>) ensures a high photocatalysis efficiency of MO dye. The TiO<sub>2</sub>/ZSM-5 mesoporous was compared with different

catalysts such as TiO<sub>2</sub> Degussa, ZSM-5, ZnO/ZSM-5, and TiO<sub>2</sub>-mesoporous. The XRD analysis confirmed the anatase phase mostly in the synthesized TiO<sub>2</sub>/ZSM-5 mesoporous. Moreover, SEM images showed that TiO<sub>2</sub> crystallites were present on the multilamellar vesicles ZSM-5. The kinetic study follows the pseudo-second-order model. TiO<sub>2</sub>/ZSM-5 was regenerated six times, with its degradation efficiency remained as high as 95.16%. The reusability of TiO<sub>2</sub>/ZSM-5 mesoporous solar-photocatalyst using MO dye was evaluated. The data revealed that 95% removal efficiency of MO dye was achieved after six cycle's treatment with no significant loss in the efficiency of the used catalyst. Thereupon, the results demonstrate that the TiO<sub>2</sub>/ZSM-5 multilamellar vesicles mesoporous exhibits promising potential application as a new photocatalyst for water purification.

## CHAPTER 5

# 5

### Synthesis of novel RGO/TiO<sub>2</sub>/ZSM-5

### Mesoporous for Adsorption and Photocatalytic Degradation of Methylene Blue from aqueous media

#### 5.1 Introduction

In chapter 4, we investigated the process of synthesizing TiO<sub>2</sub>/ZSM-5 mesoporous for solar photocatalytic degradation of MO dye from aqueous solution as well as its analysis and characterization. Although photocatalytic degradations of dyes using various photocatalysts and light sources have been widely studied, little attention has been paid to synthesized solar photocatalyst containing mesoporous nanocomposite fabricated with reduced graphene oxide (RGO). Therefore, this chapter will focus on the activity of the reduced graphene oxide in solar photocatalytic degradation of methylene blue dye. Removal of recalcitrant organic chemicals from wastewater is a crucial ecological problem. Modern synthetic dyes are one of the most prominent examples of non-biodegradable organic compounds which are common industrial contaminants of the water bodies. Methylene blue dye (MB) is a standout amongst the regular dyes utilized for wood, cotton, and silk. It is harmful when inhaled, while ingestion causes a smouldering sensation, spewing, mental perplexity and methemoglobinemia (Ghosh & Bhattacharyya, 2002). Therefore, the removal of this dye from water samples by an appropriate process is urgently demanded.



Photocatalysis is one of the advanced oxidation processes utilized for wastewater treatment and has been generally reported for efficiently degrading almost all types of water organic pollutants (Chong et al., 2010). TiO<sub>2</sub> semiconductor photocatalyst is generally being utilized in this process due to its high effectiveness, stability and non-poisonous quality (X. Chen & Mao, 2007; Fujishima et al., 2000; Liao et al., 2012). However, the use of TiO<sub>2</sub> in treatment of industrial dyes has remained very challenging because of the problem of post-separation and recovery of the used photocatalyst, as well as recombination electron/hole pair (Chong, Vimonses, et al., 2009). To mitigate the challenge of post-separation, the use of an appropriate substrate material such as clay (Chong, Vimonses, et al., 2009), activated carbon (Shi et al., 2010), and magnetite core embedded into the TiO<sub>2</sub> will be an interesting field to research (Beydoun & Amal, 2002). Zeolites emerged as a good candidate substrate in photocatalysis due to its abundance, it is also inexpensive; in addition it contains alumino-silicates with different size cavity structure, tectosilicates with microporous channels, pore spaces, high ion exchange capacity, adsorption and catalysis capacity (Vimonses et al., 2009; S. Wang & Peng, 2010). Several researchers have utilized the ZSM-5 type of zeolite in photocatalytic process to prepare efficient solar photocatalyst for wastewater treatment (Khatamian et al., 2010; Panpa et al., 2008). TiO<sub>2</sub>/ZSM-5 nanocomposite has been reported by many researchers as an excellent catalyst in water treatment applications; however, there is a still needs for further improvement in terms of its stability, adsorbability and enhancement of the electron/hole pair recombination. To the best of the author's knowledge, no research was found that studied the effect of mesoporsity on solar photocatalytic stability.

To further enhance the adsorbability and electron/hole pair separation in the TiO<sub>2</sub>/ZSM-5 nanocomposite, reduced graphene oxide (RGO) was found to be a decent potential applicant with a remarkable material characteristic. This is due to the presence of substantial amounts of oxidized functional groups such as; hydroxyl, carboxylic, and aldehyde groups on its surface which promotes adsorbability (J. C. Sun, Cheng, Fan, & Ai, 2013; Williams, Seger, & Kamat, 2008). On the other hand, it also enhances fast electron transfer between TiO<sub>2</sub> and RGO nano-sheets, thereby reflecting a high efficient electrons and holes separation. Very little was found in literatures utilizing RGO/TiO<sub>2</sub>/zeolite as multifunctional nanocomposites to remove dye pollutants. One of these studies reported that reduced-graphene oxide/TiO<sub>2</sub>/Zeolite-4A bifunctional nanocomposite catalyst has been utilized for

abatement of methylene blue dye in aqueous media (Nagarjuna, Challagulla, Alla, Ganesan, & Roy, 2015). However, the experimental data is rather controversial, and there is no general agreement about whether the adsorption or photocatalysis process has mainly affected the decolourization of the methylene blue dye. Furthermore, the data results of the above study showed no reliable evidence to compare between the adsorption and photocatalysis removal efficiency, it was reported from the study that adsorption equilibrium was obtained after only 20 min with removal efficiency of 80%, and a very low surface area of 19 m<sup>2</sup> g<sup>-1</sup> of this nanocomposite catalyst. There is also no evidence of investigations that use different weight percentage (wt %) of RGO in the nano-composite catalyst to compare the RGO performance in the nano-composite. Therefore, a new synthetic technique is required to improve efficiency and durability. Such promoting technique would deliver a multifunctional material possessing high adsorption capacity and high photocatalytic action (Nagarjuna et al., 2015; A. Sharma & Lee, 2016).

The main objectives of this study is to synthesize, characterize and investigate the adsorption/solar photocatalytic processes of RGO/TiO<sub>2</sub>/ZSM-5 mesoporous nanocomposite. To evaluate the RGO performance, different wt% of RGO; 5%, 10% and 15% (w/w) were used in the TiO<sub>2</sub>/ZSM-5 mesoporous composite, and a comparison study between photocatalysis and adsorption processes was evaluated. The TOC% and intermediate compounds of MB were also investigated. The kinetic degradation models, post-separation, mesoporosity and reusability were studied. The contribution of this study is obvious as the result of the outcomes can be utilized as guidelines to large-scale potential wastewater treatment application.

## 5.2 Experimental work

### 5.2.1 Chemicals

As mentioned in chapter 3, section (3.2.1), the zeolite type of ZSM-5 (Molar ratio SiO<sub>2</sub>/Al<sub>2</sub>O<sub>3</sub> =600, 300 m<sup>2</sup> g<sup>-1</sup> specific surface area, 2–3µm particle size; and pore size 0.5 nm) was provided from ACROS Organics; A Thermo Fisher Scientific Brand; New Jersey–USA. Titanium dioxide (TiO<sub>2</sub>, Degussa P25, 70% anatase: 30% rutile, specific surface area, 53 m<sup>2</sup>g<sup>-1</sup>).

### 5.2.2 Incorporation of TiO<sub>2</sub>/ZSM-5 mesoporous onto RGO

The preparation technique of TiO<sub>2</sub>/ZSM-5 mesoporous was mentioned in chapter 4 section 4.2.2 and also in chapter 3 section (3.3.2). To prepare RGO, Hummers method

was adopted; firstly, to prepare graphene oxide (GO) from graphite powder as reported previously (Johra & Jung, 2015). Details of this synthesis process are mentioned in section 3.3.2 of chapter 3 with illustration in Figure 3.3.

### 5.2.3 Characterizations of photocatalysts

The crystalline phases of the synthesized catalysts were characterized and studied by X-ray diffraction (XRD) technique using a Bruker D8. Field emission scanning electron microscope (FESEM) measurements were done with MIRA3TESCAN high vacuum mode microscope. The EDX (Energy-dispersive X-ray spectroscopy) analysis provided information of the elemental composition of the catalysts. Fourier-transformed infrared (FTIR) spectroscopy was conducted to observe the functional groups of the synthesized catalysts. Specific surface area ( $S_{BET}$ ) was measured via the Brunnauer-Emmett-Teller (BET), Micromeritics, Tri-Star II Surface area and Porosity.

### 5.2.4 Adsorption and photocatalytic experiments

As mentioned in chapter 3, section (3.3.2), batch adsorption process was carried out in a beaker with a magnetic stirrer using different catalysts such as; TiO<sub>2</sub>, ZSM-5, 5% TiO<sub>2</sub>/ZSM-5, 10% RGO/TiO<sub>2</sub>/ZSM-5, 15% RGO/ZSM-5 and physical mixture of RGO, TiO<sub>2</sub> and commercial ZSM-5 in darkness and solar light conditions respectively. After the adsorption process, the photocatalytic activity of the catalyst was experimented under solar light irradiation, using sun solar simulator) as a source of the solar light. The tests were performed at room temperature at a pH of 8.5 of the MB solution. During the photocatalytic process, 5 ml of the samples were withdrawn at regular intervals and the colour change during photodecomposition of MB dye was measured by UV-vis spectrophotometer. The total organic carbon (TOC) was estimated via SHIMADZU, TOC-VcpH Scientific apparatus. The chromatographic demonstrations with HPLC-UV/vis system were conducted on a Varian Prostar 210 chromatograph (for more details see chapter 3, section (3.6.2)). The removal efficiency ( $\eta$  %) of MB dye was calculated using equation (5.1); where  $c_0$  and  $c$  are the initial and final MB concentrations in the solution.

$$\eta_{MB} = \frac{c_0 - c}{c_0} \times 100 \quad (5.1)$$

## 5.3 Results and discussion

### 5.3.1 Characterizations of the catalysts

#### 5.3.1.1 XRD analysis

The XRD patterns of the RGO, ZSM-5, TiO<sub>2</sub>, TiO<sub>2</sub>/ZSM-5, 5% RGO/TiO<sub>2</sub>/ZSM-5, 10% RGO/TiO<sub>2</sub>/ZSM-5 and 15% RGO/TiO<sub>2</sub>/ZSM-5 were investigated, and the diffraction peaks obtained are shown in Figure 5.1. The signal peaks of TiO<sub>2</sub> Degussa with high crystallinity were found at 25.4°, 37.5°, 48.0°, 54.1°, 54.8°, and 62.6°. They indicated that the d 101, d 004, d 200, d 106, d 211, and d 204 planes are mainly anatase phase. Moreover, the three small intensity peaks were also found at 68.5°, 71.2°, 75.5°. They indicated that the d 110 plane is a rutile phase.

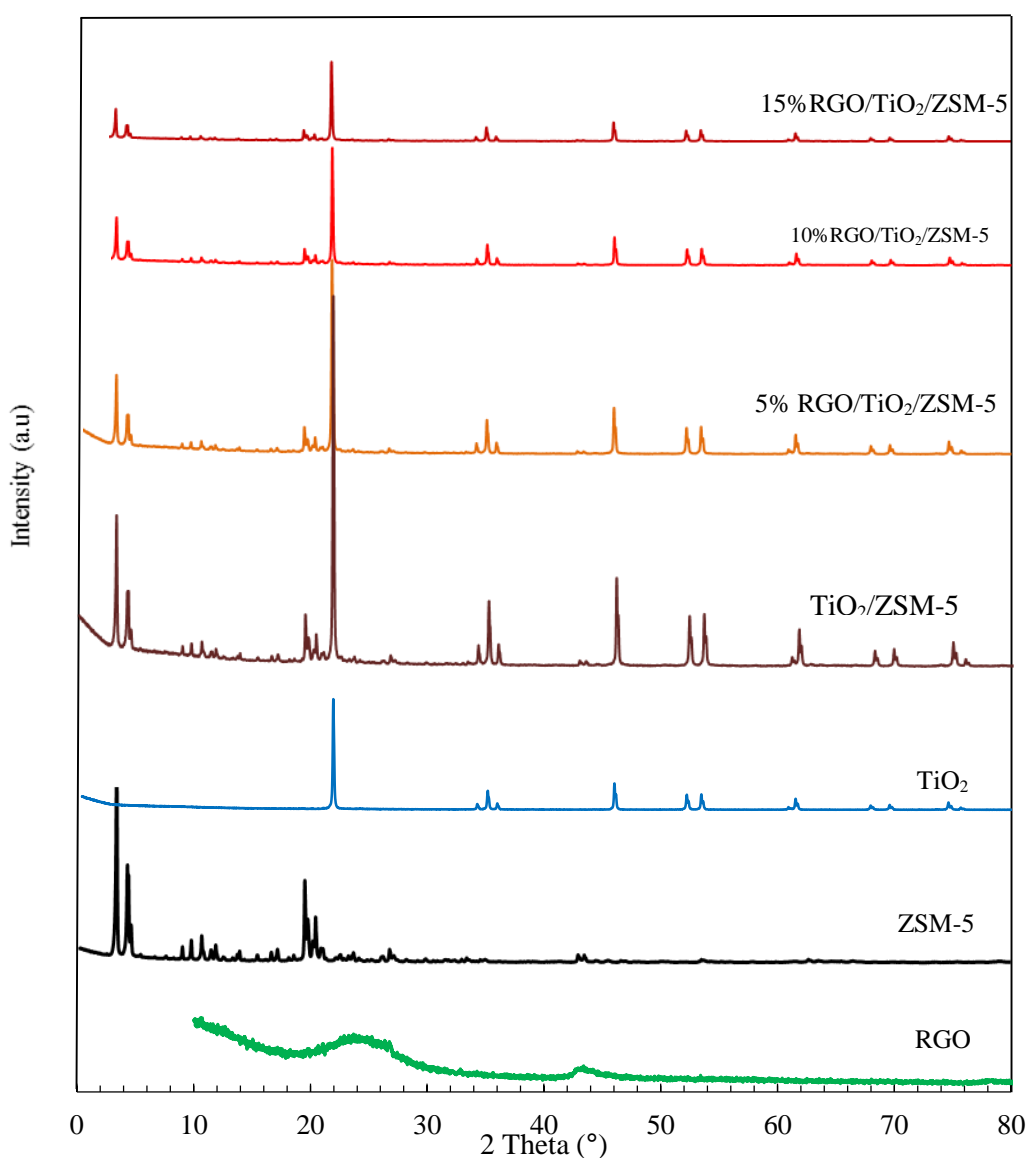


**Figure 5-1** XRD patterns of RGO, TiO<sub>2</sub>, ZSM-5, TiO<sub>2</sub>/ZSM-5 mesoporous, 5% RGO/TiO<sub>2</sub>/ZSM-5, 10% RGO/TiO<sub>2</sub>/ZSM-5 and 15% RGO/TiO<sub>2</sub>/ZSM-5

From Figure 5.1, the diffraction peaks of ZSM-5 were also observed at 7.5°, 8°, 13.2°, 13.9°, 14.7°, 15.5°, 23.1°, 29.8°, 45.0° and 45.2° which typically correlated with the data reports in the literature concerning zeolite type ZSM-5 for sodium aluminium silicate (Na<sub>1.5</sub>Si<sub>93</sub>O<sub>192</sub>) (J.-J. Wang et al., 2015). It was noted that there were no significant peaks shift after the conventional ZSM-5 is modified to mesoporous morphology with TiO<sub>2</sub> Degussa, indicating that the crystalline form of ZSM-5 did not changed during the preparation method of TiO<sub>2</sub>/ZSM-5 mesoporous as illustrated in Figure 5.1.

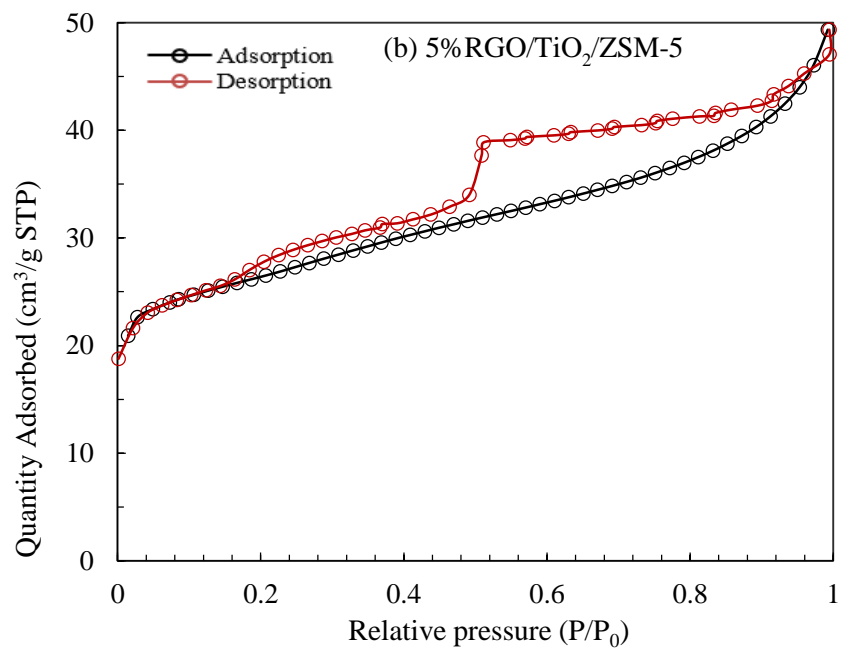
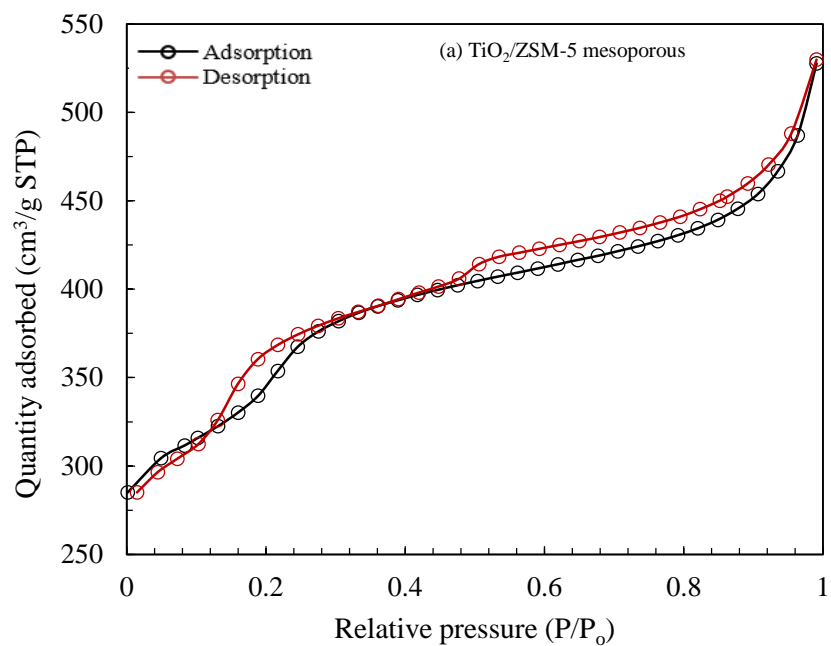
As shown in the XRD profile of the RGO, a wide peak at  $2\theta = 23.4^\circ$  that corresponds to the interplanar spacing of  $\sim 3.75 \text{ \AA}$  between the (002) planes appeared (Stankovich et al., 2007); this could be due to the high reduction of RGO associated with the ring-opening of epoxide and cleavage of some oxygen-containing functional groups; while, the small peak at  $2\theta = 42.2^\circ$  could be as a result of the turbostratic crystal structure of the disordered carbon materials. It appears from Figure 5.1 that XRD profile of 5%, 10% and 15% RGO/TiO<sub>2</sub>/ZSM-5 catalysts showed no significant reduction in the TiO<sub>2</sub> crystallinity of the nanocomposite mesoporous catalysts and the intensity peaks of these catalysts were clearly noticed at  $2\theta = 22.5^\circ$  and are mainly anatase phase without shifting from the original place, while the rutile peaks at  $2\theta = 68.5^\circ, 71.2^\circ, 75.5^\circ$  showed a much lower intensity, indicating that the rutile phase has a lower stability than the anatase phase through the synthesizing process. Also, the RGO has no significant effect on the crystallinity of the TiO<sub>2</sub>/ZSM-5 mesoporous as illustrated in Figure 5.1. The above finding revealed that the synthesis technique was successfully applied while maintaining a high degree of crystallinity of the synthesized catalysts.

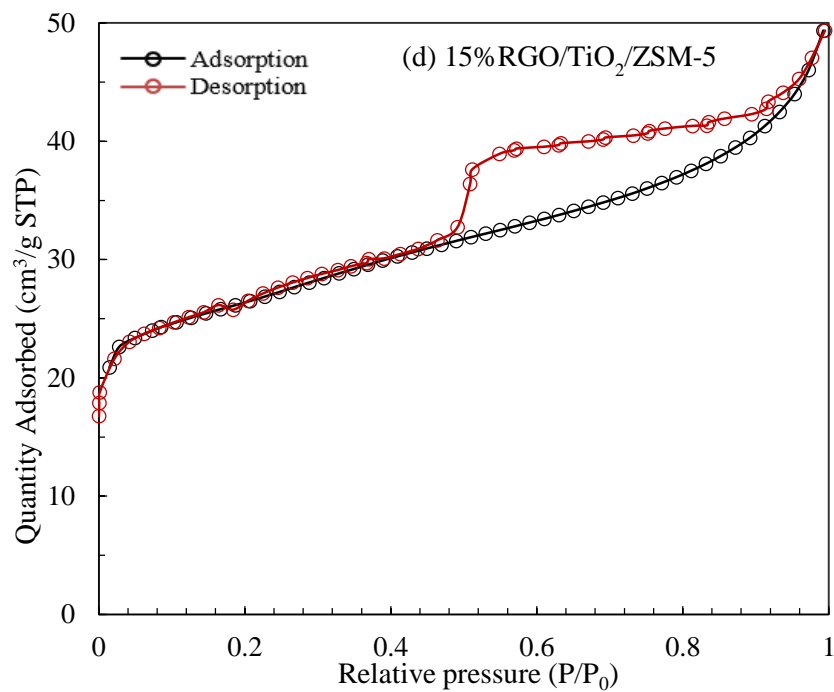
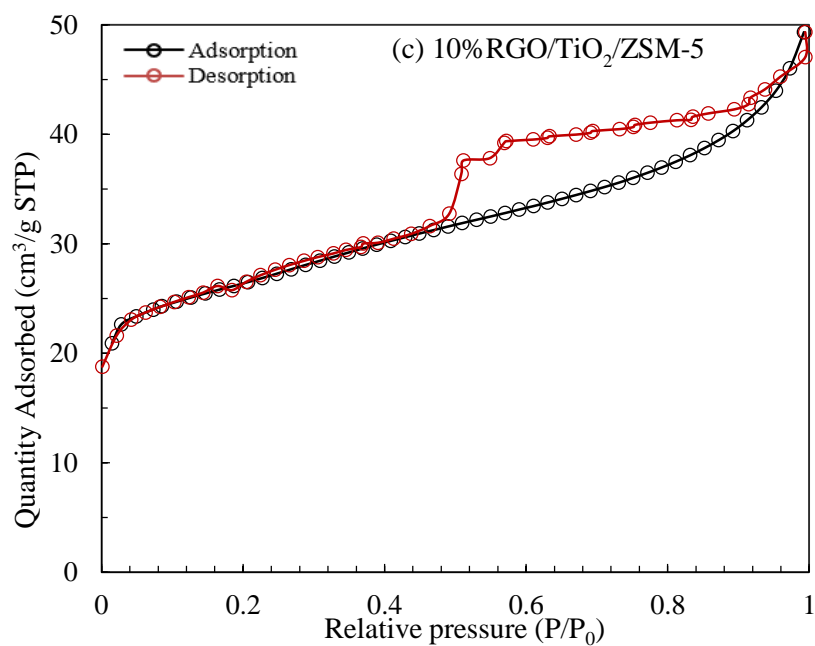
### 5.3.1.2 BET specific surface areas and pore distribution

The specific surface area and the pore structure profile of catalysts were characterized by Brunauer-Emmett-Teller method (BET) for 5%RGO/TiO<sub>2</sub>/ZSM-5, 10%RGO/TiO<sub>2</sub>/ZSM-5, 15%RGO/TiO<sub>2</sub>/ZSM-5 and TiO<sub>2</sub>/ZSM-5 mesoporous. Figures 5.2a-d illustrate nitrogen adsorption-desorption isotherms describing the specific surface area while the BJH pore size distribution of corresponding catalysts is shown in Figure 5.2e. The results obtained from the BET surface area and pore structure of the samples are summarized in table 5.1. From Figure 5.2a and as indicated by the IUPAC classification of isotherms adsorption and hysteresis loops, the

isotherms of TiO<sub>2</sub>/ZSM-5 mesoporous exhibit type H<sub>4</sub> hysteresis loops at very low relative pressures  $P/P_0 < 0.15$ , indicating micropore filling, and in relative pressure ( $P/P_0$ ) range of 0.15-1, suggesting mesopore condensation and multilayer adsorption with abundant mesoporous structure in the samples, which giving a BET specific surface area of 1151 m<sup>2</sup> g<sup>-1</sup>. The mesoporous structure in this sample was a plate-like or slit shaped pore with diameter of about 5.2 nm, and average pore volume is 0.2 cm<sup>3</sup> g<sup>-1</sup> as shown in Figure 5.2e.

Figures b-d exhibited isotherms type IV which are ascribed to the monolayer/multilayer adsorption behaviour, indicating that the capillary condensation behaviours is quite filled pores with N<sub>2</sub> gas in the structure of the catalysts. To investigate these hysteresis loops behaviour and from Figures 5.2 b and c, there are exhibited type H<sub>4</sub> at  $P/P_0$  ranges of 0.15- 0.99 which gives BET specific surface area of 57 m<sup>2</sup> g<sup>-1</sup> and 80 m<sup>2</sup> g<sup>-1</sup>, respectively, and the pore diameters about 7.8 and 8.4 nm as shown in Figures 5.2e. These hysteresis loops suggested that micro/mesoporous pores are available in the nanocomposite catalysts, and pore clogging can be possibly due to a percolation phenomenon. Figure 5.2d showed that the hysteresis loop is consistent with findings in Figures 5.2 b and c. However, an increase in wt% of RGO up to 15% led to reduction of the specific surface area to 27.6 m<sup>2</sup> g<sup>-1</sup>. This is due to the agglomeration of TiO<sub>2</sub>/ZSM-5 mesoporous particles which is partially clogged and a reduction in pore size as a result of the abundant presence of oxygen groups in the RGO nano-sheets surface. This finding highlights that the synthesized technique successfully provided mesopore structure, and the high wt% of RGO can reduce the specific surface area in the nanocomposite mesoporous catalyst.







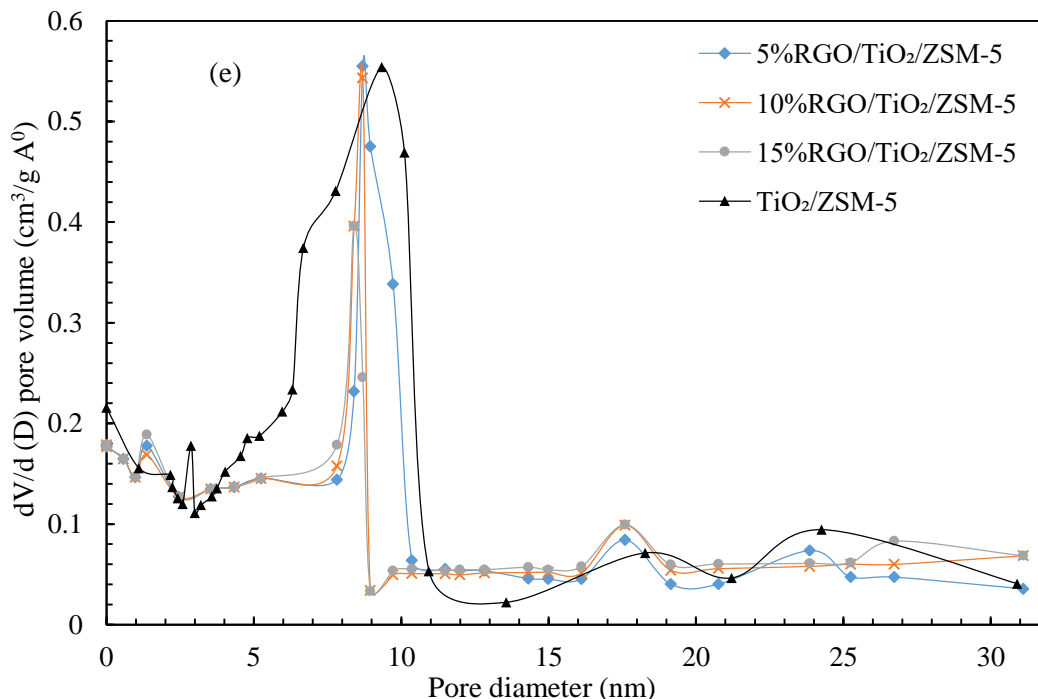


**Figure 5-2** N<sub>2</sub> adsorption-desorption isotherms of (a) TiO<sub>2</sub>/ZSM-5 mesoporous (b) 5%RGO/TiO<sub>2</sub>/ZSM-5 (c) 10%RGO/TiO<sub>2</sub>/ZSM-5 (d) 15%RGO/TiO<sub>2</sub>/ZSM-5 and also corresponding BJH pore size distribution curves of the samples (e)

**Table 5-1** Specific surface area ( $S_{BET}$ ), pore volume (V) and average pore diameter (d) for catalysts

Catalysts	$S_{BET}$ (m <sup>2</sup> g <sup>-1</sup> ) <sup>a</sup>	V (cm <sup>3</sup> g <sup>-1</sup> ) <sup>b</sup>	D (nm) <sup>c</sup>
5%RGO/TiO <sub>2</sub> /ZSM-5	57	0.51	7.8
10% RGO/TiO <sub>2</sub> /ZSM-5	80	0.55	8.4
15% RGO/TiO <sub>2</sub> /ZSM-5	27.6	0.54	8.6
TiO <sub>2</sub> /ZSM-5 mesoporous	1151	0.2	5.2

<sup>a</sup> The specific surface area was evaluated by BET method

<sup>b</sup> The pore volume was obtained from the BJH Desorption cumulative volume of pores between 1.0000 nm and 50.0000 nm diameter.

<sup>c</sup> The average pore diameter was calculated using the desorption branch of the isotherm and BJH model.

### 5.3.1.3 Fourier-transformed infrared spectroscopy (FTIR) analysis

FTIR spectrum absorbance of RGO, TiO<sub>2</sub>/ZSM-5, 5%RGO/TiO<sub>2</sub>/ZSM-5, 10%RGO/TiO<sub>2</sub>/ZSM-5, and 15%RGO/TiO<sub>2</sub>/ZSM-5 catalysts were studied. From Figure 5.3, wide peak intensity spectrum of RGO at 3400 cm<sup>-1</sup> was observed, demonstrating that the O-H stretching vibration is often available in this region; while, a weak peak intensity spectrum appeared at 3400 cm<sup>-1</sup> for TiO<sub>2</sub>/ZSM-5 mesoporous, indicating that the O-H stretching of few water molecules was present in the nanocomposite catalyst. As revealed in Figure 5.3, a small peaks intensity near 1650 cm<sup>-1</sup> were observed in RGO, 5% RGO/TiO<sub>2</sub>/ZSM-5, 10% RGO/TiO<sub>2</sub>/ZSM-5 and 15% RGO/TiO<sub>2</sub>/ZSM-5 catalysts, suggesting that the C=O stretching of carboxylic groups existed at the edges of the graphene oxide sheets. Similar behaviour peaks intensity were observed at bands 1410, 1380, and 1250 cm<sup>-1</sup> of the above catalysts due to the C-O carboxyl, C-OH and epoxy C-O groups available in the nanocomposite. The intensity peak of the RGO, which represented C-O stretching hydroxyl groups, was remarkably shifted from 1000 cm<sup>-1</sup> toward higher region 1100 cm<sup>-1</sup>, proving that the RGO was successfully incorporated into the TiO<sub>2</sub>/ZSM-5 mesoporous catalyst.

As illustrated in Figure 5.3, a wide intensity peak appeared at 700 cm<sup>-1</sup> in TiO<sub>2</sub>/ZSM-5 mesoporous, indicating that the TiO<sub>2</sub> corresponded to Ti-O-Ti bonding. This peak was shifted toward 550 cm<sup>-1</sup> in the 5%RGO/TiO<sub>2</sub>-ZSM-5, 10%RGO/TiO<sub>2</sub>-ZSM-5 and 15%RGO/TiO<sub>2</sub>-ZSM-5 catalysts, demonstrating that the Ti-O-Ti and Ti-O-C bonds were presented in the 5%RGO/TiO<sub>2</sub>-ZSM-5, 10%RGO/TiO<sub>2</sub>-ZSM-5 and 15%RGO/TiO<sub>2</sub>-ZSM-5 samples, and the chemical interference has occurred between the functional hydroxyl groups of RGO with TiO<sub>2</sub> (Williams et al., 2008; H. Zhang et al., 2009). The above results revealed that the RGO is strongly anchored into TiO<sub>2</sub>/ZSM-5 mesoporous via the chemically interfered bonds between Ti and hydroxyl containing groups of the synthesized RGO. It also shows that the RGO successfully prepared contains abundant oxygen functional groups.

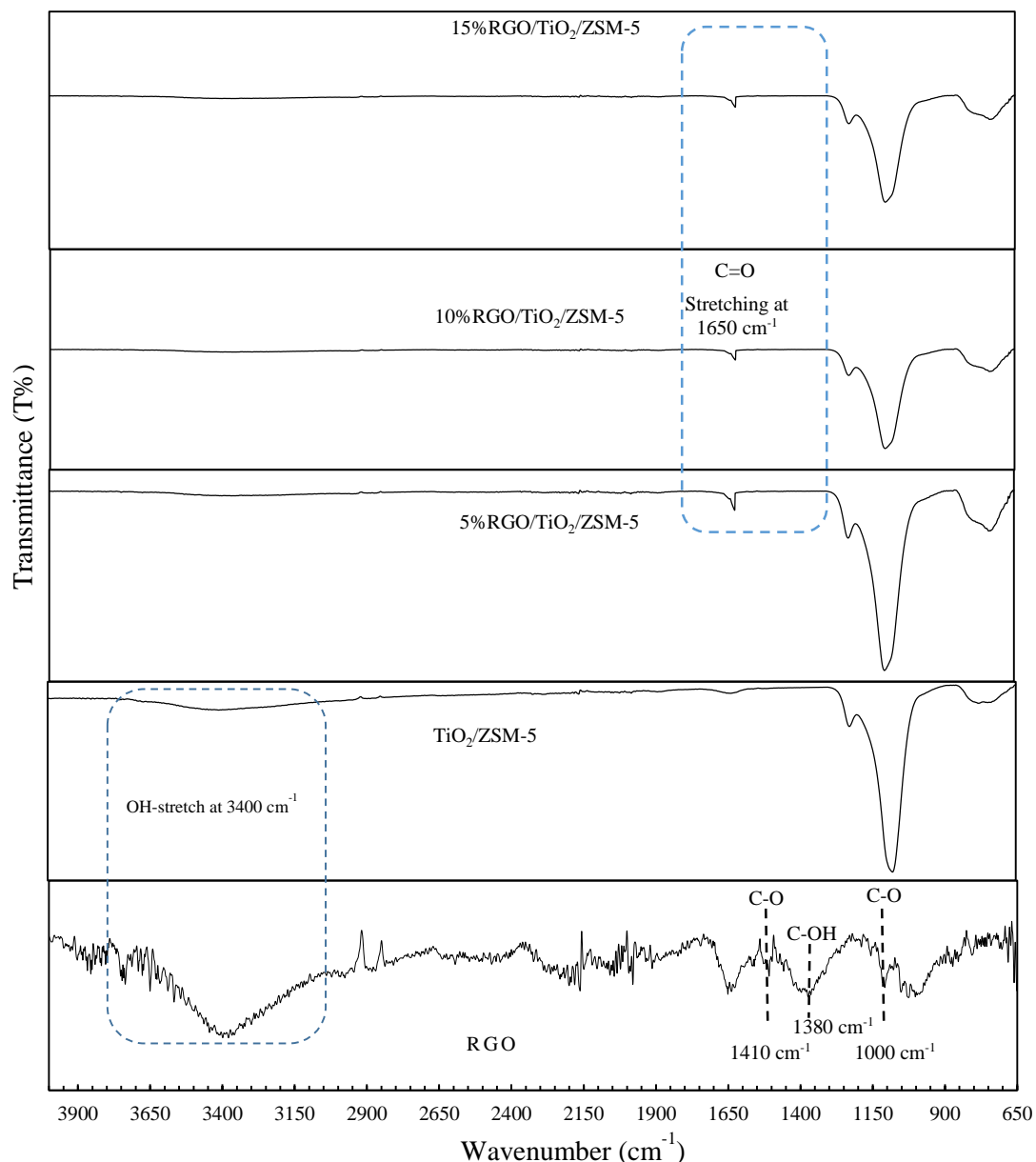


**Figure 5-3** FTIR spectra of TiO<sub>2</sub>/ZSM-5, 5% RGO/TiO<sub>2</sub>/ZSM-5, 10% RGO/TiO<sub>2</sub>/ZSM-5 and 15% RGO/TiO<sub>2</sub>/ZSM-5

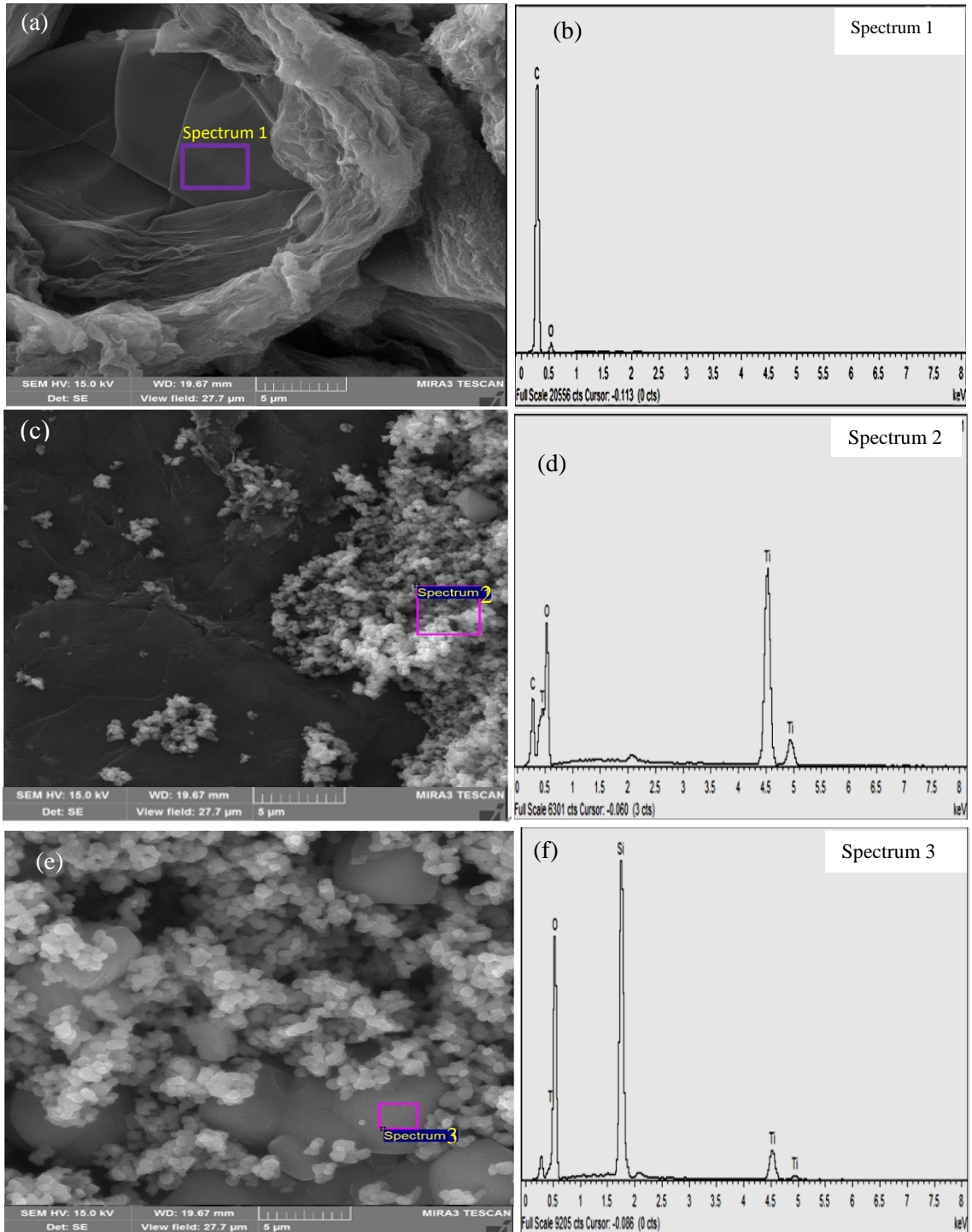
#### 5.3.1.4 FESEM images and EDX analysis

High magnification images of the RGO, TiO<sub>2</sub>/ZSM-5 mesoporous and 10% RGO/TiO<sub>2</sub>/ZSM-5 catalysts were investigated using FESEM and EDX analysis. From Figure 5.4a, it was apparent that smooth texture surface of multilayers RGO were obtained, which are likely active sites corresponding to -OH and -O functional group appropriating anchor on TiO<sub>2</sub> nanoparticles. In Figures 5.4c and e, it is apparent that the TiO<sub>2</sub> nanoparticles was well dispersed and deposited into the RGO layers, indicating the presence of -OH and -O groups in the RGO nano-sheets surface,

thereby forming a strong attachment between Ti and -OH groups as confirmed by FTIR spectra, (as discussed in section 5.3.1.3).

As illustrated in Figure 5.4g, a random distribution of the TiO<sub>2</sub>/ZSM-5 mesoporous particles onto RGO nano-sheets was observed, which highly stimulated the build-up of silanol groups (Si-OH) onto RGO surface nano-sheet as a template and an initial growth of TiO<sub>2</sub>/ZSM-5 mesoporous. This binding between Si and OH groups created a large molecule with a high porosity within the channels and the cavities that gives the catalyst have a good absorbability (Ogura et al., 2018; Qiu, Xing, & Zhang, 2018). Furthermore, it was also anticipated that easy post-separation of the mesoporous catalyst from aqueous media can possibly occur.

The EDX spectrum of the catalysts are also studied as shown in Figures 5.4 b, d, f, h. From Figure 5.4d, Ti, C and O<sub>2</sub> intensity peaks spectrum were obtained, indicating the TiO<sub>2</sub> particles are strongly incorporated onto the surface of the RGO nano-sheets. As shown in Figure 5.4f, the EDX peaks spectrum of TiO<sub>2</sub>/ZSM-5 mesoporous crystal revealed that the compositions are abundant in Si, O, Al and Ti, suggesting that Ti particles were successfully anchored onto the surface of ZSM-5 mesoporous. The spot spectrum in Figure 5.4h approved the presence of Si, O, Al and Ti along with the high carbon intensity peak obtained, confirming the successful incorporation of TiO<sub>2</sub>/ZSM-5 onto RGO surface nano-sheet. The interesting benefit in this finding is that it aids electron/hole pair transfer by significantly preventing the recombination hole/electron pair thereby enhancing photocatalysis process (Pastrana-Martínez, Morales-Torres, Figueiredo, Faria, & Silva, 2018; W. Zhang et al., 2018; M. Zhu et al., 2018).



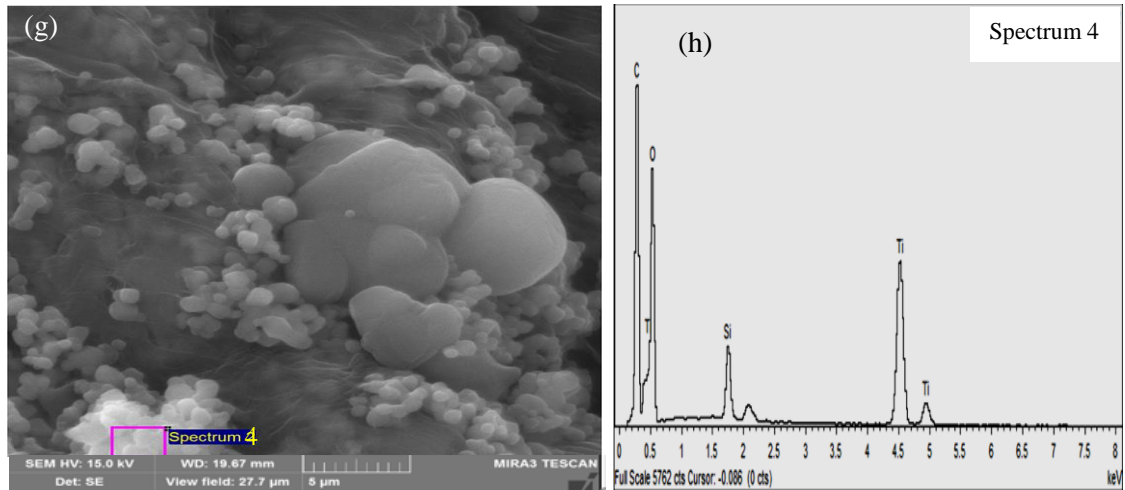


**Figure 5-4** FESEM and EDX analysis of (a, b) RGO, (c, d) 10% RGO/TiO<sub>2</sub>/ZSM-5, (e, f) TiO<sub>2</sub>/ZSM-5, (g, h) 10% RGO/TiO<sub>2</sub>/ZSM-5

### 5.3.2 Removal efficiency of MB dye

To investigate the adsorption/photocatalyst removal efficiency, batch experiments was conducted for 30 min at room temperature in the dark with an equilibrium adsorption limit of 10 mg L<sup>-1</sup> of MB dye solutions containing 0.5 g L<sup>-1</sup> each for 5% RGO/TiO<sub>2</sub>/ZSM-5, 10%RGO/TiO<sub>2</sub>/ZSM-5, 15%RGO/TiO<sub>2</sub>/ZSM-5, TiO<sub>2</sub> and TiO<sub>2</sub>/ZSM-5 catalysts. This was followed by the photocatalytic study under solar light irradiation for 90 min, samples were taken at every 30 min interval. A control which consist of ordinary mixture of RGO, TiO<sub>2</sub> and commercial ZSM-5 (wt% 8.4:8.4:8.4) was also investigated. The results of these experiments were illustrated in Figure 5.5a. The adsorption capacity of MB was calculated by the following equation:

$$q_t = \frac{(C_0 - C_t) \cdot V_0}{w} \quad (5.2)$$

Where  $q_t$  (mg/g catalyst) is adsorption capacity, the  $C_0$  and  $C_t$  (mg L<sup>-1</sup>) are the initial and concentrations at time  $t$  of MB respectively;  $V_0$  is the volume of the MB solution (L); and  $w$  is the weight of catalyst (g) (Kangwansupamonkon, Jitbunpot, & Kiatkamjornwong, 2010; Shawabkeh & Tutunji, 2003).

As illustrated in Figures 5.5a (adsorption region), the adsorption equilibrium of the used catalysts was obtained after 30 min, and from Figure 5.5b, the adsorption removal efficiencies were exceptionally increased with the presence of RGO in the composite catalysts, the removal efficiency 25%, 40% and 55% corresponds to the use of 5%

RGO/TiO<sub>2</sub>/ZSM-5, 10%RGO/TiO<sub>2</sub>/ZSM-5 and 15%RGO/TiO<sub>2</sub>/ZSM-5, respectively. The data also show that the adsorption removal efficiency using TiO<sub>2</sub> and TiO<sub>2</sub>/ZSM-5 mesoporous were 7% and 10% indicating that no significant adsorption was obtained using ZSM-5 mesoporous and TiO<sub>2</sub> in the composite catalyst (see Figure 5.5b).

The results of the decolourization of MB by photocatalysis process (see Figure 5.5b) using 5%RGO/TiO<sub>2</sub>/ZSM-5, 10%RGO/TiO<sub>2</sub>/ZSM-5, 15%RGO/TiO<sub>2</sub>/ZSM-5, TiO<sub>2</sub> and TiO<sub>2</sub>/ZSM-5 mesoporous catalysts reveals that the increase in wt % of RGO in the composite catalysts from 5% to 10% can increase the decolourization efficiency from 70% to 93%, respectively, and this was due to an increased ionic interaction and the reduced electron/hole pairs recombination at the surface of RGO photocatalysis process (Nguyen-Phan et al., 2011); however, increase of up to 15% wt of RGO decrease the decolourization reduced the removal efficiency to 83% as depicted in Figure 5.5b. This because of the opacity of the solution which prevents solar light from penetrating into the aqueous solution due to the high wt% of RGO and thus prevent excitation the electron/hole pair of the TiO<sub>2</sub>.

The feasibility of the synthesized 10% RGO/TiO<sub>2</sub>/ZSM-5 mesoporous nanocomposite was further studied, in addition a physical mixture of TiO<sub>2</sub>, RGO and the conventional ZSM-5 were also studied. As shown in Figures 5.5 a & b, the decolourization efficiency of MB dye using the physical mixture of the catalysts was 40 % and the adsorption efficiency was 10%. The common drawback of using the physical mixture of the catalyst components is the arduous separation TiO<sub>2</sub> from the water samples and also the difficulty in mixing the RGO with water sample. Therefore, the 10%RGO/TiO<sub>2</sub>/ZSM-5 is a potential appropriate catalyst in wastewater dye treatment due to easy post-separating and mixing with water particularly in the combined composite catalyst form.

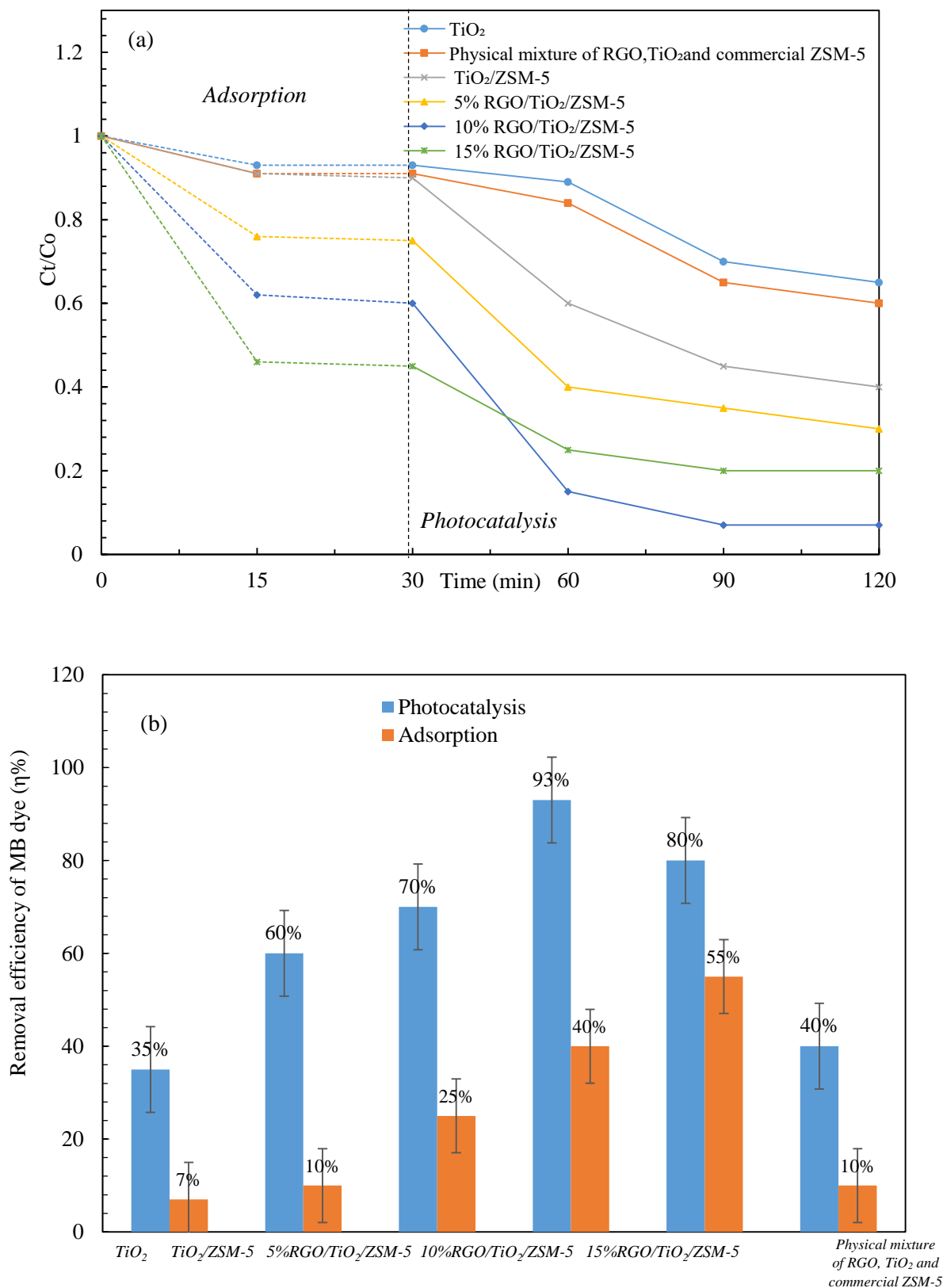


**Figure 5-5** (a) The plot of  $C_t/C_0$  versus time in the presence of photocatalyst under the solar light, the concentration of the catalysts were  $0.5 \text{ g L}^{-1}$  and a solar exposure time of 120 min (b) removal efficiency of different catalysts for adsorption and photo-degradation regions

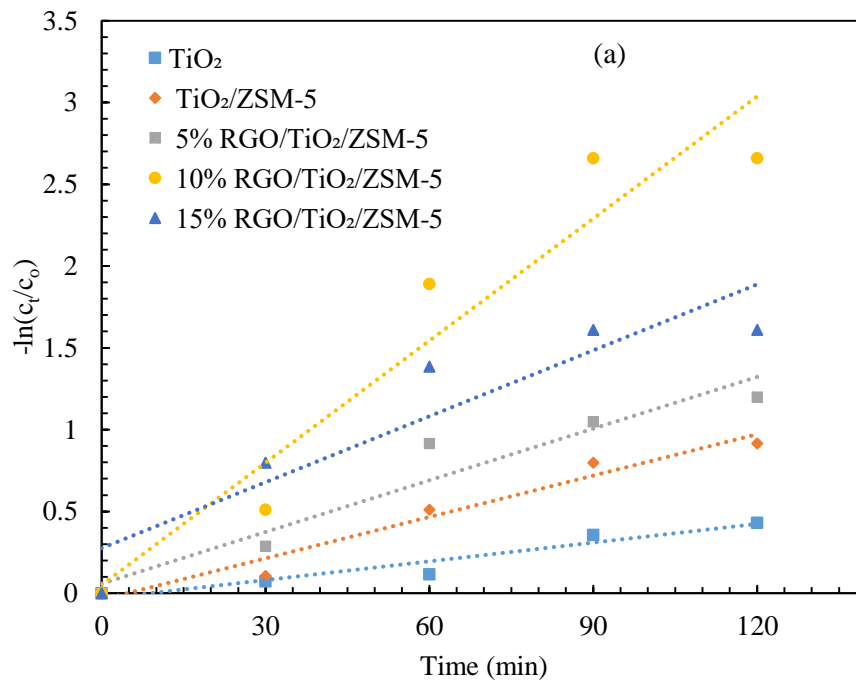


### 5.3.3 Kinetic studies

To evaluate the kinetic models, pseudo-first and second order adsorption models were studied based on the highest correlation coefficient R<sup>2</sup> value. The pseudo first order adsorption model as described by Langmuir-Hinshelwood kinetic model. Chong et al. found that the Langmuir-Hinshelwood model could be simplified when the KC-value is less than 1 to pseudo-first order kinetic model as given in Eq. (5.3) (Chong et al., 2010).

$$\ln\left(\frac{C_0}{C}\right) = k \cdot K \cdot t = k_{app} \cdot t \quad (5.3)$$

Where k is the reaction rate constant, K is the dynamic Langmuir adsorption constant, C is the dye concentration and k<sub>app</sub> is the obvious pseudo-first order reaction rate constant.



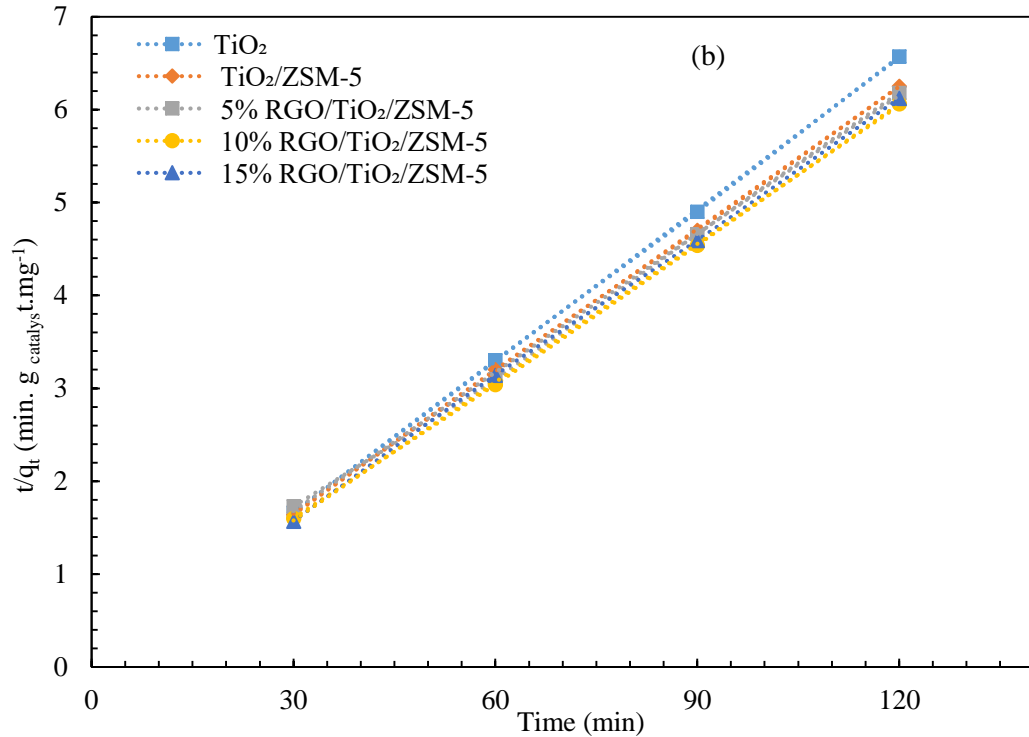


**Figure 5-6** (a) Pseudo first-order kinetic plots (b) Pseudo second-order kinetic plots for the 10 mg L<sup>-1</sup> MB dye concentration using different catalyst

The plot  $\ln(C_0/C)$  versus  $t$  for adsorption and photo-degradation of MB by different catalysts described a linear behaviour as shown in Figure 5.6a.

The experimental data were also analysed with pseudo-second order model, using the linear equation (5.4)

$$\frac{t}{q_t} = \frac{1}{k_{2\text{ MB}} \cdot q_e^2} + \frac{1}{q_e \cdot t} \quad (5.4)$$

where  $k_2$  is the reaction rate constant for pseudo-second order model,  $q_e$  is the amount of MB at equilibrium and  $q_t$  is the amount of MB adsorbed and photodegraded at time  $t$ . The plot  $t/q_t$  versus  $t$  for adsorption and photo-degradation of MB by different catalysts described a linear behaviour as shown in Figure 5.6b. The values of the correlation coefficients  $R^2$  indicated a better fit of pseudo-second order model for all used catalyst regardless of the concentration of MB dye as illustrated in table 5.2. In the present work, the  $q_e$  and  $k_2$  values ( see Table 5.2) are estimated for different concentrations of MB i.e. 10, 20, 30, 40 mg L<sup>-1</sup> using the linear equation of  $(t/q_t) = f(t)$  as depicted in Figure 5.6b for MB 10 mg L<sup>-1</sup> concentration only (slope for 20, 30, 40 mg L<sup>-1</sup> are not shown). It appears from table 5.2 that the removal efficiency of MB

dye using 10%RGO/TiO<sub>2</sub>/ZSM-5 mesoporous remained at a high value to be 70% even after using high concentration of MB dye of 40 mg L<sup>-1</sup>.

**Table 5-2** Parameters of pseudo first order and second order kinetic models with the removal efficiency

Catalysts	MB dye concentration mg L <sup>-1</sup>	Removal efficiency (%)	Pseudo first order reaction rate		Pseudo second order reaction rate		q <sub>e</sub> mg/gm catalyst
			K <sub>app</sub> (min <sup>-1</sup> )× 10 <sup>-3</sup>	R <sup>2</sup>	K <sub>2</sub> (g/mg. min)	R <sup>2</sup>	
TiO <sub>2</sub>	10	35%	3.818	0.9315	0.1141	0.9994	20.31
	20	30%	2.883	0.922	0.1354	0.9992	24.46
	30	27%	2.334	0.990	0.1671	0.9996	30.25
	40	25%	1.9523	0.9732	0.1822	0.9987	33.81
TiO <sub>2</sub> /ZSM-5	10	60%	8.416	0.9628	0.0227	0.9993	19.56
	20	50%	5.866	0.9444	0.0038	0.9978	17.85
	30	45%	5.389	0.9408	0.00248	0.9961	28.98
	40	40%	3.704	0.7796	0.00357	0.9941	46.6
5% RGO/TiO <sub>2</sub> /ZSM-5	10	70%	10.54	0.927	0.013	0.9999	20.12
	20	64%	8.66	0.9217	0.00466	0.9974	12.56
	30	52%	6.715	0.852	0.0036	0.9848	25.2
	40	48%	4.816	0.7601	0.00321	0.9983	39.37
10% RGO/TiO <sub>2</sub> /ZSM-5	10	93%	24.89	0.9202	0.027	0.9999	20.16
	20	82%	14.16	0.8989	0.00944	0.9957	6.1
	30	78%	12.55	0.8993	0.00426	0.995	10.71
	40	70%	8.77	0.6386	0.00396	0.9985	22
15% RGO/TiO <sub>2</sub> /ZSM-5	10	80%	13.43	0.8549	0.0316	0.9998	19.88
	20	72%	12.7	0.817	0.00784	0.9967	10
	30	70%	9.379	0.7949	0.00457	0.9795	15.8
	40	56%	5.751	0.7178	0.005	0.9966	33.85

### 5.3.4 Decolourisation of the MB dye

To investigate the decolourization activity, 0.5 g L<sup>-1</sup> of 10% RGO/TiO<sub>2</sub>/ZSM-5 mesoporous was added to water samples containing various MB dye concentrations (10, 20, 30, 40 mg L<sup>-1</sup>) under constant stirring condition. The photodecomposition was characterized by UV–vis spectroscopic spectra at λ =664 nm versus time, which

revealed one major band of maximum adsorption in the visible region at 664 nm with a small shoulder band at 615 nm which is due to dye dimer (Machado et al., 2003; Yogi et al., 2008), and another small band in the ultraviolet region at 326 nm (see Appendix A-1, Figure A.1). The absorbance at 664 nm was due to the conjunction between the atoms of nitrogen and sulphur present in aromatic rings, whilst the small shoulder at 615 nm was reported to be as a result of the absorbance by the dye dimer. However, the aromatic benzene rings have their absorption band in the ultraviolet region at 326 nm (Rauf, Meetani, Khaleel, & Ahmed, 2010). It was observed that wide absorption peaks at 664 nm in the different concentrations of MB were quickly diminished after treating the MB solutions with 10% RGO/TiO<sub>2</sub>/ZSM-5. The small visible band at 615 nm was also gradually diminished at the same time. The concentration of MB was plotted against time as shown in Figure 5.7. This demonstration reveals that MB dye decolourization is very effective when treated with 10% RGO/TiO<sub>2</sub>/ZSM-5 under solar light irradiation for 120 min; the removal efficiency achieved are 93% of 10 mg L<sup>-1</sup>, 82% of 20 mg L<sup>-1</sup>, 78% of 30 mg L<sup>-1</sup> and 70% of 40 mg L<sup>-1</sup> of MB.

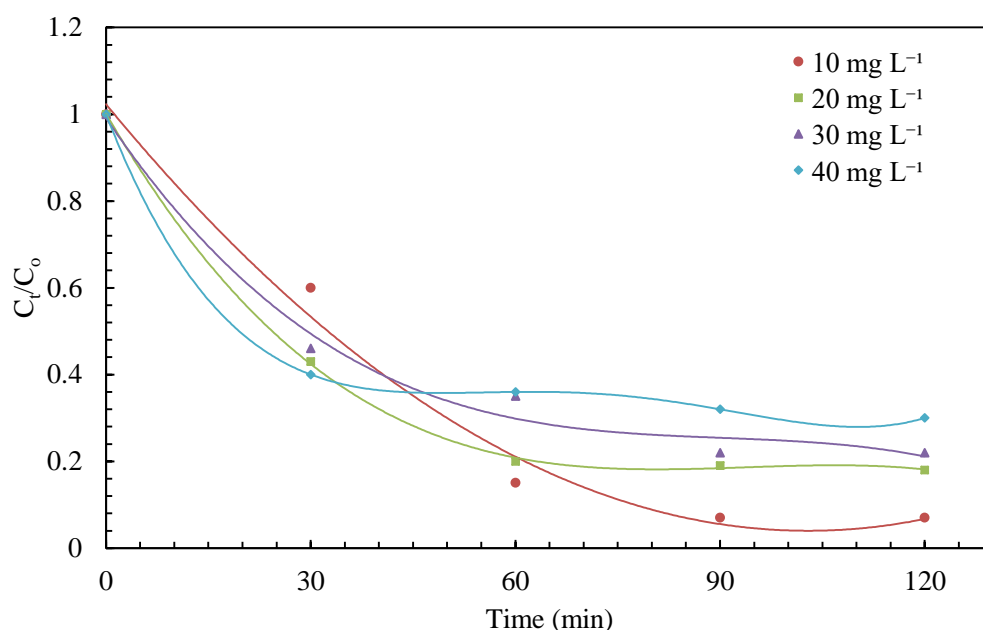


**Figure 5-7** decolonization of various concentrations of MB dye versus time

### 5.3.5 The mineralization of MB dye

The total organic carbon (TOC) removal efficiency was studied using different of the catalysts including 5% RGO/TiO<sub>2</sub>/ZSM-5, 10%RGO/TiO<sub>2</sub>/ZSM-5, 15% RGO/TiO<sub>2</sub>/ZSM-5, TiO<sub>2</sub>/ZSM-5 and TiO<sub>2</sub> at initial MB dye concentration of 10 mg

L<sup>-1</sup> for 120 min as shown in Figure 5.8. The results reveal that the removal efficiency of the TOC after 120 min under solar light irradiation increased from 65% using only TiO<sub>2</sub>/ZSM-5 mesoporous to 85% using 10% RGO/TiO<sub>2</sub>/ZSM-5 mesoporous. This finding shows that RGO nano-sheets play an important role in the composite catalyst, and this is reflected in the high adsorbability and activation sites on the surface of RGO, reduced electron/hole pair recombination and the possibility of  $\pi$ - $\pi$  interactions between RGO and intermediate organic compounds (Andreozzi et al., 2018; Pawar, Khare, & Lee, 2014; X. Wang et al., 2012). However, increase wt % of RGO up to 15% in the composite catalyst again reduced the TOC removal efficiency to 75% due to opacity of the solution, thus preventing proper penetration of solar light into the aqueous solution. This concluded that the synthesized 10% RGO/TiO<sub>2</sub>/ZSM-5 exhibited a synergistic effect of both adsorption and photocatalysis processes, thus rapidly reducing TOC content in the aqueous media.

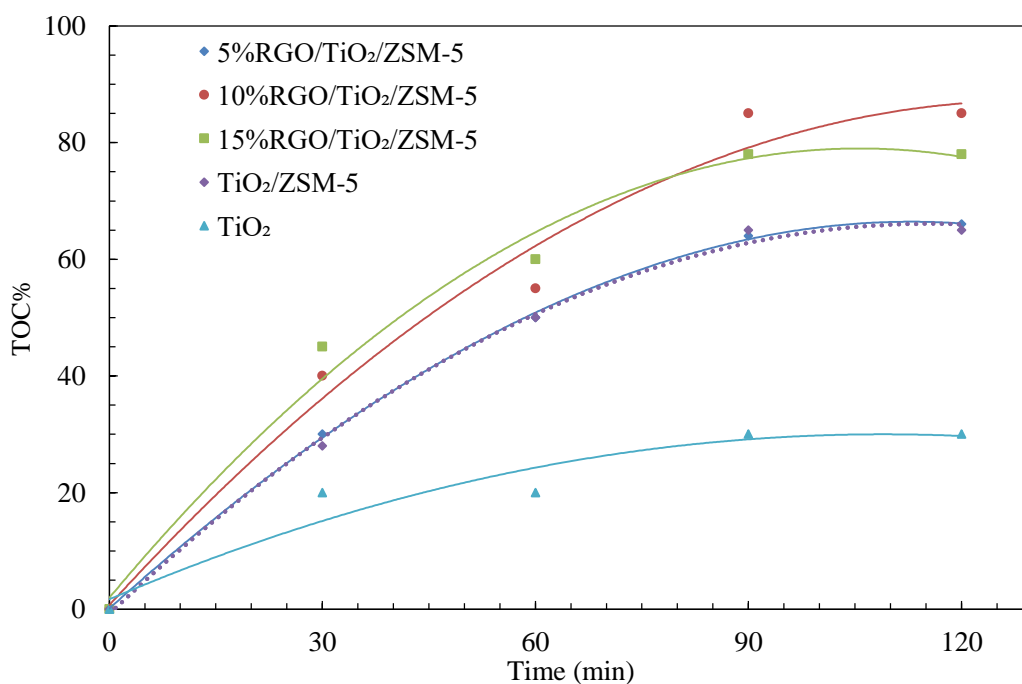


**Figure 5-8** the removal efficiency of TOC using different types of the catalysts 0.5 g L<sup>-1</sup> concentration at initial MB dye concentration is 10 mg L<sup>-1</sup>

### 5.3.6 Intermediates and mineralization of MB dye

The intermediate compounds of the 10 mg L<sup>-1</sup> MB dye after 120 min of photocatalytic degradation were analysed by the HPLC using 0.5 g L<sup>-1</sup> of 10% RGO/TiO<sub>2</sub>/ZSM-5 mesoporous. The estimated concentration of MB and two intermediate compounds of degradation were observed and plotted in Figure 5.9 (see also the calibration curves in Appendix B, Figure B.3). To identify the intermediate compounds, the demethylation

pathway for possible degradation of MB molecule as reported by Rauf et al, (Rauf et al., 2010) shown in Figure 5.10. In this pathway, the anticipated cleavage happens in one or more methyl groups presented as amine groups. The main peaks of the intermediate such as azure (A) and thionin were identified by the HPLC; see diagram as shown in Appendix B, Figure B.1. The demethylation process may also be continued to further destroy the structure of thionin by self-cleavage of the amine groups (see Figure 5.10).

With further oxidation, these complex compounds are broken until all aromatic rings are shatter and escaped as CO<sub>2</sub>, H<sub>2</sub>O, SO<sub>4</sub>, and NH<sub>4</sub> gases. The mineralization experimental data revealed that 10%RGO/TiO<sub>2</sub>/ZSM-5 not only successfully decolorized MB dye, but also resulted into a significant mineralization of the intermediate, converted to nonhazardous compounds.

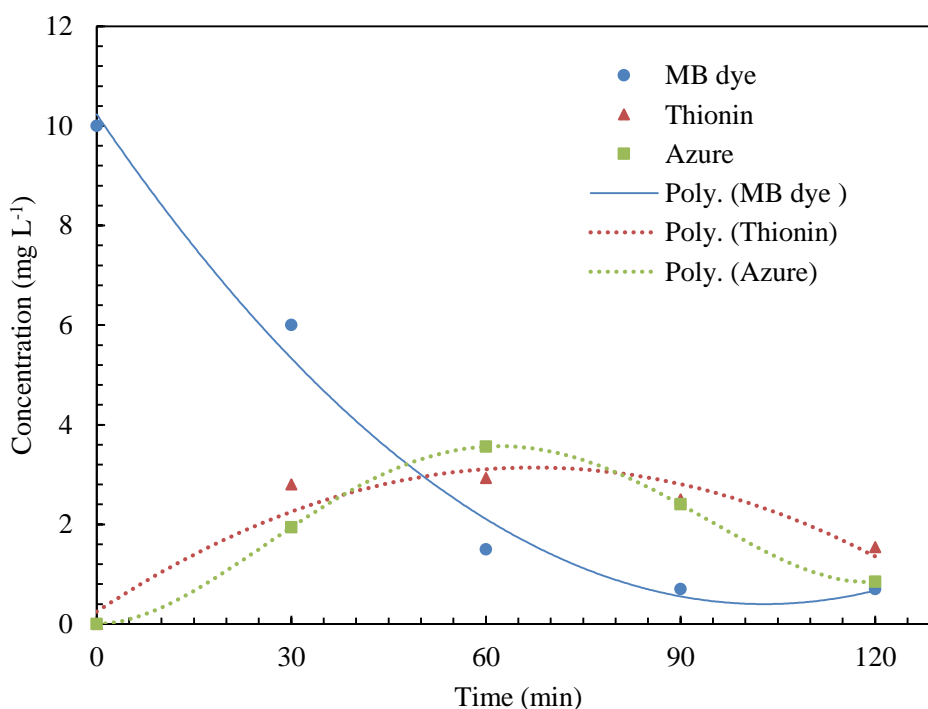


**Figure 5-9** HPLC profile of MB dye before and after photocatalytic degradation

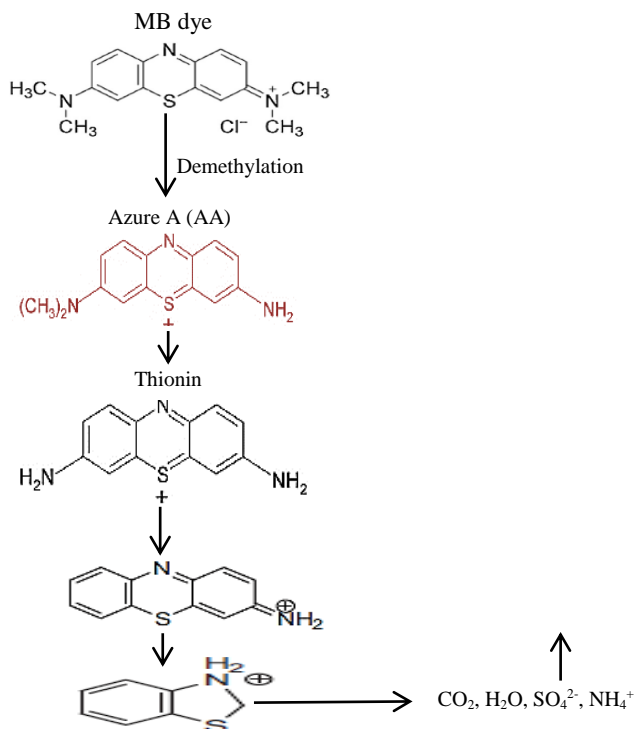


**Figure 5-10** Proposed pathways for photocatalytic degradation of MB dye solution

### 5.3.7 Stability and regeneration

In this section, the stability and regeneration of 10% RGO/TiO<sub>2</sub>/ZSM-5 mesoporous photocatalyst was studied for five cycles at optimum conditions using 10 mg L<sup>-1</sup> of MB dye. After use the suspension which consist of the catalyst and decolourized MB was centrifuged, filtered and washed with deionized water several times, thereafter the filtrate and dried at 100 °C for 1 h, followed a calcination at 300°C for 3 h to remove the organic compounds from the catalyst surface. The above steps were repeatedly done for each cycle, and the removal efficiency for the reused catalyst after each cycle was shown in Figure 5.11. The data reveals only a slight reduction in the degradation efficiency (85%) is obtained after the end of the fifth cycle, suggesting that TiO<sub>2</sub> particles may be slightly leached from the synthesized catalyst. Previous details shows that, the plate-like or slit shaped mesopores (discussed in section 5.3.1.2) are seriously sealed with TiO<sub>2</sub> particles as a result of the availability of the silanol groups (Si-OH) in the silica zeolite structure with considerable surface active sites (López-Muñoz, van Grieken, Aguado, & Marugán, 2005; W. Wang & Song, 2006) as depicted in Figure 5.11.

To investigate the effect of mesoporosity structure in the composite catalyst, 10% RGO/TiO<sub>2</sub>/ZSM-5 non-mesoporous composite was prepared with slight modification

as a mentioned in section 5.2.2 for testing the solar photocatalytic degradation of 10 mg L<sup>-1</sup> of MB dye concentration at the fifth cycles. The specific surface area and pore size distribution of the 10%RGO/TiO<sub>2</sub>/ZSM-5 non-mesoporous was evaluated and illustrated in Appendix A-1, Figure A.2.

The result revealed that the removal degradation efficiency was highly reduced to 60 % using non- mesoporous of 10%RGO/TiO<sub>2</sub>/ZSM-5, suggesting that the mesoporosity was enhanced thereby reducing the durability and regeneration of the used catalyst. Based on this finding, it could be anticipated that the 10% RGO/TiO<sub>2</sub>/ZSM-5 mesoporous is a durable morphology, used up to 5 cycles without significant reducing in the capability, this makes it highly recommended for application in large scale MB dye treatment.

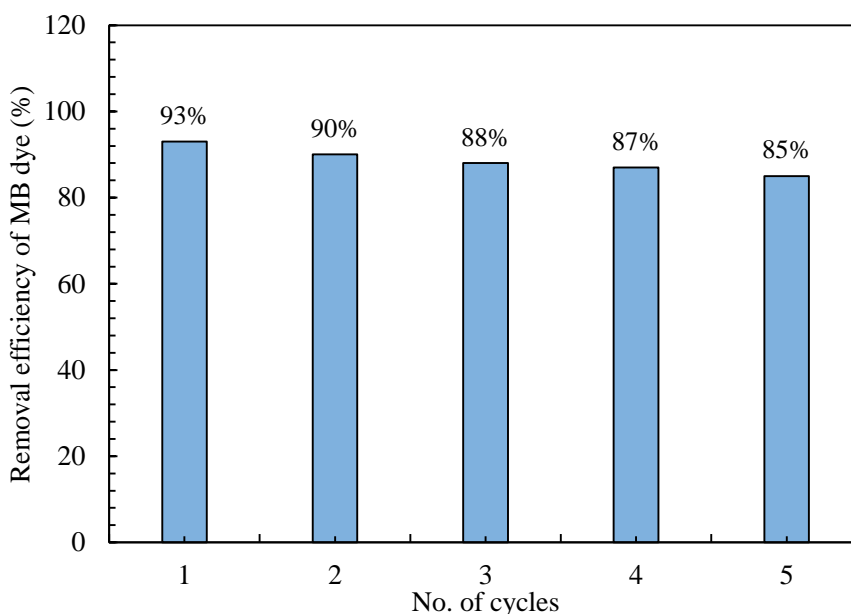


**Figure 5-11** the regeneration efficiency of 10%RGO/TiO<sub>2</sub>/ZSM-5 mesoporous after a number of cycles

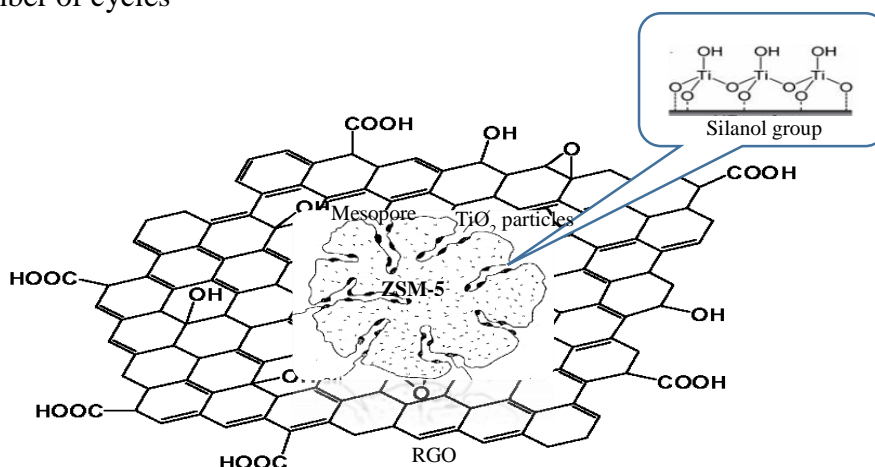


**Figure 5-12** the proposed mesoporosity effects on the TiO<sub>2</sub> particles



### 5.4 Summary

This study was undertaken to synthesize a nano composite of TiO<sub>2</sub>/ZSM-5 mesoporous and to evaluate the adsorption/solar photocatalytic activity on addition of different wt % of reduced graphene oxide (RGO) in the synthesized nanocomposite mesoporous catalyst. The pseudo first and second order kinetic degradation models, post-separation, mesoporosity, TOC% and reusability of the synthesized catalysts were then assessed. Different concentrations of methylene blue dye (MB) such as 10, 20, 30, 40 mg L<sup>-1</sup> were used for the investigation. Based on the results, it was observed that the 10% wt RGO in the composite of TiO<sub>2</sub>/ZSM-5 mesoporous significantly boosted the photocatalytic activity, enhanced the adsorption ability and the charge separation with extensive electron transfer to the carbon-based nano-sheets. Analysis of the FESEM images and EDX showed that TiO<sub>2</sub> crystallites and ZSM-5 mesoporous were present on the RGO nano-sheets. The data also reveal that the mesoporosity enhanced the stability of the used catalyst and only a slight significant lose in the removal efficiency (85%) of the catalyst activity during the regeneration process after the fifth cycles was noticed. It was also shown that the intermediate compounds which consist of Azura (A) and Thionin were significantly mineralized to non-hazardous compounds. This novel hybrid synthesized mesoporous RGO supported catalyst would therefore pave new development of multifunctional catalyst for water treatment of environmental applications.

## CHAPTER 6

# 6

### **A ligand anchored conjugate adsorbent for effective mercury (II) detection and removal from aqueous media**

#### **6.1 Introduction**

The previous chapters of this dissertation have discussed solar photocatalytic degradation of organic refractory pollutants using advanced oxidation process (AOP). However, Rapid developments in industries in many countries have also been brought out a serious environmental problem such as inorganic heavy metal ions effluent in water bodies (H. Chen, Li, Shao, Ren, & Wang, 2012; Ngomsik et al., 2009; Riaz, Nadeem, Hanif, & Ansari, 2009; Zein, Suhaili, Earnestly, & Munaf, 2010). The AOP is not sufficient to remove the risk of heavy metal ions from water bodies. Therefore, synthesis a visual adsorption catalyst is an alternative process that has studied in this chapter, suggesting the mercury ions is as a toxic target. Mercury (Hg (II)) ions is considered one of the most ubiquitous and dangerous heavy metal in water bodies. The Hg (II) ranks sixth among the most toxic chemicals in the list of hazardous compounds. The industrial activities such as the production of chlorine and caustic soda and electrical applications such as lamps, arc rectifiers and mercury cells as sources of Hg (II) caused serious human health risks when it is discharged into water bodies. The toxicological and carcinogenic effects of even ultra-trace Hg (II) ions (permissible level:  $1\mu\text{g L}^{-1}$  to  $10\mu\text{g L}^{-1}$ ) can destroy the central nervous system and possible death

(Clarkson & Magos, 2006). The Hg (II) impairs pulmonary function, as well as to induce dyspnoea and chest pain (Methylmercury, 1990). Nevertheless, the monitoring efforts by government agencies have been mainly focused on fish and marine mammals, where Hg (II) ion remain high contaminated risk product mainly in aquatic livings (Hylander & Goodsite, 2006; Von Burg, 1995). The Hg (II) ions also causes human chromosome breakage, as well as genetic defects with cell division, thus resulting in an abnormal chromosome distribution. Therefore, fabricating a selective and rapid removing Hg (II) ions pollutant to purify a raw water source is significant for health and critically needed to overcome impact the global water crisis. This technology should be affordable to the majority of the world's population (S. El-Safty, Shahat, Awual, & Mekawy, 2011; S. A. El-Safty, Awual, Shenashen, & Shahat, 2013; S. A. El-Safty, Shahat, & Awual, 2011; S. A. El-Safty, Shenashen, et al., 2013).

Various analysis equipment have been reported for Hg (II) ions detection, including ICP-MS, ICP-AES, fluorescence spectroscopy, chemiluminescence and neutron activation analysis (Arshad et al., 2017; Awual, 2017b; Awual, Hasan, Eldesoky, et al., 2016; Kamath et al., 2012; B. Li et al., 2006; Naushad et al., 2015; Sakamoto-Arnold & Johnson, 1987; Sheikh et al., 2017; Souza & Tarley, 2009; Zi et al., 2014). Although, these methods are accurate for Hg (II) ions detection, they have the disadvantages of complex operational procedures, involving a large infrastructure backup and high cost. Therefore, a simple, selective, sensitive, and rapid detection of Hg (II) ions is extremely demanding for routine analysis. Optical sensors for Hg (II) ion detection have been developed using chromophores, fluorophores, functionalized polymers, graphene, proteins, and nano-bio-modified nanoparticles (Kim, Kim, Park, & Chang, 2006; Lee, Han, & Mirkin, 2007; Yuling Li, Zhou, Liu, & Li, 2012; Nazeeruddin, Di Censo, Humphry-Baker, & Grätzel, 2006; Tian et al., 2011). The direct detection of ultra-trace Hg (II) ions still seems to be difficult due to the low selectivity and sensitivity of these methods and even it cannot be detected visually. Therefore, a functional ligand anchored mesoporous materials are excellent tools for visual inspection of Hg (II) ions in aqueous solutions, allowing eco-friendly method (Awual, 2016a, 2016c, 2017a; Awual, Alharthi, Hasan, et al., 2017; Awual, Hasan, Naushad, Shiwaku, & Yaita, 2015; Awual, Hasan, & Znad, 2015; Awual, Khaleque, et al., 2015; Awual, Yaita, & Okamoto, 2014; Singhal, Singh, & Upadhyay, 2014).

Recently, different ligands were successfully embedded in nanomaterial matrices and have been reported for various metal ion detection with high selectivity and sensitivity under mild conditions (Awual, 2016b; Awual, Alharthi, Okamoto, et al., 2017; Awual, Hasan, Ihara, & Yaita, 2014; Awual, Hasan, & Khaleque, 2015; Awual, Hasan, Shahat, et al., 2015; Awual, Miyazaki, Taguchi, Shiwaku, & Yaita, 2016; Awual, Suzuki, et al., 2014; Awual, Yaita, Taguchi, et al., 2014). Moreover, these are high mechanical stabled, cost effective, high adsorption capacity, reusability, high specific surface area, ease to use, and would be exhibited potential application in large-scale operation based on a real sample treatment.

A variety of treatment technologies have been developed during the past decade to remove the Hg(II) ions from large volumes of aqueous solution such as oxidation, chemical precipitation, ion-exchange, electrochemical operation, floatation, membrane electrolysis, liquid-liquid extraction and adsorption (Arshadi, Mousavinia, Khalafi-Nezhad, Firouzabadi, & Abbaspourrad, 2017; Awad, AbouZeid, El-Maaty, El-Wakil, & El-Shall, 2017; Duman & Ayranci, 2010; Ritchie & Bhattacharyya, 2002; Tuzen, Sari, Mendil, & Soylak, 2009; H. Zhu et al., 2017). However, many of them have been found drawbacks such as weak chemical affinity, low adsorption capacity, time consuming, requiring rigorous conditions such as carbonate free environments, and producing large secondary wastes. Thereupon, adsorption technology has emerged as one of the most effective alternative methods for removing heavy metal ions from aqueous solution. Different materials have been utilized as adsorbents such as clay minerals, coal, chitosan, iron oxide nanomaterials, and zeolite (Awual, Eldesoky, et al., 2015; Awual & Hasan, 2014a; Awual, Rahman, Yaita, Khaleque, & Ferdows, 2014; Havelcova, Mizera, Sýkorová, & Pekař, 2009; Shahat, Awual, Khaleque, et al., 2015), but they still have limited practical application due to these materials could not have particularly distinguished by bare eye and lower absorption capacity. Therefore, a ligand scaffold mesoporous materials exhibit excellent properties such as the enable visual adsorbent by colour changes that depend on Hg (II) ions concentrations in water bodies.

Several studies have been reported using the direct template method to synthesized sensitive adsorbents and utilized tetraethylorthosilicate (TEOS) or tetramethyorthosilicate (TMOS) as precursors for a silica source that is used as a template of mesoporous materials (Awual & Ismael, 2014; Md Rabiul Awual,

Mohamed Ismael, et al., 2013; Md Rabiul Awual, Tsuyoshi Yaita, Sherif A El-Safty, Hideaki Shiwaku, Yoshihiro Okamoto, et al., 2013; Awual, Yaita, & Shiwaku, 2013; M. Shenashen et al., 2013). These precursors with direct template method have been provided surface area which is almost  $900 \text{ m}^2 \text{ g}^{-1}$  (Md Rabiul Awual, Tohru Kobayashi, Hideaki Shiwaku, et al., 2013; Md Rabiul Awual, Tsuyoshi Yaita, Sherif A El-Safty, Hideaki Shiwaku, Shinichi Suzuki, et al., 2013; Awual, Yaita, Shiwaku, & Suzuki, 2015; Shahat et al., 2018). While, other researchers have been synthesized thiol-functionalized MCM-41/or SBA-15 phases as a template and silica source which are high affinity for Hg (II) ions as well as capable adsorption of divers metal ions by amino-functionalized materials (A. Liu, Hidajat, Kawi, & Zhao, 2000; Mercier & Pinnavaia, 1998). Moreover, ordered mesoporous silica MCM-41/48 materials grafted with amine or thiol groups were successfully constructed for Hg (II) and Cu (II) ions (Walcarius, Etienne, & Lebeau, 2003). The specific surface area of these functionalized groups was  $818 \text{ m}^2 \text{ g}^{-1}$ . However, these functional groups have no capability to recognize Hg (II) ions by visual detection, which is an important aspect of routine analysis. Therefore, synthesis a suitable ligand that is immobilized successfully onto mesoporous materials with high specific surface area, visual inspection capability and ease separation after treatment of aqueous solution is the key challenges of this study.

The objective of this study was to develop an adsorbent based on a ligand scaffold with high surface area mesoporous material for the selective detection and removal of Hg (II) ions from aqueous solution. The novel ligand of 2-hydroxyacetophenone-<sup>4</sup>N-pyrrolidine thiosemicarbazones (HAPT) was synthesized and successfully immobilized onto the highly ordered mesoporous silica such as zeolite type ZSM-5 (relatively high stability of framework, highly porous aluminosilicate with high silica/alumina ratio and hydrophobic material) by the direct template method. It is noted that HAPT was associated onto the ZSM-5 by non-specific interaction via hydrogen bonding, Vander Waals forces and reversible covalent bonds (Md Rabiul Awual, Tohru Kobayashi, Hideaki Shiwaku, et al., 2013; Awual, Yaita, Shiwaku, et al., 2015; Shahat et al., 2018). The Hg (II) ions detection was performed on colorimetric sensing methods without significant interference from foreign competing ions. Moreover, the Hg(II) ions recognition and removal parameters such as solution

pH, colour optimization, limit of detection, contact time, adsorption capacity, initial concentration, regeneration and reuse were optimized and evaluated.

## 6.2 Experimental work

### 6.2.1 Chemicals

All chemicals were analytical graded and used without further purification. Zeolite type of ZSM-5 (Molar ratio  $\text{SiO}_2/\text{Al}_2\text{O}_3 = 600$ ,  $300 \text{ m}^2 \text{ g}^{-1}$  specific surface area,  $2\text{--}3 \mu\text{m}$  particle size,  $0.5 \text{ nm}$  pore size) was provided from ACROS Organics, A Thermo Fisher Scientific Brand, New Jersey–USA. The triblock copolymers of ethylene oxide-block-poly (propylene oxide) block-poly (ethylene oxide) designed as  $\text{EO}_{20}\text{PO}_{70}\text{EO}_{20}$  ( $\text{P}_{123}$ ) & 1, 3,5-triisopropylbenzene (TIPB) were obtained from Sigma-Aldrich. The standard Hg (II) ions solution ( $1000 \mu\text{g L}^{-1}$ ) was supplied by High-Purity Standards Company, Australia. Ultra-pure water was used throughout in this work to prepare all the aqueous solutions.

### 6.2.2 Synthesis of 2-hydroxyacetophenone-<sup>4</sup>N –pyrrolidine

#### thiosemicarbazones (HAPT) ligand

As mentioned in chapter 3 section 3.3.3.2, the synthesis procedure was conducted with slight modification of previous studies (Scovill, 1991; Sivakumar & Prathapachandra Kurup, 2002). The pale yellow rods desired organic ligand crystals were obtained and washed with methanol for further purification (see Appendix A-1, Figure 1.3).

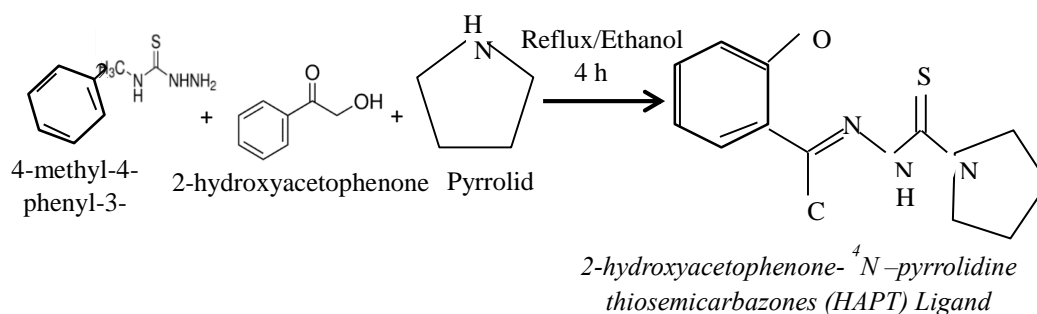


**Figure 6-1** the chemical reaction steps of synthesized 2-hydroxyacetophenone-<sup>4</sup>N –pyrrolidine thiosemicarbazones (HAPT) Ligand

### **6.2.3 Synthesis of mesoporous silica and mesoporous-conjugate adsorbent**

#### **(MCA)**

As mentioned in chapter 3, section 3.3.3.1 and 3.3.3.3, the direct-templating method with a modification of an instantly preformed liquid crystal phase was used to fabricate translucent mesoporous silica (ZSM-5) and surfactant monolithic of mesoporous materials (G. Zhou et al., 2007) . Briefly, 1g of triblock copolymers (P<sub>123</sub>) was mixed with deionized water and HCl. Following this, 0.85 g TIPB was added to solution dropwise at mass ratio of 0.85:1 (TIPB: P<sub>123</sub>). Subsequently, 2 g of ZSM5 was added directly to the solution under vigorous magnetic stirring. The MCA adsorbent was fabricated via direct immobilization method using 50 mg of the prepared HAPT dissolved in ethanol solution along with 1g of ZSM-5 mesoporous. The ligand immobilization amount (0.775 mmol g<sup>-1</sup>) was calculated by the following equation:

$$q = (C_0 - C)V / m \quad (6.1)$$

Where Q is the adsorbed amount (mmol g<sup>-1</sup>), V is the solution volume (L), m is the mass of MCA (g), C<sub>0</sub> and C were the initial concentration and supernatant concentration of the ligand, respectively.

### **6.2.4 Characterization of MCA**

The crystalline phases of samples were analysed by XRD using a Bruker D<sub>8</sub> diffractometer. The specific surface area was measured based on the N<sub>2</sub> adsorption-desorption isotherms according to the Brunnauer Emmett-Teller (BET, Micromeritics, Tristar II Surface area and Porosity) equation and the pore size distributions were derived from the adsorption of isotherms by using the Barrett–Joyner–Halenda (BJH) model. To detect the Hg (II) ions colour form, UV–Vis/spectrophotometer was used. Field emission scanning electron microscope (FESEM) measurements were carried out with MIRA3TESCAN high vacuum mode microscope. Fourier-transformed infrared (FTIR) spectroscopy was conducted to determine the functional groups of the ligand. The Hg (II) ions concentrations were measured by ICP-AES instrument (Perkin Elmer 8300).

### 6.2.5 Determination of Hg (II) ions

As mentioned in chapter 3, section (3.5.2.1), 10 mg of MCA was immersed in a 2.0 mg L<sup>-1</sup> Hg (II) ions concentration. The mixture was adjusted at appropriate pH of 2.0, 4.3, 6.2, 9.4, 11.1, 12.5, and 12.8 at constant volume. These mixtures were shaken in a temperature controlled water bath at constant agitation speed of 200 rpm to achieve good peak colour intensity. After colour optimization, the mixtures were then applied to quantitative estimation of Hg (II) ions by colour assessment and absorbance measurements via UV-spectrophotometer. The filtrated MCA was grinded to fine powder due to achieve homogeneity in the absorbance spectra. The limit of Hg (II) ions detection was determined using the linear part of the calibration plot according to Eq. (6.2) (Awual & Hasan, 2014b, 2015a, 2015b; Awual, Yaita, Suzuki, & Shiwaku, 2015):

$$LD = \frac{KS_b}{m} \quad (6.2)$$

where K is the confidence factor and equal to 3, S<sub>b</sub> is the standard deviation for the blank and m the slope of the calibration graph in the linear range, respectively.

### 6.2.6 Hg (II) ions removal, regeneration and reuses

In the case of optical removal experiments, 20 mg of MCA was immersed in a solution of different Hg (II) ions concentrations. The pH was adjusted at a specific value by adding 0.2 M KCl and HCl 100 ml of the solution at room temperature for 120 min agitation at speed 250 rpm. Then, the MCA was separated by vacuum filtration suction system. Following this, Hg (II) ions concentrations before and after adsorption were analysed by ICP-AES. The amount of adsorbed Hg (II) ions was calculated according to the following equations:

$$\text{Mass balance } q_e = (C_o - C_f) V/M \text{ (mg/g)} \quad (6.3)$$

$$\text{and Hg (II) ions removal efficiency } R = \frac{(C_o - C_t)}{C_o} \times 100\% \quad (6.4)$$

where V is the volume of the aqueous solution (L), and M is the weight of MCA catalyst (g), C<sub>o</sub> and C<sub>f</sub> are the initial and final concentrations of Hg (II) ions in solution, respectively. To evaluate the kinetics performances, 20 mg of MCA was added to 100



ml solution containing  $2.0 \text{ mg L}^{-1}$  concentrations of Hg (II). Thereafter, the mixture was stirred, and the samples were filtrated at each 20 min intervals and analysed the filtrate solution via ICP-AES. The maximum removal capacity was also studied by using  $20 \text{ mg L}^{-1}$  of MCA in different concentrations of Hg (II) ions and stirred at 700 rpm for 2h and the filtrate solutions were analysed by ICP-AES.

To determine the regeneration, an eluting agent of the MCA, firstly, the Hg(II) ions was adsorbed by mesoporous-conjugate adsorbent (MCA), and then washed with ultra-pure water, or stripping agents such as  $\text{H}_2\text{SO}_4$ , HCl or thiourea-HCl (Awual, Khaleque, Ferdows, Chowdhury, & Yaita, 2013; S. A. El-Safty, Shenashen, Ismael, et al., 2012) several times and kept in 50 ml conical flask. The filtrate solution was also analysed by ICP-AES. In this study, the suitable elution agent was 3 ml of 0.10 M thiourea- 0.10 M HCl and the mixture was stirred for 15 min. After the elution process, the MCA was simultaneously regenerated into the initial state and was ready to use for the next experiment after rinsing with ultra-pure water. The MCA was regenerated for several cycles to improve the long term use as a cost-effective adsorbent. All demonstrations in this study were duplicated to confirm the cohesion and recurrence of the results.

### 6.2.7 Influence of co-existing ions

The Hg (II) ions removal from mixture solution containing foreign ions onto the MCA was checked and the competitive adsorptions of diverse heavy metals are depicted. The solution was prepared with  $10 \text{ mg L}^{-1}$  in each of  $\text{Pb}^{2+}$ ,  $\text{Zn}^{2+}$ ,  $\text{Cd}^{2+}$ ,  $\text{Al}^{3+}$ ,  $\text{Fe}^{3+}$ ,  $\text{Mg}^{2+}$ ,  $\text{Ca}^{2+}$ ,  $\text{Ag}^+$ ,  $\text{K}^+$ ,  $\text{Na}^+$  ions and Hg (II) ions in  $2.0 \text{ mg L}^{-1}$  and adjusted the final solution volume was 50 ml. Thereafter, 20 mg of MCA was added and stirred for 2 h to assure complete removed of Hg (II) ions and the filtrate solution was checked by ICP-AES

## 6.3 Results and discussion

### 6.3.1 Characterizations

#### 6.3.1.1 BET specific surface areas and pore distribution

The specific surface area ( $S_{\text{BET}}$ ) and pore size distribution of commercial ZSM-5, ZSM-5 mesoporous and ZSM-5 mesoporous/HAPT (MCA) were determined based on  $\text{N}_2$  adsorption-desorption isotherms using the Barrett-Joyner-Halenda (BJH) method. Figure 6.2 (a–d), illustrated the  $\text{N}_2$  adsorption-desorption isotherms and BJH pore size

distribution of the samples. For comparison, the specific surface area, pore volume and average pore diameter results for the above catalysts are summarized in Table 6.1.

Table 6. 1 Specific surface area ( $S_{\text{BET}}$ ), pore volume (V) and average pore diameter (d) for commercial ZSM-5, ZSM-5mesopoures and ZSM-5mesopoures/HAPT

Catalysts	$S_{\text{BET}}$ ( $\text{cm}^2 \text{g}^{-1}$ ) <sup>a</sup>	V ( $\text{cm}^3 \text{g}^{-1}$ ) <sup>b</sup>	D (nm) <sup>c</sup>
Commercial ZSM-5	311	0.014	8.6
ZSM-5 mesoporous	1151	0.2	15.2
ZSM-5 mesoporous/HAPT	593	0.64	4.3

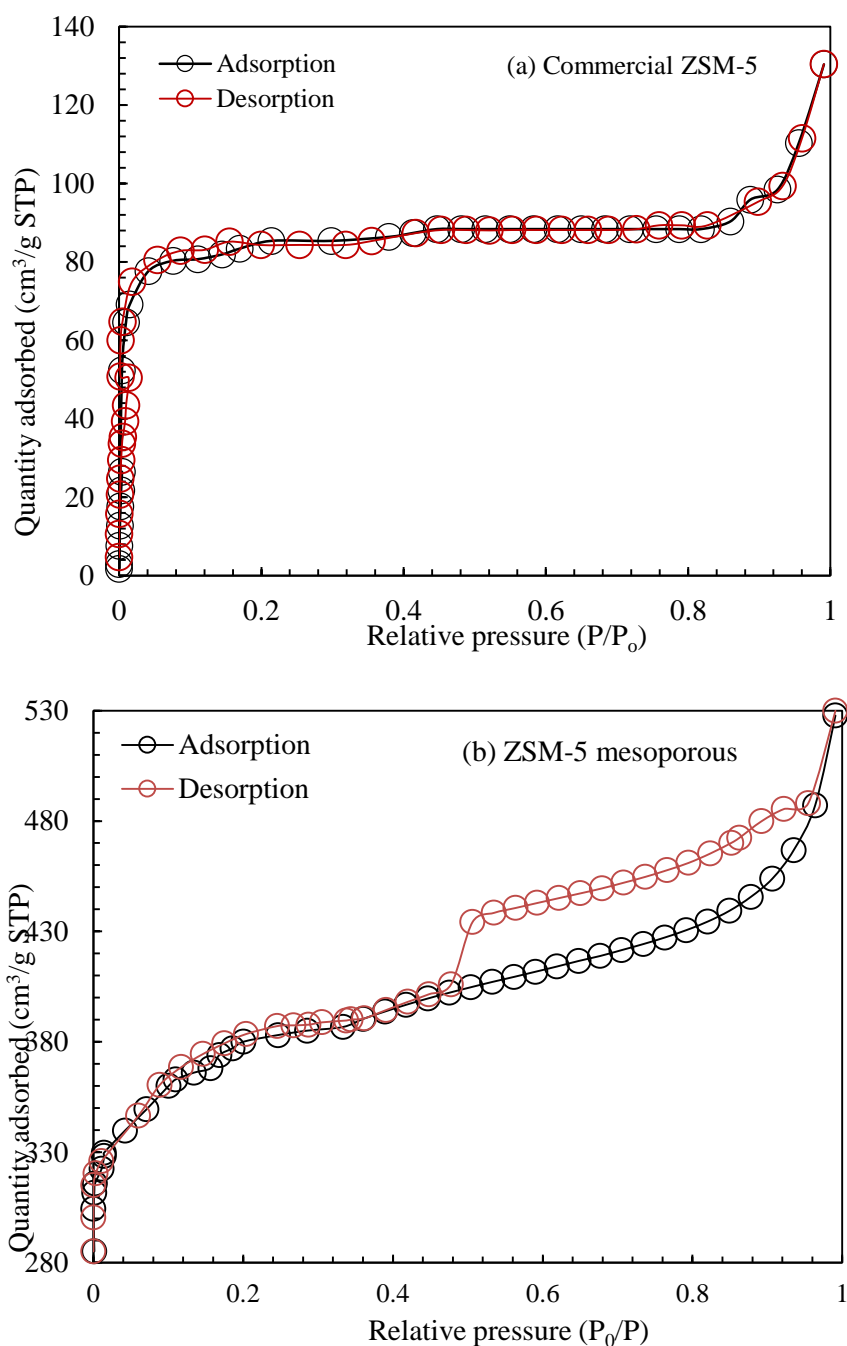
<sup>a</sup> The specific surface area was calculated by BET method.

<sup>b</sup> The pore volume was obtained from the BJH Desorption cumulative volume of pores between 1.0000nm and 50.0000nm diameter.

<sup>c</sup> The average pore diameter was estimated using the desorption branch of the isotherm and BJH model.

The adsorption isotherms of the commercial ZSM-5 is a type of I isotherm and exhibits an almost horizontal plateau starting at low relative pressure  $< 0.15$  (Valero-Romero et al., 2016), indicating that the porous morphology consist predominantly of very narrow micropores as shown in Figure 6.2a. Specific surface area and the pore diameter of commercial ZSM-5 were obtained to be  $311 \text{ m}^2 \text{ g}^{-1}$  and  $0.86 \text{ nm}$  (see Figure 6.2d). After the commercial ZSM-5 treatment, the isotherm ZSM-5 framework shape changes from type I to a clear type  $H_4$  hysteresis loops according to IUPAC classification. It was exhibited a hysteresis loop at  $P/P_0$  range (0.5–0.99). This hysteresis loop of ZSM-5 mesoporous was evidenced that the mesoporous structure highly presents in the sample as illustrated in Figure 6.2b (Valero-Romero et al., 2016). A high specific surface area and uniform pore diameter of ZSM-5 mesoporous were obtained to be  $1151 \text{ m}^2 \text{ g}^{-1}$  and  $15.2 \text{ nm}$  (see Figure 6.2d). The higher specific surface area of ZSM-5 mesoporous revealed type  $H_4$  hysteresis was not exhibit any limiting adsorption at high  $P/P_0$ , which is observed with non-rigid aggregates of plate-like particles giving rise to slit-shaped pores while the desorption branch for type  $H_4$  hysteresis contains also a steep region associated with a (forced) closure of the hysteresis loop, due to the so-called tensile strength effect. Therefore, a wide specific surface area range of  $H_4$ -loop behaviour was observed as depicted in Figure 6.2b.

After immobilizing the HAPT ligand into the ZSM-5 mesoporous, the adsorption isotherms type of H<sub>4</sub> hysteresis loop did not changed, suggesting the immobilized method preserves the mesopore structure with no obvious mesopore collapse. However, decreasing in the pore diameter (4.3 nm), surface area (593 cm<sup>2</sup> g<sup>-1</sup>) of ZSM-5 mesoporous/ HAPT were occurred, indicating that the inclusion of a significant amount of organic moieties ligand into inner pores of the mesoporous carrier with no significant change in the pore distribution curve as depicted in Figure 6.2d. It is noteworthy that the direct templating technique and the immobilized method were successfully prepared the ZSM-5 mesoporous/ HAPT ligand catalyst.



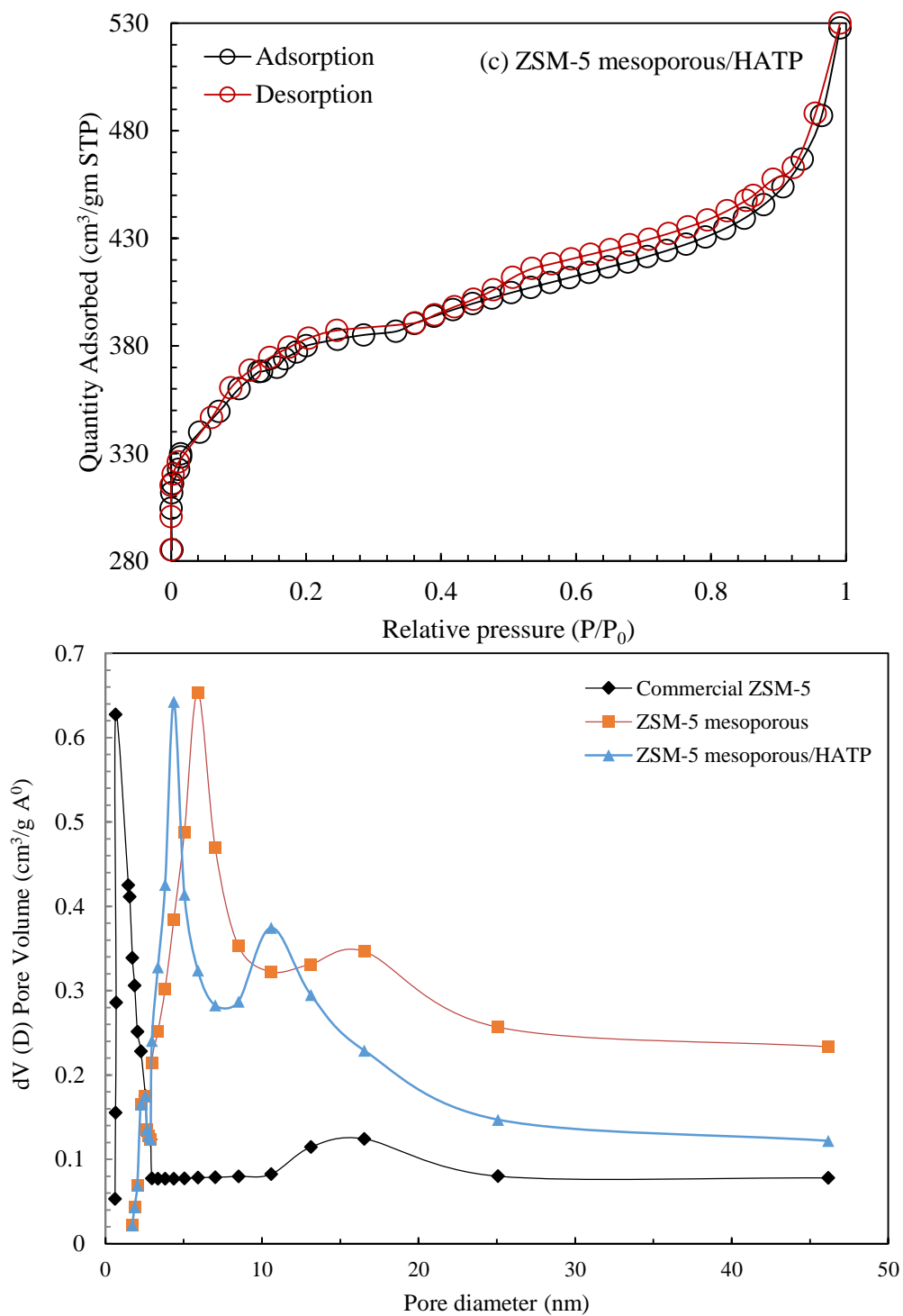


**Figure 6-2** The  $\text{N}_2$  adsorption-desorption isotherms curves (a, b, c) and corresponding the BJH pore size distribution curves of samples (d)

### 6.3.1.2 Fourier-transformed infrared spectroscopy (FTIR) analysis

The functional groups of organic ligand were investigated using the FTIR spectroscopy. It can be observed from Figure 6.3 that the intense sharp peaks were occurring at 3083, 3024, and 3265  $\text{cm}^{-1}$  indicated the possible interference from amino and amido compounds. In certain cases, the carboxylic acids may also interfere. Pyridine derivatives and related heterocyclic compounds also occurred at these peaks; while, nitrite groups were characterized by strong bands near 1650 and 800  $\text{cm}^{-1}$ . These spectrums were normally appreciably stronger, thus making the PSU relatively easy to recognize. The band occurring at 2920  $\text{cm}^{-1}$  was possible interference from non-cyclic aliphatic hydrocarbons, including both low and high molecular weight compounds. Furthermore, long chain amines, phosphines and sulphides may also interfere. This may include the corresponding heterocyclic compounds. It is possible that the specific hydroxyphenones was occurred in 1640  $\text{cm}^{-1}$ . The primary aromatic hydrocarbons that have at least three substituents on a single ring were occurred at 847  $\text{cm}^{-1}$ . The substituents are usually arranged on 1, 3, 5 carbon or at least in a way that causes ring hydrogen atoms to become separated by the substituents to the steric effect. All these intense peaks have proven the successful synthesis of the ligand and this result resembles as reported previously (Sivakumar & Prathapachandra Kurup, 2002).

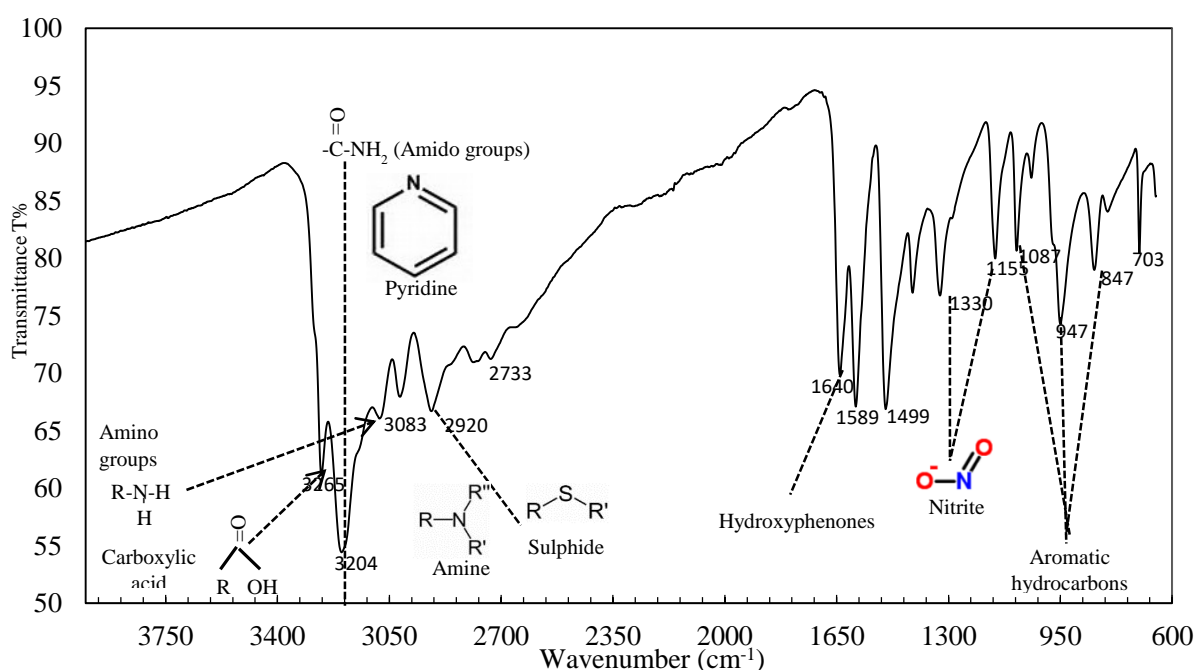
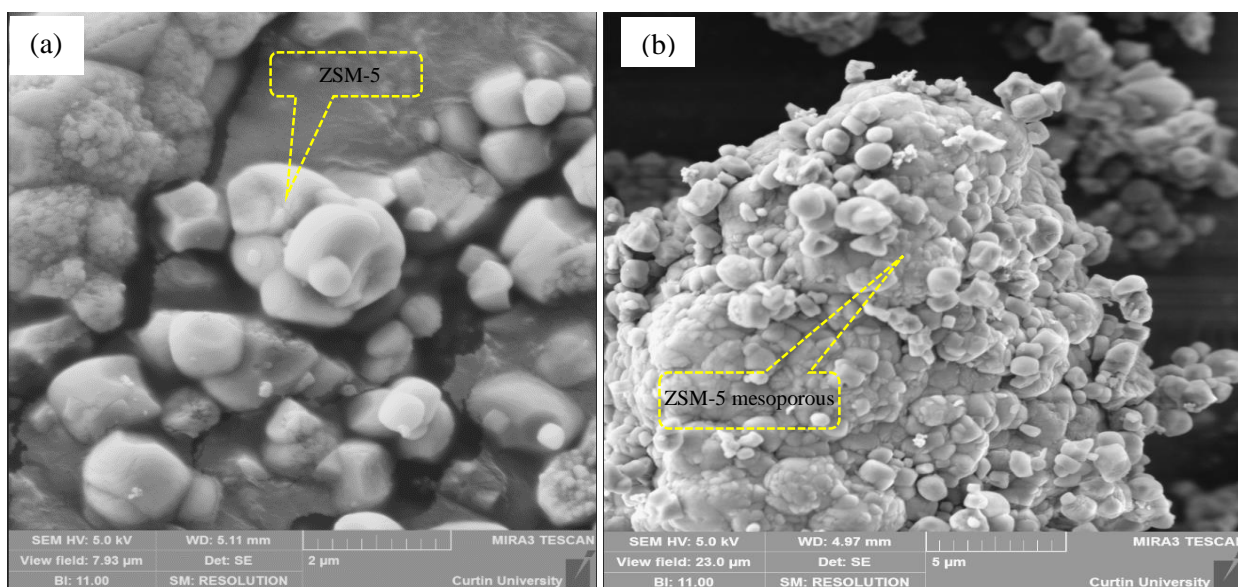


Figure 6-3 Specific functional group observation by FTIR spectrum of HAPT ligand

### 6.3.1.3 FESEM analysis

The morphology of the prepared samples, ZSM-5, ZSM-5 mesoporous and ZSM-5 mesoporous/HAPT are shown in Figure 6.4(a–d). The large particle sizes of ZSM-5 mesoporous were obtained due to the aggregation of these particles to be spherical shapes as shown in Figure 6.4(b and c). These clusters formed heavy molecule, high porosity, highly connected porous structure and also it could have channels and cavities between the ZSM-5 cubes. For that reason, it is anticipated that this behaviour of ZSM-5 mesoporous can be exhibited the capability of ease post separation of this catalyst from water samples. The FESEM image as shown in Figure 4d was clarified that the organic ligand (HTAP) was appeared and linked with ZSM5 mesoporous structure. The micrograph revealed that the link between ZSM-5 mesoporous particles and ligand were almost perfectly organized between particles (Figure 6.4d). These images were proven successfully immobilization of the ligand into mesoporous silica of ZSM-5. Another advantage of ZSM-5 mesoporous monoliths is larger pore size, which allowed functionalizing with an organic ligand for metal ions capturing, adsorption, and extraction systems.





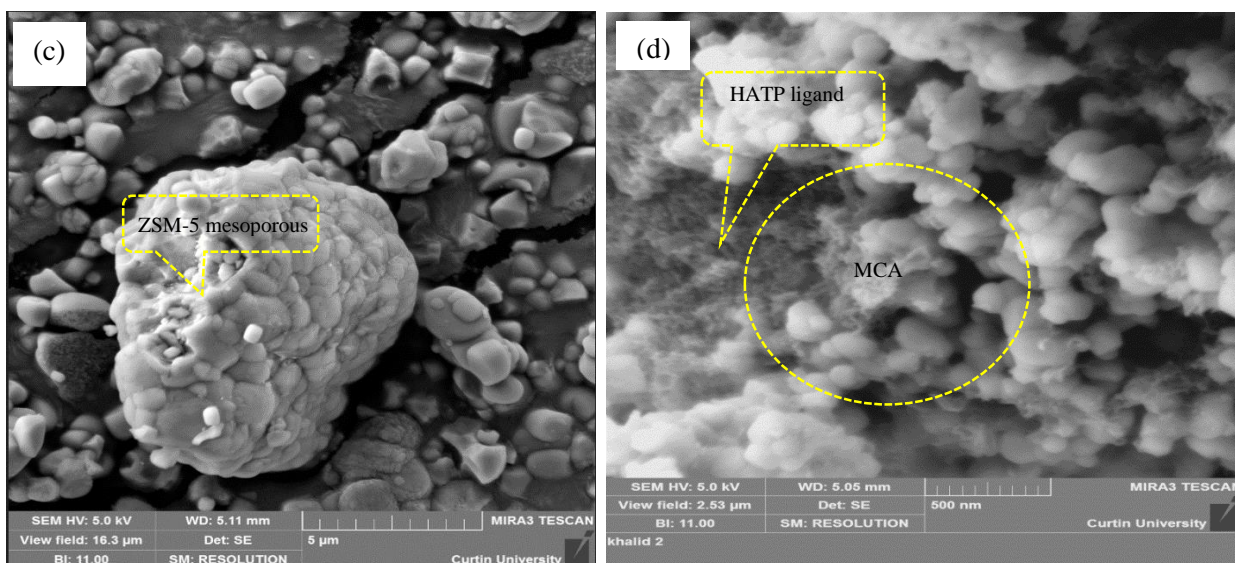


**Figure 6-4** FESEM images of ZSM-5 (a), ZSM-5 mesoporous (b, c) and micrograph of HAPT immobilized composite adsorbent (d)

### 6.3.2 Hg (II) ions recognition parameters

The pH specific value plays a vital role for selectivity and sensitivity of trace Hg (II) ions. The absorbance spectra of Hg (II)-ligand complexes on catalyst pore surfaces were investigated over a wide range of pH solutions from a range of 2.0-12.8 using different buffer solutions for obtaining different pH region (see Figure 6.5).

The absorbance spectra of the  $[\text{Hg (II)-HAPT}]^{n+}$  complexes solution at  $\lambda=387$  nm was accurately evaluated over a wide pH range as shown in Figure 6.5. The highest absorbance of Hg (II)-HAPT complexes were found at pH 12.5, at  $\lambda=387$  nm indicated that the strongest bond between Hg (II) ions and adsorbent was achieved during selective recognition system at this pH value. Therefore, the pH of the samples was adjusted to 12.5 for further experiments in subsequent detection parameters. The response time of Hg (II) ions recognition with the ligand in equilibrium colour optimization was 15 min.

The colour optimization of the  $[\text{Hg (II)-HAPT}]^{n+}$  complexes solution for different Hg (II) ions concentrations are shown in Figure 6.6a. The absorbance spectra change was resulted in the Hg (II) addition followed by complex formation between ligand and Hg (II) ions. The absorbance spectra of  $[\text{Hg-HAPT}]^{n+}$  complexes solution was increased when Hg(II) ions concentrations increase too, and the recognition sensitive of Hg(II) ions was observed in ultra-trace concentrations. UV-Vis spectroscopy was used for

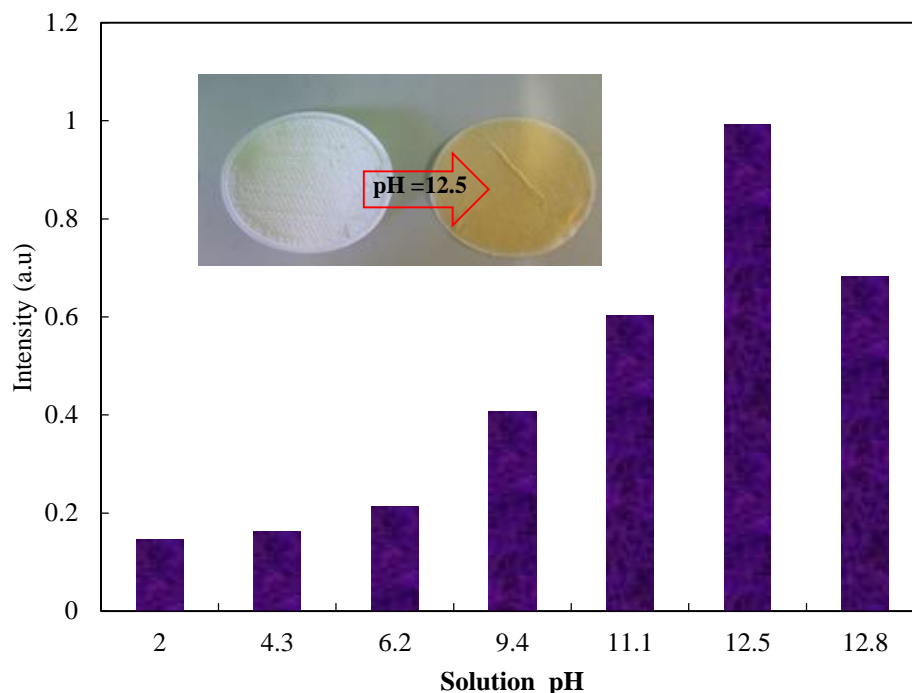
evaluating and optimizing the colour of [Hg (II)-HAPT]<sup>n+</sup> complexes at solid state as shown in Figure 6.6a. The sensitive colorimetric Hg (II) ions recognition was mainly depended on pH and the formed of the [Hg (II)-HAPT]<sup>n+</sup> complexes. It is noted that the remarkable absorbance in the solid adsorbent colour change from the white to yellowish, which can be observed by bared eye. The visible Hg (II) ions concentrations with a colorimetric MCA catalyst pictures are depicted in Figure 6.6a with both solid and liquid state (inset).

The detection limit of Hg (II) ions and the linear response range were measured from the linear part of the calibration plot, which is obtained from the signal intensity of [Hg (II)-HAPT]<sup>n+</sup> complexes at 387 nm against Hg (II) ions concentrations according to Eq. (6.2). The calibration plot of the MCA catalyst is shown in Figure 6.6b at different concentrations of Hg (II) ions. This plot clarifies the linear relationship within the range of 0.0249–0.4985  $\mu\text{M}$  and the correlation coefficient value was  $R^2=0.9978$ , indicating that the concentrations of Hg (II) ions can be detected with the highest sensitivity in an aqueous medium within this concentration range. However, up to 0.4985  $\mu\text{M}$  concentration of Hg (II), the relationship was nonlinear due to the effect of Hg (II) ions saturation. From the calibration curve as shown in Figure 6.6b, the lowest detection limit of Hg (II) ions by the composite adsorption was 3.69  $\mu\text{g L}^{-1}$  which is calculated according to Eq. (6.2), even in the absence of the matrix ZSM-5 mesoporous substrate (calibration curve with dotted line as shown in Figure 6.6b). Thus, such evidence confirms that the HAPT novel ligand based ZSM-5 mesoporous adsorbent can be utilized effectively to detect traces of Hg (II) ions concentrations.

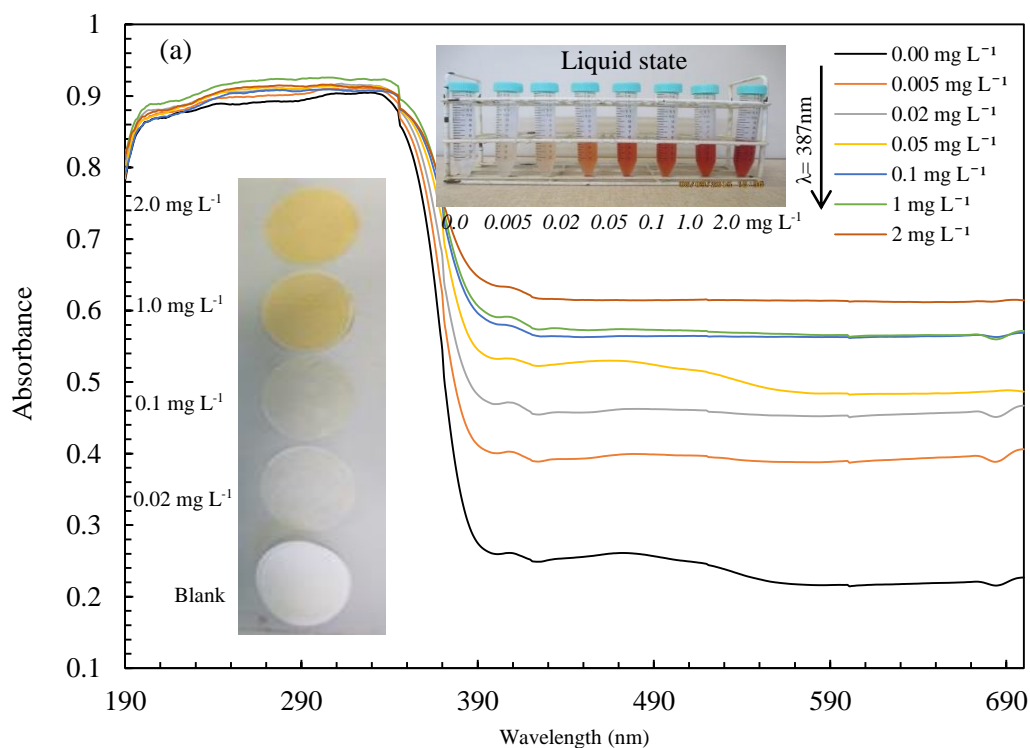
The effects of foreign competition ions on detecting 2.0  $\text{mg L}^{-1}$  Hg (II) ions were investigated in water samples. These competition ions did not interfere as the data provided. Therefore, a series of solutions containing 40  $\text{mg L}^{-1}$  in each of cations  $\text{Pb}^{2+}$ ,  $\text{Zn}^{2+}$ ,  $\text{Cd}^{2+}$ ,  $\text{Al}^{3+}$ ,  $\text{Fe}^{3+}$ ,  $\text{Mg}^{2+}$ ,  $\text{Ca}^{2+}$ ,  $\text{Ag}^{2+}$ ,  $\text{K}^+$ ,  $\text{Na}^+$  and divers anions were added such as chloride, sulphate, carbonate, citrate, nitrate, bicarbonate and phosphate. The absorbance intensity of each of these ions is shown in Figure 6.7. The signal responses of the adsorbent were conducted at pH 12.5 to assure the detection at optimum conditions. From Figure 6.7, the data confirmed that these competition ions was not exhibit any significant colour change and measurable absorbance intensity of Hg (II) ions at pH 12.5. The results revealed that the selectivity of the conjugate materials



toward Hg (II) ions detection was high even in the presence of the completion foreign ions.



**Figure 6-5** The pH effect for Hg(II) ions treatment during the measurement of absorbance spectra of  $[\text{Hg}(\text{II})\text{-HAPT}]^{n+}$  complexes solution at  $\lambda=387$  nm and with condition  $2.0 \text{ mg L}^{-1}$  of Hg (II) ions, 20 mg of MCA catalyst at  $25^\circ\text{C}$  in 10 ml volume for 15 min



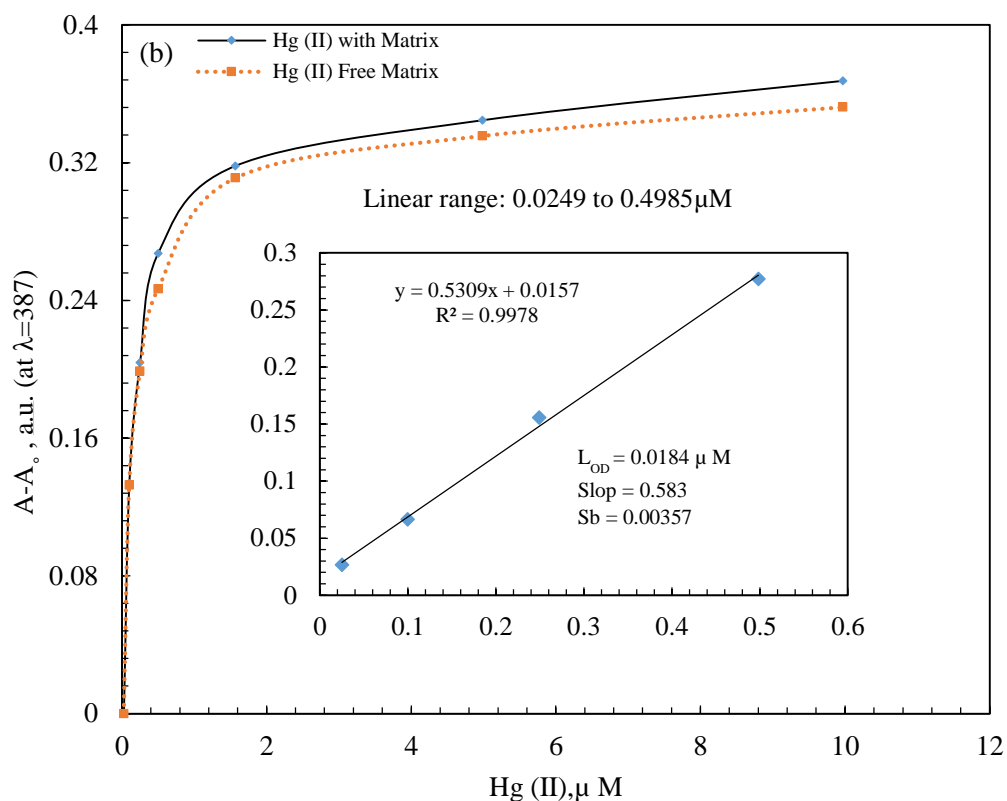


**Figure 6-6** The change of colour optimization of Hg (II) ions concentrations at pH 12.5 and (b) was represented the calibration profile of Hg (II) ions concentrations with spectral absorbance at  $\lambda=387$  nm. The inset in graph (b) shows the low limited responses for Hg (II) ions with a liner fit in the Hg (II) ions concentration range. The A and  $A_0$  are represented the absorbance signal responses of the solution after and before addition of Hg (II) ions

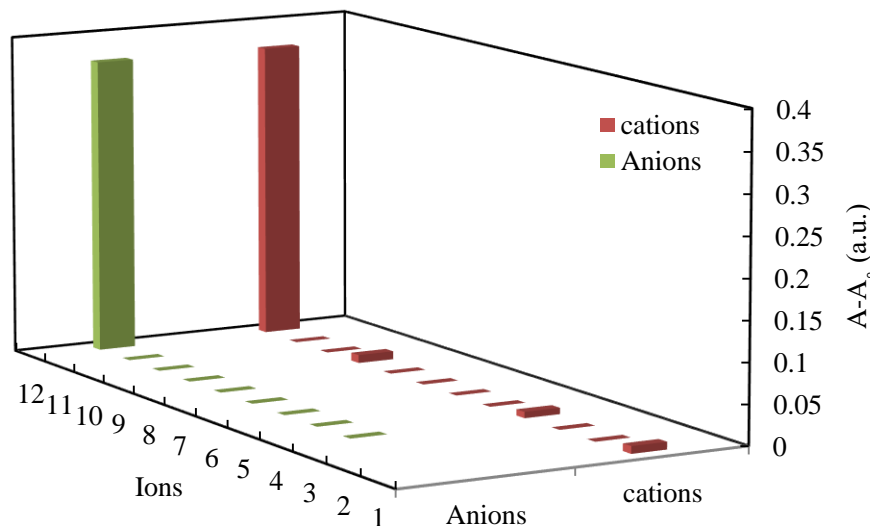


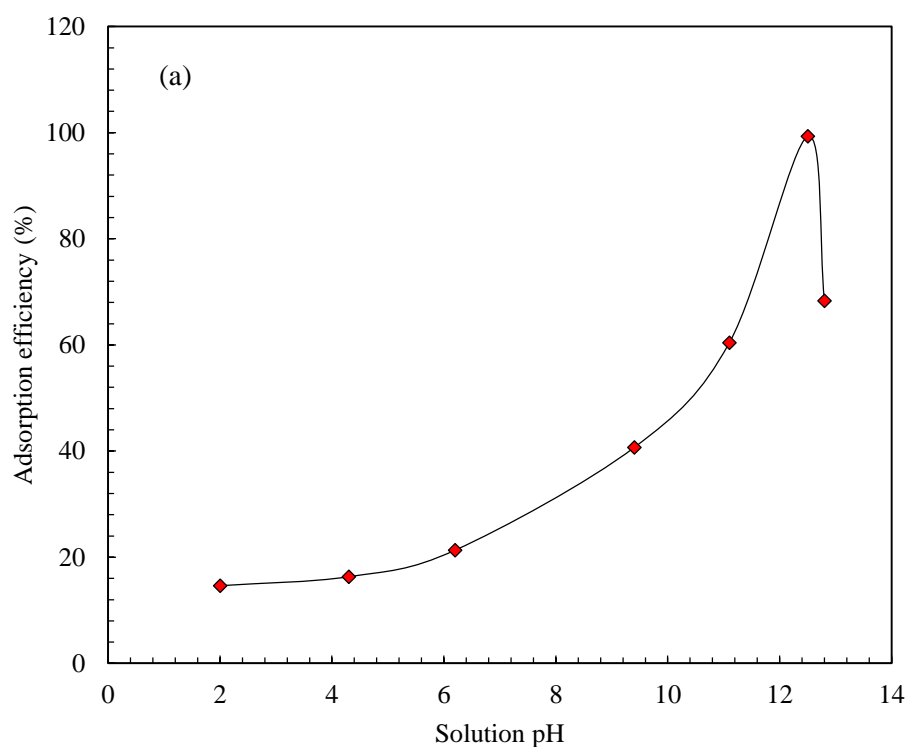
**Figure 6-7** Effect of competing ions (cations and anions) when the Hg (II) ions concentration was  $2.0 \text{ mg L}^{-1}$ , the cations concentration was  $40 \text{ mg L}^{-1}$ . The listed foreign ions area: (1)  $\text{Pb}^{2+}$ , (2)  $\text{Zn}^{2+}$ , (3)  $\text{Cd}^{2+}$ , (4)  $\text{Al}^{3+}$ , (5)  $\text{Fe}^{3+}$ , (6)  $\text{Mg}^{2+}$ , (7)  $\text{Ca}^{2+}$ , (8)  $\text{Ag}^{2+}$ , (9)  $\text{K}^+$ , (10)  $\text{Na}^+$  (11) (blank and (12) Hg(II) ions  $2.0 \text{ mg L}^{-1}$ . The interfering ( $150 \text{ mg L}^{-1}$ ) anions listed in order (4–10): (4) chloride, (5) sulphate, (6) carbonate, (7) citrate, (8) nitrate, (9) bicarbonate and (10) phosphate

**6.3.3 Hg (II) ions adsorption**

The pH solution is a significant factor affecting the Hg (II) ions adsorption from aqueous solutions. The metal ions adsorption directly relied on the theories of metal chemistry in solution and also the ionization state of the functional groups of the adsorbent. Figure 6.8a depicts that the basic solution is playing an important role in efficiency adsorption of Hg (II). In other words, the solution pH influences the hydrolysis, surface functionality, precipitation and complexation of Hg (II) ions (Md Rabiul Awwal, Md Abdul Khaleque, et al., 2013; S. A. El-Safty, Shenashen, Ismael, et al., 2012). The increasing pH solution leads to increase Hg (II) ions adsorption as judged from Figure 6.8a and the higher adsorption was obtained at pH 12.5. However, the acidity is not quite favourable region due to the most functional groups of HAPT on the surface of MCA are protonated, as a result of this the competition could be occurred between protons and Hg (II) ions species thus explain the weak adsorption in the acidity region. This phenomenon can be demonstrated by the hydrolysis of Hg (II) ions in aqueous solution. The hydrolysis constants of Hg (II) are calculated as  $\log K_1 = -2.7$ ;  $\log K_2 = -6.19$ . Therefore, the Hg (II) are exhibited as  $\text{Hg}^{2+}$ ,  $\text{Hg}(\text{OH})^+$ ,  $\text{Hg}(\text{OH})_2^0$  at different pH regions (Dean, 1990; Sarkar, Essington, & Misra, 2000) . According to the hydrolysis constant equation, the pH of the solution was calculated theoretically. It was found that the  $K_a = 6.45 \times 10^{-7}$ ,  $K_w = 1 \times 10^{-14}$ ,  $[\text{OH}]^- = 0.0393 \times 10^{-5}$ , and then  $\text{pH} = 7.6$ . Practically, the pH solution of Hg (II) ions that is commenced the precipitation to be occurred at  $\text{pH} = 7.6$  also. Over  $\text{pH} 7.6$ , the main species are  $\text{Hg}^{2+}$ ,  $\text{Hg}(\text{OH})^+$  and the  $\text{Hg}(\text{OH})_2^0$  begins to form at  $\text{pH} > 7.6$ , and it can be reached at maximum value about 12.5.

To evaluate Hg (II) ions adsorption kinetics on the synthesized MCA, the Hg (II) ions adsorption capacity was investigated at different contact time while the initial Hg (II) ions concentration was fixed at  $2.0 \text{ mg L}^{-1}$ . It's noteworthy that the adsorption kinetics depends on morphological properties of the adsorbent, initial Hg (II) ions concentration, interaction between Hg(II) ions species and protonated adsorbent active sites (Awwal & Hasan, 2015a, 2015b; Awwal, Yaita, Suzuki, et al., 2015). The results are depicted in Figure 6.8b, indicating that the two stages of adsorption are occurring. First stage was during the first 40 min when the adsorption capacity increased rapidly to be 73% and the second stage after next 40 min that slowly increased to reach the equilibrium state in 80 min to be 92%. The fast adsorption is occurring due to the

abundance active sites on the synthesized adsorbent and the slow adsorption observed due to less availability of active sites to make a gradual adsorption curve until its reach equilibrium state as shown in Figure 6.8b. The data also clarified that the Hg (II) ions adsorption increased with the time and the maximum adsorption time was attained within 120 min for clarifying the maximum adsorption capacity to be 95% efficiency (Awual, El-Safty, et al., 2011; M Rabiul Awual et al., 2013; Awual & Jyo, 2009, 2011; Awual, Jyo, El-Safty, Tamada, & Seko, 2011; Awual, Jyo, Ihara, et al., 2011; Awual, Jyo, Tamada, & Katakai, 2007; Awual, Shenashen, Jyo, Shiwaku, & Yaita, 2014; Awual, Shenashen, Yaita, Shiwaku, & Jyo, 2012; Awual, Urata, Jyo, Tamada, & Katakai, 2008; Naushad, Khan, ALOthman, & Awual, 2016). The high selectivity of MCA adsorbent to Hg (II) ions can be explained to the high affinity between Hg (II) ions and functional groups of HAPT ligand molecule to be judged from complicated mechanism as illustrated in Figure 6.9.



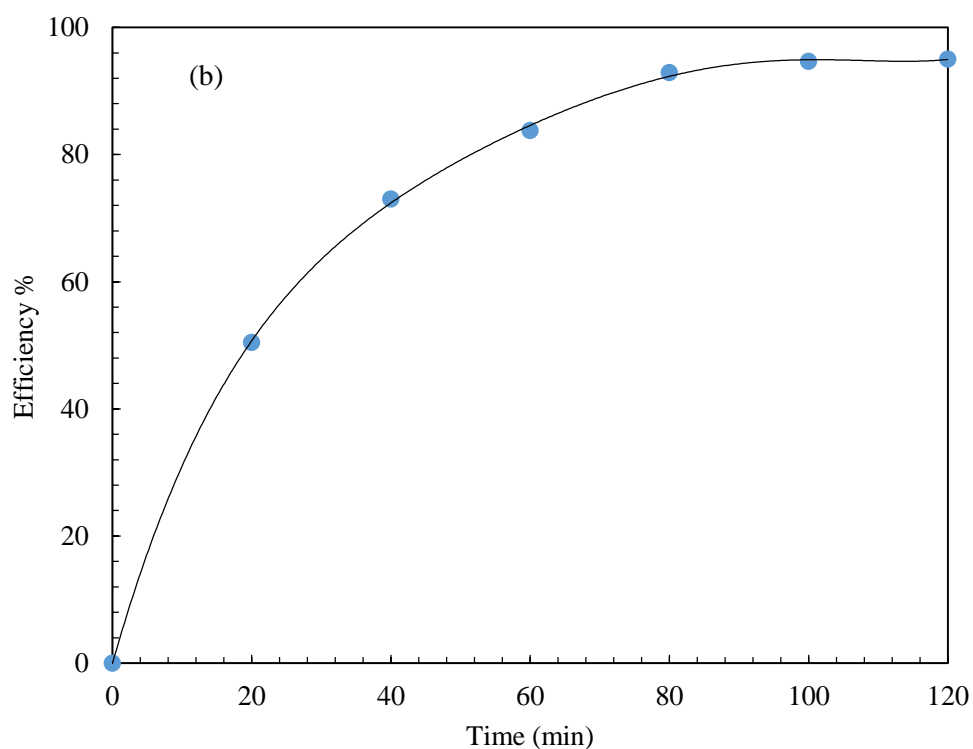


**Figure 6-8** the pH effect on the Hg (II) ions adsorption on the ligand (HAPT) anchored mesoporous adsorbent where initial Hg (II) ions concentration was  $2.0 \text{ mg L}^{-1}$  (a) and the effect of reaction time for Hg (II) ions where the initial Hg (II) ions concentration was  $2.0 \text{ mg L}^{-1}$  (b)

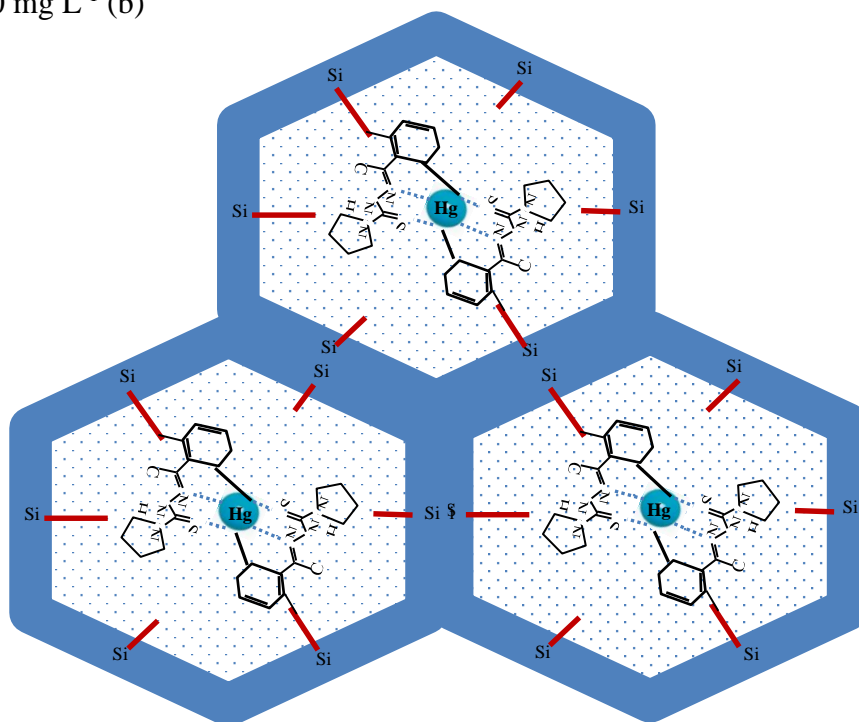


**Figure 6-9** the possible stable complex formation of Hg (II) ions and HAPT ligand at optimum conditions

**6.3.4 Equilibrium adsorption isotherms**

The substantial equilibrium adsorption isotherm is to describe the performance of interaction between the adsorbate and adsorbent. Hg (II) ions concentrations were in the range 2.65–75 mg L<sup>-1</sup>. The relationship between the equilibrium concentrations of Hg (II) ions and the amount of Hg (II) ions adsorbed on the MCA is depicted in Figure 6.10. Then the maximum amount of Hg (II) ions adsorbed on MCA can be defined by adsorption isotherms. The adsorption of Hg (II) ions is increased with increasing the initial Hg (II) ions concentration and then can be obtained like a plateau as shown in Figure 6.10. To explain this behaviour, the Langmuir adsorption model is described the adsorption take place in the specific homogenous sites of MCA material. The assumption of the Langmuir isotherms model is that once an adsorbed species occupies the availability of adsorbent sites, therefore no further adsorption will occur on the material surface sites (Vieira, Oliveira, Guibal, Rodríguez-Castellón, & Beppu, 2011). The Langmuir isotherm model also relied on the assumption that maximum adsorption takes place when the saturation of solute molecules on MCA monolayer is present on the MCA surface and the energy of the adsorption (Md Rabiul Awual, Tohru Kobayashi, Yuji Miyazaki, et al., 2013; X.-s. Wang & Qin, 2005). However, the Langmuir isotherms model cannot provide clear understanding of the mechanistic adsorption phenomena, but it is convenient to determine the maximum adsorption capacity from the experimental data. The linear form of Langmuir expression is:

$$\frac{C_e}{q_e} = \left( \frac{1}{K_L q_m} \right) + \left( \frac{1}{q_m} \right) C_e \quad (6.5)$$

Where  $q_e$  and  $C_e$  are the adsorption capacity (mg/g) and liquid-phase Hg (II) ions concentration at equilibrium state (mg L<sup>-1</sup>), respectively. While,  $q_m$  represents the maximum adsorption capacity of the MCA material (mg/g) and  $K_L$  is the Langmuir constant (L mg<sup>-1</sup>) associated with the affinity of binding sites and it is a measure of the adsorption energy. The  $K_L$  and  $q_m$  were calculated from the intercept and slope of the linear plot of  $C_e/q_e$  versus  $C_e$  as shown in Figure 6.10 (inset). The fitting result clarified that the maximum adsorption  $q_m$  of MCA was 166.7 mg/g with the correlation coefficient  $R^2 = 0.9979$ . Also, the Langmuir adsorption constant  $K_L$  value was calculated to be 0.178 L mg<sup>-1</sup>. The experimental data were indicated that Hg (II) ions

adsorption on the MCA is strongly convenient corresponded to the Langmuir isothermal behaviour.

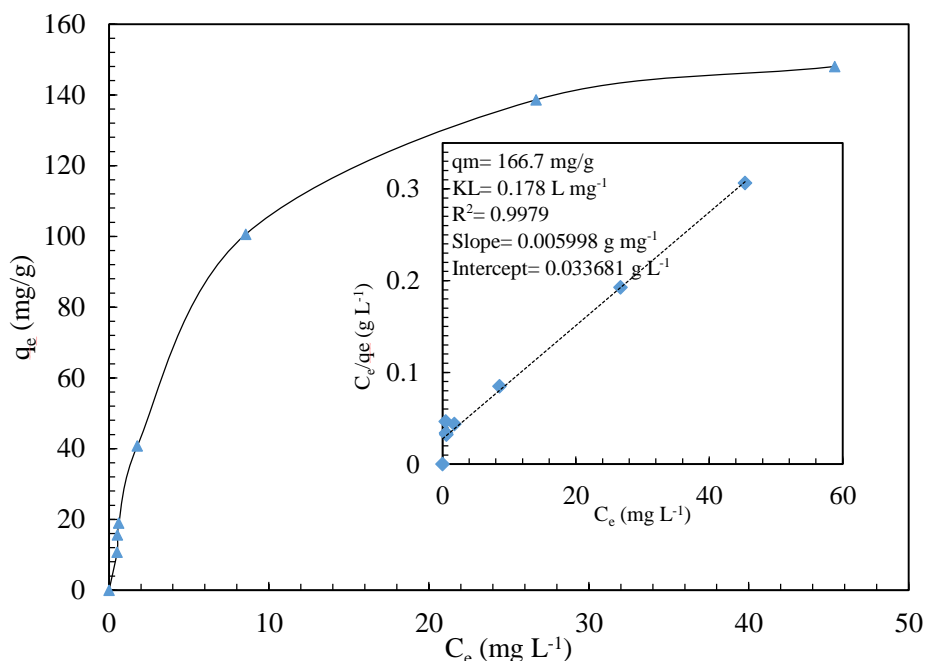


**Figure 6-10** Adsorption isotherm of Hg (II) ions of the MCA with the linear form as fitted by the Langmuir isotherms model (initial concentrations: 2.65–75 mg L<sup>-1</sup>; shaking time: 2 h; adsorbent amount (MCA): 20 mg; volume of solution: 100 ml)

### 6.3.5 Comparison of adsorption capacity

The ligand anchored mesoporous-conjugate material MCA could be used as a potential candidate to remove Hg (II) ions pollutant from water bodies. Also, this conjugate type provides ease post separation after water treatment and also the higher specific surface area of ZSM-5 mesoporous (1151m<sup>2</sup> g<sup>-1</sup>) was allowed a plenty of ligand to immobilize effectively onto surface of ZSM-5 mesoporous. Several literatures have been reported the utilization of other conjugate materials for individual metal ion pollutant removal from water (Awual, 2014; Awual, Hasan, Khaleque, & Sheikh, 2016; Awual, Hasan, & Shahat, 2014; Awual, Ismael, Khaleque, & Yaita, 2014; Awual & Yaita, 2013; Awual, Yaita, et al., 2016; Shahat, Awual, & Naushad, 2015). However, in this project, this is the first time using the synthesized ZSM-5 mesoporous as a matrix substrate material. The results are encouraging for removing Hg (II) ions from industrial wastewater. Compared with other forms of conjugate materials, conjugate material exhibits a high adsorption capacity toward Hg (II) ions as shown in Table 6.2.

The maximum adsorption capacity of MCA in this study was relatively high when it is compared with several other adsorbents due to the properties of functional groups, high specific surface area and particle size of the adsorbent. The present modified conjugate material can be used as one the of the effective mesoporous-conjugate adsorbent for efficient Hg (II) ions capturing from aqueous solution.

**Table 6-2** Comparison of maximum adsorption capacity of Hg (II) ions with different forms of adsorbent materials

Used adsorbent	Capacity (mg/g)	References
Thiol-functional magnetic nanoparticles	9.5	(Hakami, Zhang, & Banks, 2012)
Chitosan spheres	31.3	(Vieira & Beppu, 2006)
CoFe <sub>2</sub> O <sub>4</sub> - reduced graphene Oxide	158	(Y. Zhang et al., 2014)
Nature wool fibre	154.32	(Monier, Nawar, & Abdel-Latif, 2010)
Buckwheat hulls	116.34	(Z. Wang et al., 2013)
SiO <sub>2</sub> - multiwall CNT	163.9	(Saleh, 2015)
Thiol-functionalized graphene oxide	107.52	(Kumar, Jiang, & Tseng, 2016)
γ-AIOOH	124.2	(Y.-X. Zhang et al., 2012)
MIL-101-Thymine	59.28	(Luo et al., 2016)
Diatom silica Micro-particles	169.5	(Yu, Addai-Mensah, & Losic, 2012)
ZSM-5 mesoporous/HAPT (MCA)	166.7	This chapter

---

### 6.3.6 Effect of foreign ions

The co-existing foreign cations in water are generally potentially interfering with selective metal removal from aqueous water samples. The results showed that the presence of these foreign ions did not affect the Hg (II) ions removal as shown in Figure 6.11. The data also proposed that the suggested MCA could be applied to the sensitivity analysis and capturing of ultra-trace level of Hg (II) ions in aqueous solutions.



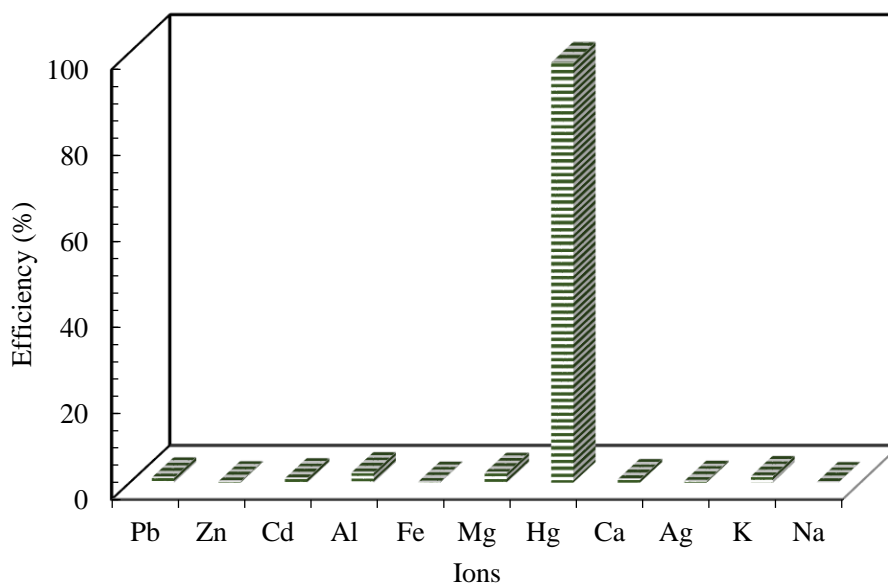


**Figure 6-11** Selectivity of the MCA catalyst towards Hg (II) ions in the presence of different ions

### 6.3.7 Elution and recycle of MCA catalyst

The recovery of Hg (II) from the MCA was studied using different eluting solutions or stripping agents such as H<sub>2</sub>SO<sub>4</sub>, HCl and thiourea–HCl (Md Rabiul Awwal, Md Abdul Khaleque, et al., 2013; S. A. El-Safty, Shenashen, Ismael, et al., 2012). The reusability of MCA was evaluated after the elution/regeneration process for six cycles. The results are summarized in Figure 6.12. The experimental data revealed that the mixture solution of 0.1M thiourea- 0.1M HCl was sufficient to extract and release the adsorbed Hg (II) ions from the MCA catalyst. However, the adsorption efficiency of the Hg (II) ions was slightly decreased to 10% after six cycle operations. It can be confirmed that the MCA catalyst has a good stability and reusability for long time users.

FTIR test was also carried out for the MCA after and before it uses for 6th cycle. It can be observed that the intensive band was occurred at 1100 cm<sup>-1</sup> before the catalyst usage (data shown at Appendix A-1, Figure A.4). However, a very small reduction in the intensity of band was occurring at 1100 cm<sup>-1</sup>. It indicated that there was no affected on the immobilized HAPT through the experimental work. This proven that the ZSM-5 mesoporous framework supported HAPT ligand was not compromised or decomposed in the chemical structure during the adsorption and desorption process.

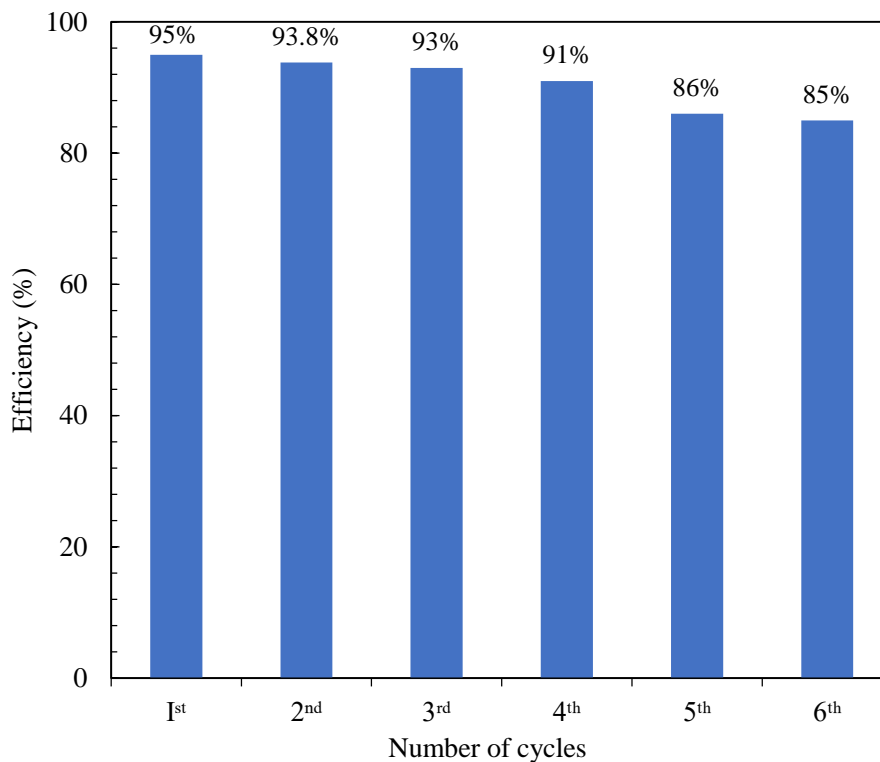


**Figure 6-12** Regeneration of the adsorbent where elution was performed with 0.10M thiourea-0.10M HCl

#### 6.4 Summary

In this chapter, the laboratory experiments were extensively carried out for selective detection and removal of Hg (II) ions from aqueous medium, using an organic-inorganic based meso-conjugate adsorbent (MCA). The organic ligand of 2-hydroxyacetophenone-<sup>4</sup>N-pyrrolidine thiosemicarbazones (HAPT) and inorganic ZSM-5 mesoporous was successfully synthesized as a conjugated material by the direct immobilization method. The MCA was exhibited high specific surface area, easy post separation and cost effective material with excellent detection, high adsorption capacity and rapid adsorption rate for Hg (II) ions from aqueous solution due to the hydroxyl, nitrogen and sulphur donor atoms on the ligand, which was created intensive interaction with Hg (II) ions via the electrostatic effect to form the stable complexation mechanism. The lower detection limit was found to be  $3.69 \mu\text{g L}^{-1}$  of Hg (II). The MCA was adsorbed Hg (II) ions at an optimum pH condition to be 12.5 and it was exhibited fast kinetic performance. The data was also clarified that the MCA material was capable to capture the Hg (II) ions in aqueous solution in spite of the presence of

the various foreign ions. The sorption efficiency of Hg (II) ions was 95% during 120 min. The adsorption of Hg (II) ions was followed the Langmuir adsorption model and the maximum adsorption capacity was 166.7 mg/g. The elution and recycles of MCA was successfully evaluated for six adsorption-elution-recycles by using 0.10M thiourea-0.10M HCl. Therefore, the MCA is an efficient and eco-friendly material for Hg (II) ions detection and removal from wastewater. It is also expected that the functionalized MCA has potential application in real waste environmental samples.

## CHAPTER 7

# 7

### **A novel optical mesoporous conjugate adsorbent for monitoring and sorption of ultra-trace Lead (II) from aqueous media**

#### **7.1 Introduction**

Toxic heavy metal ions in ultra-trace quantities are difficult to detect and remove from aqueous solution. The removal of ultra-trace level of toxic metal ions contaminants from wastewater is one of the crucial issues that should be addressed in water treatment (Lu & Astruc, 2018; Martín, Faccini, García, & Amantia, 2018; Nyairo et al., 2018; Riaz et al., 2009; Zein et al., 2010). Different industrial activities are known to generate large amount of effluent, causing the increased concentration of diverse metal ions in water bodies. In this chapter, lead a heavy metal ion ( $\text{Pb}^{2+}$ ) was selected as a pollutant model because it is a globally hazardous pollutant, which is considered as a one of the common heavy metal ions in the ecosystem (Karunanayake et al., 2018; Karve & Rajgor, 2007; Shahat et al., 2018; P. R. Sharma et al., 2018). The most widely recognized of lead, which have generated environmental and health concern is it applications in petrol as antiknock agent and paint pigments; also, the  $\text{Pb}^{2+}$  presents in water bodies is generated from ore processing and mining, industrial effluents discharge,  $\text{Pb}^{2+}$  plumbing, and public road or motorways runoff (Awual & Hasan, 2014b; Citak & Tuzen, 2010; J. Zhou, Liu, Zhou, Ren, & Zhong, 2018).  $\text{Pb}^{2+}$

contaminants constitute a serious environmental problem due to the steadiness in the polluted locations and the complexity of its mechanism for biological intoxication (Chooto et al., 2010; G. Li, Wang, Sun, Xu, & Han, 2017; Baozhu Zhang & Wei, 2018). Trace quantities of lead ( $\text{Pb}^{2+}$ ) in ecological samples can lead to environmental contamination as well as several deadly diseases, which include damage to neurological systems and dysfunction of renal blood, breakdown of nervous system, reproductive system and brain; high level of lead ( $\text{Pb}^{2+}$ ) may cause irreversible brain damage, severe anaemia and colic shock (Memon et al., 2005; B. Xiang, Ling, Lou, & Gu, 2017). To diminish the toxic impacts of this metals on the environment drastic measure should be taken by environmental and health agencies to enforce the compliance with the maximum allowable limits of metal ions released into the lakes, rivers and landscapes. The maximum permissible limit of  $\text{Pb}^{2+}$  in potable water reported by The World Health Organization (WHO) in 2010 is  $10 \mu\text{g L}^{-1}$  (Organization, 2004). Therefore, the efficient detection and removal of ultra-trace level of lead (II) from wastewater is imperative for hygienically safe-guarding water quality.

Numerous analytical methodologies and strategies have been proposed for detecting lead ( $\text{Pb}^{2+}$ ) in trace levels, for examples, the inductively coupled plasma emission spectrometry (ICP), flame atomic absorption spectrometry (FAAS) and the electro thermal atomic absorption spectrometry (ETAAS) (Cabon, 2002; de Campos, dos Santos, & Grinberg, 2002; de Mattos, Nunes, Martins, Dressler, & de Moraes Flores, 2005; dos Santos, dos Santos, Costa, Andrade, & Ferreira, 2004; Soylak, Narin, de Almeida Bezerra, & Ferreira, 2005; Soylak & Yilmaz, 2011; Zachariadis, Anthemidis, Bettas, & Stratis, 2002). ETAAS is widely used because of its sensitive technique with a low detection limit to sub-pictogram range for generally all heavy metal ions (Kokšal, Synek, & Janoš, 2002; Wagner, Batchelor, & Jones, 1998). Similarly, the inductively coupled plasma-mass spectrometry (ICP-MS) also detects ultra-trace limit of  $\text{Pb}^{2+}$  (Ndung'u, Hibdon, & Flegal, 2004; Rodríguez, Barciela, Herrero, García, & Peña, 2005), however, it becomes very difficult to detect when the concentration is extremely low and also due to matrix influences (J. Chen, Xiao, Wu, Fang, & Liu, 2005). Flame atomic absorption spectrometry (FAAS) is the mostly utilized technique. Separation techniques and pre-concentration are also used, for example, the liquid-liquid extraction, electrochemical operation, floatation, solid phase extraction, ion

exchange, and co-precipitation (Doner & Ege, 2005; Jamali et al., 2006; Jamali, Assadi, Shemirani, & Salavati-Niasari, 2007; Mesquita, Fernandes, & Rangel, 2004; Ndung'u, Franks, Bruland, & Flegal, 2003). However, the disadvantages of these techniques are: the difficulty and complexity of operation, large infrastructural backup and support by expertise technician, pre-concentration step, less sensitivity, producing large secondary wastes and high cost of operation (Araujo, Costa, & Lima, 1999; Karadjova, Zachariadis, Boskou, & Stratis, 1998).

Different adsorption materials such as clay minerals of the Kaolinite and Montmorillonite type, which exothermally adsorbed  $Pb^{2+}$  from aqueous media (S. S. Gupta & Bhattacharyya, 2009), natural zeolitic tuff (Stojakovic, Jovanovic, & Rajic, 2017), synthesized activated carbon (Adebisi, Chowdhury, & Alaba, 2017) and the mesoporous silica incorporated graphene oxide (Mo et al., 2017) have been recently investigated. The restricted functional application of these adsorbents is because they have no optical-capability to recognize toxic ions and they have lower adsorption capacity. Therefore, a new technique such as organic ligand grafted mesoporous substrate has emerged as an exceptional alternative for detecting and removing lead ( $Pb^{2+}$ ) in water samples. Such an optical adsorbent produces color change, has high sensitivity and selectivity, eco-friendly, easy-to-use showing a conceivably substantial scale operation from the point of view of real sample remediation.

Precursor silica sources such as the tetraethyl orthosilicate (TEOS,  $Si(OH)_4$ ) and the tetramethyl orthosilicate (TMOS,  $Si(OCH_3)_4$ ) have been commonly utilized by researchers as mesoporous substrate of the visual organic-inorganic adsorbent using the direct template method providing specific surface area range is roughly between  $300-900\text{ m}^2\text{ g}^{-1}$  (Awual & Ismael, 2014; Md Rabiul Awual, Mohamed Ismael, et al., 2013; Awual, Khaleque, et al., 2015; Md Rabiul Awual, Tsuyoshi Yaita, Sherif A El-Safty, Hideaki Shiwaku, Yoshihiro Okamoto, et al., 2013; Md Rabiul Awual, Tsuyoshi Yaita, & Hideaki Shiwaku, 2013; M. Shenashen et al., 2013). The disadvantages of utilizing these substrates in water treatment are: The hydrolysis of  $Si(OCH_3)_4$  produces insoluble  $SiO_2$  and  $CH_3OH$  (methanol) a poisonous liquid. At low concentrations inhalation of methanol causes lung lesions, and at slightly higher concentrations eye contact with the vapour causes blindness. Worse, at low concentrations ( $200\text{ mg L}^{-1}$ ), the damage is often insidious, with onset of symptoms hours after exposure (Love, Arnesen, Phillips, & Windom, 2014); the effect of TEOS is much less damaging of it

lower hydrolysis and solubility of the ethoxy groups. Therefore, the search for an alternative substrate which has a high specific surface area, multi-active sites and ease post separation, highly affinity to anchor organic ligand, are the key challenges of this work.

The objectives of this chapter is to develop an visual conjugated mesoporous adsorbent fabricated by anchoring a ligand into a high specific surface area mesoporous zeolite type ZSM-5 for detecting and selectively removing  $\text{Pb}^{2+}$  from portable water using batch experiments. The novel organic ligand of 2,6-Pyridinedicarboxaldehyde-Thiosemicarbazone (PDCTC) was successfully prepared and fabricated onto the inorganic mesoporous silica Zeolite type ZSM-5 (relatively high stability of framework, highly porous aluminosilicate with high silica/alumina ratio, hydrophobic and non-toxic material) by the direct template approach. The synthesized ZSM-5 mesoporous anchors a copious hydroxyl group and PDCTS ligand conjugated by hydrogen bonding, Van der Waals forces and reversible covalent bonds (Md Rabiul Awwal, Tohru Kobayashi, Hideaki Shiwaku, et al., 2013; Md Rabiul Awwal, Tsuyoshi Yaita, Sherif A El-Safty, Hideaki Shiwaku, Shinichi Suzuki, et al., 2013; Awwal, Yaita, Shiwaku, et al., 2015; Shahat et al., 2018).

## **7.2 Experimental work**

### **7.2.1 Chemicals**

All chemicals are analytical grade and were used as purchased without further purification. Zeolite ZSM-5 (Molar ratio  $\text{SiO}_2/\text{Al}_2\text{O}_3 = 600$ ,  $300 \text{ m}^2 \text{ g}^{-1}$  specific surface area, 2–3  $\mu\text{m}$  particle size, 0.5 nm pore size) was provided from ACROS Organics, A Thermo Fisher Scientific Brand, New Jersey–USA. Triblock copolymers of ethylene oxide-block-poly (propylene oxide) block-poly (ethylene oxide) designed as  $\text{EO}_{20}\text{PO}_{70}\text{EO}_{20}$  ( $\text{P}_{123}$ ) & 1, 3,5-triisopropylbenzene (TIPB) were obtained from Sigma-Aldrich Company Ltd., USA. The standard  $\text{Pb}^{2+}$  solution ( $1000 \mu\text{g L}^{-1}$ ) was supplied by High-Purity Standards Company. Ultra-pure water was used throughout in this study to prepare all the aqueous solution.

### 7.2.2 Synthesis of 2,6-Pyridinedicarboxaldehyde-Thiosemicarbazone (PDCTC) ligand

The chemical reaction process of synthesizing PDCTC ligand is depicted in Figure 7.1. As mentioned in chapter 3 section 3.3.4.2, a slight modification of previous study was conducted (Ahmed & Yunus, 2014).

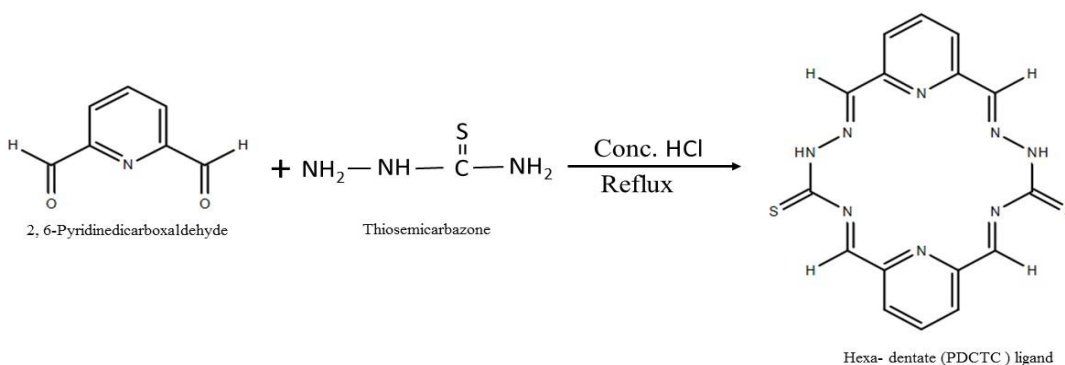


**Figure 7-1** Chemical reaction of synthesized 2,6-Pyridinedicarboxaldehyde-Thiosemicarbazone (PDCTC) ligand

### 7.2.3 Synthesis of mesoporous silica and mesoporous-conjugate adsorbent (MzCA)

As mentioned in chapter 3 section 3.3.3.1 and chapter 6 section 6.2.3, the mesoporous silica zeolite type of ZSM-5 is synthesized by the direct templating approach with a slightly modified (Abbas et al., 2018; G. Zhou et al., 2007). In typical conditions, 1 g of P<sub>123</sub> surfactant type of triblock copolymer was added to solution of ultra-pure water 20 ml and HCl. After that, 3 g of ZSM-5 was mixed together to this solution with vigorous magnetic agitating. Eventually, the filtrated particles was calcined at 500<sup>0</sup>C for 4 h. Then the resulted material was properly refined and prepared for fabrication unto the mesoporous silica zeolite (ZSM-5).

As mentioned in chapter 3 section 3.3.4.3, MzCA (mesoporous /ligand) adsorbent was prepared by direct incorporation method. 100 mg of ligand type of PDCTC in absolute ethanol solution was mixed with 2 g mesoporous silica monoliths. Thereafter, the conjugated mesoporous adsorbent was dried and grinded into fine particles for visual Pb<sup>2+</sup> removal and sensing experiments. Herein, the amount of PDCTC ligand immobilized was 0.14 mmol/g and is evaluated using the following equation:



$$Q = \frac{(C_i - C_f)V}{m} \quad (7.1)$$

Where  $Q$  is the adsorbed amount (mmol/g),  $C_i$  and  $C_f$  were the initial concentration and supernatant concentration of the PDCTC, respectively.  $V$  is the solution volume (L),  $m$  is the mass of the conjugated mesoporous adsorbent (g).

#### 7.2.4 Characterization of MzCA

The  $N_2$  adsorption/desorption isotherms were investigated utilizing the specific surface area and porosity analyzer (Micromeritics (Tri-Star II, Germany)). The pore size distribution was calculated by the Barrett–Joyner–Halenda (BJH) model. Fourier-transformed infrared spectroscopy (FTIR) was used to investigate the functional groups of the ligand and MzCA. Field emission scanning electron microscope (FESEM) analyzer type of MIRA3TESCAN high vacuum mode microscope was utilized.

#### 7.2.5 Optical $Pb^{2+}$ sensing and capturing

As mentioned in chapter 3, section (3.5.2.2), 10 mg of MzCA was immersed in 2.0 mg  $L^{-1}$  of  $Pb^{2+}$  solution. Then, the solution was well-adjusted to appropriate pH of 1.5, 2.2, 3.0, 4.0 (using 0.1 M of KCl with HCl), pH of 6.0 & 7.7 (using 3-morpholinopropane sulfonic acid (MOPS) with NaOH), pH of 11.7 (using 2-cyclohexylamino) ethane sulfonic acid (CHES) with NaOH) at constant volume. A blank solution (without  $Pb^{2+}$ ) was also prepared following the same procedure for the comparison of color formation. After the color optimization, a quantitative estimation of lead ( $Pb^{2+}$ ) using solid-state UV–Vis–NIR spectrophotometer were conducted to assess the color absorbance measurements. After that the mesoporous adsorbent MzCA was grinded to fine homogenous particles to determine the absorbance spectra. The recognition ( $L_D$ ) limit of  $Pb^{2+}$  was measured according to the following equation (Shrivastava & Gupta, 2011):

$$L_D = K S_b/m \quad (7.2)$$

where  $K$  is the confidence factor and equal to 3,  $S_b$  is the standard deviation for the blank and  $m$  is the slope of the calibration graph in the linear range.

**7.2.6 Lead (Pb<sup>2+</sup>) sorption, regeneration and reuses**

To demonstrate the visual adsorption, 10 mg of MzCA was immersed in various concentration of Pb<sup>2+</sup> solutions and the pH was adjusted to a specific value using KCl/HCl or MOPS as buffer solutions in 20 ml volume. The mixture was stirred with agitation speed of 200 rpm at room temperature for 45. Thereafter the MzCA was separated by vacuum filtration system and the filtrated solutions which containing the different concentrations of lead (Pb<sup>2+</sup>) were analyzed by ICP-AES. The adsorbed quantities and the removal efficiency were evaluated according to the following equations:

$$\text{Mass balance } q_e = (C_i - C) V/m \quad (\text{mg/g}) \quad (7.3)$$

And

$$\%RE = \frac{(C_i - C)}{C_i} \times 100 \quad (7.4)$$

Where  $q_e$  is adsorption equilibrium capacity ( $\text{mg g}^{-1}$ ),  $C_i$  and  $C$  are the initial and final concentrations of Pb<sup>2+</sup> in the solution ( $\text{mg L}^{-1}$ ), respectively,  $V$  is the volume of the aqueous solution (L),  $m$  is the weight of the adsorbent (g).

To assess the kinetic performances, 10 mg of MzCA was added to 20 ml solution of lead (II) ions containing 2.0  $\text{mg L}^{-1}$  concentration and the mixture was magnetically stirred. Each 10 min intervals, the samples were filtrated and analyzed via ICP-AES. The maximum adsorption capacity was also evaluated using 10 mg each of MzCA in different concentrations of Pb<sup>2+</sup> solution and stirred at 800 rpm for 2 h, thereafter, the filtrate solutions were analyzed by ICP-AES. To detect the color formation of lead (Pb<sup>2+</sup>), UV-Vis/spectrophotometer (JASCO/V-670) was used at different spectra absorption of the ionic solution. The concentrations of Pb<sup>2+</sup> solutions were estimated by ICP-AES analyzer (Perkin Elmer, Germany, 8300). It was calibrated using five standard solutions containing 0, 1, 10, 15, 20, and 50.0  $\text{mg L}^{-1}$  of Pb<sup>2+</sup> (also for each foreign element) and the correlation coefficient of the calibration curve was 0.988.

In order to determine the eluting agent for lead, mesoporous conjugated adsorbent used in Pb<sup>2+</sup> solutions was removed and washed with cool or hot ultra-pure water (10 - 40°C) or stripping agents such as NaOH, H<sub>2</sub>SO<sub>4</sub>, thiourea, thiourea-HCl, and HCl several times. The filtrated were transferred to 10 ml test tubes, magnetically stirred

for 30 min and then analyzed by ICP-AES. It was observed that the best elution agent was 0.1 M HCl. After this elution operation, the conjugate adsorbent was simultaneously renewed and reuses for a number of cycles to evaluate the reusability.

All the experiments were duplicated in this work to assure a comprehensive coherence and exactness of the results. Moreover, the data presented in the tables and in the Figures are average values.

### 7.2.7 Influence of foreign co-existing ions

A solution containing a mixture of lead ( $\text{Pb}^{2+}$ ) and foreign competing ions were investigated to check the competitive adsorption capability of co-existing diverse heavy metal ions in aqueous media. The mixed solution contained 20 mg  $\text{L}^{-1}$  each of following ions:  $\text{Cu}^{2+}$ ,  $\text{Fe}^{3+}$ ,  $\text{Hg}^{2+}$ ,  $\text{Ag}^{2+}$ ,  $\text{Co}^{2+}$ ,  $\text{Na}^{1+}$ ,  $\text{AL}^{2+}$ ,  $\text{Ca}^{1+}$ ,  $\text{K}^{1+}$ ,  $\text{Mn}^{2+}$ ,  $\text{Zn}^{2+}$ ,  $\text{Cd}^{2+}$  ions and 2.0 mg  $\text{L}^{-1}$  of  $\text{Pb}^{2+}$ . The final solution was adjusted to 20 ml volume. Then, 10 mg of the conjugated adsorbent was added to this solution and magnetically stirred at 400 rpm for 2 h to assure a complete removal  $\text{Pb}^{2+}$ , and then the filtrated was checked by ICP-AES analyzer.

## 7.3 Results and discussion

### 7.3.1 BET specific surface areas and pore distribution

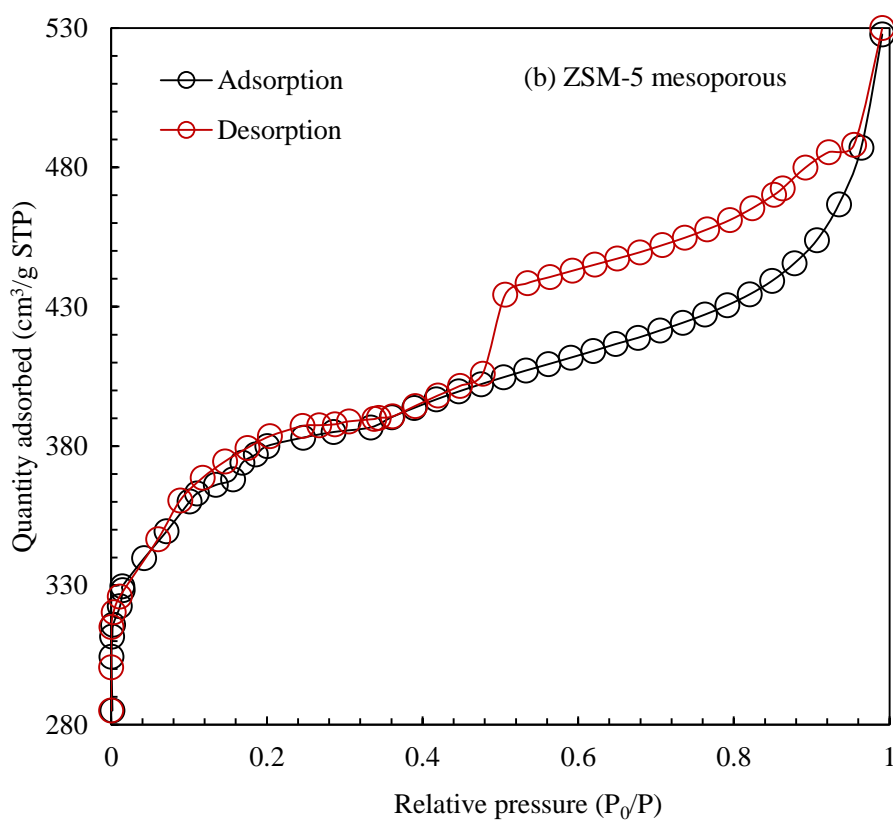
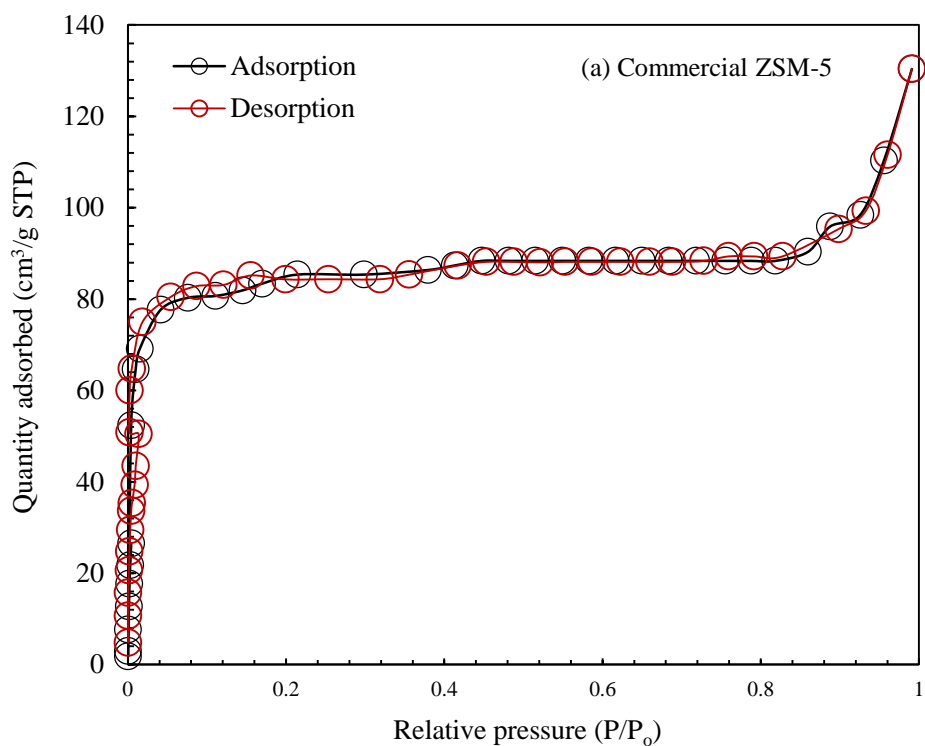
The specific surface area ( $S_{\text{BET}}$ ) and pore size distribution of commercial ZSM-5, ZSM-5 mesoporous and ZSM-5 mesoporous/PDCTC were measured based on  $\text{N}_2$  adsorption-desorption isotherms using the Barrett-Joyner-Halenda (BJH) method. Figure 7.2(a–d) depicted the  $\text{N}_2$  adsorption-desorption isotherms and BJH pore size distribution of the samples. For comparison, the specific surface area, pore volume and average pore diameter results for the above catalysts are summarized in Table 7.1.

According to IUPAC classification, the adsorption/desorption isotherms of the commercial ZSM-5 is a type I isotherm and exhibits horizontal plateau starting at low relative pressure  $< 0.15$  (Thommes et al., 2015; Valero-Romero et al., 2016), indicating that the porous morphology consist predominantly of very narrow micropores with relatively small external surfaces as shown in Figure 7.2a. The steep uptake at very low  $P/P_0$  is due to enhanced adsorbent-adsorptive interactions in narrow micropores, resulting in micropore filling at very low  $P/P_0$  (Thommes et al., 2015). The specific

surface area and the pore diameter of commercial ZSM-5 were estimated to be  $311 \text{ m}^2 \text{ g}^{-1}$  and  $0.86 \text{ nm}$ , respectively (see Figure 7.2d).

After the treatment of the commercial ZSM-5, the isotherm curve of the treated ZSM-5 framework shape was changed from type I to a clear type  $H_4$  hysteresis loops according to the IUPAC classification, which exhibited a hysteresis loop at  $P/P_0$  range (0.5–0.99) as shown in Figure 7.2b, indicating that the mesoporous structure was highly present in the sample as illustrated in Figure 6.2b (Thommes et al., 2015; Valero-Romero et al., 2016). High specific surface area and uniform pore diameter of ZSM-5 mesoporous that were obtained are  $1151 \text{ m}^2 \text{ g}^{-1}$  and  $15.2 \text{ nm}$ , respectively (see Figure 6.2d). This high specific surface area revealed that the type  $H_4$  hysteresis was exhibited no limiting adsorption at high  $P/P_0$ , which was observed with the non-rigid aggregates of plate-like particles giving rise to slit-shaped pores, the desorption branch for type  $H_4$  hysteresis on the other hand contains a steep region associated with a (forced) closure of the hysteresis loop, due to the so-called tensile strength effect (Valero-Romero et al., 2016). Therefore, a wide specific surface area range of  $H_4$ -loop behaviour was observed as depicted in Figure 7.2b. From the data in Figure 7.2b, it is apparent that the low pressure hysteresis loop (LPH) regularly relates with the expansion and contraction of adsorbent (ZSM-5 mesoporous), which produce slight inelastic distortion of the ZSM-5 mesoporous morphology, which usually appeared in the zeolites samples (Valero-Romero et al., 2016).

The adsorption/desorption isotherms of ZSM-5 mesoporous embedded PDCTC ligand also exhibited a type of  $H_4$  hysteresis loop as depicted in Figure 7.2c, suggesting that the mesopore structure was preserved in the framework after the treatment procedure without collapsing; This further decreased the pore diameter and the surface area of ZSM-5 mesoporous/ PDCTC to  $4.0 \text{ nm}$  and  $580 \text{ m}^2 \text{ g}^{-1}$ , respectively due to the inclusion of a significant amount of organic ligand moiety into the inner pores of the mesoporous carrier. Also there were no significant change in the pore distribution curve as depicted in Figure 7.2d. These outcomes point that the ligand PDCTC is efficaciously anchored into ZSM-5-mesoporous.



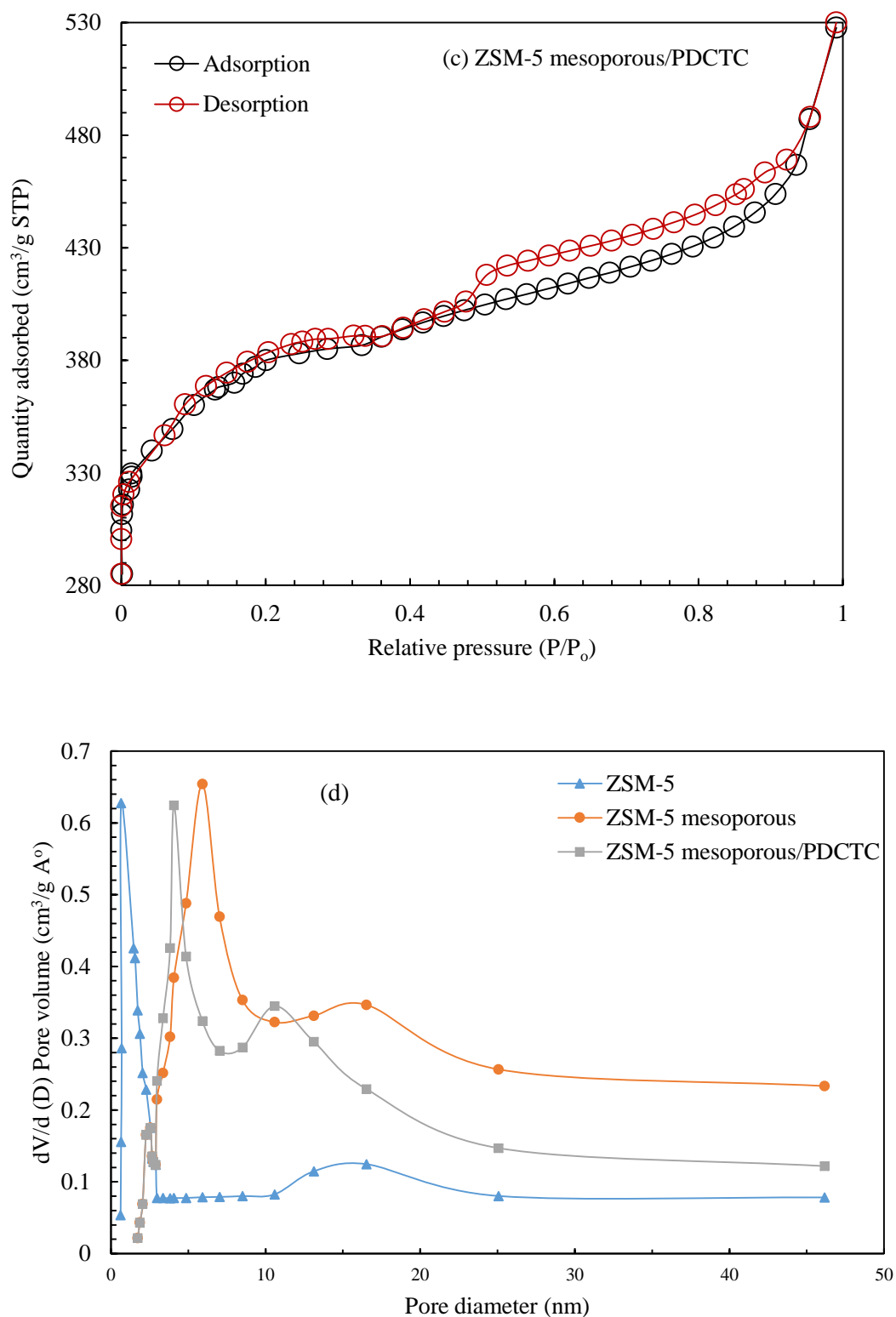


**Figure 7-2**  $N_2$  adsorption-desorption isotherms curves (a) ZSM-5, (b) mesoporous ZSM-5 (c) mesoporous ZSM-5 conjugate adsorbent (MzCA) and corresponding the BJH pore size distribution curves of samples (d)

**Table 7-1** Specific surface area ( $S_{\text{BET}}$ ), pore volume (V) and average pore diameter (D) for ZSM-5, ZSM-5mesopoures and ZSM-5 mesoporous/ PDCTC

Catalyst	$S_{\text{BET}}$ ( $\text{m}^2 \text{g}^{-1}$ ) <sup>a</sup>	V ( $\text{cm}^3 \text{g}^{-1}$ ) <sup>b</sup>	D (nm) <sup>c</sup>
ZSM-5	311	0.014	8.6
ZSM-5 mesoporous	1151	0.2	15.2
ZSM-5 mesoporous/ PDCTC (MzCA)	580	0.62	4.0

<sup>a</sup> The specific surface area was calculated by BET method.

<sup>b</sup> The pore volume was obtained from the BJH Desorption cumulative volume of pores between 1.0000 nm and 50.0000 nm diameter.

<sup>c</sup> The average pore diameter was evaluated using the desorption branch of the isotherm and BJH model.

### 7.3.2 Fourier-transformed infrared spectroscopy (FTIR) analysis

The organic functional groups of PDCTC ligand were investigated using the FTIR spectroscopy. The sample was analysed three times at different environmental conditions to assure that the ligand has a good stability. It can be observed from Figure 7.3 that the intense high peaks existed at  $2980 \text{ cm}^{-1}$  and  $3150 \text{ cm}^{-1}$  indicating the possible interference from a hybridized carbon  $\text{Sp}^3$  -C-H and  $\text{Sp}^2$  =C-H stretch bonds respectively; while, a low peak was observed at  $3265 \text{ cm}^{-1}$  confirming the presence of amide group (O=C-N) in the ligand chemical structure. Another high strong peak observed at  $1520 \text{ cm}^{-1}$  indicated the interference of unsaturated Alkenes (C=C) in the aromatic rings, which are considered the major structural compound of the ligand. Another strong intense peak observed near  $1600 \text{ cm}^{-1}$  indicated an existing amine group (C-N) bending vibration. Moreover, the thiocarbonyl (C=S) may also interfere at  $1100 \text{ cm}^{-1}$ ; this possible includes the corresponding heterocyclic compounds. The Meta substitution patterns for aromatic hydrocarbons on a single ring observed at  $800, 690 \text{ cm}^{-1}$  caused ring hydrogen atoms. All these intense peaks confirmed the original structural ligand was successfully synthesized. The synthesis and result of this procedure have been similarly reported in previous study (David & Priyadharsini, 2015).

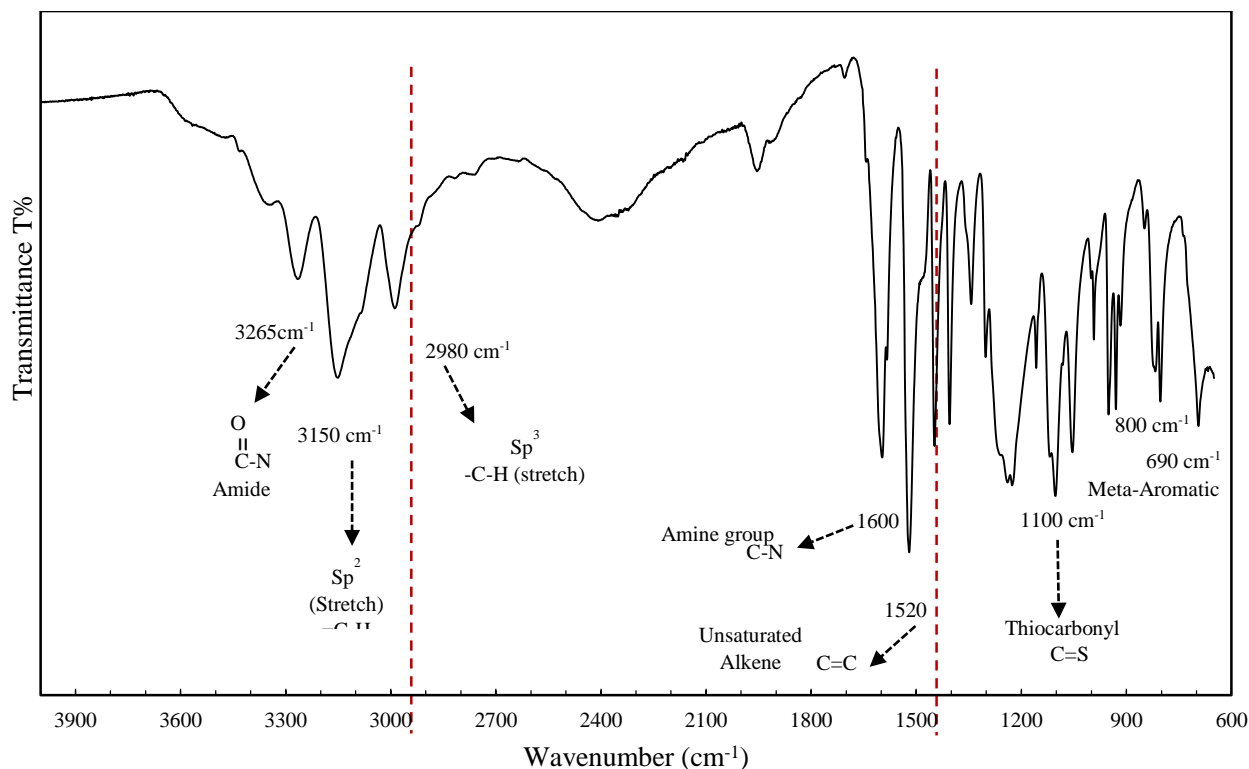


**Figure 7-3** Specific functional groups of PDCTC ligand analysed by FTIR spectroscopy

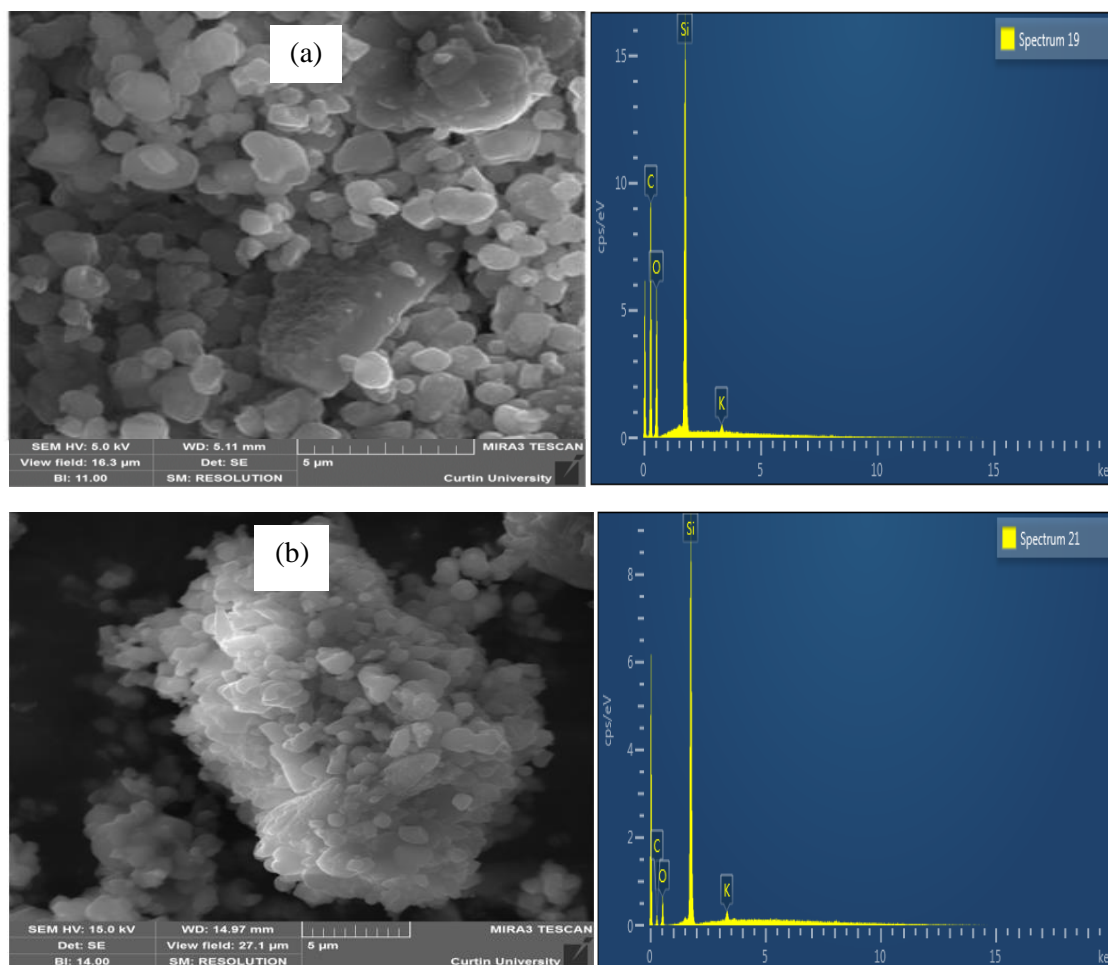
### 7.3.3 FESEM analysis

High magnification images sizes 5  $\mu\text{m}$  and EDX analyses of commercial zeolite, ZSM-5 mesoporous and the synthesized MzCA before and after use in the adsorption experiments were investigated as illustrated in Figure 7.4(a-d). The commercial cubic zeolite morphology were shown in Figure 7.4a, exhibiting a high silica ratio as depicted in the attached EDX analysis. After the treatment of the commercial ZSM-5, large particle size of ZSM-5 mesoporous was obtained as spherical cluster-like shapes as shown in Figure 7.4b. This cluster contains high porosity with channels and cavities, which provides abundant silanol groups (Si-OH). The ratio of the silica content remained at higher in the ZSM-5 mesoporous, indicating no significant change in the morphology through ZSM-5 treatment process as shown in the attached EDX analysis of Figures 7.4a and b. After the functionalized process, the FESEM analysis of the MzCA catalyst morphology showed that the organic ligand has a good binding onto the ZSM-5 mesoporous structure as illustrated in Figure 7.4c, and the EDX results confirmed that the ligand components contains nitrogen and sulphur as well as the



intact mesoporous morphology. This result indicated that the functionalized process was successfully achieved with no loss of the ligand molecule.

Also after using MzCA in the adsorption experiments, the FESEM and EDX characterisations were also investigated. The data revealed that the white brightness of  $\text{Pb}^{2+}$  onto surface of MzCA particles were formed as a  $[\text{Pb}^{2+}\text{-PDCTC ligand}]^{n+}$  complexes on the mesopore adsorbent as shown in Figure 7.4d. With further investigation, the EDX spectrum in Figure 7.4d confirmed evidence that the foreign heavy metal ions ( $\text{Zn}^{2+}$ ,  $\text{Cd}^{2+}$ ,  $\text{Al}^{3+}$ ,  $\text{Fe}^{3+}$ ,  $\text{Ca}^{2+}$ ,  $\text{Ag}^{+1}$ ,  $\text{K}^{+1}$ ,  $\text{Na}^{+1}$ ,  $\text{Hg}^{2+}$ ,  $\text{Mn}^{2+}$ ,  $\text{Co}^{2+}$ ,  $\text{Cu}^{2+}$ ) were not adsorbed by the MzCA catalyst; however, a little of  $\text{Cu}^{2+}$  was adsorbed as illustrated in the attached of EDX Figure 7.4d. The most striking observation that emerged from this data is the high selective adsorption capability of MzCA towards  $\text{Pb}^{2+}$ .



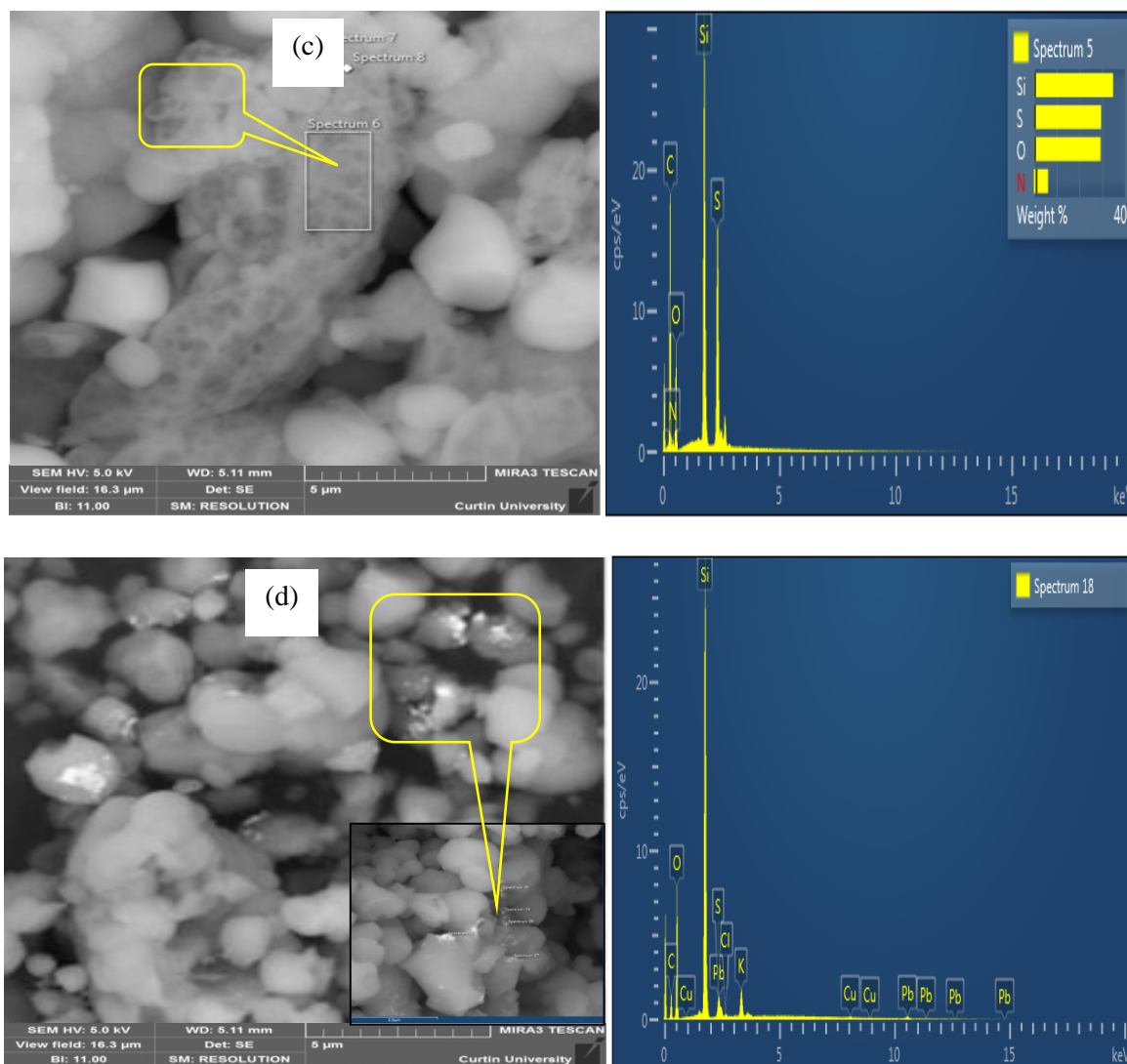


**Figure 7-4** FESEM images of ZSM-5 (a), ZSM-5 mesoporous (b) and micrograph of PDCTC incorporated into composite adsorbent (c), MzCA after used in the adsorption process (d)

### 7.3.4 Lead ( $Pb^{2+}$ ) detection

The performance of selectivity and sensitivity of ultra-trace  $Pb^{2+}$  for the substantial color change were assessed at different pH values. Accordingly, the absorbance spectra of  $[Pb^{2+}-PDCTC]^{n+}$  complexes by the mesoporous adsorbent were investigated using  $2.0 \text{ mg L}^{-1} Pb^{2+}$  solution at the pH range of 1.5-11.7; the solutions' pH was adjusted using specific buffer reagents as indicated in Section 7.2.5. The absorbance spectra of the  $[Pb^{2+}- PDCTC]^{n+}$  complexes solution was observed over a wide pH range precisely as seen in Figure 7.5 at  $\lambda = 440 \text{ nm}$ ; the maximum net absorbance was

evaluated at pH 6.0. The data also proposed that the quantity of the meso-adsorbent is a contributing factor for achieving a good color separation between the meso-adsorbent “Blank” and  $[\text{Pb}^{2+}\text{-PDCTC}]^{n+}$  complexes “Sample” even at a trace-level of  $\text{Pb}^{2+}$  concentrations. It is also clarified that the complex reaction occurs at “pH= 6.0”. As shown in Figure 7.5, the absorbance intensity was dramatically decreased below pH= 6.0. When pH value was 6.0, the best possible spectrum intensity was achieved; while, low spectrum intensity was obtained at pH values over 6.0 (see Figure 7.5), indicating that the hydrolysis of  $\text{Pb}^{2+}$  formed water insoluble lead hydroxide/ or oxide (Awual & Hasan, 2014a, 2014b; Awual, Hasan, & Shahat, 2014). Moreover, low spectrum intensity was also observed in the acid region, confirming that  $\text{H}_3\text{O}^+$  ions were interfering in the aqueous solution. The signal intensity and the color change suggest that the  $[\text{Pb}^{2+}\text{-PDCTC}]^{n+}$  complexes are strongly anchored within the stable complex formation under appropriate pH condition. It is important to note that the pH 6.0 was selected as the superior experimental condition in the recognition procedures due to the sensitivity and selectivity at this pH. The detective response time of the  $[\text{Pb}^{2+}\text{-PDCTC}]^{n+}$  in equilibrium color optimization was 30 min.

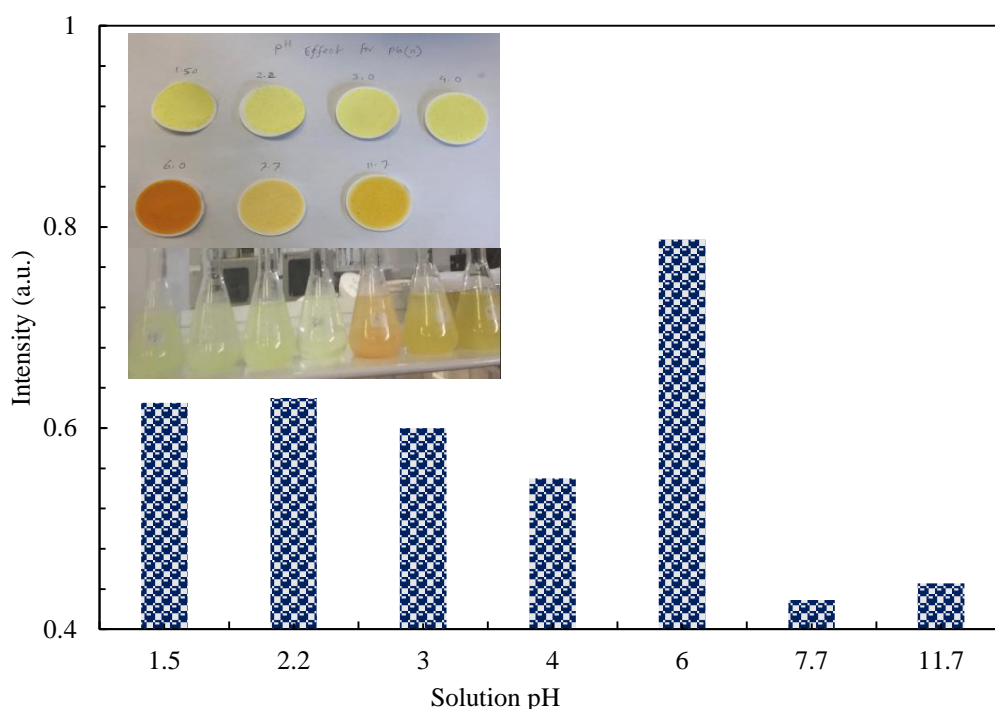


**Figure 7-5** Effect of pH on the  $\text{Pb}^{2+}$  during the absorbance spectra measurement of  $[\text{Pb}^{2+}\text{-PDCTC}]^{n+}$  complexes solution at  $\lambda = 440 \text{ nm}$ , concentration of  $2.0 \text{ mg L}^{-1}$  of  $\text{Pb}^{2+}$ , 10 mg of MzCA at  $25^\circ\text{C}$  in 20 ml volume for 30 minutes

The signal color change intensity of the conjugated adsorbent was measured during the charge transmission (intense  $\pi$ - $\pi$  transition) of the reflection band of the  $[\text{Pb}^{2+}\text{-PDCTC}]^{n+}$  complexes formation, which has increased by an increase in the  $\text{Pb}^{2+}$  concentration as illustrated in Figure 7.6. The absorbance color was remarkably changed from yellowish, yellowish white, to orange, which can be obviously recognized by the naked eye. It is noteworthy that the equilibrium color formation between the conjugated adsorbent and  $\text{Pb}^{2+}$  corresponds to the increase in signal intensity, which imply the detective sensitivity in ultra-trace concentration of  $\text{Pb}^{2+}$  from  $\text{mg L}^{-1}$  to  $\mu\text{g L}^{-1}$  can be achieved without using sophisticated instruments. It is additionally observed that the color intensity of  $\text{Pb}^{2+}$  with conjugated adsorbent at  $\lambda = 440$  nm was stable during the complex formation. Therefore, the detection of  $\text{Pb}^{2+}$  based on the analytical color signal intensity is a technological benefit due to its ease of use, cost-effectiveness, precision and sensitivity.

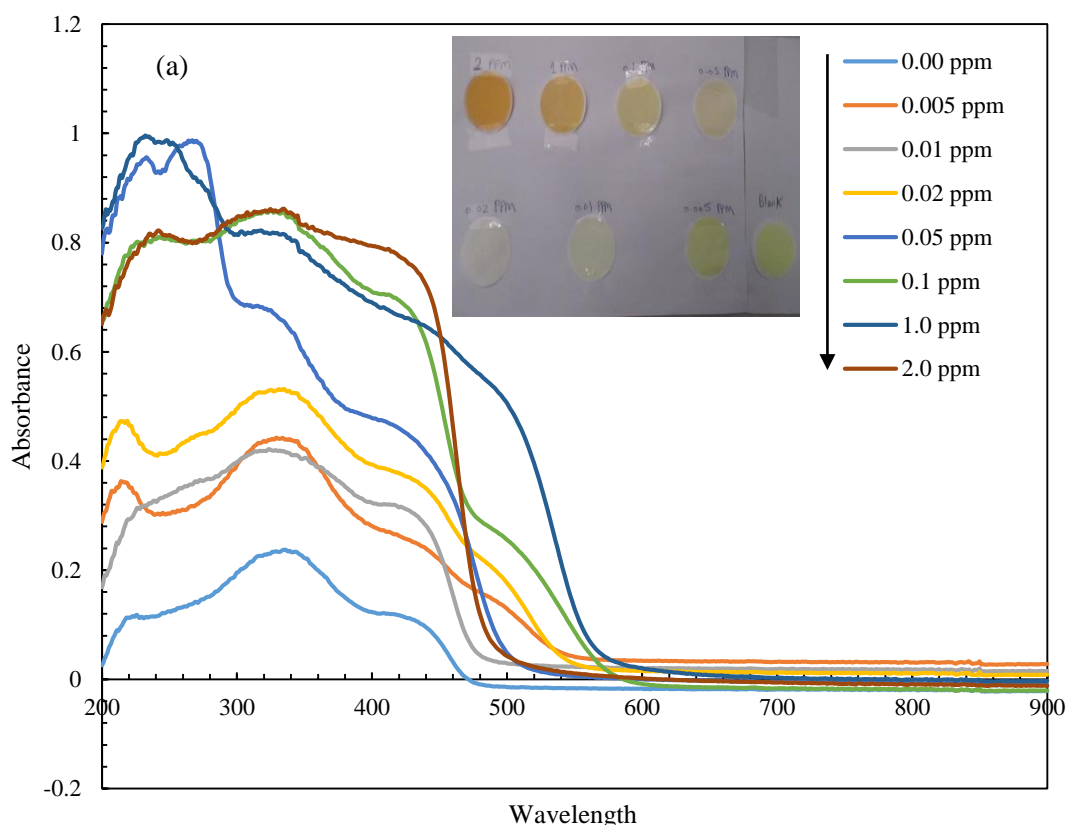


**Figure 7-6** The optimization of the change of different  $\text{Pb}^{2+}$  concentrations at pH 6.0

From Figure 7.7, the calibration curves of  $[\text{Pb}^{2+}\text{-PDCTC}]^{n+}$  complexes matrix free and  $[\text{Pb}^{2+}\text{-PDCTC}]^{n+}$  with conjugated adsorbent ‘matrix’ were plotted and determined under the most efficient conditions; while, the linear correlation was determined possibly at lower concentration ranges of  $\text{Pb}^{2+}$  as depicted in Figure 7.7 (inset).

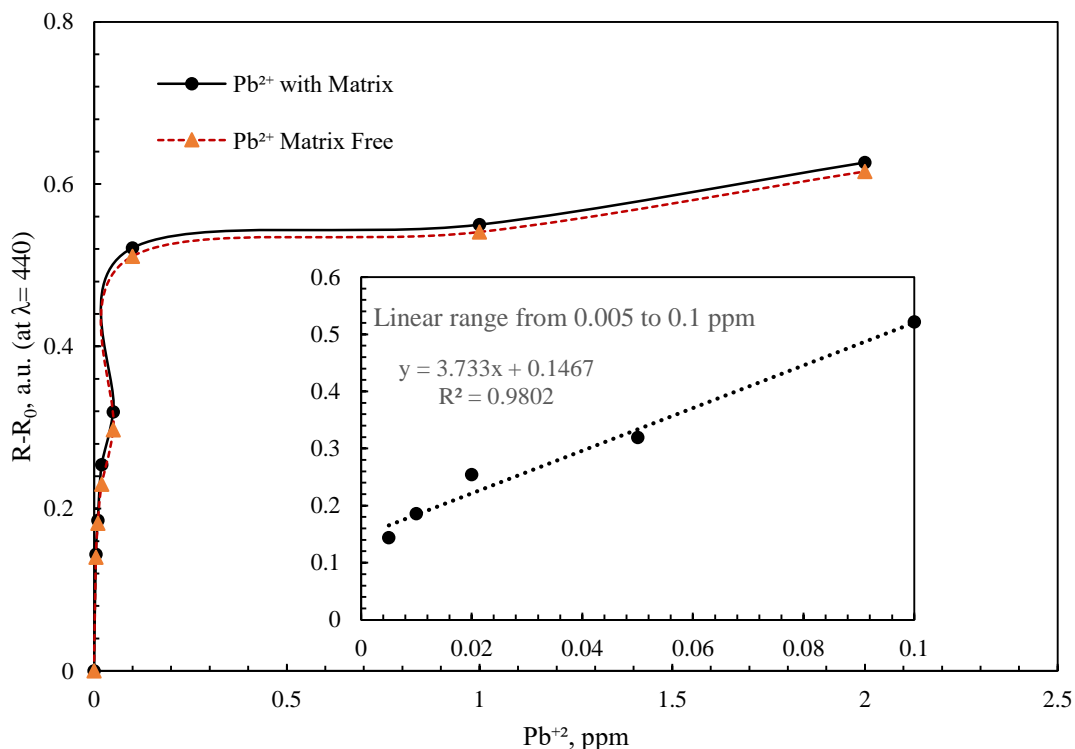


**Figure 7-7** The calibration curve of  $\text{Pb}^{2+}$  concentrations with spectral absorbance at  $\lambda= 440$  nm. The inset in graph (B) shows the low limited responses for  $\text{Pb}^{2+}$  with a linear fit in the  $\text{Pb}^{2+}$  concentration range. The  $R$  and  $R_0$  represented the absorbance signal responses of the solution after and before addition of  $\text{Pb}^{2+}$

The data indicated that the various concentrations of  $\text{Pb}^{2+}$  can be recognized with high sensitivity; additionally, the nonlinear correlation at high concentration of  $\text{Pb}^{2+}$  confirmed that the low concentration systems was applied to detect higher concentrations of  $\text{Pb}^{2+}$ . As illustrated in Figure 7.7 the linear calibration plot shows an excellent recognition range with correlation coefficient value ( $R^2= 0.9802$ ) from the value of the linear correlation concentrations in the range from 0.10 to 0.005  $\text{mg L}^{-1}$  can be detected; however, a nonlinear curve was observed when the  $\text{Pb}^{2+}$  concentration was above 0.10  $\text{mg L}^{-1}$  resulting in the saturation effect. The detection limit ( $L_D$ ) of  $\text{Pb}^{2+}$  using the conjugated adsorbent was 5.0  $\mu\text{g L}^{-1}$  according to Eq. (7.2), which confirm that the conjugated adsorbent can detect ultra-trace  $\text{Pb}^{2+}$  level concentrations even in the presence of the many sample matrices (calibration curve with dash line).

The ion selectivity is an indispensable parameter in sensing technique because various cations and anions are extensively reachable in environmental water samples. Therefore, the influence of competing foreign ions on Pb<sup>2+</sup> detection using conjugated adsorbent was investigated under optimum condition. Various concentrations of these competing ions (Zn<sup>2+</sup>, Cd<sup>2+</sup>, Al<sup>3+</sup>, Fe<sup>3+</sup>, Ca<sup>2+</sup>, Ag<sup>+</sup>, K<sup>+</sup>, Na<sup>+</sup>, Hg<sup>2+</sup>, Mn<sup>2+</sup>, Co<sup>2+</sup>, & Cu<sup>2+</sup> ions) were investigated with a constant concentration of 2.0 mg L<sup>-1</sup> Pb<sup>2+</sup> solution. The color formation and signal intensity of each ion are illustrated in Figure 7.8. The spectral intensity of the blank sample and additional foreign ions was calculated at λ= 440 nm. The data revealed that the signal intensity of the blank sample was unchanged expect with the addition of Pb<sup>2+</sup>. It was also observed that the addition of chloride, carbonate, sulfite, phosphate, sulfate, bicarbonate, nitrate and perchlorate reduced the signal intensity. Therefore, the conjugated adsorbent was confirmed to specifically selective toward Pb<sup>2+</sup> forming a stable complex with PDCTC ligand at pH 6.0. The tolerance limit of cations and anions were summarized in Table 7.2.

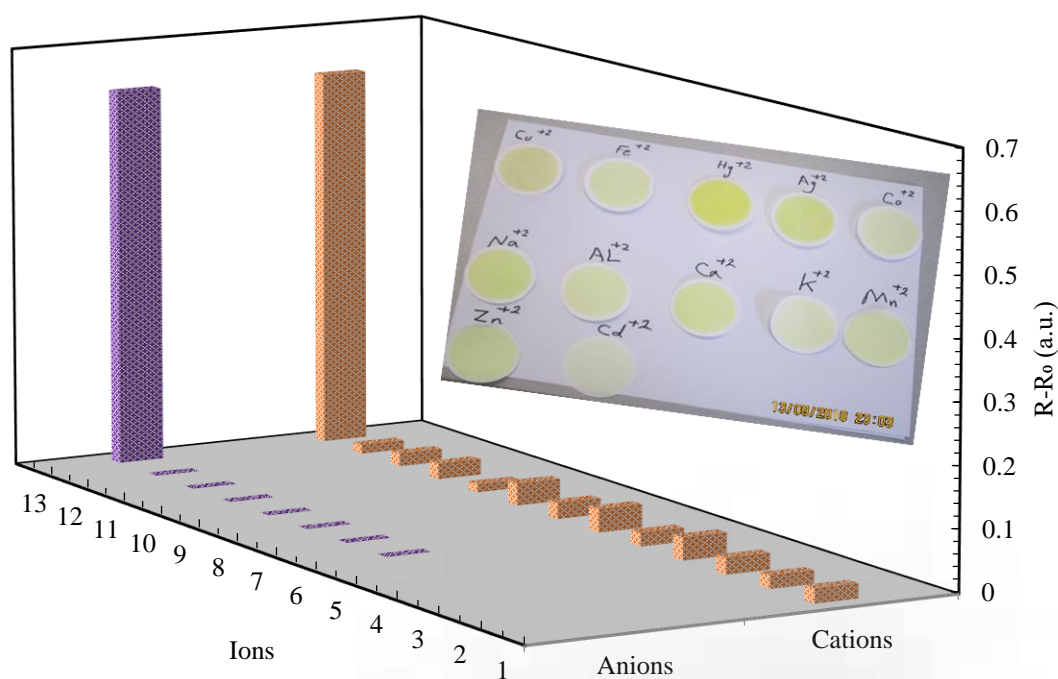


**Figure 7-8** Effect of competing ions (cations/ anions) when the Pb<sup>2+</sup> concentration was 2.0 mg L<sup>-1</sup>, the cations concentration was 20 mg L<sup>-1</sup>. The listed foreign ions area: (1) Cu<sup>2+</sup>, (2) Fe<sup>3+</sup>, (3) Hg<sup>2+</sup>, (4) Ag<sup>2+</sup>, (5) Co<sup>2+</sup>, (6) Na<sup>+</sup>, (7) AL<sup>3+</sup> (8) Ca<sup>2+</sup>, (9)K<sup>+</sup>, (10)Mn<sup>2+</sup>, (11)Zn<sup>2+</sup>, (12 ) Cd<sup>2+</sup> (blank and (13) Pb<sup>2+</sup> 2.0 mg L<sup>-1</sup>. The different concentrations of interfering anions listed in order (6–13): (6) Cl<sup>-</sup>, (7) HCO<sub>3</sub><sup>-</sup>, (8) NO<sub>3</sub><sup>-</sup>, (9) CO<sub>3</sub><sup>2-</sup>, (10) PO<sub>4</sub><sup>3-</sup>, (11) SO<sub>4</sub><sup>2-</sup>, (12) SO<sub>3</sub><sup>2-</sup>, (13) SCN<sup>-</sup>

**Table 7-2** Tolerance limit for competing cations and anions adding 2.0 mg L<sup>-1</sup> of Pb<sup>2+</sup> detection with conjugated adsorbent

Tolerance limit for cations in solution (mg L <sup>-1</sup> )												
Zn <sup>2+</sup>	Cd <sup>2+</sup>	Al <sup>3+</sup>	Fe <sup>3+</sup>	Mg <sup>2+</sup>	Ca <sup>2+</sup>	Ag <sup>1+</sup>	K <sup>1+</sup>	Na <sup>1+</sup>	Hg <sup>2+</sup>	Mn <sup>2+</sup>	Co <sup>2+</sup>	Cu <sup>2+</sup>
60	77	120	87	45	30	100	46	90	55	100	34	67
Tolerance limit for anions in solution (mg L <sup>-1</sup> )												
Cl <sup>-</sup>		600										
HCO <sub>3</sub> <sup>-</sup>		450										
NO <sub>3</sub> <sup>-</sup>		500										
CO <sub>3</sub> <sup>2-</sup>		680										
PO <sub>4</sub> <sup>3-</sup>		800										
SO <sub>4</sub> <sup>2-</sup>		750										
SO <sub>3</sub> <sup>2-</sup>		650										

### 7.3.5 Lead (Pb<sup>2+</sup>) sorption parameters

#### 7.3.5.1 Effect of pH

The solution's acidity plays a significant role in adsorbing Pb<sup>2+</sup> onto MzCA surface, this is because ionization on the adsorbent during the sorption process and is necessary better solubility of Pb<sup>2+</sup> and reverse ions concentration to obtain a ligand's complexation functional groups (Amuda, Giwa, & Bello, 2007; Hernández-Morales et al., 2012; Shahat et al., 2018). The pH effects on the sorption efficiency of Pb<sup>2+</sup> solutions was studied on a wide range between pH of 1.5 to 11.7.

The results are illustrated in Figure 7.9. In strong acidic pH 1.5, the sorption efficiency was a minimal 5.7% because of the consistency of H<sub>3</sub>O<sup>+</sup> ions onto the adsorbent surface; however, the sorption efficiency behavior was dramatically increased from 8 % to 98.9% by increasing the pH from 2.2 to 6.0 indicating the disappearance of H<sub>3</sub>O<sup>+</sup> ions from the surface of the adsorbent (Awual, 2016a; Awual & Hasan, 2014a, 2014b). To compare with the basic region, the sorption efficiency was significantly decreased



above pH 6.0 due to the presence of water-insoluble of lead hydroxide/oxide which is present in the alkaline region. Judging from Figure 7.9, the higher Pb<sup>2+</sup> sorption efficiency of 98.9% and 78.7%, was obtained between pH 6.0 to 7.7 respectively. This pH region is appropriate because no precipitation took place in the Pb<sup>2+</sup> sorption system. Therefore, pH 6.0 was selected as the optimum pH for high sorption efficiency using the conjugated mesoporous adsorbent and also for analyzing other factors for subsequent sorption ions experiment in this chapter.

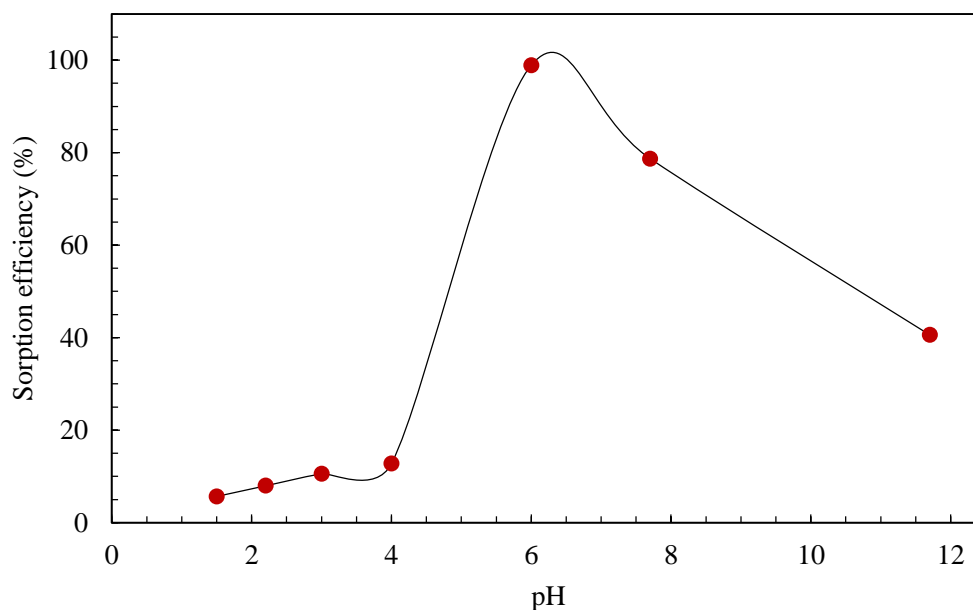


**Figure 7-9** The effect of pH on the sorption efficiency of Pb<sup>2+</sup> when the initial Pb<sup>2+</sup> concentration was 2.0 mg L<sup>-1</sup>

### 7.3.5.2 Effect of contact time

Convenient contact time is a fundamental parameter to determine the maximum sorption efficiency and the kinetic model of the conjugated adsorbent. Hence, the equilibrium contact time was evaluated to detect the maximum Pb<sup>2+</sup> sorption efficiency under optimum conditions. The data revealed that the beginning 60% of Pb<sup>2+</sup> sorption was observed after 10 min as shown in Figure 7.10. The outcomes additionally revealed that the preliminary sorption was rapid and subsequently slowdown until it attained an equilibrium sorption. The fast sorption is perhaps because of the high specific surface area which provided several active sites to make a strong binding complexation onto the adsorbent surface. Similar sorption behavior were also reported in different literatures (Arshadi et al., 2017; Benhima, Chiban, Sinan, Seta, & Persin, 2008; Futralan et al., 2011; Motsa, Mamba, Thwala, & Msagati, 2011; J. Zhou et al., 2018; Y. Zhou, Yu, & Jiang, 2017). The conjugated adsorbent



comparatively demonstrated fast kinetics for  $\text{Pb}^{2+}$  sorption with the equilibrium time at 60 minutes. The distributed homogeneity of PDCTC ligand onto the conjugated adsorbent surface makes  $\text{Pb}^{2+}$  effortlessly linked with the sorption sites which are trapped to fabricate a stable complex. To obtain a maximum sorption capacity, an equilibrium contact time of 2 h was chosen with a concentration of  $2.0 \text{ mg L}^{-1}$   $\text{Pb}^{2+}$  in 20 ml solution.

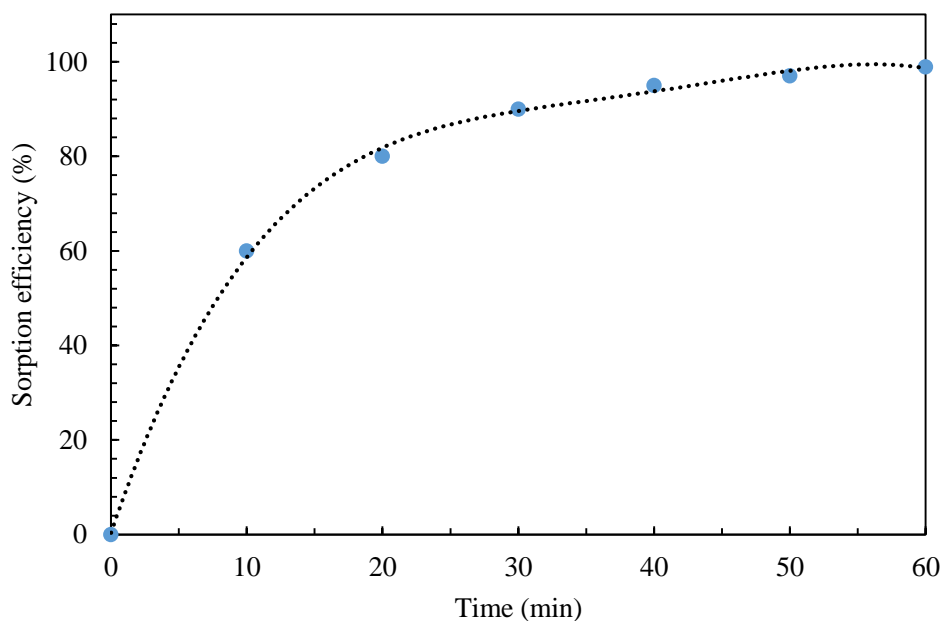


**Figure 7-10** Effect of reaction time on the sorption efficiency of  $\text{Pb}^{2+}$  when the initial concentration of  $\text{Pb}^{2+}$  was  $2.0 \text{ mg L}^{-1}$

### 7.3.5.3 Equilibrium sorption isotherm

The sorption isotherm basically clarifies the relevance between  $\text{Pb}^{2+}$  concentrations and the quantity of  $\text{Pb}^{2+}$  adsorbed on the solid phase at equilibrium. To investigate this, 20 ml of sample solutions containing different concentrations of  $\text{Pb}^{2+}$  ( $8.0$ -  $50.0 \text{ mg L}^{-1}$ ) adjusted to pH 6.0 and equal amount of the conjugated adsorbent 10 mg. The experiments was conducted using a batch approach for 2 h. After equilibrium was achieved, the filtrated solutions were tested via ICP-AES to consider the amount of  $\text{Pb}^{2+}$  left in the aqueous solution. From Figure 7.11, the data shown that the uptake efficiency rate of  $\text{Pb}^{2+}$  was increased as the concentration  $\text{Pb}^{2+}$  increased until it reached a plateau corresponding to the maximum sorption capacity. To understand this behaviour of the sorption system, several sorption isotherms are investigated to evaluate  $\text{Pb}^{2+}$  interference with the conjugated adsorbent. The Langmuir sorption isotherm is one of the most valid model for the monolayer, they propose no

corrugations on the conjugate adsorbent surface suggesting the homogenous surface in terms of all sorption sites are energetically equivalent. The Langmuir equation stated below was applied to this sorption system:

$$C_e/q_e = 1/(K_L q_m) + \left(\frac{1}{q_m}\right) C_e \quad (7.5)$$

where  $C_e$  ( $\text{mg L}^{-1}$ ) is the equilibrium concentration of  $\text{Pb}^{2+}$ ,  $q_e$  ( $\text{mg/g}$ ) is the amount of  $\text{Pb}^{2+}$  adsorbed per unit mass of conjugate adsorbent at equilibrium,  $K_L$  ( $\text{L mg}^{-1}$ ) is the Langmuir constant related to the affinity of binding sites and also the measurement of the stability bond formed between  $\text{Pb}^{2+}$  and conjugated adsorbent under optimum conditions, and  $q_m$  ( $\text{mg g}^{-1}$ ) is the maximum quantity of the adsorbed  $\text{Pb}^{2+}$  per unit mass of adsorbent (capacity parameter). The sorption capacity  $q_m$  ( $\text{mg/g}$ ) and  $K_L$  ( $\text{L mg}^{-1}$ ) was calculated by the slope and intercept of the linear plot by  $C_e / q_e$  versus  $C_e$  as depicted in Figure 7.11 (inset). The data show that the sorption process (plateau plot) coincided in the Langmuir isotherm model, and the maximum sorption capacity of the conjugate adsorbent was estimated to be  $15.75 \text{ mg/g}$  with high correlation coefficient ( $R^2 = 0.9355$ ). The sorption Langmuir coefficient  $K_L$ , which is associated with the apparent sorption energy, was evaluated to be  $K_L = 0.65 \text{ L mg}^{-1}$ .

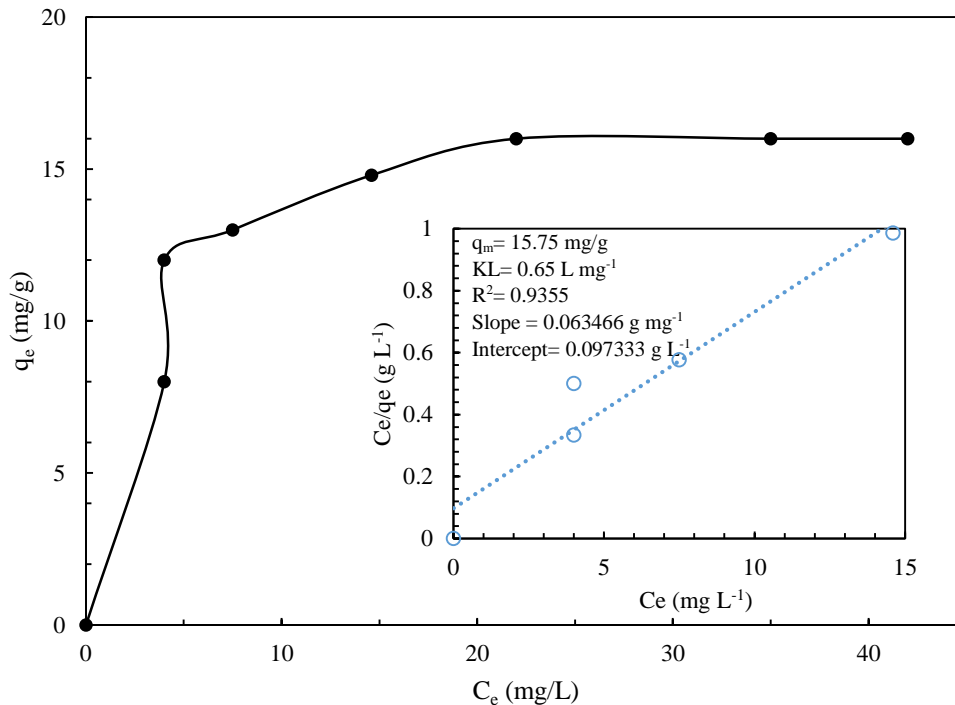


**Figure 7-11** Adsorption isotherm of  $\text{Pb}^{2+}$  as fitted by the Langmuir isotherms model with the linear form (inset). The initial concentrations of  $\text{Pb}^{2+}$ :  $8.0\text{-}50.0 \text{ mg L}^{-1}$ ; stirring time: 2h; conjugated adsorbent amount is 10 mg; the solution volume is 20 ml

**7.3.5.4 Effect of foreign competing ions**

In aquatic ecosystem, the presence of many co-existing metal ions such as  $\text{Hg}^{2+}$ ,  $\text{Zn}^{2+}$ ,  $\text{Al}^{3+}$ ,  $\text{Cd}^{2+}$ ,  $\text{Co}^{2+}$ ,  $\text{Ag}^+$ ,  $\text{Fe}^{3+}$ ,  $\text{Ca}^{2+}$ ,  $\text{Na}^+$ ,  $\text{K}^+$ ,  $\text{Mn}^{2+}$ , &  $\text{Cu}^{2+}$  are also competing with lead ( $\text{Pb}^{2+}$ ) in the adsorbed operation; therefore, the sorption selectivity of  $\text{Pb}^{2+}$  by the conjugated adsorbent was studied. In this experiment, a mixed solution containing the various competing ions at a concentration of  $20 \text{ mg L}^{-1}$  each and  $2.0 \text{ mg L}^{-1}$  of  $\text{Pb}^{2+}$  was investigated. The foreign competing ions multi-mixture system is described in and data shown in Figure 7.12. The result confirmed that  $\text{Pb}^{2+}$  was selectively adsorbed by 98.9% with slightly lower sorption for competing ions of  $\text{Al}^{3+}$ ,  $\text{Ag}^{2+}$  and  $\text{Co}^{2+}$  were observed, confirming that the conjugate adsorbent possess high selectivity for  $\text{Pb}^{2+}$ . The proposed complex mechanism is depicted in Figure 7.13.

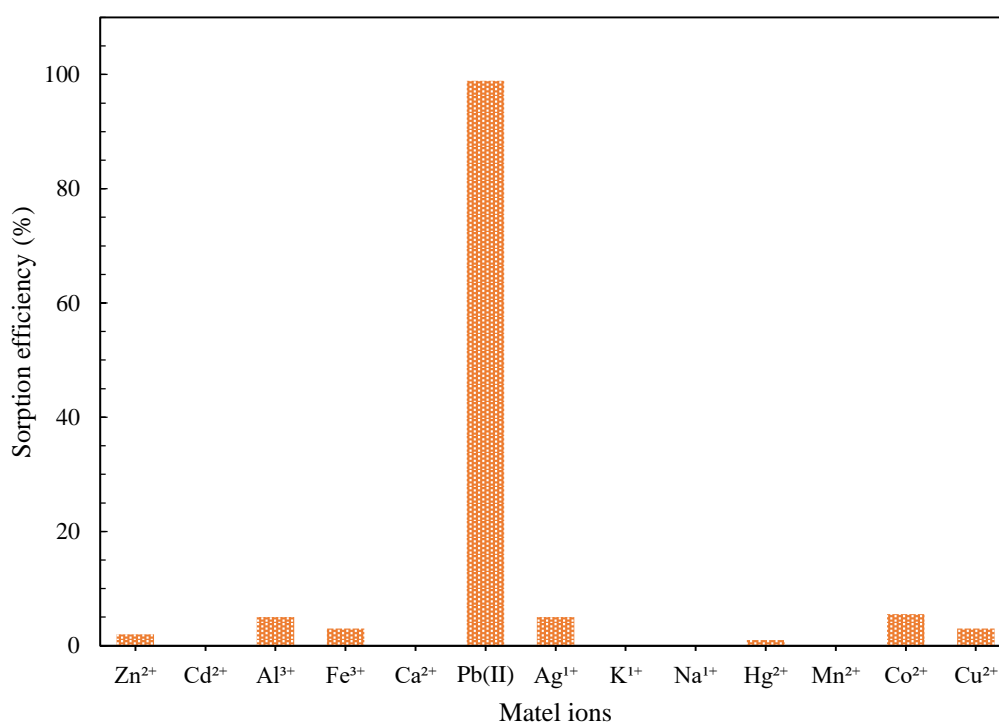


**Figure 7-12** The sorption efficiency of  $\text{Pb}^{2+}$  in the presence of different metal ions in aqueous media

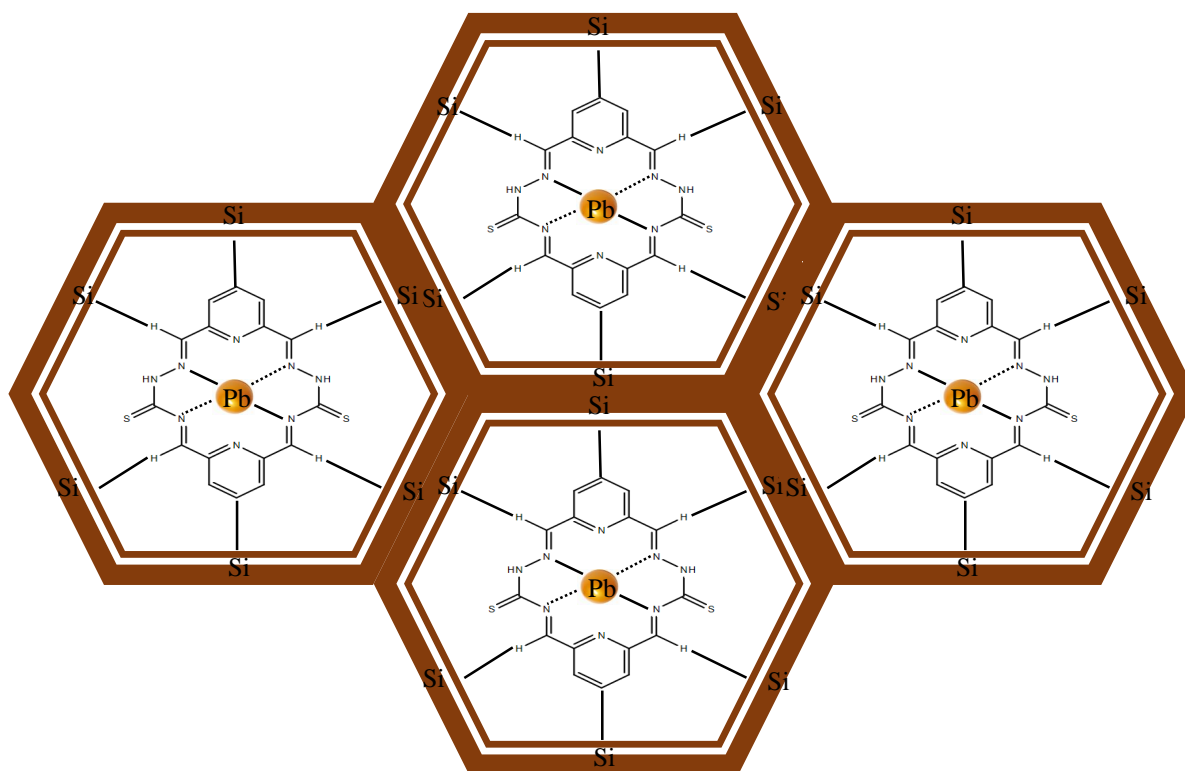


**Figure 7-13** The proposed stable complex formation of  $Pb^{2+}$  and PDCTC ligand at optimum conditions

#### 7.4 Elution and regeneration

Extracted of the metal ions from the conjugate adsorbent is a pivotal parameter that makes the sorption process of this technology suitable and cost-effective (Awual, 2016a, 2017a; Awual & Ismael, 2014; Md Rabiul Awual, Mohamed Ismael, et al., 2013; Md Rabiul Awual, Tsuyoshi Yaita, Sherif A El-Safty, Hideaki Shiwaku, Yoshihiro Okamoto, et al., 2013; Md Rabiul Awual, Tsuyoshi Yaita, & Hideaki Shiwaku, 2013; M. Shenashen et al., 2013). The reuse of the adsorbent is a substantial stage for its design and used in appropriate large scale process. The elution process involves the extraction of the  $Pb^{2+}$  from the conjugated adsorbent, which concurrently regenerates into the preliminary form for further use for adsorbing  $Pb^{2+}$ . From the experimental data, 0.10 M HCl was found to be most appropriate reagent to extract  $Pb^{2+}$  from conjugate adsorbent without a considerable deterioration to its original performance. The proposed elution mechanism is illustrated in Figure 7.14.

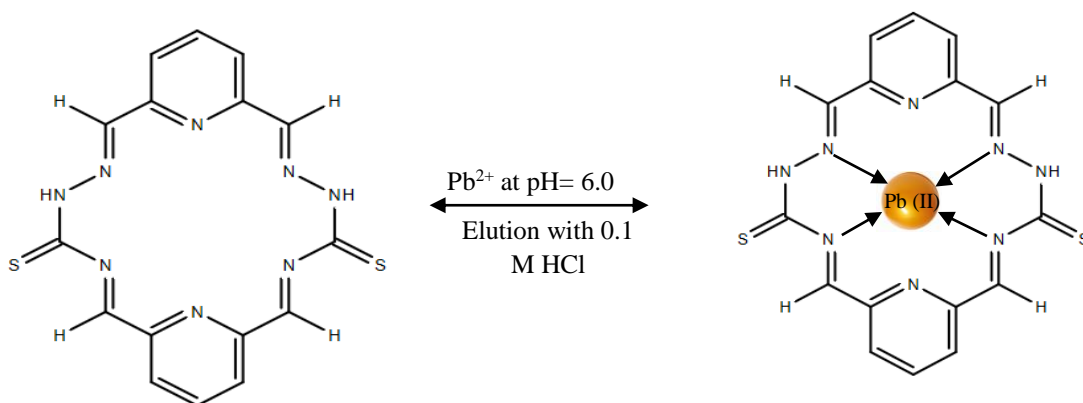


**Figure 7-14** The stable complex formation of  $Pb^{2+}$  and PDCTC ligand at pH 6.0 and elution/regeneration is 0.1 M HCl eluent

The sorption/elution procedures for eight cycles with sorption efficiency in each cycle were evaluated and compared to the first sorption cycle as depicted in Figure 6.10(b). The data showed that the sorption efficiency of the adsorbent gradually decreased to 93.5% after the eighth cycles (Fig. 7.15), indicating the several reuses will not affect the sorption efficiency for the  $Pb^{2+}$ - conjugated mesoporous adsorbent.

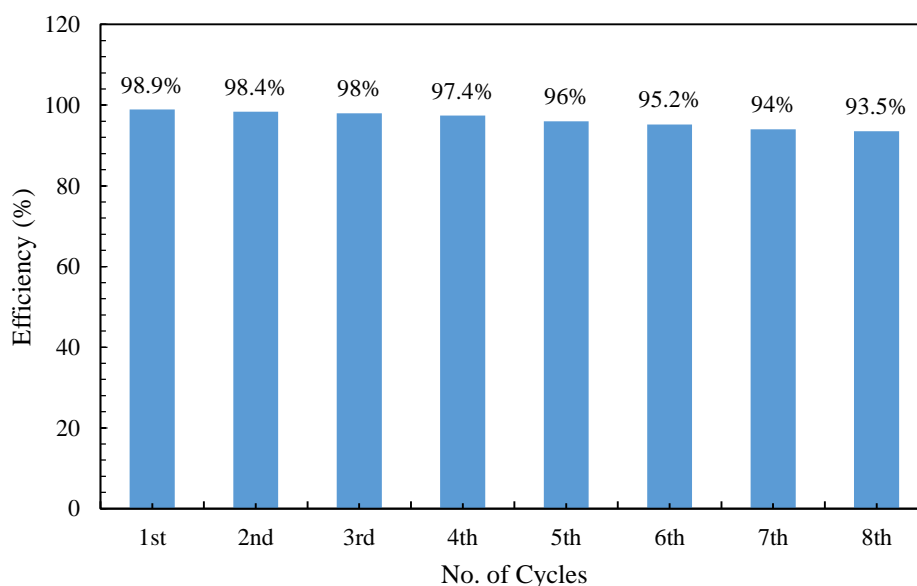


**Figure 7-15** The performance of the regenerated conjugated mesoporous adsorbent after conducting several cycles using 0.1 M HCl eluent

## 7.5 Summary

The purpose of the current chapter was designed a visual conjugate adsorbent catalyst using functionalized organic ligand anchored ZSM-5 mesoporous to detect ultra-trace amount of  $Pb^{2+}$  in aqueous media. To achieve this goal, the organic ligand

of 2,6-Pyridinedicarboxaldehyde-Thiosemicarbazone (PDCTC) was prepared and then fabricated onto ZSM-5 mesoporous, which is prepared by direct templating technique. This conjugated adsorbent (MzCA) showed a remarkable colour intensity that based on charge transfer transduction to achieve visual detection of  $\text{Pb}^{2+}$  by the bare eye without using sophisticated instruments. The influence of several factors such as colour optimization, limit of detection, solution pH, adsorption capacity, contact time, initial concentration of  $\text{Pb}^{2+}$  on the detection and selectivity were evaluated. The regeneration and elution process for the conjugated adsorbent in acidic medium was additionally investigated to assess the conjugated adsorbent as a cost effective. The detection limit of  $\text{Pb}^{2+}$  was  $5.0 \mu\text{g L}^{-1}$  with no considerable interference of foreign competing ions. The MzCA followed the equivalent monolayer sorption represented by the Langmuir model and the maximum sorption capacity was  $15.75 \text{ mg/g}$ . The sorption efficiency of  $\text{Pb}^{2+}$  was 98.9% for 60 minutes. The presence of competing foreign ions were no effective on the  $\text{Pb}^{2+}$  adsorbent sorption capacity. The MzCA can be re-utilized and regenerated for as much as eight cycles using suitable eluent of 0.1 M HCl without significant deterioration in its essential performances.

# CHAPTER 8

## 8

## Conclusion and Recommendations

### 8.1 General Conclusions and Discussions

The objective of this thesis was to synthesize and characterize different types of novel hybrid photocatalysts such as TiO<sub>2</sub>/ZSM-5 and RGO/TiO<sub>2</sub>/ZSM-5 mesoporous for organic refractory dyes degradation, and also the ligands functionalized novel visual ZSM-5 mesoporous adsorbents for removing inorganic heavy metal ions (mercury (Hg<sup>+2</sup>) and lead (Pb<sup>+2</sup>)) from aqueous medium.

According to the results presented in this study, different photocatalytic efficiency and adsorption capacities were demonstrated and below are the main conclusions made from this work:

- The highly ZSM-5 multilayer mesoporous TiO<sub>2</sub> photocatalyst content was effectively enhanced, providing not only several effective sites on its surface but also a high molecular weight necessary for post separation. The decolourization and mineralization removal efficiency of MO dye can reach 99.55% and 99%, respectively, for initial MO concentration of 20 mg L<sup>-1</sup> under low sunlight intensity of 100 mW/cm<sup>2</sup> for 180 minutes. High specific surface area of 1151 m<sup>2</sup> g<sup>-1</sup> for TiO<sub>2</sub>/ZSM-5 mesoporous was remarkably obtained using the modified direct templating technique thus ensuring a high photocatalytic efficiency of MO dye.

- Further work, various weight ratios of reduced graphene oxide (RGO) combined with TiO<sub>2</sub>/ZSM-5 mesoporous were synthesized to study MB dye photocatalysis degradation. It was found that 93 % of MB dye was efficiently degraded using 10% RGO/TiO<sub>2</sub>/ZSM-5 mesoporous at initial concentration 10 mg L<sup>-1</sup> for 120 min; while, the adsorption efficiency was 40% for 30 min in the dark. The solar photocatalysis using high initial concentration of 40 mg L<sup>-1</sup> MB dye was also studied obtaining a good photocatalysis efficiency of 70%. The evidence from this study suggests that RGO was enhanced the adsorption/photocatalysis process; furthermore, an ionic interaction and the reduced electron/hole pairs recombination at the surface of RGO also played a vital role in this work. One of the more significant findings that emerge from the experimental works in this research is that increasing the weight ratio of RGO up 15%, reduced the photocatalyst degradation efficiency to 80%. The Brunauer-Emmett-Teller (BET) adsorption/desorption isotherms method demonstrated that the pores size distribution was mainly a mesoporous which enhanced the stability of the used catalyst without losing its capability during the regeneration process. This novel synthesized RGO supported TiO<sub>2</sub>/ZSM-5 mesoporous catalyst would pave for new development of multifunctional catalyst for textile dyes water environmental applications.

- To study the visual adsorption technique, new ligand of 2-hydroxyacetophenone-<sup>4</sup>N-pyrrolidine thiosemicarbazones (HAPT) was successfully immobilized into ZSM-5 mesoporous using the direct immobilization method. This novel visual catalyst exhibits feature including high specific surface area, easy post separation and cost effective material with excellent detection, high adsorption capacity and rapid adsorption rate of Hg (II) ions from aqueous solution.
- The hydroxyl, nitrogen and sulphur donor atoms of 2-hydroxyacetophenone-<sup>4</sup>N-pyrrolidine thiosemicarbazones (HAPT) ligand created intensive interaction with Hg (II) ions by electrostatic effect to form stable complexation mechanism. The lower detection limit of Hg<sup>2+</sup> ions was found to be 3.69 µg L<sup>-1</sup> at optimum pH of 12.5 and exhibiting fast kinetic performance.
- The sorption efficiency of Hg (II) ions was 95% for 120 minutes. The adsorption of Hg (II) ions followed the Langmuir adsorption model and the maximum



adsorption capacity was 166.7 mg/g. The elution and recycles of this novel visual catalyst was successfully evaluated for six adsorption-elution-recycles by using 0.10M thiourea-0.10M HCl. This novel visual catalyst is an efficient and eco-friendly catalyst for detection and removal of  $\text{Hg}^{2+}$  from wastewater without using sophisticated instruments.

- Further investigation to study the visual conjugate adsorption technique was conducted. In this investigation, a newly fabricated ligand of 2,6-Pyridinedicarboxaldehyde-Thiosemicarbazone (PDCTC) was immobilized onto ZSM-5 mesoporous to remove ultra-trace of lead ( $\text{Pb}^{2+}$ ) from aqueous solution. This conjugate adsorbent (MzCA) shows a remarkable significant colour change intensity which rely on the charge transfer transduction to achieve visible detection of  $\text{Pb}^{2+}$  ions by naked-eye observation.
- The recognition limit of  $\text{Pb}^{2+}$  was  $5.0 \mu\text{g L}^{-1}$  with no significant interference of foreign competing ions. This visual conjugate adsorbent obeyed the monolayer sorption represented by the Langmuir model and the maximum sorption capacity was 15.75 mg/g. The sorption efficiency of  $\text{Pb}^{2+}$  was 98.9% for 60 min. This visual conjugate adsorbent can also be regenerated and re-utilized for many cycles (using appropriate eluent of 0.1 M HCl) with no significant damage to in its essential performances. Accordingly, this visual conjugate adsorbent is an efficient and ecofriendly synthesized catalyst with high research values and attainable application for the simultaneous sorption and detection of  $\text{Pb}^{2+}$  in acidic aqueous media, suggesting potential on-site implementations without using sophisticated instruments.
- The better stability, regenerations after many cycles and the post separation of all the above catalysts have been satisfactory achieved.

### 8.2 Recommendations for future research

This research focused on synthesizing different types of novel mesoporous catalysts for solar photocatalytic degradation of organic pollutants such as dyes and; also visible adsorption for removal of heavy metal ions such as  $\text{Hg}^{2+}$  and  $\text{Pb}^{2+}$  from aqueous solutions was painstakingly investigated. The data revealed the effectiveness of these novel mesoporous catalysts in completely removing the toxic contaminates from water

samples. However, some other issues still require to be further investigated to complement and enhance this PhD research before its industrial applications. Based on the findings of the current study the following future research is recommended:

- To enhance the photocatalytic degradation, further work can focus on increase the harvest of sunlight which can be achieved by either modifying the photocatalyst  $\text{TiO}_2$  or looking for new semiconductor-metal (S-M) heterojunction photocatalyst immobilized new mesoporous materials.
- Crucial key factors of the photocatalysis process such as photo-reactor geometry and solar light distribution need to be investigated. Thus, design new photo-reactor configurations and studying of different solar irradiation intensities is recommended.
- Future research in wastewater treatment can focus on the photocatalytic degradation of real pharmaceutical industry pollutants which consist of several persistent drug materials.
- To support the visible adsorption process, further research can focus on design two new ligands anchored together into a mesoporous material for removing multiple heavy metal ions in aqueous solution such as  $\text{As}^{3+}$ ,  $\text{Co}^{3+}$ ,  $\text{Cr}^{3+}$ ,  $\text{Cu}^{2+}$ ,  $\text{Ag}^{2+}$  and  $\text{Pd}^{2+}$ , which are classified as either hard or soft ions according to the HSAB Principle of Pearson.
- In this study, the synthesized mesoporous zeolite type of ZSM-5 was extensively studied to obtain high specific surface area and ordered mesoporous substrate which incorporated considerable amount of a ligand. Further investigation of new zeolite substrate such as Faujasite x and y types, ZSM-12 and ZSM-22 also with good qualities should be considered.
- Design of a new synergistic catalyst that has the ability to remove organic and inorganic substances together in water samples is highly recommended. This can be achieved by modifying conjugate mesoporous adsorbent with Titania Ti (MCA-Ti), which is anticipated to be a new effective technology in large-scale water treatment.
- The potential application of solar photocatalytic degradation and the visual adsorption technologies in a large-scale operation need to be carefully evaluated due to the configuration design which in this case is too complex depending on different key parameters such as adsorption/photocatalytic kinetic models which

should be considered. Thus, the possibility of creating new advanced software which could significantly reduce the design cost of a large-scale technology.

- Finally, it is also suggested to experimentally test the different applications of the proposed MCA-Ti such as drug delivery, energy storage and sensing organic materials.

## References

- Abbas, K., Znad, H., & Awual, M. R. (2018). A ligand anchored conjugate adsorbent for effective mercury (II) detection and removal from aqueous media. *Chemical Engineering Journal*, 334, 432-443.
- Adebisi, G. A., Chowdhury, Z. Z., & Alaba, P. A. (2017). Equilibrium, kinetic, and thermodynamic studies of lead ion and zinc ion adsorption from aqueous solution onto activated carbon prepared from palm oil mill effluent. *Journal of cleaner production*, 148, 958-968.
- Ahmed, M. F. A., & Yunus, V. M. (2014). Microwave Synthesis and Antimicrobial Activity of some Copper (II), Cobalt (II), Nickel (II) and Chromium (III) Complexes with Schiff Base 2, 6-Pyridinedi carboxaldehyde-Thiosemicarbazone. *Oriental Journal of Chemistry*, 30(1), 111-117.
- Akhavan, O., & Ghaderi, E. (2009). Photocatalytic reduction of graphene oxide nanosheets on TiO<sub>2</sub> thin film for photoinactivation of bacteria in solar light irradiation. *The Journal of Physical Chemistry C*, 113(47), 20214-20220.
- Allen, M. J., Tung, V. C., & Kaner, R. B. (2009). Honeycomb carbon: a review of graphene. *Chemical reviews*, 110(1), 132-145.
- ALothman, Z. A. (2012). A review: fundamental aspects of silicate mesoporous materials. *Materials*, 5(12), 2874-2902.
- Amini, N., Soleimani, M., & Mirghaffari, N. (2018). Photocatalytic removal of SO<sub>2</sub> using natural zeolite modified by TiO<sub>2</sub> and polyoxypropylene surfactant. *Environmental Science and Pollution Research*, 1-10.
- Amuda, O., Giwa, A., & Bello, I. (2007). Removal of heavy metal from industrial wastewater using modified activated coconut shell carbon. *Biochemical Engineering Journal*, 36(2), 174-181.
- Andreozzi, M., Álvarez, M. G., Contreras, S., Medina, F., Clarizia, L., Vitiello, G., otta, R. (2018). Treatment of saline produced water through photocatalysis using rGO-TiO<sub>2</sub> nanocomposites. *Catalysis Today*.
- Apollo, S., Onyongo, M. S., & Ochieng, A. (2014). UV/H<sub>2</sub>O<sub>2</sub>/TiO<sub>2</sub>/zeolite hybrid system for treatment of molasses wastewater. *Iranian Journal of Chemistry and Chemical Engineering (IJCCE)*, 33(2), 107-117.
- Araujo, A. N., Costa, R. C. C., & Lima, J. L. (1999). Application of sequential injection analysis to the assay of lead retention characteristics by poly (vinylpyrrolidone): Trace analysis of lead in waters. *Analytical sciences*, 15(10), 991-994.
- Arshad, M. N., Sheikh, T. A., Rahman, M. M., Asiri, A. M., Marwani, H. M., & Awual, M. R. (2017). Fabrication of cadmium ionic sensor based on (E)-4-Methyl-N'-(1-(pyridin-2-yl) ethylidene) benzenesulfonohydrazide (MPEBSH) by electrochemical approach. *Journal of Organometallic Chemistry*, 827, 49-55.
- Arshadi, M., Mousavinia, F., Khalafi-Nezhad, A., Firouzabadi, H., & Abbaspourrad, A. (2017). Adsorption of mercury ions from wastewater by a hyperbranched and multi-functionalized dendrimer modified mixed-oxides nanoparticles. *Journal of colloid and interface science*, 505, 293-306.
- Awad, F. S., AbouZeid, K. M., El-Maaty, W. M. A., El-Wakil, A. M., & El-Shall, M. S. (2017). Efficient Removal of Heavy Metals from Polluted Water with High Selectivity for Mercury (II) by 2-Imino-4-thiobiuret-Partially Reduced Graphene Oxide (IT-PRGO). *ACS applied materials & interfaces*, 9(39), 34230-34242.
- Awual, M. R. (2014). Investigation of potential conjugate adsorbent for efficient ultra-trace gold (III) detection and recovery. *Journal of Industrial and Engineering Chemistry*, 20(5), 3493-3501.

- Awual, M. R. (2016a). Assessing of lead (III) capturing from contaminated wastewater using ligand doped conjugate adsorbent. *Chemical Engineering Journal*, 289, 65-73.
- Awual, M. R. (2016b). Ring size dependent crown ether based mesoporous adsorbent for high cesium adsorption from wastewater. *Chemical Engineering Journal*, 303, 539-546.
- Awual, M. R. (2016c). Solid phase sensitive palladium (II) ions detection and recovery using ligand based efficient conjugate nanomaterials. *Chemical Engineering Journal*, 300, 264-272.
- Awual, M. R. (2017a). New type mesoporous conjugate material for selective optical copper (II) ions monitoring & removal from polluted waters. *Chemical Engineering Journal*, 307, 85-94.
- Awual, M. R. (2017b). Novel nanocomposite materials for efficient and selective mercury ions capturing from wastewater. *Chemical Engineering Journal*, 307, 456-465.
- Awual, M. R., Alharthi, N. H., Hasan, M. M., Karim, M. R., Islam, A., Znad, H., Khaleque, M. A. (2017). Inorganic-organic based novel nano-conjugate material for effective cobalt (II) ions capturing from wastewater. *Chemical Engineering Journal*, 324, 130-139.
- Awual, M. R., Alharthi, N. H., Okamoto, Y., Karim, M. R., Halim, M. E., Hasan, M. M., Sheikh, M. C. (2017). Ligand field effect for Dysprosium (III) and Lutetium (III) adsorption and EXAFS coordination with novel composite nanomaterials. *Chemical Engineering Journal*, 320, 427-435.
- Awual, M. R., El-Safty, S. A., & Jyo, A. (2011). Removal of trace arsenic (V) and phosphate from water by a highly selective ligand exchange adsorbent. *Journal of Environmental Sciences*, 23(12), 1947-1954.
- Awual, M. R., Eldesoky, G. E., Yaita, T., Naushad, M., Shiwaku, H., AlOthman, Z. A., & Suzuki, S. (2015). Schiff based ligand containing nano-composite adsorbent for optical copper (II) ions removal from aqueous solutions. *Chemical Engineering Journal*, 279, 639-647.
- Awual, M. R., & Hasan, M. M. (2014a). Novel conjugate adsorbent for visual detection and removal of toxic lead (II) ions from water. *Microporous and Mesoporous Materials*, 196, 261-269.
- Awual, M. R., & Hasan, M. M. (2014b). A novel fine-tuning mesoporous adsorbent for simultaneous lead (II) detection and removal from wastewater. *Sensors and Actuators B: Chemical*, 202, 395-403.
- Awual, M. R., & Hasan, M. M. (2015a). Colorimetric detection and removal of copper (II) ions from wastewater samples using tailor-made composite adsorbent. *Sensors and Actuators B: Chemical*, 206, 692-700.
- Awual, M. R., & Hasan, M. M. (2015b). Fine-tuning mesoporous adsorbent for simultaneous ultra-trace palladium (II) detection, separation and recovery. *Journal of Industrial and Engineering Chemistry*, 21, 507-515.
- Awual, M. R., Hasan, M. M., Eldesoky, G. E., Khaleque, M. A., Rahman, M. M., & Naushad, M. (2016). Facile mercury detection and removal from aqueous media involving ligand impregnated conjugate nanomaterials. *Chemical Engineering Journal*, 290, 243-251.
- Awual, M. R., Hasan, M. M., Ihara, T., & Yaita, T. (2014). Mesoporous silica based novel conjugate adsorbent for efficient selenium (IV) detection and removal from water. *Microporous and Mesoporous Materials*, 197, 331-338.
- Awual, M. R., Hasan, M. M., & Khaleque, M. A. (2015). Efficient selenium (IV) detection and removal from water by tailor-made novel conjugate adsorbent. *Sensors and Actuators B: Chemical*, 209, 194-202.
- Awual, M. R., Hasan, M. M., Khaleque, M. A., & Sheikh, M. C. (2016). Treatment of copper (II) containing wastewater by a newly developed ligand based facial conjugate materials. *Chemical Engineering Journal*, 288, 368-376.

- Awual, M. R., Hasan, M. M., Naushad, M., Shiwaku, H., & Yaita, T. (2015). Preparation of new class composite adsorbent for enhanced palladium (II) detection and recovery. *Sensors and Actuators B: Chemical*, 209, 790-797.
- Awual, M. R., Hasan, M. M., & Shahat, A. (2014). Functionalized novel mesoporous adsorbent for selective lead (II) ions monitoring and removal from wastewater. *Sensors and Actuators B: Chemical*, 203, 854-863.
- Awual, M. R., Hasan, M. M., Shahat, A., Naushad, M., Shiwaku, H., & Yaita, T. (2015). Investigation of ligand immobilized nano-composite adsorbent for efficient cerium (III) detection and recovery. *Chemical Engineering Journal*, 265, 210-218.
- Awual, M. R., Hasan, M. M., & Znad, H. (2015). Organic-inorganic based nano-conjugate adsorbent for selective palladium (II) detection, separation and recovery. *Chemical Engineering Journal*, 259, 611-619.
- Awual, M. R., Hossain, M. A., Shenashen, M., Yaita, T., Suzuki, S., & Jyo, A. (2013). Evaluating of arsenic (V) removal from water by weak-base anion exchange adsorbents. *Environmental Science and Pollution Research*, 20(1), 421-430.
- Awual, M. R., & Ismael, M. (2014). Efficient gold (III) detection, separation and recovery from urban mining waste using a facial conjugate adsorbent. *Sensors and Actuators B: Chemical*, 196, 457-466.
- Awual, M. R., Ismael, M., Khaleque, M. A., & Yaita, T. (2014). Ultra-trace copper (II) detection and removal from wastewater using novel meso-adsorbent. *Journal of Industrial and Engineering Chemistry*, 20(4), 2332-2340.
- Awual, M. R., Ismael, M., Yaita, T., El-Safty, S. A., Shiwaku, H., Okamoto, Y., & Suzuki, S. (2013). Trace copper (II) ions detection and removal from water using novel ligand modified composite adsorbent. *Chemical Engineering Journal*, 222, 67-76.
- Awual, M. R., & Jyo, A. (2009). Rapid column-mode removal of arsenate from water by crosslinked poly (allylamine) resin. *Water research*, 43(5), 1229-1236.
- Awual, M. R., & Jyo, A. (2011). Assessing of phosphorus removal by polymeric anion exchangers. *Desalination*, 281, 111-117.
- Awual, M. R., Jyo, A., El-Safty, S. A., Tamada, M., & Seko, N. (2011). A weak-base fibrous anion exchanger effective for rapid phosphate removal from water. *Journal of hazardous materials*, 188(1-3), 164-171.
- Awual, M. R., Jyo, A., Ihara, T., Seko, N., Tamada, M., & Lim, K. T. (2011). Enhanced trace phosphate removal from water by zirconium (IV) loaded fibrous adsorbent. *Water research*, 45(15), 4592-4600.
- Awual, M. R., Jyo, A., Tamada, M., & Katakai, A. (2007). Zirconium (IV) loaded bifunctional fiber containing both phosphonate and sulfonate as arsenate adsorbent. *Journal of Ion Exchange*, 18(4), 422-427.
- Awual, M. R., Khaleque, M. A., Ferdows, M., Chowdhury, A. S., & Yaita, T. (2013). Rapid recognition and recovery of gold (III) with functional ligand immobilized novel mesoporous adsorbent. *Microchemical Journal*, 110, 591-598.
- Awual, M. R., Khaleque, M. A., Ratna, Y., & Znad, H. (2015). Simultaneous ultra-trace palladium (II) detection and recovery from wastewater using new class meso-adsorbent. *Journal of Industrial and Engineering Chemistry*, 21, 405-413.
- Awual, M. R., Kobayashi, T., Miyazaki, Y., Motokawa, R., Shiwaku, H., Suzuki, S., Yaita, T. (2013). Selective lanthanide sorption and mechanism using novel hybrid Lewis base (N-methyl-N-phenyl-1, 10-phenanthroline-2-carboxamide) ligand modified adsorbent. *Journal of hazardous materials*, 252, 313-320.
- Awual, M. R., Kobayashi, T., Shiwaku, H., Miyazaki, Y., Motokawa, R., Suzuki, S., Yaita, T. (2013). Evaluation of lanthanide sorption and their coordination mechanism by EXAFS measurement using novel hybrid adsorbent. *Chemical Engineering Journal*, 225, 558-566.
- Awual, M. R., Miyazaki, Y., Taguchi, T., Shiwaku, H., & Yaita, T. (2016). Encapsulation of cesium from contaminated water with highly selective facial organic-inorganic mesoporous hybrid adsorbent. *Chemical Engineering Journal*, 291, 128-137.

- Awual, M. R., Rahman, I. M., Yaita, T., Khaleque, M. A., & Ferdows, M. (2014). pH dependent Cu (II) and Pd (II) ions detection and removal from aqueous media by an efficient mesoporous adsorbent. *Chemical Engineering Journal*, 236, 100-109.
- Awual, M. R., Shenashen, M., Jyo, A., Shiwaku, H., & Yaita, T. (2014). Preparing of novel fibrous ligand exchange adsorbent for rapid column-mode trace phosphate removal from water. *Journal of Industrial and Engineering Chemistry*, 20(5), 2840-2847.
- Awual, M. R., Shenashen, M., Yaita, T., Shiwaku, H., & Jyo, A. (2012). Efficient arsenic (V) removal from water by ligand exchange fibrous adsorbent. *Water research*, 46(17), 5541-5550.
- Awual, M. R., Suzuki, S., Taguchi, T., Shiwaku, H., Okamoto, Y., & Yaita, T. (2014). Radioactive cesium removal from nuclear wastewater by novel inorganic and conjugate adsorbents. *Chemical Engineering Journal*, 242, 127-135.
- Awual, M. R., Urata, S., Jyo, A., Tamada, M., & Katakai, A. (2008). Arsenate removal from water by a weak-base anion exchange fibrous adsorbent. *Water research*, 42(3), 689-696.
- Awual, M. R., & Yaita, T. (2013). Rapid sensing and recovery of palladium (II) using N, N-bis (salicylidene) 1, 2-bis (2-aminophenylthio) ethane modified sensor ensemble adsorbent. *Sensors and Actuators B: Chemical*, 183, 332-341.
- Awual, M. R., Yaita, T., El-Safty, S. A., Shiwaku, H., Okamoto, Y., & Suzuki, S. (2013). Investigation of palladium (II) detection and recovery using ligand modified conjugate adsorbent. *Chemical Engineering Journal*, 222, 172-179.
- Awual, M. R., Yaita, T., El-Safty, S. A., Shiwaku, H., Suzuki, S., & Okamoto, Y. (2013). Copper (II) ions capturing from water using ligand modified a new type mesoporous adsorbent. *Chemical Engineering Journal*, 221, 322-330.
- Awual, M. R., Yaita, T., Miyazaki, Y., Matsumura, D., Shiwaku, H., & Taguchi, T. (2016). A reliable hybrid adsorbent for efficient radioactive cesium accumulation from contaminated wastewater. *Scientific reports*, 6, 19937.
- Awual, M. R., Yaita, T., & Okamoto, Y. (2014). A novel ligand based dual conjugate adsorbent for cobalt (II) and copper (II) ions capturing from water. *Sensors and Actuators B: Chemical*, 203, 71-80.
- Awual, M. R., Yaita, T., & Shiwaku, H. (2013). Design a novel optical adsorbent for simultaneous ultra-trace cerium (III) detection, sorption and recovery. *Chemical Engineering Journal*, 228, 327-335.
- Awual, M. R., Yaita, T., Shiwaku, H., & Suzuki, S. (2015). A sensitive ligand embedded nano-conjugate adsorbent for effective cobalt (II) ions capturing from contaminated water. *Chemical Engineering Journal*, 276, 1-10.
- Awual, M. R., Yaita, T., Suzuki, S., & Shiwaku, H. (2015). Ultimate selenium (IV) monitoring and removal from water using a new class of organic ligand based composite adsorbent. *Journal of hazardous materials*, 291, 111-119.
- Awual, M. R., Yaita, T., Taguchi, T., Shiwaku, H., Suzuki, S., & Okamoto, Y. (2014). Selective cesium removal from radioactive liquid waste by crown ether immobilized new class conjugate adsorbent. *Journal of hazardous materials*, 278, 227-235.
- Ba-Abbad, M. M., Kadhum, A. A. H., Mohamad, A. B., Takriff, M. S., & Sopian, K. (2012). Synthesis and catalytic activity of TiO<sub>2</sub> nanoparticles for photochemical oxidation of concentrated chlorophenols under direct solar radiation. *Int. J. Electrochem. Sci*, 7, 4871-4888.
- Barpuzary, D., & Qureshi, M. (2013). Enhanced photovoltaic performance of semiconductor-sensitized ZnO-CdS coupled with graphene oxide as a novel photoactive material. *ACS applied materials & interfaces*, 5(22), 11673-11682.
- Bell, N. J., Ng, Y. H., Du, A., Coster, H., Smith, S. C., & Amal, R. (2011). Understanding the enhancement in photoelectrochemical properties of photocatalytically prepared TiO<sub>2</sub>-reduced graphene oxide composite. *The Journal of Physical Chemistry C*, 115(13), 6004-6009.

- Benhima, H., Chiban, M., Sinan, F., Seta, P., & Persin, M. (2008). Removal of lead and cadmium ions from aqueous solution by adsorption onto micro-particles of dry plants. *Colloids and Surfaces B: Biointerfaces*, 61(1), 10-16.
- Beydoun, D., & Amal, R. (2002). Implications of heat treatment on the properties of a magnetic iron oxide–titanium dioxide photocatalyst. *Materials Science and Engineering: B*, 94(1), 71-81.
- Boisen, A., Schmidt, I., Carlsson, A., Dahl, S., Brorson, M., & Jacobsen, C. J. (2003). TEM stereo-imaging of mesoporous zeolite single crystals. *Chemical Communications*(8), 958-959.
- Brown, J. P., & Dietrich, P. S. (1983). Mutagenicity of selected sulfonated azo dyes in the Salmonella/microsome assay: use of aerobic and anaerobic activation procedures. *Mutation Research/Genetic Toxicology*, 116(3-4), 305-315.
- Cabon, J. (2002). Determination of Cd and Pb in seawater by graphite furnace atomic absorption spectrometry with the use of hydrofluoric acid as a chemical modifier. *Spectrochimica Acta Part B: Atomic Spectroscopy*, 57(3), 513-524.
- Chal, R., Gerardin, C., Bulut, M., & Van Donk, S. (2011). Overview and industrial assessment of synthesis strategies towards zeolites with mesopores. *ChemCatChem*, 3(1), 67-81.
- Chang, C.-T., Wang, J.-J., Ouyang, T., Zhang, Q., & Jing, Y.-H. (2015). Photocatalytic degradation of acetaminophen in aqueous solutions by TiO<sub>2</sub>/ZSM-5 zeolite with low energy irradiation. *Materials Science and Engineering: B*, 196, 53-60.
- Chen, H., Li, J., Shao, D., Ren, X., & Wang, X. (2012). Poly (acrylic acid) grafted multiwall carbon nanotubes by plasma techniques for Co (II) removal from aqueous solution. *Chemical Engineering Journal*, 210, 475-481.
- Chen, H., Wang, X., Li, J., & Wang, X. (2015). Cotton derived carbonaceous aerogels for the efficient removal of organic pollutants and heavy metal ions. *Journal of Materials Chemistry A*, 3(11), 6073-6081.
- Chen, J., Xiao, S., Wu, X., Fang, K., & Liu, W. (2005). Determination of lead in water samples by graphite furnace atomic absorption spectrometry after cloud point extraction. *Talanta*, 67(5), 992-996.
- Chen, L., Moon, J.-H., Ma, X., Zhang, L., Chen, Q., Chen, L., Li, Y. (2018). High performance graphene oxide nanofiltration membrane prepared by electrospraying for wastewater purification. *carbon*.
- Chen, X., & Mao, S. S. (2007). Titanium dioxide nanomaterials: synthesis, properties, modifications, and applications. *Chemical reviews*, 107(7), 2891-2959.
- Cheng, M., Zeng, G., Huang, D., Lai, C., Liu, Y., Zhang, C., Xiong, W. (2018). Efficient degradation of sulfamethazine in simulated and real wastewater at slightly basic pH values using Co-SAM-SCS/H<sub>2</sub>O<sub>2</sub> Fenton-like system. *Water research*, 138, 7-18.
- Choi, M., Cho, H. S., Srivastava, R., Venkatesan, C., Choi, D.-H., & Ryoo, R. (2006). Amphiphilic organosilane-directed synthesis of crystalline zeolite with tunable mesoporosity. *Nature materials*, 5(9), 718.
- Choi, M., Srivastava, R., & Ryoo, R. (2006). Organosilane surfactant-directed synthesis of mesoporous aluminophosphates constructed with crystalline microporous frameworks. *Chemical Communications*(42), 4380-4382.
- Chong, M. N., Cho, Y. J., Poh, P. E., & Jin, B. (2015). Evaluation of Titanium dioxide photocatalytic technology for the treatment of reactive Black 5 dye in synthetic and real greywater effluents. *Journal of cleaner production*, 89, 196-202.
- Chong, M. N., Jin, B., Chow, C. W., & Saint, C. (2010). Recent developments in photocatalytic water treatment technology: a review. *Water research*, 44(10), 2997-3027.
- Chong, M. N., Jin, B., Zhu, H. Y., Chow, C., & Saint, C. (2009). Application of H-titanate nanofibers for degradation of Congo Red in an annular slurry photoreactor. *Chemical Engineering Journal*, 150(1), 49-54.
- Chong, M. N., Tneu, Z. Y., Poh, P. E., Jin, B., & Aryal, R. (2015). Synthesis, characterisation and application of TiO<sub>2</sub>-zeolite nanocomposites for the advanced



- treatment of industrial dye wastewater. *Journal of the Taiwan Institute of Chemical Engineers*, 50, 288-296.
- Chong, M. N., Vimonses, V., Lei, S., Jin, B., Chow, C., & Saint, C. (2009). Synthesis and characterisation of novel titania impregnated kaolinite nano-photocatalyst. *Microporous and Mesoporous Materials*, 117(1-2), 233-242.
- Chooto, P., Wararatnanurak, P., & Innuphat, C. (2010). Determination of trace levels of Pb (II) in tap water by anodic stripping voltammetry with boron-doped diamond electrode. *Science Asia* 2010; 36: 150, 156.
- Choudhary, B., Goyal, A., & Khokra, S. L. (2009). New visible spectrophotometric method for estimation of itopride hydrochloride from tablets formulations using methyl orange reagent. *International Journal of Pharmacy and Pharmaceutical Sciences*, 1, 159-162.
- Christensen, C. H., Johannsen, K., Schmidt, I., & Christensen, C. H. (2003). Catalytic benzene alkylation over mesoporous zeolite single crystals: improving activity and selectivity with a new family of porous materials. *Journal of the American Chemical Society*, 125(44), 13370-13371.
- Citak, D., & Tuzen, M. (2010). A novel preconcentration procedure using cloud point extraction for determination of lead, cobalt and copper in water and food samples using flame atomic absorption spectrometry. *Food and Chemical Toxicology*, 48(5), 1399-1404.
- Clarkson, T. W., & Magos, L. (2006). The toxicology of mercury and its chemical compounds. *Critical reviews in toxicology*, 36(8), 609-662.
- David, S. T., & Priyadharsini, J. P. (2015). Schiff base ligand its complexes and their FT-IR spectroscopy Studies. *International Journal on Applied Bioengineering*, 9(1).
- de Campos, R. C., dos Santos, H. R., & Grinberg, P. (2002). Determination of copper, iron, lead and nickel in gasoline by electrothermal atomic absorption spectrometry using three-component solutions. *Spectrochimica Acta Part B: Atomic Spectroscopy*, 57(1), 15-28.
- de Mattos, J. C. P., Nunes, A. M., Martins, A. F., Dressler, V. L., & de Moraes Flores, É. M. (2005). Influence of citric acid as chemical modifier for lead determination in dietary calcium supplement samples by graphite furnace atomic absorption spectrometry. *Spectrochimica Acta Part B: Atomic Spectroscopy*, 60(5), 687-692.
- Dean, J. A. (1990). Lange's handbook of chemistry. *Material and manufacturing process*, 5(4), 687-688.
- Di, Y., Yu, Y., Sun, Y., Yang, X., Lin, S., Zhang, M., Xiao, F.-S. (2003). Synthesis, characterization, and catalytic properties of stable mesoporous aluminosilicates assembled from preformed zeolite L precursors. *Microporous and Mesoporous Materials*, 62(3), 221-228.
- Ding, S., Chen, J. S., Luan, D., Boey, F. Y. C., Madhavi, S., & Lou, X. W. D. (2011). Graphene-supported anatase TiO<sub>2</sub> nanosheets for fast lithium storage. *Chemical Communications*, 47(20), 5780-5782.
- Doner, G., & Ege, A. (2005). Determination of copper, cadmium and lead in seawater and mineral water by flame atomic absorption spectrometry after coprecipitation with aluminum hydroxide. *Analytica Chimica Acta*, 547(1), 14-17.
- Dong, Z., Wang, D., Liu, X., Pei, X., Chen, L., & Jin, J. (2014). Bio-inspired surface-functionalization of graphene oxide for the adsorption of organic dyes and heavy metal ions with a superhigh capacity. *Journal of Materials Chemistry A*, 2(14), 5034-5040.
- dos Santos, W. L., dos Santos, C. M., Costa, J. L., Andrade, H. M., & Ferreira, S. L. (2004). Multivariate optimization and validation studies in on-line pre-concentration system for lead determination in drinking water and saline waste from oil refinery. *Microchemical Journal*, 77(2), 123-129.
- Duman, O., & Ayranci, E. (2010). Attachment of benzo-crown ethers onto activated carbon cloth to enhance the removal of chromium, cobalt and nickel ions from aqueous solutions by adsorption. *Journal of hazardous materials*, 176(1-3), 231-238.

- Egeblad, K., Christensen, C. H., Kustova, M., & Christensen, C. H. (2007). Templating mesoporous zeolites. *Chemistry of materials*, 20(3), 946-960.
- Eissa, F., Zidan, N. E.-H., & Sakugawa, H. (2015). Photodegradation of the herbicide diuron in water under simulated sunlight. *Geochemical Journal*, 49(3), 309-318.
- El-Safty, S., Shahat, A., Awual, M. R., & Mekawy, M. (2011). Large three-dimensional mesoporous silica tailoring silica nanotubes as membrane filters: nanofiltration and permeation flux of proteins. *Journal of Materials Chemistry*, 21(15), 5593-5603.
- El-Safty, S. A., Awual, M. R., Shenashen, M., & Shahat, A. (2013). Simultaneous optical detection and extraction of cobalt (II) from lithium ion batteries using nanocollector monoliths. *Sensors and Actuators B: Chemical*, 176, 1015-1025.
- El-Safty, S. A., Ismail, A. A., Matsunaga, H., Nanjo, H., & Mizukami, F. (2008). Uniformly mesoporous cubic Fd<sub>3m</sub> monoliths as modal carriers for optical chemosensors. *The Journal of Physical Chemistry C*, 112(13), 4825-4835.
- El-Safty, S. A., Khairy, M., & Ismael, M. (2012). Visual detection and reversible supermicrostructure sensor systems of Cu (II) analytes. *Sensors and Actuators B: Chemical*, 166, 253-263.
- El-Safty, S. A., Prabhakaran, D., Ismail, A., Matsunaga, H., & Mizukami, F. (2008). Three-dimensional wormhole and ordered mesostructures and their applicability as optically ion-sensitive probe templates. *Chemistry of materials*, 20(8), 2644-2654.
- El-Safty, S. A., Shahat, A., & Awual, M. R. (2011). Efficient adsorbents of nanoporous aluminosilicate monoliths for organic dyes from aqueous solution. *Journal of colloid and interface science*, 359(1), 9-18.
- El-Safty, S. A., Shahat, A., & Ismael, M. (2012). Mesoporous aluminosilicate monoliths for the adsorptive removal of small organic pollutants. *Journal of hazardous materials*, 201, 23-32.
- El-Safty, S. A., & Shenashen, M. (2013). Optical mesosensor for capturing of Fe (III) and Hg (II) ions from water and physiological fluids. *Sensors and Actuators B: Chemical*, 183, 58-70.
- El-Safty, S. A., Shenashen, M., Ismael, M., Khairy, M., & Awual, M. R. (2012). Optical mesosensors for monitoring and removal of ultra-trace concentration of Zn (II) and Cu (II) ions from water. *Analyst*, 137(22), 5278-5290.
- El-Safty, S. A., Shenashen, M., Ismael, M., Khairy, M., & Awual, M. R. (2013). Mesoporous aluminosilicate sensors for the visual removal and detection of Pd (II) and Cu (II) ions. *Microporous and Mesoporous Materials*, 166, 195-205.
- El-Safty, S. A., Shenashen, M. A., & Khairy, M. (2012). Optical detection/collection of toxic Cd (II) ions using cubic Ia<sub>3d</sub> aluminosilicate mesoporous sensors. *Talanta*, 98, 69-78.
- El-Safty, S. A., Ismail, A. A., Matsunaga, H., Hanaoka, T., & Mizukami, F. (2008). Optical Nanoscale Pool-on-Surface Design for Control Sensing Recognition of Multiple Cations. *Advanced Functional Materials*, 18(10), 1485-1500.
- El-Safty, S. A., Ismail, A. A., Matsunaga, H., & Mizukami, F. (2007). Optical nanosensor design with uniform pore geometry and large particle morphology. *Chemistry-A European Journal*, 13(33), 9245-9255.
- El-Safty, S. A., Prabhakaran, D., Ismail, A. A., Matsunaga, H., & Mizukami, F. (2007). Nanosensor design packages: a smart and compact development for metal ions sensing responses. *Advanced Functional Materials*, 17(18), 3731-3745.
- Evans, D. F., & Wennerström, H. (1999). The colloidal domain: where physics, chemistry, biology, and technology meet.
- Fan, W., Lai, Q., Zhang, Q., & Wang, Y. (2011). Nanocomposites of TiO<sub>2</sub> and reduced graphene oxide as efficient photocatalysts for hydrogen evolution. *The Journal of Physical Chemistry C*, 115(21), 10694-10701.
- Fayed, T. A., Shaaban, M. H., El-Nahass, M. N., & Hassan, F. M. (2014). Chalcones isothiocyanate anchored into mesoporous silicate: Synthesis, characterization and metal ions sensing response. *Microporous and Mesoporous Materials*, 198, 144-152.

- Fowler, C. E., Mann, S., & Lebeau, B. (1998). Covalent coupling of an organic chromophore into functionalized MCM-41 mesophases by template-directed co-condensation. *Chemical Communications*(17), 1825-1826.
- Fujishima, A., Rao, T. N., & Tryk, D. A. (2000). Titanium dioxide photocatalysis. *Journal of photochemistry and photobiology C: Photochemistry reviews*, 1(1), 1-21.
- Futalan, C. M., Kan, C.-C., Dalida, M. L., Hsien, K.-J., Pascua, C., & Wan, M.-W. (2011). Comparative and competitive adsorption of copper, lead, and nickel using chitosan immobilized on bentonite. *Carbohydrate polymers*, 83(2), 528-536.
- Gamba, A., Colella, C., & Coluccia, S. (2001). Effect of Ti insertion in the silicalite framework on the vibrational modes of the structure: an abinitio, and vibrational study.
- Geim, A. K., & Kim, P. (2008). Carbon wonderland. *Scientific American*, 298(4), 90-97.
- Georgakilas, V., Tiwari, J. N., Kemp, K. C., Perman, J. A., Bourlinos, A. B., Kim, K. S., & Zboril, R. (2016). Noncovalent functionalization of graphene and graphene oxide for energy materials, biosensing, catalytic, and biomedical applications. *Chemical reviews*, 116(9), 5464-5519.
- Gholami, N., Ghasemi, B., Anvaripour, B., & Jorfi, S. (2018). Enhanced photocatalytic degradation of furfural and a real wastewater using UVC/TiO<sub>2</sub> nanoparticles immobilized on white concrete in a fixed-bed reactor. *Journal of Industrial and Engineering Chemistry*, 62, 291-301.
- Ghosh, D., & Bhattacharyya, K. G. (2002). Adsorption of methylene blue on kaolinite. *Applied Clay Science*, 20(6), 295-300.
- Giannakis, S., Androulaki, B., Comninellis, C., & Pulgarin, C. (2018). Wastewater and urine treatment by UVC-based advanced oxidation processes: Implications from the interactions of bacteria, viruses, and chemical contaminants. *Chemical Engineering Journal*, 343, 270-282.
- Gogate, P. R., & Pandit, A. B. (2004). A review of imperative technologies for wastewater treatment I: oxidation technologies at ambient conditions. *Advances in Environmental Research*, 8(3-4), 501-551.
- Guesh, K., Márquez-Álvarez, C., Chebude, Y., & Díaz, I. (2016). Enhanced photocatalytic activity of supported TiO<sub>2</sub> by selective surface modification of zeolite Y. *Applied Surface Science*, 378, 473-478.
- Gupta, S. S., & Bhattacharyya, K. G. (2009). Treatment of water contaminated with Pb (II) and Cd (II) by adsorption on kaolinite, montmorillonite and their acid-activated forms.
- Gupta, V., Gupta, B., Rastogi, A., Agarwal, S., & Nayak, A. (2011). A comparative investigation on adsorption performances of mesoporous activated carbon prepared from waste rubber tire and activated carbon for a hazardous azo dye—Acid Blue 113. *Journal of hazardous materials*, 186(1), 891-901.
- Hakami, O., Zhang, Y., & Banks, C. J. (2012). Thiol-functionalised mesoporous silica-coated magnetite nanoparticles for high efficiency removal and recovery of Hg from water. *Water research*, 46(12), 3913-3922.
- Hamadani, M., Reisi-Vanani, A., & Majedi, A. (2009). Preparation and characterization of S-doped TiO<sub>2</sub> nanoparticles, effect of calcination temperature and evaluation of photocatalytic activity. *Materials Chemistry and Physics*, 116(2-3), 376-382.
- Hameed, B., Mahmoud, D., & Ahmad, A. (2008). Sorption equilibrium and kinetics of basic dye from aqueous solution using banana stalk waste. *Journal of hazardous materials*, 158(2-3), 499-506.
- Han, Y., Wu, S., Sun, Y., Li, D., Xiao, F.-S., Liu, J., & Zhang, X. (2002). Hydrothermally stable ordered hexagonal mesoporous aluminosilicates assembled from a triblock copolymer and preformed aluminosilicate precursors in strongly acidic media. *Chemistry of materials*, 14(3), 1144-1148.
- Han, Y., Xiao, F.-S., Wu, S., Sun, Y., Meng, X., Li, D., Ai, X. (2001). A novel method for incorporation of heteroatoms into the framework of ordered mesoporous silica

- materials synthesized in strong acidic media. *The Journal of Physical Chemistry B*, 105(33), 7963-7966.
- Havelcova, M., Mizera, J., Sýkorová, I., & Pekař, M. (2009). Sorption of metal ions on lignite and the derived humic substances. *Journal of hazardous materials*, 161(1), 559-564.
- Hernández-Morales, V., Nava, R., Acosta-Silva, Y., Macías-Sánchez, S., Pérez-Bueno, J., & Pawelec, B. (2012). Adsorption of lead (II) on SBA-15 mesoporous molecular sieve functionalized with  $-NH_2$  groups. *Microporous and Mesoporous Materials*, 160, 133-142.
- Ho, Y.-S. (2006). Review of second-order models for adsorption systems. *Journal of hazardous materials*, 136(3), 681-689.
- Hoffmann, F., Cornelius, M., Morell, J., & Fröba, M. (2006). Silica-based mesoporous organic-inorganic hybrid materials. *Angewandte Chemie International Edition*, 45(20), 3216-3251.
- Holmberg, K., Jönsson, B., Kronberg, B., & Lindman, B. (2003). *Surfactants and polymers in aqueous solution* (Vol. 2): Wiley Online Library.
- Hua, Z., Yang, B., Chen, W., Bai, X., Xu, Q., & Gu, H. (2014). Surface functionalized magnetic PVA microspheres for rapid naked-eye recognizing of copper (II) ions in aqueous solutions. *Applied Surface Science*, 317, 226-235.
- Huang, L., Wang, Z., Sun, J., Miao, L., Li, Q., Yan, Y., & Zhao, D. (2000). Fabrication of ordered porous structures by self-assembly of zeolite nanocrystals. *Journal of the American Chemical Society*, 122(14), 3530-3531.
- Huang, M., Xu, C., Wu, Z., Huang, Y., Lin, J., & Wu, J. (2008). Photocatalytic discolorization of methyl orange solution by Pt modified  $TiO_2$  loaded on natural zeolite. *Dyes and pigments*, 77(2), 327-334.
- Huang, X., Qi, X., Boey, F., & Zhang, H. (2012). Graphene-based composites. *Chemical Society Reviews*, 41(2), 666-686.
- Hummers Jr, W. S., & Offeman, R. E. (1958). Preparation of graphitic oxide. *Journal of the American Chemical Society*, 80(6), 1339-1339.
- Hylander, L. D., & Goodsite, M. E. (2006). Environmental costs of mercury pollution. *Science of the Total Environment*, 368(1), 352-370.
- Ismail, L., Chovelon, J., Ferronato, C., Jaber, F., & Rifai, A. (2016). *comparative study of the degradation of sulfaclozine in uv/TiO<sub>2</sub>, uv/K<sub>2</sub>S<sub>2</sub>O<sub>8</sub>, uv/TiO<sub>2</sub>/K<sub>2</sub>S<sub>2</sub>O<sub>8</sub> system*. Paper presented at the 9<sup>th</sup> European meeting on Solar Chemistry and Photocatalysis: Environmental Applications (SPEA).
- Iwase, A., Ng, Y. H., Ishiguro, Y., Kudo, A., & Amal, R. (2011). Reduced graphene oxide as a solid-state electron mediator in Z-scheme photocatalytic water splitting under visible light. *Journal of the American Chemical Society*, 133(29), 11054-11057.
- Jacobsen, C. J., Madsen, C., Houzvicka, J., Schmidt, I., & Carlsson, A. (2000). Mesoporous zeolite single crystals. *Journal of the American Chemical Society*, 122(29), 7116-7117.
- Jain, R., & Sikarwar, S. (2008). Removal of hazardous dye congedred from waste material. *Journal of hazardous materials*, 152(3), 942-948.
- Jamali, M. R., Assadi, Y., Shemirani, F., Hosseini, M. R. M., Kozani, R. R., Masteri-Farahani, M., & Salavati-Niasari, M. (2006). Synthesis of salicylaldehyde-modified mesoporous silica and its application as a new sorbent for separation, preconcentration and determination of uranium by inductively coupled plasma atomic emission spectrometry. *Analytica Chimica Acta*, 579(1), 68-73.
- Jamali, M. R., Assadi, Y., Shemirani, F., & Salavati-Niasari, M. (2007). Application of thiophene-2-carbaldehyde-modified mesoporous silica as a new sorbent for separation and preconcentration of palladium prior to inductively coupled plasma atomic emission spectrometric determination. *Talanta*, 71(4), 1524-1529.
- Jin, Z., Wang, L., Hu, Q., Zhang, L., Xu, S., Dong, X., Xiao, F.-S. (2018). Hydrophobic Zeolite Containing Titania Particles as Wettability-Selective Catalyst for Formaldehyde Removal. *ACS Catalysis*.

- Johra, F. T., & Jung, W.-G. (2015). RGO–TiO<sub>2</sub>–ZnO composites: synthesis, characterization, and application to photocatalysis. *Applied Catalysis A: General*, 491, 52-57.
- Joseph, A. I. J., & Thiripuranthagan, S. (2018). Non-Metal Doped Titania Photocatalysts for the Degradation of Neonicotinoid Insecticides Under Visible Light Irradiation. *Journal of nanoscience and nanotechnology*, 18(5), 3158-3164.
- Jung, Y. J., Kim, W. G., Yoon, Y., Kang, J.-W., Hong, Y. M., & Kim, H. W. (2012). Removal of amoxicillin by UV and UV/H<sub>2</sub>O<sub>2</sub> processes. *Science of the Total Environment*, 420, 160-167.
- Kamath, A., Netalkar, S. P., Kokare, D. G., Naik, K., & Revankar, V. K. (2012). Phenoxide bridged tetranuclear Co (II), Ni (II), Cu (II) and Zn (II) complexes: Syntheses, characterization and fluorescence studies. *Journal of Luminescence*, 132(10), 2763-2768.
- Kangwansupamonkon, W., Jitbunpot, W., & Kiatkamjornwong, S. (2010). Photocatalytic efficiency of TiO<sub>2</sub>/poly [acrylamide-co-(acrylic acid)] composite for textile dye degradation. *Polymer Degradation and Stability*, 95(9), 1894-1902.
- Kaplan, O., Yildirim, N. C., Yildirim, N., & Tayhan, N. (2011). Assessment of some heavy metals in drinking water samples of Tunceli, Turkey. *Journal of Chemistry*, 8(1), 276-280.
- Karadjova, I., Zachariadis, G., Boskou, G., & Stratis, J. (1998). Electrothermal atomic absorption spectrometric determination of aluminium, cadmium, chromium, copper, iron, manganese, nickel and lead in olive oil. *Journal of Analytical Atomic Spectrometry*, 13(3), 201-204.
- Karci, A., Wurtzler, E. M., Armah, A., Wendell, D., & Dionysiou, D. D. (2018). Solar photo-Fenton treatment of microcystin-LR in aqueous environment: Transformation products and toxicity in different water matrices. *Journal of hazardous materials*.
- Karunanayake, A. G., Todd, O. A., Crowley, M., Ricchetti, L., Pittman Jr, C. U., Anderson, R., Mlsna, T. (2018). Lead and cadmium remediation using magnetized and nonmagnetized biochar from Douglas fir. *Chemical Engineering Journal*, 331, 480-491.
- Karve, M., & Rajgor, R. V. (2007). Solid phase extraction of lead on octadecyl bonded silica membrane disk modified with Cyanex302 and determination by flame atomic absorption spectrometry. *Journal of hazardous materials*, 141(3), 607-613.
- Khataee, A., Pons, M.-N., & Zahraa, O. (2009). Photocatalytic degradation of three azo dyes using immobilized TiO<sub>2</sub> nanoparticles on glass plates activated by UV light irradiation: Influence of dye molecular structure. *Journal of hazardous materials*, 168(1), 451-457.
- Khatamian, M., Hashemian, S., & Sabae, S. (2010). Preparation and photo-catalytic activity of nano-TiO<sub>2</sub>–ZSM-5 composite. *Materials Science in Semiconductor Processing*, 13(3), 156-161.
- Khattari, S., & Singh, M. (2009). Removal of malachite green from dye wastewater using neem sawdust by adsorption. *Journal of hazardous materials*, 167(1-3), 1089-1094.
- Khavar, A. H. C., Moussavi, G., & Mahjoub, A. R. (2018). The preparation of TiO<sub>2</sub>@ rGO nanocomposite efficiently activated with UVA/LED and H<sub>2</sub>O<sub>2</sub> for high rate oxidation of acetaminophen: Catalyst characterization and acetaminophen degradation and mineralization. *Applied Surface Science*, 440, 963-973.
- Khavar, A. H. C., Moussavi, G., Mahjoub, A. R., Satari, M., & Abdolmaleki, P. (2018). Synthesis and visible-light photocatalytic activity of In, S-TiO<sub>2</sub>@ rGO nanocomposite for degradation and detoxification of pesticide atrazine in water. *Chemical Engineering Journal*, 345, 300-311.
- Kim, S. H., Kim, J. S., Park, S. M., & Chang, S.-K. (2006). Hg<sup>2+</sup>-selective off– on and Cu<sup>2+</sup>-selective on– off type fluoroionophore based upon cyclam. *Organic letters*, 8(3), 371-374.
- Kokšal, J., Synek, V., & Janoš, P. (2002). Extraction-spectrometric determination of lead in high-purity aluminium salts. *Talanta*, 58(2), 325-330.

- Kumar, A. S. K., Jiang, S.-J., & Tseng, W.-L. (2016). Facile synthesis and characterization of thiol-functionalized graphene oxide as effective adsorbent for Hg (II). *Journal of Environmental Chemical Engineering*, 4(2), 2052-2065.
- Kusvuran, E., & Erbatur, O. (2004). Degradation of aldrin in adsorbed system using advanced oxidation processes: comparison of the treatment methods. *Journal of hazardous materials*, 106(2-3), 115-125.
- Lafjah, M., Djafri, F., Bengueddach, A., Keller, N., & Keller, V. (2011). Beta zeolite supported sol-gel TiO<sub>2</sub> materials for gas phase photocatalytic applications. *Journal of hazardous materials*, 186(2-3), 1218-1225.
- Lebeau, B., Fowler, C. E., Hall, S. R., & Mann, S. (1999). Transparent thin films and monoliths prepared from dye-functionalized ordered silica mesostructures. *Journal of Materials Chemistry*, 9(10), 2279-2281.
- Lee, J. S., Han, M. S., & Mirkin, C. A. (2007). Colorimetric detection of mercuric ion (Hg<sup>2+</sup>) in aqueous media using DNA-functionalized gold nanoparticles. *Angewandte Chemie*, 119(22), 4171-4174.
- Li, B., Wang, D., Lv, J., & Zhang, Z. (2006). Chemometrics-assisted simultaneous determination of cobalt (II) and chromium (III) with flow-injection chemiluminescence method. *Spectrochimica Acta Part A: Molecular and Biomolecular Spectroscopy*, 65(1), 67-72.
- Li, G., Wang, B., Sun, Q., Xu, W. Q., & Han, Y. (2017). Adsorption of lead ion on amino-functionalized fly-ash-based SBA-15 mesoporous molecular sieves prepared via two-step hydrothermal method. *Microporous and Mesoporous Materials*, 252, 105-115.
- Li, W.-C., Lu, A.-H., Palkovits, R., Schmidt, W., Spliethoff, B., & Schüth, F. (2005). Hierarchically structured monolithic silicalite-1 consisting of crystallized nanoparticles and its performance in the Beckmann rearrangement of cyclohexanone oxime. *Journal of the American Chemical Society*, 127(36), 12595-12600.
- Li, X., Xiong, Y., Li, Z., & Xie, Y. (2006). Large-scale fabrication of TiO<sub>2</sub> hierarchical hollow spheres. *Inorganic chemistry*, 45(9), 3493-3495.
- Li, Y., Liu, Z., Li, Y., Wu, Y., Chen, J., Liu, Y., & Na, P. (2018). One-step hydrothermal synthesis of Bi<sub>2</sub>S<sub>3</sub>-TiO<sub>2</sub>-RGO composites with enhanced visible light photocatalytic activities. *NANO*.
- Li, Y., Zhou, J., Liu, C., & Li, H. (2012). Composite quantum dots detect Cd (II) in living cells in a fluorescence “turning on” mode. *Journal of Materials Chemistry*, 22(6), 2507-2511.
- Liao, Y., Xie, C., Liu, Y., Chen, H., Li, H., & Wu, J. (2012). Comparison on photocatalytic degradation of gaseous formaldehyde by TiO<sub>2</sub>, ZnO and their composite. *Ceramics International*, 38(6), 4437-4444.
- Lin, K., Sun, Z., Lin, S., Jiang, D., & Xiao, F.-S. (2004). Ordered mesoporous titanosilicates with better catalytically active titanium sites assembled from preformed titanosilicate precursors with zeolite building units in alkaline media. *Microporous and Mesoporous Materials*, 72(1-3), 193-201.
- Liu, A., Hidajat, K., Kawi, S., & Zhao, D. (2000). A new class of hybrid mesoporous materials with functionalized organic monolayers for selective adsorption of heavy metal ions. *Chemical Communications*(13), 1145-1146.
- Liu, S., Lim, M., & Amal, R. (2014). TiO<sub>2</sub>-coated natural zeolite: rapid humic acid adsorption and effective photocatalytic regeneration. *Chemical Engineering Science*, 105, 46-52.
- Liu, W., Cai, J., Ding, Z., & Li, Z. (2015). TiO<sub>2</sub>/RGO composite aerogels with controllable and continuously tunable surface wettability for varied aqueous photocatalysis. *Applied Catalysis B: Environmental*, 174, 421-426.
- Liu, Y., & Pinnavaia, T. J. (2003). Aluminosilicate nanoparticles for catalytic hydrocarbon cracking. *Journal of the American Chemical Society*, 125(9), 2376-2377.
- Liu, Y., & Pinnavaia, T. J. (2004). Assembly of wormhole aluminosilicate mesostructures from zeolite seeds. *Journal of Materials Chemistry*, 14(7), 1099-1103.

- Loneragan, S. C. (2018). Water and conflict: Rhetoric and reality. In *Environmental conflict* (pp. 109-124): Routledge.
- López-Muñoz, M.-J., van Grieken, R., Aguado, J., & Marugán, J. (2005). Role of the support on the activity of silica-supported TiO<sub>2</sub> photocatalysts: structure of the TiO<sub>2</sub>/SBA-15 photocatalysts. *Catalysis Today*, *101*(3-4), 307-314.
- Love, C. B., Arnesen, S. J., Phillips, S. J., & Windom, R. E. (2014). National Library of Medicine Disaster Information Management Research Center: Achieving the vision, 2010–2013. *Information services & use*, *34*(1-2), 149-170.
- Loy, D. A., & Shea, K. J. (1995). Bridged polysilsesquioxanes. Highly porous hybrid organic-inorganic materials. *Chemical reviews*, *95*(5), 1431-1442.
- Lu, F., & Astruc, D. (2018). Nanomaterials for removal of toxic elements from water. *Coordination Chemistry Reviews*, *356*, 147-164.
- Luo, X., Shen, T., Ding, L., Zhong, W., Luo, J., & Luo, S. (2016). Novel thymine-functionalized MIL-101 prepared by post-synthesis and enhanced removal of Hg<sup>2+</sup> from water. *Journal of hazardous materials*, *306*, 313-322.
- Lv, F., Wang, H., Li, Z., Zhang, Q., Liu, X., & Su, Y. (2018). Fabrication and photocatalytic ability of an Au/TiO<sub>2</sub>/reduced graphene oxide nanocomposite. *Frontiers of Environmental Science & Engineering*, *12*(1), 4.
- Ma, F., Guo, J.-b., Zhao, L.-j., Chang, C.-c., & Cui, D. (2009). Application of bioaugmentation to improve the activated sludge system into the contact oxidation system treating petrochemical wastewater. *Bioresource technology*, *100*(2), 597-602.
- Ma, P., Ma, H., Sabatino, S., Galia, A., & Scialdone, O. (2018). Electrochemical treatment of real wastewater. Part 1: Effluents with low conductivity. *Chemical Engineering Journal*, *336*, 133-140.
- Machado, A. E. H., de Miranda, J. A., de Freitas, R. F., Duarte, E. T. F., Ferreira, L. F., Albuquerque, Y. D., de Oliveira, L. (2003). Destruction of the organic matter present in effluent from a cellulose and paper industry using photocatalysis. *Journal of Photochemistry and Photobiology A: Chemistry*, *155*(1-3), 231-241.
- Mahadwad, O., Parikh, P., Jasra, R., & Patil, C. (2011). Photocatalytic degradation of reactive black-5 dye using TiO<sub>2</sub> impregnated ZSM-5. *Bulletin of Materials Science*, *34*(3), 551-556.
- Mahalakshmi, M., Priya, S. V., Arabindoo, B., Palanichamy, M., & Murugesan, V. (2009). Photocatalytic degradation of aqueous propoxur solution using TiO<sub>2</sub> and H $\beta$  zeolite-supported TiO<sub>2</sub>. *Journal of hazardous materials*, *161*(1), 336-343.
- Maraschi, F., Sturini, M., Speltini, A., Pretali, L., Profumo, A., Pastorello, A., Caratto, V. (2014). TiO<sub>2</sub>-modified zeolites for fluoroquinolones removal from wastewaters and reuse after solar light regeneration. *Journal of Environmental Chemical Engineering*, *2*(4), 2170-2176.
- Marco, M., Claudio, M., & Fabrizio, S. (2017). New insights into the Photocatalytic activity of TiO<sub>2</sub>/reduced-Graphene Oxide: from the role of the substrate adsorption to the evidence of the electron transfer from rGO to TiO<sub>2</sub>. Paper presented at the Italian Photochemistry Meeting 2017.
- Martín, D. M., Faccini, M., García, M., & Amantia, D. (2018). Highly efficient removal of heavy metal ions from polluted water using ion-selective polyacrylonitrile nanofibers. *Journal of Environmental Chemical Engineering*, *6*(1), 236-245.
- Mathur, N., Bhatnagar, P., & Sharma, P. (2012). Review of the Mutagenicity of Textile Dye Products. *Universal Journal of Environmental Research & Technology*, *2*(2).
- Melo Zurita, M. d. L., Thomsen, D. C., Holbrook, N. J., Smith, T. F., Lyth, A., Munro, P. G., Baird, J. (2018). Global Water Governance and Climate Change: Identifying Innovative Arrangements for Adaptive Transformation. *Water*, *10*(1), 29.
- Memon, S. Q., Hasany, S., Bhangar, M., & Khuhawar, M. (2005). Enrichment of Pb (II) ions using phthalic acid functionalized XAD-16 resin as a sorbent. *Journal of colloid and interface science*, *291*(1), 84-91.
- Meng, X., Nawaz, F., & Xiao, F.-S. (2009). Templating route for synthesizing mesoporous zeolites with improved catalytic properties. *Nano Today*, *4*(4), 292-301.

- Mercier, L., & Pinnavaia, T. J. (1998). Heavy metal ion adsorbents formed by the grafting of a thiol functionality to mesoporous silica molecular sieves: factors affecting Hg (II) uptake. *Environmental Science & Technology*, 32(18), 2749-2754.
- Mesquita, R. B., Fernandes, S. M., & Rangel, A. O. (2004). A flow system for the spectrophotometric determination of lead in different types of waters using ion-exchange for pre-concentration and elimination of interferences. *Talanta*, 62(2), 395-401.
- Methylmercury, W. (1990). environmental health criteria 101. *Geneva: World Health Organization*, 1-144.
- MiarAlipour, S., Friedmann, D., Scott, J., & Amal, R. (2018). TiO<sub>2</sub>/porous adsorbents: Recent advances and novel applications. *Journal of hazardous materials*, 341, 404-423.
- Mittal, A., Gupta, V., Malviya, A., & Mittal, J. (2008). Process development for the batch and bulk removal and recovery of a hazardous, water-soluble azo dye (Metanil Yellow) by adsorption over waste materials (Bottom Ash and De-Oiled Soya). *Journal of hazardous materials*, 151(2-3), 821-832.
- Mittal, A., Malviya, A., Kaur, D., Mittal, J., & Kurup, L. (2007). Studies on the adsorption kinetics and isotherms for the removal and recovery of Methyl Orange from wastewaters using waste materials. *Journal of hazardous materials*, 148(1-2), 229-240.
- Mo, J., Zhou, L., Li, X., Li, Q., Wang, L., & Wang, Z. (2017). On-line separation and pre-concentration on a mesoporous silica-grafted graphene oxide adsorbent coupled with solution cathode glow discharge-atomic emission spectrometry for the determination of lead. *Microchemical Journal*, 130, 353-359.
- Mohagheghian, A., Karimi, S.-A., Yang, J.-K., & Shirzad-Siboni, M. (2015). Photocatalytic degradation of a textile dye by illuminated tungsten oxide nanopowder. *Journal of Advanced Oxidation Technologies*, 18(1), 61-68.
- Mohammed, A. S., Kapri, A., & Goel, R. (2011). Heavy metal pollution: source, impact, and remedies. In *Biomangement of metal-contaminated soils* (pp. 1-28): Springer.
- Monier, M., Nawar, N., & Abdel-Latif, D. (2010). Preparation and characterization of chelating fibers based on natural wool for removal of Hg (II), Cu (II) and Co (II) metal ions from aqueous solutions. *Journal of hazardous materials*, 184(1-3), 118-125.
- Montañez, J. P., Gómez, S., Santiago, A. N., & Pierella, L. B. (2015). TiO<sub>2</sub> Supported on HZSM-11 Zeolite as Efficient Catalyst for the Photodegradation of Chlorobenzoic Acids. *Journal of the Brazilian Chemical Society*, 26(6), 1191-1200.
- Motsa, M. M., Mamba, B. B., Thwala, J. M., & Msagati, T. A. (2011). Preparation, characterization, and application of polypropylene-clinoptilolite composites for the selective adsorption of lead from aqueous media. *Journal of colloid and interface science*, 359(1), 210-219.
- Mutuma, B. K., Shao, G. N., Kim, W. D., & Kim, H. T. (2015). Sol-gel synthesis of mesoporous anatase-brookite and anatase-brookite-rutile TiO<sub>2</sub> nanoparticles and their photocatalytic properties. *Journal of colloid and interface science*, 442, 1-7.
- Nagarjuna, R., Challagulla, S., Alla, N., Ganesan, R., & Roy, S. (2015). Synthesis and characterization of reduced-graphene oxide/TiO<sub>2</sub>/Zeolite-4A: A bifunctional nanocomposite for abatement of methylene blue. *Materials & Design*, 86, 621-626.
- Naushad, M., AlOthman, Z., Awual, M. R., Alam, M. M., & Eldesoky, G. (2015). Adsorption kinetics, isotherms, and thermodynamic studies for the adsorption of Pb<sup>2+</sup> and Hg<sup>2+</sup> metal ions from aqueous medium using Ti (IV) iodovanadate cation exchanger. *Ionics*, 21(8), 2237-2245.
- Naushad, M., Khan, M. R., AlOthman, Z. A., & Awual, M. R. (2016). Bromate removal from water samples using strongly basic anion exchange resin Amberlite IRA-400: kinetics, isotherms and thermodynamic studies. *Desalination and Water Treatment*, 57(13), 5781-5788.



- Nazeeruddin, M. K., Di Censo, D., Humphry-Baker, R., & Grätzel, M. (2006). Highly selective and reversible optical, colorimetric, and electrochemical detection of mercury (II) by amphiphilic ruthenium complexes anchored onto mesoporous oxide films. *Advanced Functional Materials*, 16(2), 189-194.
- Ndung'u, K., Franks, R. P., Bruland, K. W., & Flegal, A. R. (2003). Organic complexation and total dissolved trace metal analysis in estuarine waters: comparison of solvent-extraction graphite furnace atomic absorption spectrometric and chelating resin flow injection inductively coupled plasma-mass spectrometric analysis. *Analytica Chimica Acta*, 481(1), 127-138.
- Ndung'u, K., Hibdon, S., & Flegal, A. R. (2004). Determination of lead in vinegar by ICP-MS and GFAAS: evaluation of different sample preparation procedures. *Talanta*, 64(1), 258-263.
- Ngomsik, A.-F., Bee, A., Siaugue, J.-M., Talbot, D., Cabuil, V., & Cote, G. (2009). Co (II) removal by magnetic alginate beads containing Cyanex 272®. *Journal of hazardous materials*, 166(2-3), 1043-1049.
- Nguyen-Phan, T.-D., Pham, V. H., Shin, E. W., Pham, H.-D., Kim, S., Chung, J. S., Hur, S. H. (2011). The role of graphene oxide content on the adsorption-enhanced photocatalysis of titanium dioxide/graphene oxide composites. *Chemical Engineering Journal*, 170(1), 226-232.
- Nidheesh, P., Zhou, M., & Oturan, M. A. (2018). An overview on the removal of synthetic dyes from water by electrochemical advanced oxidation processes. *Chemosphere*.
- Nyairo, W. N., Eker, Y. R., Kowenje, C., Akin, I., Bingol, H., Tor, A., & Onger, D. M. (2018). Efficient adsorption of lead (II) and copper (II) from aqueous phase using oxidized multiwalled carbon nanotubes/polypyrrole composite. *Separation Science and Technology*, 1-13.
- Ogura, M., Fukuzawa, S., Fukunaga, S., Yamazaki, H., Kondo, J. N., Morimoto, M., Thommes, M. (2018). Identification of the basic sites on nitrogen-substituted microporous and mesoporous silicate frameworks using CO<sub>2</sub> as a probe molecule. *Langmuir*.
- Ooka, C., Yoshida, H., Suzuki, K., & Hattori, T. (2003). Adsorption and photocatalytic degradation of toluene vapor in air on highly hydrophobic TiO<sub>2</sub> pillared clay. *Chemistry Letters*, 32(10), 896-897.
- Organization, W. H. (2004). *Guidelines for drinking-water quality: recommendations* (Vol. 1): World Health Organization.
- Organization, W. H. (2013). *Oral health surveys: basic methods*: World Health Organization.
- Paek, S.-M., Yoo, E., & Honma, I. (2008). Enhanced cyclic performance and lithium storage capacity of SnO<sub>2</sub>/graphene nanoporous electrodes with three-dimensionally delaminated flexible structure. *Nano letters*, 9(1), 72-75.
- Panpa, W., Sujaridworakun, P., & Jinawath, S. (2008). Photocatalytic activity of TiO<sub>2</sub>/ZSM-5 composites in the presence of SO<sub>4</sub><sup>2-</sup> ion. *Applied Catalysis B: Environmental*, 80(3-4), 271-276.
- Parshetti, G., Telke, A., Kalyani, D., & Govindwar, S. (2010). Decolorization and detoxification of sulfonated azo dye methyl orange by *Kocuria rosea* MTCC 1532. *Journal of hazardous materials*, 176(1-3), 503-509.
- Pastrana-Martínez, L. M., Morales-Torres, S., Figueiredo, J. L., Faria, J. L., & Silva, A. M. (2018). Graphene photocatalysts. In *Multifunctional Photocatalytic Materials for Energy* (pp. 79-101): Elsevier.
- Paul, B., Martens, W. N., & Frost, R. L. (2012). Immobilised anatase on clay mineral particles as a photocatalyst for herbicides degradation. *Applied Clay Science*, 57, 49-54.
- Pawar, R. C., Khare, V., & Lee, C. S. (2014). Hybrid photocatalysts using graphitic carbon nitride/cadmium sulfide/reduced graphene oxide (gC<sub>3</sub>N<sub>4</sub>/CdS/RGO) for superior photodegradation of organic pollutants under UV and visible light. *Dalton Transactions*, 43(33), 12514-12527.

- Pearson, R. G. (1963). Hard and soft acids and bases. *Journal of the American Chemical Society*, 85(22), 3533-3539.
- Peng, L., Ni, Y., Wei, X., Hanyu, W., Duoqiang, P., & Wangsuo, W. (2017). Removal of U (VI) from aqueous solution using TiO<sub>2</sub> modified  $\beta$ -zeolite. *Radiochimica Acta*, 105(12), 1005-1013.
- Plazinski, W., Rudzinski, W., & Plazinska, A. (2009). Theoretical models of sorption kinetics including a surface reaction mechanism: a review. *Advances in colloid and interface science*, 152(1-2), 2-13.
- Prakash, A., & Malhotra, R. (2018). Co (II), Ni (II), Cu (II) and Zn (II) complexes of aminothiazole-derived Schiff base ligands: Synthesis, characterization, antibacterial and cytotoxicity evaluation, bovine serum albumin binding and density functional theory studies. *Applied Organometallic Chemistry*, 32(2), e4098.
- Qiu, B., Xing, M., & Zhang, J. (2018). Recent advances in three-dimensional graphene based materials for catalysis applications. *Chemical Society Reviews*, 47(6), 2165-2216.
- Rajamohan, N., Rajasimman, M., Rajeshkannan, R., & Sivaprakash, B. (2013). Kinetic modeling and isotherm studies on a batch removal of acid red 114 by an activated plant biomass. *Journal of Engineering Science and Technology*, 8(6), 778-792.
- Rauf, M. A., Meemani, M. A., Khaleel, A., & Ahmed, A. (2010). Photocatalytic degradation of methylene blue using a mixed catalyst and product analysis by LC/MS. *Chemical Engineering Journal*, 157(2-3), 373-378.
- Reddy, E. P., Davydov, L., & Smirniotis, P. (2003). TiO<sub>2</sub>-loaded zeolites and mesoporous materials in the sonophotocatalytic decomposition of aqueous organic pollutants: the role of the support. *Applied Catalysis B: Environmental*, 42(1), 1-11.
- Riaz, M., Nadeem, R., Hanif, M. A., & Ansari, T. M. (2009). Pb (II) biosorption from hazardous aqueous streams using *Gossypium hirsutum* (Cotton) waste biomass. *Journal of hazardous materials*, 161(1), 88-94.
- Ritchie, S., & Bhattacharyya, D. (2002). Membrane-based hybrid processes for high water recovery and selective inorganic pollutant separation. *Journal of hazardous materials*, 92(1), 21-32.
- Rodman, D. L., Pan, H., Clavier, C. W., Feng, X., & Xue, Z.-L. (2005). Optical metal ion sensor based on diffusion followed by an immobilizing reaction. Quantitative analysis by a mesoporous monolith containing functional groups. *Analytical Chemistry*, 77(10), 3231-3237.
- Rodríguez, J. G., Barciela, J. G., Herrero, C. L., García, S. M., & Peña, R. C. (2005). Direct and combined methods for the determination of chromium, copper, and nickel in honey by electrothermal atomic absorption spectroscopy. *Journal of agricultural and food chemistry*, 53(17), 6616-6623.
- Ross, S. M. (1994). *Toxic metals in soil-plant systems*: John Wiley and Sons Ltd.
- Sacco, O., Vaiano, V., & Matarangolo, M. (2018). ZnO supported on zeolite pellets as efficient catalytic system for the removal of caffeine by adsorption and photocatalysis. *Separation and Purification Technology*, 193, 303-310.
- Sakamoto-Arnold, C. M., & Johnson, K. S. (1987). Determination of picomolar levels of cobalt in seawater by flow injection analysis with chemiluminescence detection. *Analytical Chemistry*, 59(14), 1789-1794.
- Sakthivel, B., Josephine, D. S. R., Sethuraman, K., & Dhakshinamoorthy, A. (2018). Oxidation of styrene using TiO<sub>2</sub>-graphene oxide composite as solid heterogeneous catalyst with hydrogen peroxide as oxidant. *Catalysis Communications*, 108, 41-45.
- Saleh, T. A. (2015). Isotherm, kinetic, and thermodynamic studies on Hg (II) adsorption from aqueous solution by silica-multiwall carbon nanotubes. *Environmental Science and Pollution Research*, 22(21), 16721-16731.
- Saratale, R. G., Saratale, G. D., Chang, J.-S., & Govindwar, S. (2011). Bacterial decolorization and degradation of azo dyes: a review. *Journal of the Taiwan Institute of Chemical Engineers*, 42(1), 138-157.
- Sarkar, D., Essington, M., & Misra, K. (2000). Adsorption of mercury (II) by kaolinite. *Soil Science Society of America Journal*, 64(6), 1968-1975.

- Sassi, H., Lafaye, G., Amor, H. B., Gannouni, A., Jeday, M. R., & Barbier, J. (2018). Wastewater treatment by catalytic wet air oxidation process over Al-Fe pillared clays synthesized using microwave irradiation. *Frontiers of Environmental Science & Engineering*, 12(1), 2.
- Schmidt, I., Boisen, A., Gustavsson, E., Ståhl, K., Pehrson, S., Dahl, S., Jacobsen, C. J. (2001). Carbon nanotube templated growth of mesoporous zeolite single crystals. *Chemistry of materials*, 13(12), 4416-4418.
- Scovill, J. P. (1991). A FACILE SYNTHESIS OF THIOSEMICARBAZIDES AND THIOSEMICARBAZONES BY THE TRANSAMINATION OF 4-METHYL-4-PHENYL-3-THIOSEMICARBAZIDE. *Phosphorus, Sulfur, and Silicon and the Related Elements*, 60(1-2), 15-19.
- Selvaraj, S., Sun, Y., Sukumaran, P., & Singh, B. B. (2016). Resveratrol activates autophagic cell death in prostate cancer cells via downregulation of STIM1 and the mTOR pathway. *Molecular carcinogenesis*, 55(5), 818-831.
- Setthaya, N., Chindaprasirt, P., Yin, S., & Pimraksa, K. (2017). TiO<sub>2</sub>-zeolite photocatalysts made of metakaolin and rice husk ash for removal of methylene blue dye. *Powder Technology*, 313, 417-426.
- Shahat, A., Awual, M. R., Khaleque, M. A., Alam, M. Z., Naushad, M., & Chowdhury, A. S. (2015). Large-pore diameter nano-adsorbent and its application for rapid lead (II) detection and removal from aqueous media. *Chemical Engineering Journal*, 273, 286-295.
- Shahat, A., Awual, M. R., & Naushad, M. (2015). Functional ligand anchored nanomaterial based facial adsorbent for cobalt (II) detection and removal from water samples. *Chemical Engineering Journal*, 271, 155-163.
- Shahat, A., Hassan, H. M., Azzazy, H. M., El-Sharkawy, E., Abdou, H. M., & Awual, M. R. (2018). Novel hierarchical composite adsorbent for selective lead (II) ions capturing from wastewater samples. *Chemical Engineering Journal*, 332, 377-386.
- Shang, J.-K., Wu, P., & Xie, R.-C. (2016). Co-doped titanium oxide foam and water disinfection device. In: Google Patents.
- Shankar, M., Anandan, S., Venkatachalam, N., Arabindoo, B., & Murugesan, V. (2006). Fine route for an efficient removal of 2, 4-dichlorophenoxyacetic acid (2, 4-D) by zeolite-supported TiO<sub>2</sub>. *Chemosphere*, 63(6), 1014-1021.
- Sharma, A., & Lee, B.-K. (2016). Rapid photo-degradation of 2-chlorophenol under visible light irradiation using cobalt oxide-loaded TiO<sub>2</sub>/reduced graphene oxide nanocomposite from aqueous media. *Journal of environmental management*, 165, 1-10.
- Sharma, P. R., Chattopadhyay, A., Zhan, C., Sharma, S. K., Geng, L., & Hsiao, B. S. (2018). Lead removal from water using carboxycellulose nanofibers prepared by nitro-oxidation method. *Cellulose*, 25(3), 1961-1973.
- Shawabkeh, R. A., & Tutunji, M. F. (2003). Experimental study and modeling of basic dye sorption by diatomaceous clay. *Applied Clay Science*, 24(1-2), 111-120.
- Shea, K. J., & Loy, D. A. (2001). Bridged polysilsesquioxanes. Molecular-engineered hybrid organic-inorganic materials. *Chemistry of materials*, 13(10), 3306-3319.
- Sheikh, T. A., Arshad, M. N., Rahman, M. M., Asiri, A. M., Marwani, H. M., Awual, M. R., & Bawazir, W. A. (2017). Trace electrochemical detection of Ni<sup>2+</sup> ions with bidentate N, N'-(ethane-1, 2-diyl) bis (3, 4-dimethoxybenzenesulfonamide)[EDBDMBS] as a chelating agent. *Inorganica Chimica Acta*, 464, 157-166.
- Shenashen, M., El-Safty, S., & Elshehy, E. (2013). Architecture of optical sensor for recognition of multiple toxic metal ions from water. *Journal of hazardous materials*, 260, 833-843.
- Shenashen, M. A., El-Safty, S. A., & Elshehy, E. A. (2014). Monolithic scaffolds for highly selective ion sensing/removal of Co (II), Cu (II), and Cd (II) ions in water. *Analyst*, 139(24), 6393-6405.

- Shi, J.-W., Zheng, J.-T., & Ji, X.-J. (2010). TiO<sub>2</sub>-SiO<sub>2</sub>/activated carbon fibers photocatalyst: preparation, characterization, and photocatalytic activity. *Environmental Engineering Science*, 27(11), 923-930.
- Shintre, S., & Thakur, P. (2016). Influence of operational parameters on photomineralization of Evans blue by Ag-TiO<sub>2</sub> composite.
- Shrivastava, A., & Gupta, V. (2011). Methods for the determination of limit of detection and limit of quantitation of the analytical methods. *Chronicles of Young Scientists*, 2(1), 21-21.
- Sing, K. S. (1985). Reporting physisorption data for gas/solid systems with special reference to the determination of surface area and porosity (Recommendations 1984). *Pure and Applied Chemistry*, 57(4), 603-619.
- Singhal, D., Singh, A. K., & Upadhyay, A. (2014). Highly selective potentiometric and colorimetric determinations of cobalt (II) ion using thiazole based ligands. *Materials Science and Engineering: C*, 45, 216-224.
- Sivakumar, S., & Prathapachandra Kurup, M. (2002). *Structural, Spectral, Biological and Electrochemical Studies Of Some 3d Transition Metal Complexes of ONS and NNS Donor Ligands*. Department of Applied Chemistry,
- Slokar, Y. M., & Le Marechal, A. M. (1998). Methods of decoloration of textile wastewaters. *Dyes and pigments*, 37(4), 335-356.
- Souza, J. M., & Tarley, C. R. (2009). Sorbent separation and enrichment method for cobalt ions determination by graphite furnace atomic absorption spectrometry in water and urine samples using multiwall carbon nanotubes. *International Journal of Environmental and Analytical Chemistry*, 89(7), 489-502.
- Soylak, M., Narin, I., de Almeida Bezerra, M., & Ferreira, S. L. C. (2005). Factorial design in the optimization of preconcentration procedure for lead determination by FAAS. *Talanta*, 65(4), 895-899.
- Soylak, M., & Yilmaz, E. (2011). Ionic liquid dispersive liquid-liquid microextraction of lead as pyrrolidinedithiocarbamate chelate prior to its flame atomic absorption spectrometric determination. *Desalination*, 275(1-3), 297-301.
- Srivastava, R., Choi, M., & Ryoo, R. (2006). Mesoporous materials with zeolite framework: remarkable effect of the hierarchical structure for retardation of catalyst deactivation. *Chemical Communications*(43), 4489-4491.
- Stankovich, S., Dikin, D. A., Piner, R. D., Kohlhaas, K. A., Kleinhammes, A., Jia, Y., Ruoff, R. S. (2007). Synthesis of graphene-based nanosheets via chemical reduction of exfoliated graphite oxide. *carbon*, 45(7), 1558-1565.
- Stojakovic, D., Jovanovic, M., & Rajic, N. (2017). Lead (II) removal from aqueous solutions by serbian zeolitic Tuff. *Environmental Engineering & Management Journal (EEMJ)*, 16(1).
- Sun, J. C., Cheng, J., Fan, H., & Ai, S. Y. (2013). *Bifunctional Ag/AgCl/ $\alpha$ -Co (OH)<sub>2</sub> nanocomposite with selective adsorption and photocatalytic properties for dyes removal*. Paper presented at the Advanced Materials Research.
- Sun, Q., Hu, X., Zheng, S., Sun, Z., Liu, S., & Li, H. (2015). Influence of calcination temperature on the structural, adsorption and photocatalytic properties of TiO<sub>2</sub> nanoparticles supported on natural zeolite. *Powder Technology*, 274, 88-97.
- Sun, Y., Han, Y., Yuan, L., Ma, S., Jiang, D., & Xiao, F.-S. (2003). Microporosity in ordered mesoporous aluminosilicates characterized by catalytic probing reactions. *The Journal of Physical Chemistry B*, 107(8), 1853-1857.
- Takeda, N., Torimoto, T., Sampath, S., Kuwabata, S., & Yoneyama, H. (1995). Effect of inert supports for titanium dioxide loading on enhancement of photodecomposition rate of gaseous propionaldehyde. *The Journal of Physical Chemistry*, 99(24), 9986-9991.
- Takeuchi, M., Deguchi, J., Hidaka, M., Sakai, S., Woo, K., Choi, P.-P., Anpo, M. (2009). Enhancement of the photocatalytic reactivity of TiO<sub>2</sub> nano-particles by a simple mechanical blending with hydrophobic mordenite (MOR) zeolite. *Applied Catalysis B: Environmental*, 89(3-4), 406-410.

- Takeuchi, M., Hidaka, M., & Anpo, M. (2012). Efficient removal of toluene and benzene in gas phase by the TiO<sub>2</sub>/Y-zeolite hybrid photocatalyst. *Journal of hazardous materials*, 237, 133-139.
- Takeuchi, M., Kimura, T., Hidaka, M., Rakhmawaty, D., & Anpo, M. (2007). Photocatalytic oxidation of acetaldehyde with oxygen on TiO<sub>2</sub>/ZSM-5 photocatalysts: Effect of hydrophobicity of zeolites. *Journal of Catalysis*, 246(2), 235-240.
- Tanev, P. T., & Pinnavaia, T. J. (1996). Mesoporous silica molecular sieves prepared by ionic and neutral surfactant templating: a comparison of physical properties. *Chemistry of materials*, 8(8), 2068-2079.
- Tang, X., Wang, Z., & Wang, Y. (2018). Visible active N-doped TiO<sub>2</sub>/reduced graphene oxide for the degradation of tetracycline hydrochloride. *Chemical Physics Letters*, 691, 408-414.
- Tao, H., Nguyen, N.-T., Hei, X.-H., Liang, X., & Chang, C.-T. (2015). Photocatalytic Degradation of Di-n-Butyl Phthalate by N-Doped Ti/13X/MCM-41 Molecular Sieve. *Journal of nanoscience and nanotechnology*, 15(7), 5418-5423.
- Tao, Y., Hattori, Y., Matumoto, A., Kanoh, H., & Kaneko, K. (2005). Comparative study on pore structures of mesoporous ZSM-5 from resorcinol-formaldehyde aerogel and carbon aerogel templating. *The Journal of Physical Chemistry B*, 109(1), 194-199.
- Tao, Y., Kanoh, H., Abrams, L., & Kaneko, K. (2006). Mesopore-modified zeolites: preparation, characterization, and applications. *Chemical reviews*, 106(3), 896-910.
- Tao, Y., Kanoh, H., Hanzawa, Y., & Kaneko, K. (2004). Template synthesis and characterization of mesoporous zeolites. *Colloids and Surfaces A: Physicochemical and Engineering Aspects*, 241(1-3), 75-80.
- Tao, Y., Kanoh, H., & Kaneko, K. (2003a). Uniform mesopore-donated zeolite Y using carbon aerogel templating. *The Journal of Physical Chemistry B*, 107(40), 10974-10976.
- Tao, Y., Kanoh, H., & Kaneko, K. (2003b). ZSM-5 monolith of uniform mesoporous channels. *Journal of the American Chemical Society*, 125(20), 6044-6045.
- Tao, Y., Kanoh, H., & Kaneko, K. (2005). Synthesis of mesoporous zeolite A by resorcinol-formaldehyde aerogel templating. *Langmuir*, 21(2), 504-507.
- Tayade, R. J., Kulkarni, R. G., & Jaska, R. V. (2007). Enhanced photocatalytic activity of TiO<sub>2</sub>-coated NaY and HY zeolites for the degradation of methylene blue in water. *Industrial & engineering chemistry research*, 46(2), 369-376.
- Thamaphat, K., Limsuwan, P., & Ngotawornchai, B. (2008). Phase characterization of TiO<sub>2</sub> powder by XRD and TEM. *Kasetsart J.(Nat. Sci.)*, 42(5), 357-361.
- Thommes, M., Kaneko, K., Neimark, A. V., Olivier, J. P., Rodriguez-Reinoso, F., Rouquerol, J., & Sing, K. S. (2015). Physisorption of gases, with special reference to the evaluation of surface area and pore size distribution (IUPAC Technical Report). *Pure and Applied Chemistry*, 87(9-10), 1051-1069.
- Tian, H., Li, B., Wang, H., Li, Y., Wang, J., Zhao, S., Yao, X. (2011). A nanocontainer that releases a fluorescence sensor for cadmium ions in water and its biological applications. *Journal of Materials Chemistry*, 21(28), 10298-10303.
- Triantafyllidis, K., Lappas, A., Vasalos, I., Liu, Y., Wang, H., & Pinnavaia, T. (2006). Gas-oil cracking activity of hydrothermally stable aluminosilicate mesostructures (MSU-S) assembled from zeolite seeds: Effect of the type of framework structure and porosity. *Catalysis Today*, 112(1-4), 33-36.
- Tuzen, M., Sari, A., Mendil, D., & Soylak, M. (2009). Biosorptive removal of mercury (II) from aqueous solution using lichen (*Xanthoparmelia conspersa*) biomass: kinetic and equilibrium studies. *Journal of hazardous materials*, 169(1-3), 263-270.
- Uchida, H., Itoh, S., & Yoneyama, H. (1993). Photocatalytic decomposition of propylamide using TiO<sub>2</sub> supported on activated carbon. *Chemistry Letters*, 22(12), 1995-1998.
- Valero-Romero, M., Sartipi, S., Sun, X., Rodríguez-Mirasol, J., Cordero, T., Kapteijn, F., & Gascon, J. (2016). Carbon/H-ZSM-5 composites as supports for bi-functional Fischer-Tropsch synthesis catalysts. *Catalysis Science & Technology*, 6(8), 2633-2646.

- Vieira, R. S., & Beppu, M. M. (2006). Dynamic and static adsorption and desorption of Hg (II) ions on chitosan membranes and spheres. *Water research*, 40(8), 1726-1734.
- Vieira, R. S., Oliveira, M. L. M., Guibal, E., Rodríguez-Castellón, E., & Beppu, M. M. (2011). Copper, mercury and chromium adsorption on natural and crosslinked chitosan films: an XPS investigation of mechanism. *Colloids and Surfaces A: Physicochemical and Engineering Aspects*, 374(1-3), 108-114.
- Vimonses, V., Lei, S., Jin, B., Chow, C. W., & Saint, C. (2009). Kinetic study and equilibrium isotherm analysis of Congo Red adsorption by clay materials. *Chemical Engineering Journal*, 148(2-3), 354-364.
- Von Burg, R. (1995). Inorganic mercury. *Journal of Applied Toxicology*, 15(6), 483-493.
- Wagner, K., Batchelor, J., & Jones, B. (1998). A Rowland Circle, multielement graphite furnace atomic absorption spectrometer. *Spectrochimica Acta Part B: Atomic Spectroscopy*, 53(13), 1805-1813.
- Walcarius, A., Etienne, M., & Lebeau, B. (2003). Rate of access to the binding sites in organically modified silicates. 2. Ordered mesoporous silicas grafted with amine or thiol groups. *Chemistry of materials*, 15(11), 2161-2173.
- Wang, C., Shi, H., & Li, Y. (2012). Synthesis and characterization of natural zeolite supported Cr-doped TiO<sub>2</sub> photocatalysts. *Applied Surface Science*, 258(10), 4328-4333.
- Wang, H., Liu, Y., & Pinnavaia, T. J. (2006). Highly acidic mesostructured aluminosilicates assembled from surfactant-mediated zeolite hydrolysis products. *The Journal of Physical Chemistry B*, 110(10), 4524-4526.
- Wang, J.-J., Jing, Y.-H., Ouyang, T., & Chang, C.-T. (2015). Preparation of 13X from waste quartz and photocatalytic reaction of methyl orange on TiO<sub>2</sub>/ZSM-5, 13X and Y-zeolite. *Journal of nanoscience and nanotechnology*, 15(8), 6141-6149.
- Wang, S., & Peng, Y. (2010). Natural zeolites as effective adsorbents in water and wastewater treatment. *Chemical Engineering Journal*, 156(1), 11-24.
- Wang, W., & Song, M. (2006). Photocatalytic activity of titania-containing mesoporous SBA-15 silica. *Microporous and Mesoporous Materials*, 96(1-3), 255-261.
- Wang, X.-s., & Qin, Y. (2005). Equilibrium sorption isotherms for of Cu<sup>2+</sup> on rice bran. *Process Biochemistry*, 40(2), 677-680.
- Wang, X., Tian, H., Yang, Y., Wang, H., Wang, S., Zheng, W., & Liu, Y. (2012). Reduced graphene oxide/CdS for efficiently photocatalytic degradation of methylene blue. *Journal of Alloys and Compounds*, 524, 5-12.
- Wang, Z., Yin, P., Qu, R., Chen, H., Wang, C., & Ren, S. (2013). Adsorption kinetics, thermodynamics and isotherm of Hg (II) from aqueous solutions using buckwheat hulls from Jiaodong of China. *Food chemistry*, 136(3-4), 1508-1514.
- Wei, H., McMaster, W. A., Tan, J. Z., Chen, D., & Caruso, R. A. (2018). Tricomponent brookite/anatase TiO<sub>2</sub>/gC<sub>3</sub>N<sub>4</sub> heterojunction in mesoporous hollow microspheres for enhanced visible-light photocatalysis. *Journal of Materials Chemistry A*.
- Williams, G., Seger, B., & Kamat, P. V. (2008). TiO<sub>2</sub>-graphene nanocomposites. UV-assisted photocatalytic reduction of graphene oxide. *ACS nano*, 2(7), 1487-1491.
- Wu, X., Zeng, M., Tong, X., Li, H., & Xu, Y. (2018). Preparation of surface modified TiO<sub>2</sub>/rGO microspheres and application in the photocatalytic decomposition of oleic acid. *Materials Research Express*.
- Xiang, B., Ling, D., Lou, H., & Gu, H. (2017). 3D hierarchical flower-like nickel ferrite/manganese dioxide toward lead (II) removal from aqueous water. *Journal of hazardous materials*, 325, 178-188.
- Xiang, Q., Yu, J., & Jaroniec, M. (2012). Graphene-based semiconductor photocatalysts. *Chemical Society Reviews*, 41(2), 782-796.
- Xiao, F.-S., Han, Y., Yu, Y., Meng, X., Yang, M., & Wu, S. (2002). Hydrothermally stable ordered mesoporous titanosilicates with highly active catalytic sites. *Journal of the American Chemical Society*, 124(6), 888-889.
- Xiao, F. S., Wang, L., Yin, C., Lin, K., Di, Y., Li, J., Yokoi, T. (2006). Catalytic properties of hierarchical mesoporous zeolites templated with a mixture of small organic

- ammonium salts and mesoscale cationic polymers. *Angewandte Chemie*, 118(19), 3162-3165.
- Xing, B., Chen, H., & Zhang, X. (2018). Efficient degradation of organic phosphorus in glyphosate wastewater by catalytic wet oxidation using modified activated carbon as a catalyst. *Environmental technology*, 39(6), 749-758.
- Yamashita, H., Harada, M., Tani, A., Honda, M., Takeuchi, M., Ichihashi, Y., Hirao, T. (2000). Preparation of efficient titanium oxide photocatalysts by an ionized cluster beam (ICB) method and their photocatalytic reactivities for the purification of water. *Catalysis Today*, 63(1), 63-69.
- Yan, W., Mahurin, S. M., Overbury, S. H., & Dai, S. (2005). Nonhydrolytic Layer-by-Layer Surface Sol–Gel Modification of Powdered Mesoporous Silica Materials with TiO<sub>2</sub>. *Chemistry of materials*, 17(8), 1923-1925.
- Yang, L., Wang, F., Hakki, A., Macphee, D. E., Liu, P., & Hu, S. (2017). The influence of zeolites fly ash bead/TiO<sub>2</sub> composite material surface morphologies on their adsorption and photocatalytic performance. *Applied Surface Science*, 392, 687-696.
- Yener, H., Yılmaz, M., Deliismail, Ö., Özkan, S. F., & Helvacı, Ş. Ş. (2017). Clinoptilolite supported rutile TiO<sub>2</sub> composites: Synthesis, characterization, and photocatalytic activity on the degradation of terephthalic acid. *Separation and Purification Technology*, 173, 17-26.
- Yıldız, O., Citak, D., Tuzen, M., & Soylak, M. (2011). Determination of copper, lead and iron in water and food samples after column solid phase extraction using 1-phenylthiosemicarbazide on Dowex Optipore L-493 resin. *Food and Chemical Toxicology*, 49(2), 458-463.
- Yogi, C., Kojima, K., Wada, N., Tokumoto, H., Takai, T., Mizoguchi, T., & Tamiaki, H. (2008). Photocatalytic degradation of methylene blue by TiO<sub>2</sub> film and Au particles-TiO<sub>2</sub> composite film. *Thin Solid Films*, 516(17), 5881-5884.
- Yu, Y., Addai-Mensah, J., & Losic, D. (2012). Functionalized diatom silica microparticles for removal of mercury ions. *Science and technology of advanced materials*, 13(1), 015008.
- Zachariadis, G. A., Anthemidis, A. N., Bettas, P. G., & Stratis, J. A. (2002). Determination of lead by on-line solid phase extraction using a PTFE micro-column and flame atomic absorption spectrometry. *Talanta*, 57(5), 919-927.
- Zein, R., Suhaili, R., Earnestly, F., & Munaf, E. (2010). Removal of Pb (II), Cd (II) and Co (II) from aqueous solution using *Garcinia mangostana* L. fruit shell. *Journal of hazardous materials*, 181(1-3), 52-56.
- Zepp, R. G., Faust, B. C., & Hoigne, J. (1992). Hydroxyl radical formation in aqueous reactions (pH 3-8) of iron (II) with hydrogen peroxide: the photo-Fenton reaction. *Environmental Science & Technology*, 26(2), 313-319.
- Zhang, B., Davis, S. A., Mendelson, N. H., & Mann, S. (2000). Bacterial templating of zeolite fibres with hierarchical structure. *Chemical Communications*(9), 781-782.
- Zhang, B., & Wei, C. (2018). Highly sensitive and selective detection of Pb<sup>2+</sup> using a turn-on fluorescent aptamer DNA silver nanoclusters sensor. *Talanta*, 182, 125-130.
- Zhang, H., Lv, X., Li, Y., Wang, Y., & Li, J. (2009). P<sub>25</sub>-graphene composite as a high performance photocatalyst. *ACS nano*, 4(1), 380-386.
- Zhang, L., Lv, F., Zhang, W., Li, R., Zhong, H., Zhao, Y., Wang, X. (2009). Photo degradation of methyl orange by attapulgite–SnO<sub>2</sub>–TiO<sub>2</sub> nanocomposites. *Journal of hazardous materials*, 171(1-3), 294-300.
- Zhang, W., Li, G., Wang, W., Qin, Y., An, T., Xiao, X., & Choi, W. (2018). Enhanced photocatalytic mechanism of Ag<sub>3</sub>PO<sub>4</sub> nano-sheets using MS<sub>2</sub> (M= Mo, W)/rGO hybrids as co-catalysts for 4-nitrophenol degradation in water. *Applied Catalysis B: Environmental*, 232, 11-18.
- Zhang, Y.-X., Jia, Y., Jin, Z., Yu, X.-Y., Xu, W.-H., Luo, T., Huang, X.-J. (2012). Self-assembled, monodispersed, flower-like  $\gamma$ -AlOOH hierarchical superstructures for efficient and fast removal of heavy metal ions from water. *CrystEngComm*, 14(9), 3005-3007.

- Zhang, Y., Yan, L., Xu, W., Guo, X., Cui, L., Gao, L., Du, B. (2014). Adsorption of Pb (II) and Hg (II) from aqueous solution using magnetic CoFe<sub>2</sub>O<sub>4</sub>-reduced graphene oxide. *Journal of Molecular Liquids*, 191, 177-182.
- Zhang, Z., Han, Y., Zhu, L., Wang, R., Yu, Y., Qiu, S., Xiao, F. S. (2001). Strongly acidic and high-temperature hydrothermally stable mesoporous aluminosilicates with ordered hexagonal structure. *Angewandte Chemie*, 113(7), 1298-1302.
- Zheng, S., Gao, L., Zhang, Q.-h., & Guo, J.-k. (2000). Synthesis, characterization and photocatalytic properties of titania-modified mesoporous silicate MCM-41. *Journal of Materials Chemistry*, 10(3), 723-727.
- Zhou, G., Chen, Y., Yang, J., & Yang, S. (2007). From cylindrical-channel mesoporous silica to vesicle-like silica with well-defined multilamella shells and large inter-shell mesopores. *Journal of Materials Chemistry*, 17(27), 2839-2844.
- Zhou, J., Liu, Y., Zhou, X., Ren, J., & Zhong, C. (2018). Magnetic multi-porous bio-adsorbent modified with amino siloxane for fast removal of Pb (II) from aqueous solution. *Applied Surface Science*, 427, 976-985.
- Zhou, Y., Yu, J., & Jiang, X. (2017). Removing lead ions from aqueous solutions by the thiosemicarbazide grafted multi-walled carbon nanotubes. *Water Science and Technology*, 76(2), 302-310.
- Zhu, H., Shen, Y., Wang, Q., Chen, K., Wang, X., Zhang, G., Bai, R. (2017). Highly promoted removal of Hg (ii) with magnetic CoFe<sub>2</sub>O<sub>4</sub>@ SiO<sub>2</sub> core-shell nanoparticles modified by thiol groups. *RSC Advances*, 7(62), 39204-39215.
- Zhu, M., Muhammad, Y., Hu, P., Wang, B., Wu, Y., Sun, X., Zhao, Z. (2018). Enhanced interfacial contact of dopamine bridged melamine-graphene/TiO<sub>2</sub> nano-capsules for efficient photocatalytic degradation of gaseous formaldehyde. *Applied Catalysis B: Environmental*, 232, 182-193.
- Zi, L., Huang, Y., Yan, Z., & Liao, S. (2014). Thioglycolic acid-capped CuInS<sub>2</sub>/ZnS quantum dots as fluorescent probe for cobalt ion detection. *Journal of Luminescence*, 148, 359-363.

***Every reasonable effort has been made to acknowledge the owners of copyright material. I would be pleased to hear from any copyright owner who has been omitted or incorrectly acknowledge***



# APPENDICES

## APPENDIX A

### Section A-1: Raw data for the solar photocatalytic degradation

**Table A.1** the raw data of the first order reaction rate of MO dye

Time (min)	concentration (C <sub>t</sub> ) using 1g L <sup>-1</sup> of TiO <sub>2</sub> /ZSM-5	concentration (C <sub>t</sub> ) using 2g L <sup>-1</sup> of TiO <sub>2</sub> /ZSM-5	concentration (C <sub>t</sub> ) using 2.5g L <sup>-1</sup> of TiO <sub>2</sub> /ZSM-5	concentration (C <sub>t</sub> ) using 3g L <sup>-1</sup> of TiO <sub>2</sub> /ZSM-5
0	0	0	0	0
30	11.8	6.36	10.1	14.48
60	8.0	3.4	6.8	10.1
90	4.2	1.38	2.59	6.54
120	2.5	0.58	0.98	3.2
150	0.62	0.30	0.43	1.2
180	0.2	0.09	0.15	0.89
Time (min)	ln (C <sub>0</sub> /C <sub>t</sub> ) using 1g/l of TiO <sub>2</sub> /ZSM-5	ln (C <sub>0</sub> /C <sub>t</sub> ) using 2g/l of TiO <sub>2</sub> /ZSM-5	ln (C <sub>0</sub> /C <sub>t</sub> ) using 2.5g/l of TiO <sub>2</sub> /ZSM-5	ln (C <sub>0</sub> /C <sub>t</sub> ) using 3g/l of TiO <sub>2</sub> /ZSM-5
0	0	0	0	0
30	0.527378	1.14507516	0.68013224	0.3229638
60	0.9162907	1.7719568	1.07265218	0.6816337
90	1.546463	2.673648	2.044074	1.1177951
120	2.066722	3.540459	3.0078048	1.8291498
150	3.473768	4.199705077	3.83274	2.8134107
180	4.50081017	5.40367788	4.8928522	3.102204518
<i>K<sub>app(MO)</sub></i>	<b>0.024459097</b>	<b>0.028677138</b>	<b>0.027284434</b>	<b>0.018375028</b>
<b>R<sup>2</sup></b>	<b>0.9867</b>	<b>0.9949</b>	<b>0.9514</b>	<b>0.9675</b>

**Table A.2** the raw data of the second order reaction rate of MO dye

Time (min)	concentration (C <sub>t</sub> ) using 1g L <sup>-1</sup> of TiO <sub>2</sub> /ZSM-5	concentration (C <sub>t</sub> ) using 2g L <sup>-1</sup> of TiO <sub>2</sub> /ZSM-5	concentration (C <sub>t</sub> ) using 2.5g L <sup>-1</sup> of TiO <sub>2</sub> /ZSM-5	concentration (C <sub>t</sub> ) using 3g L <sup>-1</sup> of TiO <sub>2</sub> /ZSM-5
0	0	0	0	0
30	11.8	6.3	10.1	14.48
60	8.0	3.4	6.8	10.1
90	4.2	1.38	2.59	6.54
120	2.5	0.58	0.98	3.2
150	0.62	0.3	0.43	1.2
180	0.2	0.09	0.15	0.89
Time (min)	q <sub>t</sub> (mg/g) using 1 g L <sup>-1</sup> of catalyst	q <sub>t</sub> (mg/g) using 2 g L <sup>-1</sup> of catalyst	q <sub>t</sub> (mg/g) using 2.5g L <sup>-1</sup> of catalyst	q <sub>t</sub> (mg/g) using 3 g L <sup>-1</sup> of catalyst
30	8.196	6.818	3.036	1.8386
60	12	8.3	5.263	3.2947
90	15.74	9.31	6.964	4.486
120	17.56	9.71	7.6	5.596
150	19.38	9.85	7.82	6.266
180	19.778	9.955	7.94	6.367
Time (min)	t/q <sub>t</sub> using 1 g L <sup>-1</sup> of catalyst TiO <sub>2</sub> /ZSM-5	t/q <sub>t</sub> using 2 g L <sup>-1</sup> of catalyst TiO <sub>2</sub> /ZSM-5	t/q <sub>t</sub> using 2.5 g L <sup>-1</sup> of catalyst TiO <sub>2</sub> /ZSM-5	t/q <sub>t</sub> using 3 g L <sup>-1</sup> of catalyst TiO <sub>2</sub> /ZSM-5
30	3.66	4.4	7.6	16.316
60	5	7.228	11.4	18.211
90	5.718	9.66	12.923	20.06
120	6.87	12.358	15.789	21.44
150	7.739	15.228	19.18	23.938
180	9.1	18.081	22.67	28.27
<b>slope</b>	<b>0.034827619</b>	<b>0.090574286</b>	<b>0.09672</b>	<b>0.074600952</b>
<b>q<sub>c</sub></b>	<b>28.7128</b>	<b>11.0406</b>	<b>10.3391</b>	<b>13.40466</b>
<b>Intercept</b>	<b>2.690933333</b>	<b>1.648866667</b>	<b>4.7714</b>	<b>13.5394</b>
<b>K2(MO)</b>	<b>0.0004507</b>	<b>0.004975</b>	<b>0.00196</b>	<b>0.000411</b>
<b>R<sup>2</sup></b>	<b>0.994</b>	<b>0.9994</b>	<b>0.9585</b>	<b>0.9893</b>

**Table A.3** the raw data of the first order reaction rate of the 10 mg L<sup>-1</sup> concentration of the MB degradation

Time (min)	TiO <sub>2</sub>	C <sub>t</sub> /C <sub>0</sub> TiO <sub>2</sub> /ZSM-5	C <sub>t</sub> /C <sub>0</sub> 5% RGO/TiO <sub>2</sub> /ZSM-5	C <sub>t</sub> /C <sub>0</sub> 10% RGO/TiO <sub>2</sub> /ZSM-5	C <sub>t</sub> /C <sub>0</sub> 15% RGO/TiO <sub>2</sub> /ZSM-5
0	1	1	1	1	1
30	0.93	0.9	0.75	0.6	0.45
60	0.89	0.6	0.4	0.15	0.25
90	0.7	0.45	0.35	0.07	0.2
120	0.65	0.4	0.3	0.07	0.2
Time (min)	ln (C <sub>t</sub> /C <sub>0</sub> ) TiO <sub>2</sub>	ln (C <sub>t</sub> /C <sub>0</sub> ) TiO <sub>2</sub> /ZSM-5	ln (C <sub>t</sub> /C <sub>0</sub> ) 5% RGO/TiO <sub>2</sub> /ZSM-5	ln (C <sub>t</sub> /C <sub>0</sub> ) 10% RGO/TiO <sub>2</sub> /ZSM-5	ln (C <sub>t</sub> /C <sub>0</sub> ) 15% RGO/TiO <sub>2</sub> /ZSM-5
0	0	0	0	0	0
30	0.0725	0.105	0.287	0.51	0.7985
60	0.1165	0.5108	0.916	1.89	1.386
90	0.356	0.798	1.049	2.659	1.61
120	0.431	0.916	1.2	2.659	1.61
Kapp(min)×10 <sup>3</sup>	3.818	8.416	10.54	24.89	13.43
R <sup>2</sup>	0.9315	0.9628	0.927	0.9202	0.8549

**Table A.4** the raw data of the second order reaction rate of the 10 mg L<sup>-1</sup> concentration of the MB degradation

Time (min)	TiO <sub>2</sub> q <sub>t</sub>	TiO <sub>2</sub> /ZSM-5 q <sub>t</sub>	5% RGO/TiO <sub>2</sub> /ZSM-5 q <sub>t</sub>	10% RGO/TiO <sub>2</sub> /ZSM-5 q <sub>t</sub>	15% RGO/TiO <sub>2</sub> /ZSM-5 q <sub>t</sub>
30	18	18.2	18.5	18.8	19.1
60	18.2	18.8	19.2	19.7	19.5
90	18.2	19.1	19.3	19.8	19.6
120	18.26	19.2	19.4	19.8	19.6
Time (min)	TiO <sub>2</sub> t/q <sub>t</sub>	t/q <sub>t</sub> TiO <sub>2</sub> /ZSM-5	t/q <sub>t</sub> 5% RGO/TiO <sub>2</sub> /ZSM-5	t/q <sub>t</sub> 10% RGO/TiO <sub>2</sub> /ZSM-5	t/q <sub>t</sub> 15% RGO/TiO <sub>2</sub> /ZSM-5
30	1.66	1.64	1.73	1.6	1.57
60	3.3	3.2	3.1	3.04	3.14
90	4.9	4.7	4.66	4.54	4.59
120	6.57	6.25	6.18	6.06	6.12
Slope	0.05443	0.0511	0.0497	0.0496	0.05033
q <sub>e</sub>	20.31	19.56	20.12	20.16	19.88
Intercept	0.025	0.115	0.19	0.09	0.08
K <sub>2</sub>	.1141	0.0227	0.013	0.027	0.0316
R <sup>2</sup>	0.9994	0.9993	0.9999	0.9989	0.999

**Table A.5** the raw data of the first order reaction rate of the 20 mg L<sup>-1</sup> concentration of the MB degradation

Time (min)	TiO <sub>2</sub>	C <sub>t</sub> /C <sub>0</sub> TiO <sub>2</sub> /ZSM-5	C <sub>t</sub> /C <sub>0</sub> 5% RGO/TiO <sub>2</sub> /ZSM-5	C <sub>t</sub> /C <sub>0</sub> 10% RGO/TiO <sub>2</sub> /ZSM-5	C <sub>t</sub> /C <sub>0</sub> 15% RGO/TiO <sub>2</sub> /ZSM-5
0	1	1	1	1	1
30	0.98	0.8	0.7	0.43	0.4
60	0.96	0.6	0.45	0.2	0.34
90	0.9	0.55	0.4	0.19	0.28
120	0.9	0.5	0.36	0.18	0.28
Time (min)	ln (C <sub>t</sub> /C <sub>0</sub> ) TiO <sub>2</sub>	ln (C <sub>t</sub> /C <sub>0</sub> ) TiO <sub>2</sub> /ZSM-5	ln (C <sub>t</sub> /C <sub>0</sub> ) 5% RGO/TiO <sub>2</sub> /ZSM-5	ln (C <sub>t</sub> /C <sub>0</sub> ) 10% RGO/TiO <sub>2</sub> /ZSM-5	ln (C <sub>t</sub> /C <sub>0</sub> ) 15% RGO/TiO <sub>2</sub> /ZSM-5
0	0	0	0	0	0
30	0.02	0.2231	0.3566	0.844	0.916
60	0.041	0.51	0.798	1.61	1.08
90	0.105	0.597	0.916	1.661	1.273
120	0.105	0.693	1.02	1.714	1.73
Kapp(min) × 10 <sup>3</sup>	2.883	5.86	8.66	14.15	12.72
R <sup>2</sup>	0.922	0.9444	0.9217	0.817	0.8989

**Table A.6** the raw data of the second order reaction rate of the 20 mg L<sup>-1</sup> concentration of the MB degradation.

Time (min)	TiO <sub>2</sub> q <sub>t</sub>	TiO <sub>2</sub> /ZSM-5 q <sub>t</sub>	5% RGO/TiO <sub>2</sub> /ZSM-5 q <sub>t</sub>	10% RGO/TiO <sub>2</sub> /ZSM-5 q <sub>t</sub>	15% RGO/TiO <sub>2</sub> /ZSM-5 q <sub>t</sub>
30	39.2	32	28	17.2	16
60	38.4	24	18	8	13.6
90	36	22	16	7.6	11.2
120	36	20	14.4	7.2	11.2
time	t/q <sub>t</sub> TiO <sub>2</sub>	t/q <sub>t</sub> TiO <sub>2</sub> /ZSM-5	t/q <sub>t</sub> 5% RGO/TiO <sub>2</sub> /ZSM-5	t/q <sub>t</sub> 10% RGO/TiO <sub>2</sub> /ZSM-5	t/q <sub>t</sub> 15% RGO/TiO <sub>2</sub> /ZSM-5
30	0.76	0.93	1.14	1.74	1.87
60	1.56	2.5	3.34	7.5	4.41
90	2.5	4.1	5.62	11.84	8
120	3.34	6	8.34	16.67	10.7
Slope	0.02893	0.05603	0.0796	0.16376	0.10026
q <sub>e</sub>	24.46	17.85	12.56	6.1	10
Intercept	-0.13	-0.82	-1.36	-2.845	-1.275
K <sub>2</sub>	0.1354	0.0038	0.00466	0.00944	0.00784
R <sup>2</sup>	0.9992	0.9978	0.9974	0.9967	0.9957

**Table A.7** the raw data of the first order reaction rate of the 30 mg L<sup>-1</sup> concentration of the MB degradation

Time (min)	C <sub>t</sub> /C <sub>0</sub> TiO <sub>2</sub>	C <sub>t</sub> /C <sub>0</sub> TiO <sub>2</sub> /ZSM-5	C <sub>t</sub> /C <sub>0</sub> 5% RGO/TiO <sub>2</sub> /ZSM-5	C <sub>t</sub> /C <sub>0</sub> 10% RGO/TiO <sub>2</sub> /ZSM-5	C <sub>t</sub> /C <sub>0</sub> 15% RGO/TiO <sub>2</sub> /ZSM-5
0	1	1	1	1	1
30	0.98	0.84	0.76	0.46	0.45
60	0.96	0.67	0.53	0.35	0.37
90	0.94	0.55	0.44	0.22	0.3
120	0.92	0.55	0.48	0.22	0.3
Time (min)	ln (C <sub>t</sub> /C <sub>0</sub> ) of TiO <sub>2</sub>	ln (C <sub>t</sub> /C <sub>0</sub> ) of TiO <sub>2</sub> /ZSM-5	ln (C <sub>t</sub> /C <sub>0</sub> ) 5% RGO/TiO <sub>2</sub> /ZSM-5	ln (C <sub>t</sub> /C <sub>0</sub> ) of 10% RGO/TiO <sub>2</sub> /ZSM-5	ln (C <sub>t</sub> /C <sub>0</sub> ) 15% RGO/TiO <sub>2</sub> /ZSM-5
0	0	0	0	0	0
30	0.02	0.1743	0.2744	0.7765	0.798
60	0.0408	0.4	0.634	1.05	0.9942
90	0.0618	0.597	0.821	1.514	1.2039
120	0.0833	0.597	0.734	1.514	1.2039
Kapp(min)×10 <sup>3</sup>	2.334	5.38	6.71	12.5	9.37
R <sup>2</sup>	0.99	0.9408	0.852	0.7949	0.8993

**Table A.8** The raw data of the second order reaction rate of the 30 mg L<sup>-1</sup> concentration of the MB degradation.

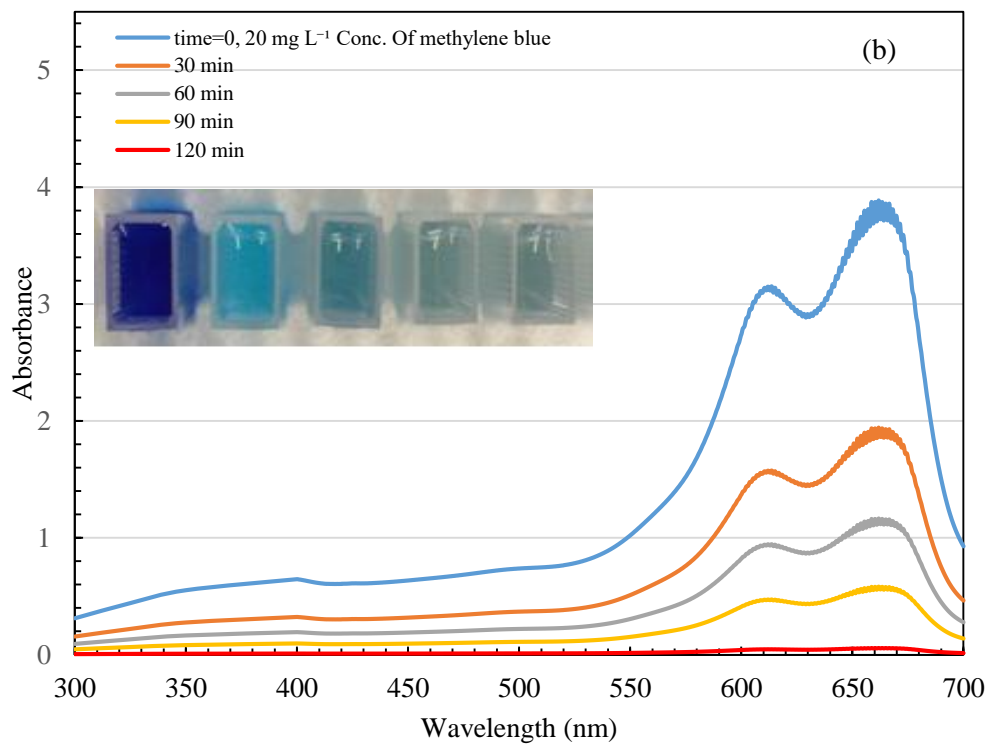
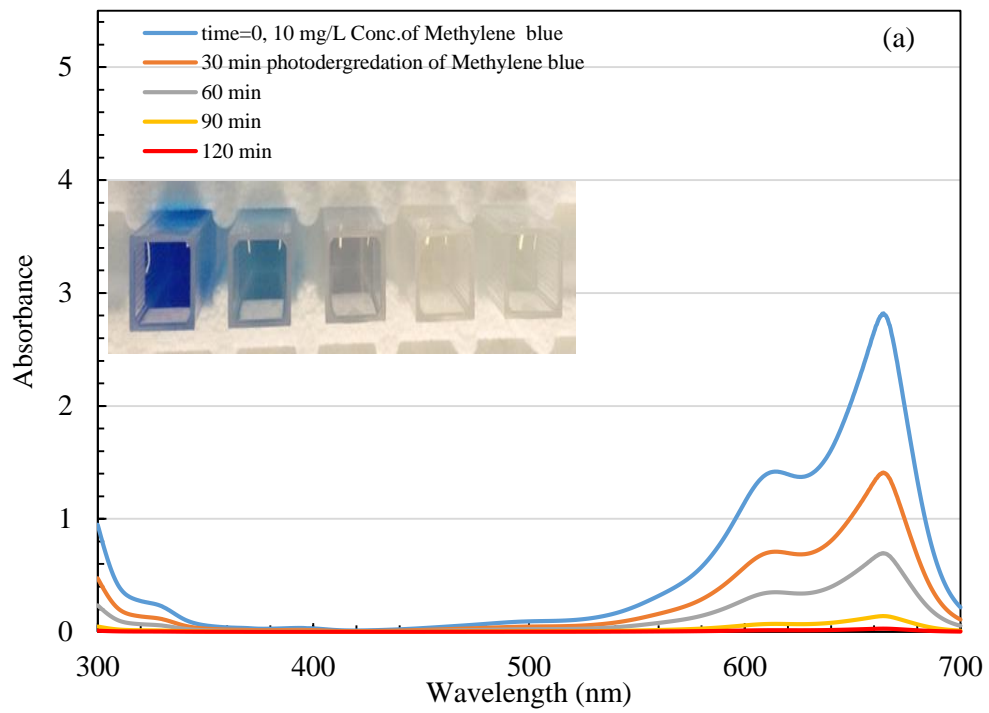
Time (min)	TiO <sub>2</sub> q <sub>t</sub>	TiO <sub>2</sub> /ZSM-5 q <sub>t</sub>	5% RGO/TiO <sub>2</sub> /ZSM-5 q <sub>t</sub>	10% RGO/TiO <sub>2</sub> /ZSM-5 q <sub>t</sub>	15% RGO/TiO <sub>2</sub> /ZSM-5 q <sub>t</sub>
30	58.8	50.4	45.6	27.6	27
60	57.6	40.2	31.8	21	22.2
90	56.4	33	26.4	13.2	18
120	55.2	33	28.8	13.2	18
Time (min)	t/q <sub>t</sub> TiO <sub>2</sub>	t/q <sub>t</sub> TiO <sub>2</sub> /ZSM-5	t/q <sub>t</sub> 5% RGO/TiO <sub>2</sub> /ZSM-5	t/q <sub>t</sub> 10% RGO/TiO <sub>2</sub> /ZSM-5	t/q <sub>t</sub> 15% RGO/TiO <sub>2</sub> /ZSM-5
30	0.51	0.59	0.7	1.08	1.11
60	1.04	1.49	1.8867	2.85	2.7
90	1.59	2.72	3.41	6.82	5
120	2.17	3.63	4.16	9.1	6.67
Slope	0.01843	0.0345	0.03967	0.09343	0.06326
q <sub>e</sub>	30.25	28.98	25.2	10.71	15.8
Intercept	-0.055	-0.48	-0.43665	-2.045	-0.875
K <sub>2</sub>	0.1671	0.00248	0.0036	0.00426	0.00457
R <sup>2</sup>	0.9996	0.9961	0.9848	0.9795	0.995

**Table A.9** The raw data of the first order reaction rate of the 40 mg L<sup>-1</sup> concentration of the MB degradation

Time (min)	C <sub>t</sub> /C <sub>0</sub> TiO <sub>2</sub>	C <sub>t</sub> /C <sub>0</sub> TiO <sub>2</sub> /ZSM-5	C <sub>t</sub> /C <sub>0</sub> 5% RGO/TiO <sub>2</sub> /ZSM-5	C <sub>t</sub> /C <sub>0</sub> 10% RGO/TiO <sub>2</sub> /ZSM-5	C <sub>t</sub> /C <sub>0</sub> 15% RGO/TiO <sub>2</sub> /ZSM-5
0	1	1	1	1	1
30	0.99	0.7	0.63	0.4	0.5
60	0.97	0.68	0.58	0.36	0.48
90	0.95	0.64	0.55	0.32	0.46
120	0.94	0.6	0.52	0.3	0.44
Time (min)	ln (C <sub>t</sub> /C <sub>0</sub> ) TiO <sub>2</sub>	ln (C <sub>t</sub> /C <sub>0</sub> ) TiO <sub>2</sub> /ZSM-5	ln (C <sub>t</sub> /C <sub>0</sub> ) 5% RGO/TiO <sub>2</sub> /ZSM-5	ln (C <sub>t</sub> /C <sub>0</sub> ) 10% RGO/TiO <sub>2</sub> /ZSM-5	ln (C <sub>t</sub> /C <sub>0</sub> ) 15% RGO/TiO <sub>2</sub> /ZSM-5
0	0	0	0	0	0
30	0.01	0.3566	0.46	0.916	0.693
60	0.03	0.3856	0.544	1.02	0.733
90	0.051	0.446	0.597	1.139	0.7765
120	0.061	0.511	0.6539	1.204	0.821
Kapp(min)×10 <sup>3</sup>	1.9523	3.704	4.816	8.77	5.751
R <sup>2</sup>	0.9732	0.7796	0.7601	0.7178	0.6386

**Table A.10** The raw data of the second order reaction rate of the 40 mg L<sup>-1</sup> concentration of the MB degradation.

Time (min)	TiO <sub>2</sub> q <sub>t</sub>	TiO <sub>2</sub> /ZSM-5 q <sub>t</sub>	5% RGO/TiO <sub>2</sub> /ZS M-5 q <sub>t</sub>	10% RGO/TiO <sub>2</sub> /ZS M-5 q <sub>t</sub>	15% RGO/TiO <sub>2</sub> /ZS M-5 q <sub>t</sub>
30	79.2	56	50.4	32	40
60	77.6	54.4	46.4	28.8	38.4
90	76	51.2	44	25.6	36.8
120	75.2	48	41.6	24	35.2
Time (min)	TiO <sub>2</sub> t/q <sub>t</sub>	TiO <sub>2</sub> /ZSM-5 t/q <sub>t</sub>	5% RGO/TiO <sub>2</sub> /ZS M-5 t/q <sub>t</sub>	10% RGO/TiO <sub>2</sub> /ZS M-5 t/q <sub>t</sub>	15% RGO/TiO <sub>2</sub> /ZS M-5 t/q <sub>t</sub>
30	0.378	0.571	0.595	0.937	0.75
60	0.773	1.1	1.293	2.083	1.562
90	1.184	1.75	2.045	3.515	2.445
120	1.59	2.5	2.884	5	3.41
Slope	0.01349	0.02145	0.02539	0.045403	0.02954
q <sub>e</sub>	33.81	46.6	39.37	22	33.852
Intercept	-0.0305	-0.129	-0.2005	-0.5215	-0.174
K <sub>2</sub>	0.1822	0.00357	0.00321	0.00396	0.005
R <sup>2</sup>	0.9987	0.9941	0.9983	0.9966	0.9985





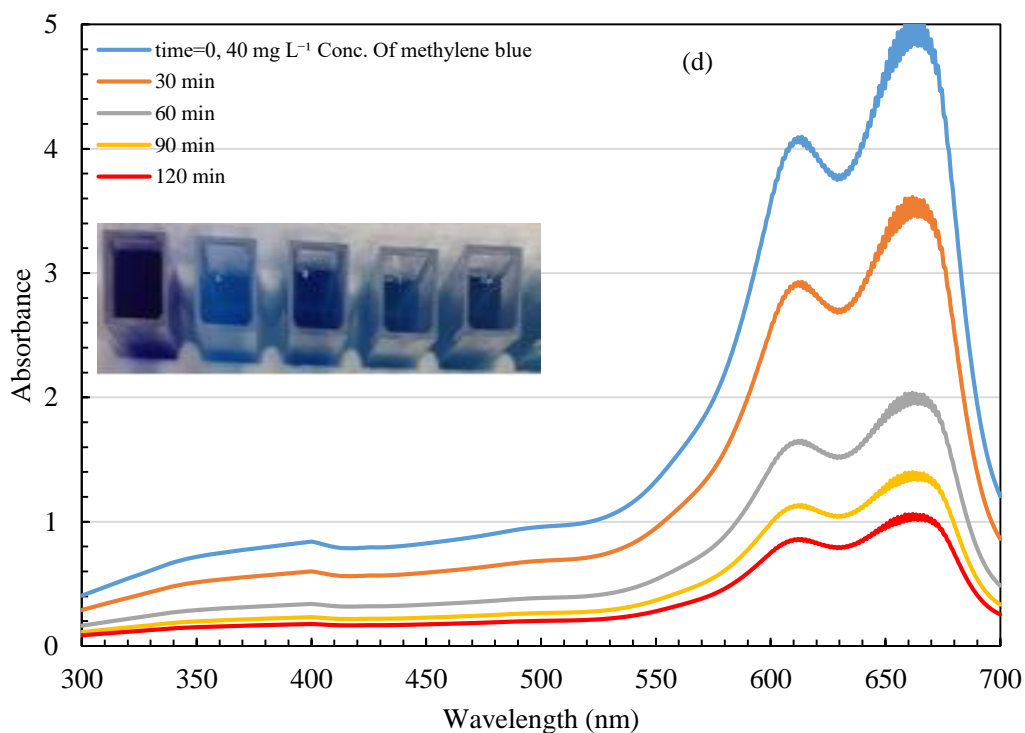
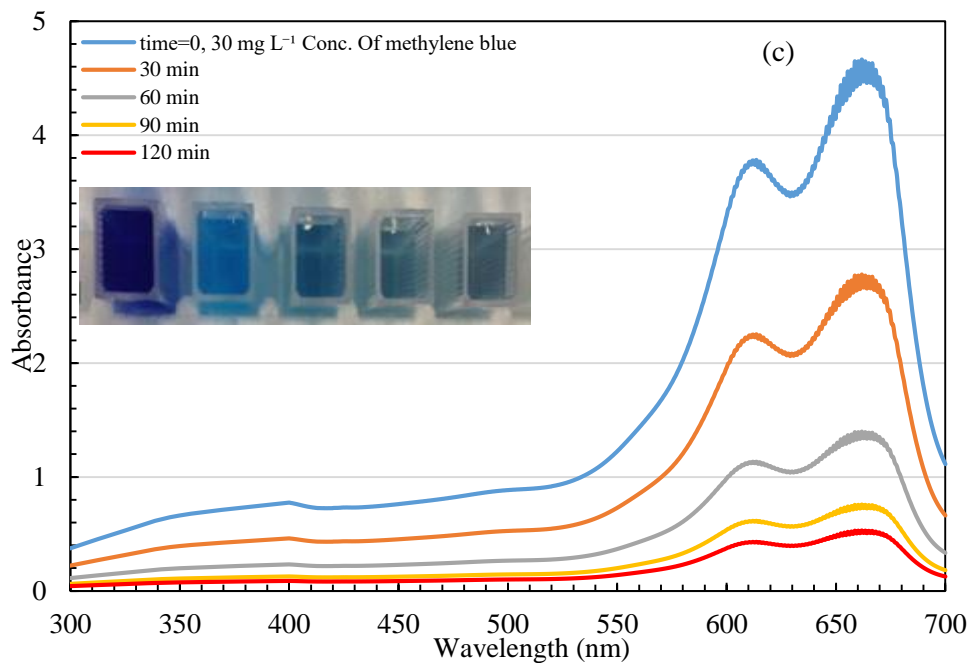


**Figure A. 1** the spectra absorbance of MB dye at different concentration (a)  $10 \text{ mg L}^{-1}$ ,  $20 \text{ mg L}^{-1}$ ,  $30 \text{ mg L}^{-1}$  and  $40 \text{ mg L}^{-1}$  during 120 min contact time,  $500 \text{ mg L}^{-1}$  of 10%RGO/TiO<sub>2</sub>/ZSM-5 mesoporous at room temperature

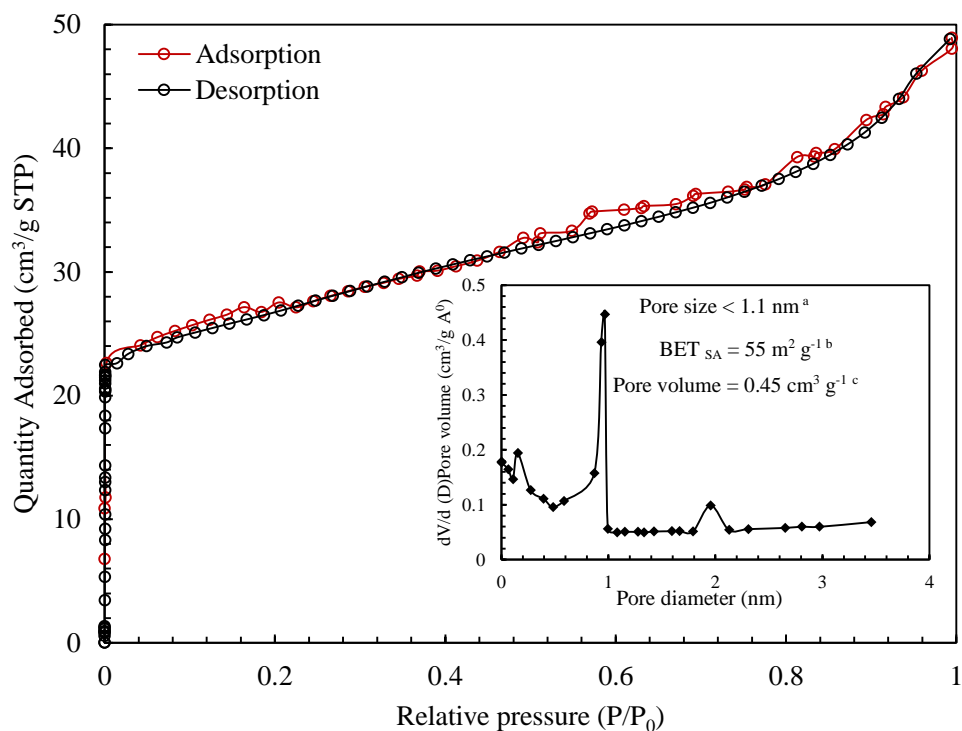


**Figure A. 2** BET specific surface area of the Non-mesoporous 10% RGO/TiO<sub>2</sub>/ZSM-5

<sup>a</sup> The specific surface area was evaluated by BET method.

<sup>b</sup> The pore volume was obtained from the BJH Desorption cumulative volume of pores between 1.0000 nm and 50.0000 nm diameter.

<sup>c</sup> The average pore diameter was calculated using the desorption branch of the isotherm and BJH model

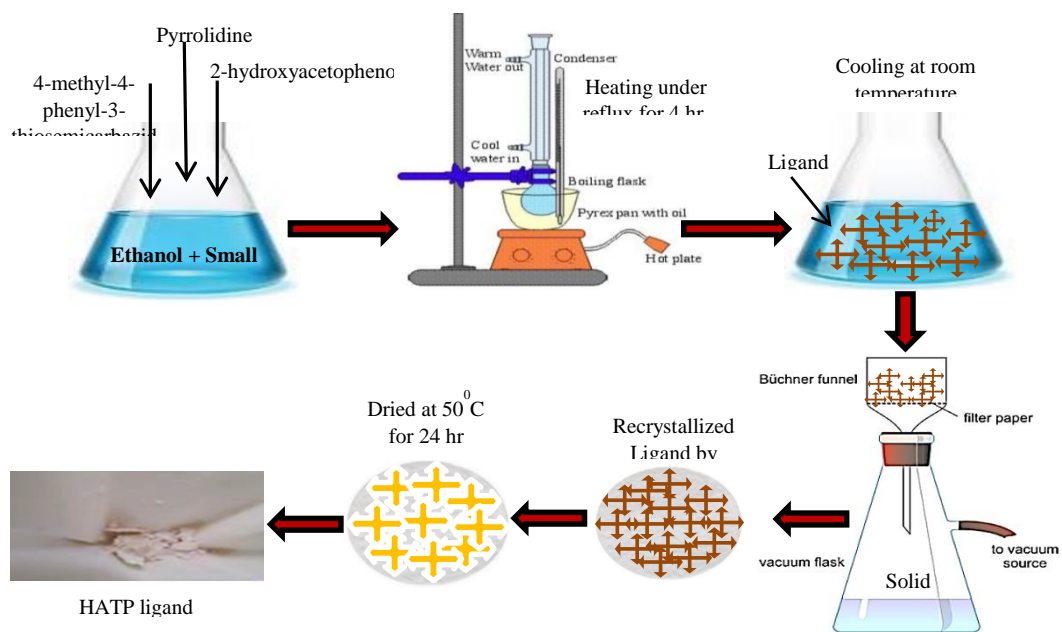


**Figure A. 3** Preparation procedure of the HATP ligand

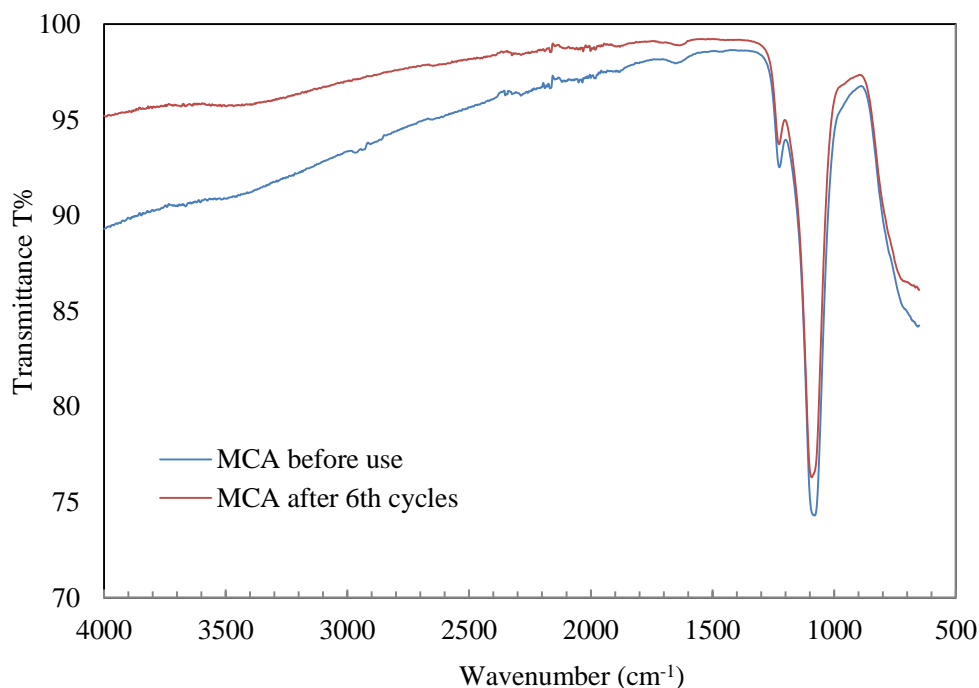


**Figure A. 4** FTIR analysis spectrum of the synthesized MCA before and after used

### Section A-2 Raw data for visual adsorption detection of Hg (II)

**Table A. 11** the change of colour optimization of Hg(II) ions concentrations at pH 12.5 and (b) was represented the calibration profile of Hg(II) ions concentrations with spectral absorbance at  $\lambda=387$  nm

Hg (II) ion concentrations ( $\mu\text{m}$ )	A-A <sub>0</sub> a.u. (at $\lambda= 325$ ), with Matrix	A-A <sub>0</sub> a.u. (at $\lambda= 325$ ), Free Matrix
0.0249	0	0
0.0997	0.133637	0.132667
0.249	0.203969	0.198826
0.4985	0.26727	0.246615
1.5672	0.318053	0.3111
4.985	0.34456	0.33556
9.9705	0.367421	0.352241

**Table A. 12** the low limited responses for Hg (II) ions with a liner fit in the Hg (II) ions concentration range

Hg (II) ion concentrations ( $\mu\text{m}$ )	A-A0 a.u. (at $\lambda= 325$ ), with Matrix
0.0249	0.0266
0.0997	0.06651
0.249	0.15562
0.4985	0.277

**Table A. 13** Adsorption isotherm of Hg (II) ions of the MCA. (Initial concentrations: 2.65–75  $\text{mg L}^{-1}$ ; shaking time: 2 h; adsorbent amount (MCA): 20 mg; volume of solution: 100 ml

$C_0 \text{ mg L}^{-1}$	$C_e \text{ mg L}^{-1}$	$q_e(\text{mg/g})$
2.65	0.5	10.75
3.66	0.53	15.65
4.41	0.61	19
9.93	1.77	40.8
28.67	8.55	100.6
54.43	26.71	138.6
75	45.38	148

**Table A. 14** the linear form as fitted by the Langmuir isotherms model

$C_e \text{ mg L}^{-1}$	$C_e /q_e ( \text{ g L}^1)$
0.5	0.0465
0.53	0.0338
0.61	0.032
1.77	0.0433
8.55	0.085
26.71	0.1927
45.38	0.3066

### Section A-3 Raw data for visual adsorption detection of lead (Pb<sup>2+</sup>)

**Table A. 15** the change of colour optimization of Pb<sup>2+</sup> concentrations at pH 6.0 and (b) was

Pb (II) ion concentrations (µm)	R-R <sub>0</sub> a.u. (at λ= 440), with Matrix	R-R <sub>0</sub> a.u. (at λ= 440), Free Matrix
0.005	0.1436	0.14
0.02	0.18562	0.18
0.05	0.254	0.23
0.1	0.31933	0.297
0.5	0.52135	0.5111
1.0	0.55	0.541
2.0	0.6266	0.6156

represented the calibration profile of Pb<sup>2+</sup> concentrations with spectral absorbance at λ= 440 nm

**Table A. 16** the low limited responses for Pb<sup>2+</sup> with a liner fit in the Pb<sup>2+</sup> concentration range

Pb <sup>2+</sup> concentrations (µm)	R-R <sub>0</sub> a.u. (at λ= 440), with Matrix
0.005	0.1436
0.01	0.18568
0.02	0.254
0.05	0.319333
0.1	0.521355

**Table A. 17** Adsorption isotherm of Pb<sup>2+</sup> of the MzCA. (Initial concentrations: 8.0-50.0 mg L<sup>-1</sup>; shaking time: 2 h; adsorbent amount (MzCA): 10 mg; volume of solution: 20 ml

C <sub>0</sub> mg L <sup>-1</sup>	C <sub>e</sub> mg L <sup>-1</sup>	q <sub>e</sub> (mg/g)
8	4	8
15	4	12
22	7.5	13
30	14.6	14.8
35	22	16
40	35	16
50	42	16

**Table A. 18** the linear form as fitted by the Langmuir isotherms model for lead ions detection.

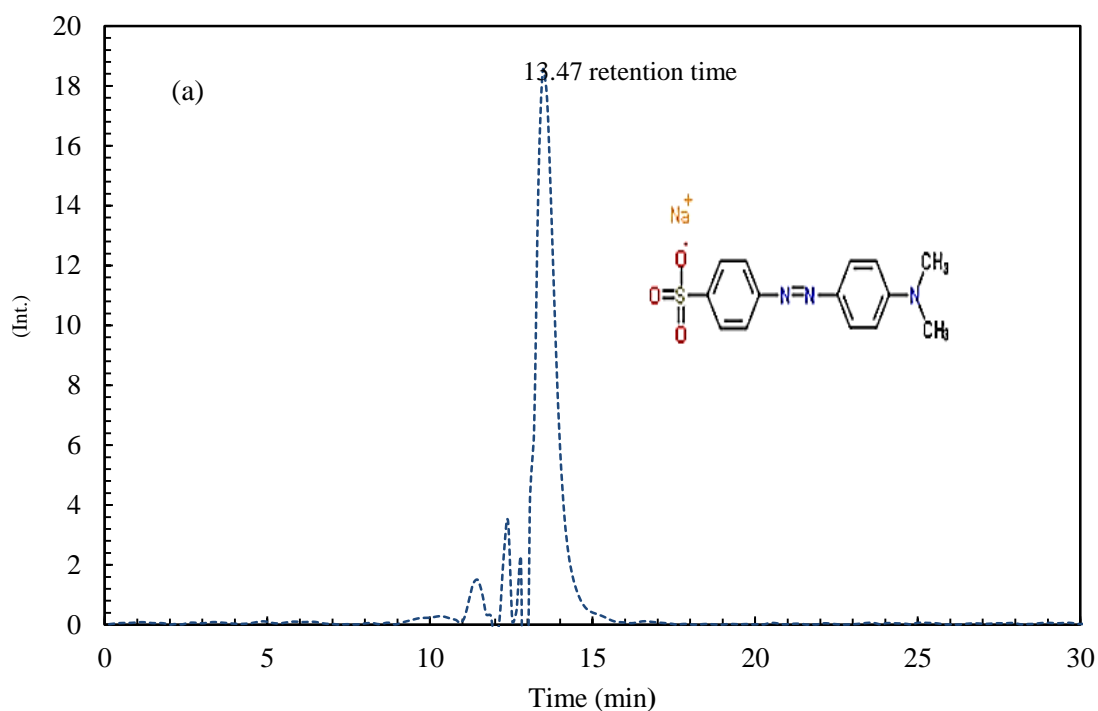
C <sub>e</sub> mg L <sup>-1</sup>	C <sub>e</sub> /q <sub>e</sub> (g L <sup>-1</sup> )
4	0.3
4	0.5
7.5	0.56
14.6	0.981

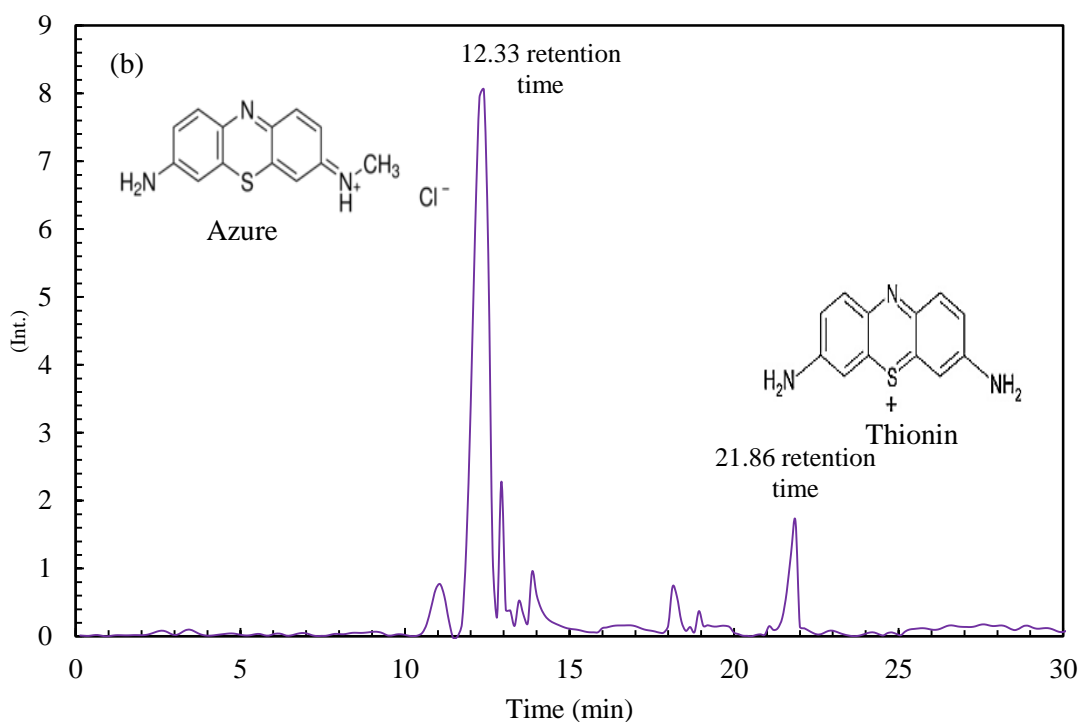
## APPENDIX B

### Detection of Organic Compounds And calibration curves

#### B-1 HPLC Detections

As described in the chapter 3, the detection of the main pollutants and their intermediates were identified and quantified by employing the High Performance Liquid Chromatograph (HPLC) analysis. Figure B-1 depicts the typical HPLC chromatograms results of the retention time for all the organic compounds used in this project. Interestingly, each compound has a different retention time peak as a result of different absorption rates even their concentrations are equal.

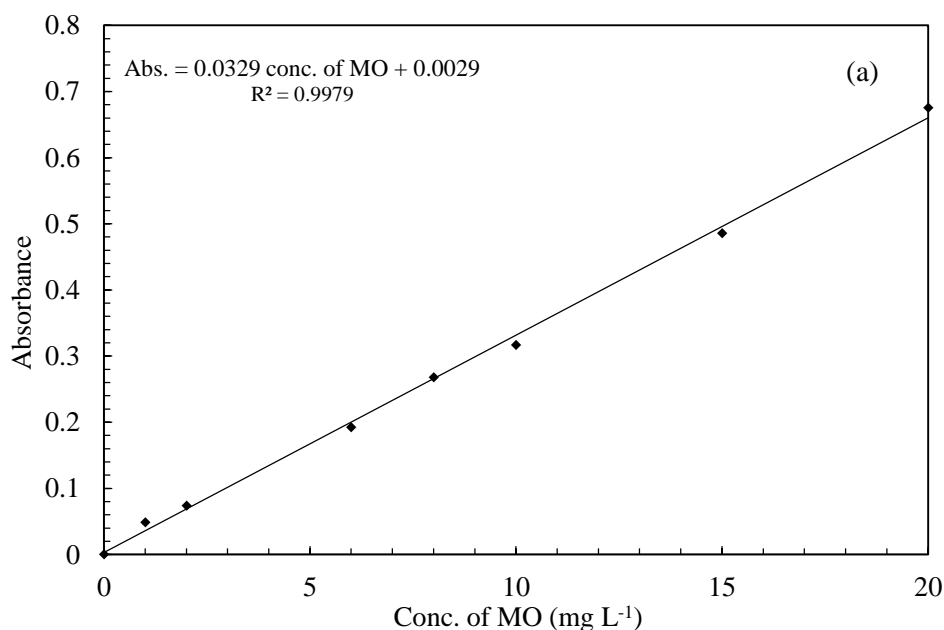




**Figure B. 1** typical HPLC chromatograms results of the retention time for the organic compounds used in this research: (a) Methylene blue (b) their intermediates (Azure and Thionin)

### B-2 Calibration curves

The experimental calibration measurements were duplicated to assure obtaining the accuracy values. The following linear calibration equations with a correlation coefficients were obtained for the pollutant model with their intermediate compounds.



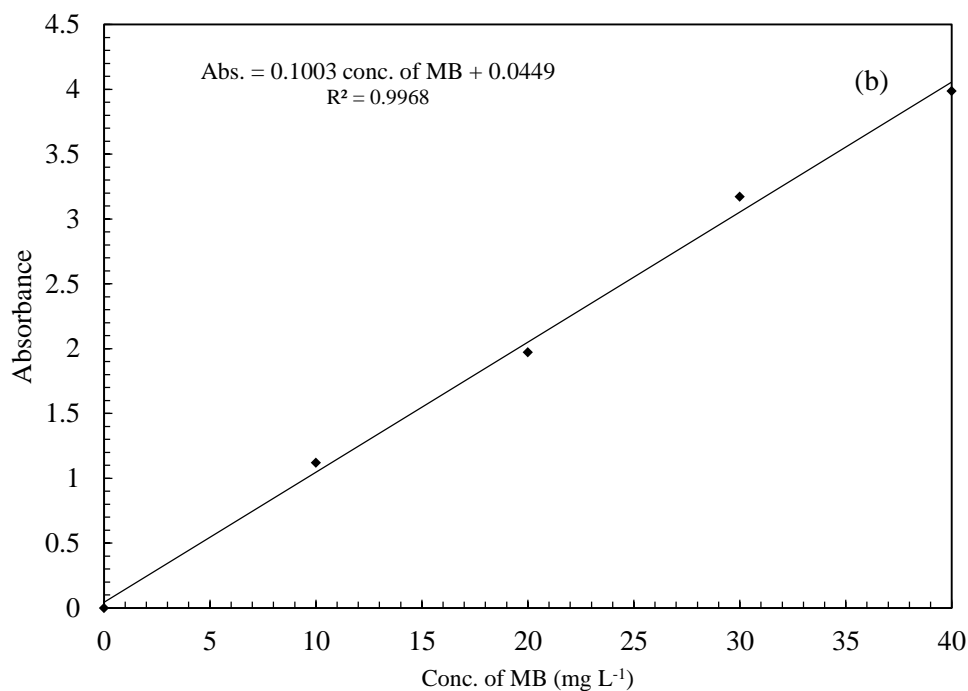


**Figure B. 2** The calibration curves with equations and correlation coefficients of (a) MO dye and (b) MB dye using UV-Vis diffuse spectrophotometer analysis between the absorption wavelength ( $\lambda$ ) range of 300-700nm

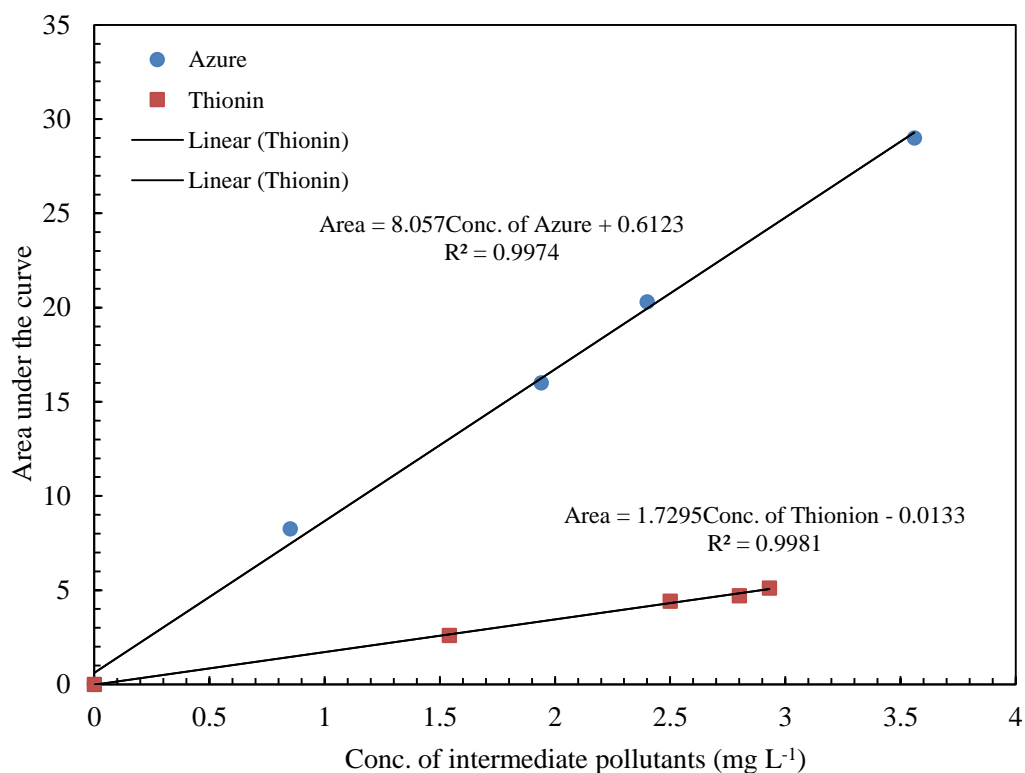


**Figure B. 3** The calibration curves with equations of intermediates compounds of Azure and Thionin



## APPENDIX C

### *Publisher permission for Chapter 4*

Home Account Info Help



**Title:** Synthesis a novel multilamellar mesoporous TiO<sub>2</sub>/ZSM-5 for photo-catalytic degradation of methyl orange dye in aqueous media

**Author:** Hussein Znad, Khalid Abbas, Sufia Hena, Md. Rabiul Awual

**Publication:** Journal of Environmental Chemical Engineering

**Publisher:** Elsevier

**Date:** February 2018

© 2017 Elsevier Ltd. All rights reserved.

Logged in as:  
Khalid Abbas  
Account #:  
3001367435

LOGOUT

Please note that, as the author of this Elsevier article, you retain the right to include it in a thesis or dissertation, provided it is not published commercially. Permission is not required, but please ensure that you reference the journal as the original source. For more information on this and on your other retained rights, please visit: <https://www.elsevier.com/about/our-business/policies/copyright#Author-rights>

BACK CLOSE WINDOW

Copyright © 2018 Copyright Clearance Center, Inc. All Rights Reserved. [Privacy statement](#). [Terms and Conditions](#). Comments? We would like to hear from you. E-mail us at [customercare@copyright.com](mailto:customercare@copyright.com)

### *Publisher permission for Chapter 6*

Home Account Info Help



**Title:** A ligand anchored conjugate adsorbent for effective mercury (II) detection and removal from aqueous media

**Author:** Khalid Abbas, Hussein Znad, Md. Rabiul Awual

**Publication:** Chemical Engineering Journal

**Publisher:** Elsevier

**Date:** 15 February 2018

© 2017 Elsevier B.V. All rights reserved.

Logged in as:  
Khalid Abbas  
Account #:  
3001367435

LOGOUT

Please note that, as the author of this Elsevier article, you retain the right to include it in a thesis or dissertation, provided it is not published commercially. Permission is not required, but please ensure that you reference the journal as the original source. For more information on this and on your other retained rights, please visit: <https://www.elsevier.com/about/our-business/policies/copyright#Author-rights>

BACK CLOSE WINDOW

Copyright © 2018 Copyright Clearance Center, Inc. All Rights Reserved. [Privacy statement](#). [Terms and Conditions](#). Comments? We would like to hear from you. E-mail us at [customercare@copyright.com](mailto:customercare@copyright.com)

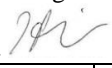
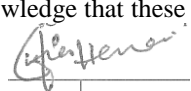
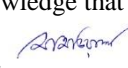
Co-Author Attribution Statement

**Paper 1:** Synthesis a novel multilamellar mesoporous TiO<sub>2</sub>/ZSM-5 for photo-catalytic degradation of methyl orange dye in aqueous media.

Volume 6, Issue 1, February 2018, Pages 218-227

Hussein Znad , Khalid Abbas, Sufia Hena , Md. Rabiul Awual

**Table 1-C: Co-Author attribution for chapter 4**

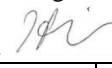
	<i>Conception &amp; design</i>	<i>Acquisition Of data &amp; method</i>	<i>Data Conditioning &amp; manipulation</i>	<i>Analysis &amp; Statistical method</i>	<i>Interpretation &amp; discussion</i>	<i>Final approval</i>
Dr. Hussein Znad	x		x	x		x
I acknowledge that these represent my contribution to the above research output. Signed. 						
Dr. Sufia Hena	x			x	x	x
I acknowledge that these represent my contribution to the above research output. Signed. 						
Dr. Md. Rabiul Awual	x			x	x	x
I acknowledge that these represent my contribution to the above research output. Signed. 						

**Paper 2:** A ligand anchored conjugate adsorbent for effective mercury (II) detection and removal from aqueous media.

Chemical Engineering Journal Vol (334), (2018) pages 432–443

Khalid Abbas , Hussein Znad, Md. Rabiul Awual

**Table 2-C: Co-Author attribution for chapter 6**

	<i>Conception And design</i>	<i>Acquisition Of data &amp; method</i>	<i>Data Conditioning &amp; manipulation</i>	<i>Analysis &amp; Statistical method</i>	<i>Interpretation &amp; discussion</i>	<i>Final approval</i>
Dr. Hussein Znad	x		x	x		x
I acknowledge that these represent my contribution to the above research output. Signed. 						
Dr. Md. Rabiul Awual	x			x	x	x
I acknowledge that these represent my contribution to the above research output. Signed. 